A path towards better cancer drugs: Modeling interactions between antimitotic agents and tubulin

by

Cassandra Churchill

A thesis submitted in partial fulfillment of the requirements for the degree of

Doctor of Philosophy

Department of Chemistry

University of Alberta

Abstract

Antimitotic agents, a class of cancer chemotherapies, target the tubulin protein in microtubules to suppress microtubule dynamics and affect the segregation of chromosomes during cell division. A variety of antimitotic agents are known, which range in status from clinically-approved agents to those in preclinical studies. For example, three clinically-approved taxanes are in use, while laulimalide has experienced many issues in preclinical studies. Regardless of the status of a compound, in many instances there is limited information regarding the ligand–tubulin interactions in the binding site, as well as the global effects on tubulin that result from the binding of the compound. Atomic-resolution models of ligand–tubulin interactions are necessary to develop an enhanced understanding of how these agents work. Using molecular modeling, methods derived from classical mechanics and quantum mechanics are used to investigate ligand–tubulin interactions on a local and global scale.

The binding of laulimalide and laulimalide analogues to tubulin is examined using an expanded computational model and molecular mechanics, which provided the first atomistic model of laulimalide in a microtubule-like environment. Specific laulimalide–residue interactions were identified, indicating the importance of an intramolecular hydrogen bond, direct and water-mediated ligand–tubulin hydrogen bonds, and ligand–tubulin π–π interactions. A correlation was noted between cytotoxicity and select ligand–protein interactions, establishing a laulimalide pharmacophore that may be used in the design of novel laulimalide compounds. The importance of a specific macrocycle conformation was also established. Using the information gained from this computational model of the laulimalides, novel laulimalide-like compounds

ii

were also considered and their efficacy predicted, illustrating the utility of such a computational model.

Despite the clinical success of the taxanes, the mechanism of action of this class of drugs remains elusive, making rational design of related compounds difficult. A classical model revealed that the taxanes adopt different conformations in the binding site, but bring about a similar allosteric effect on tubulin. For the first time, this allosteric effect was traced from the drug binding site, across the tubulin protein. This establishes a metric by which the efficacy of other taxane-domain binders may be ranked in future rational drug design studies using computational models.

Quantum-mechanical descriptions of ligand–protein complexes are also obtained in this Thesis. The effects of electron correlation and implicit solvent are examined, and it is found that electron correlation plays a larger role in ranking taxane binding than the implicit solvent. The quantum-mechanical treatment also reveals that some ligand–residue interactions are destabilizing, a result that cannot be obtained through classical descriptions.

The work in this Thesis provides significant insights into the binding of different microtubule-targeting agents to tubulin. Atomic-resolution models allow for enhanced examination of ligand–tubulin complexes. The results obtained in this Thesis will be useful in guiding future drug design strategies for novel compounds with enhanced activity.

Preface

This Thesis contains material that has been previously published by C.D.M. Churchill and supervisors M. Klobukowski and J.A. Tuszynski.

A version of Chapter 2 of this Thesis has been published as Churchill, C. D. M.; Klobukowski, M.; Tuszynski, J. A. "The unique binding mode of laulimalide to two tubulin protofilaments." *Chemical Biology & Drug Design* 2015, *86*, 190–199. C.D.M. Churchill conducted the calculations, performed the analysis, and composed the manuscript for publication. M. Klobukowski and J.A. Tuszynski are the supervisory authors, and contributed to the project design and manuscript editing.

A version of Chapter 3 of this Thesis has been published as Churchill, C. D. M.; Klobukowski, M.; Tuszynski, J. A. "Analysis of the binding mode of laulimalide to microtubules: Establishing a laulimalide–tubulin pharmacophore." *The Journal of Biomolecular Structure and Dynamics.* 2015, DOI: 10.1080/07391102.2015.1078115. C.D.M. Churchill conducted the calculations, performed the analysis, and composed the manuscript for publication. M. Klobukowski and J.A. Tuszynski are the supervisory authors, and contributed to the project design and manuscript editing.

Chapter 4 contains unpublished work.

A version of Chapter 5 of this Thesis has been published as Churchill, C. D. M.; Klobukowski, M.; Tuszynski, J. A. "Elucidating the mechanism of action of the clinically approved taxanes: A comprehensive comparison of local and allosteric effects." *Chemical Biology & Drug Design* 2015, DOI 10.1111/cbdd.12595. C.D.M. Churchill conducted the calculations, performed the analysis, and composed the manuscript for publication M. Klobukowski and J.A. Tuszynski are the supervisory authors, and contributed to the project design and manuscript editing.

A version of Chapter 6 of this Thesis has been published as Churchill, C. D. M. "The Fragment Molecular Orbital method and understanding monomer polarization."

Chemical Physics Letters 2012, *554*, 185–189.

Chapter 7 contains unpublished work.

Chapter 1 (Introduction) and Chapter 8 (Conclusions) contain material from all of the aforementioned publications.

For my family.

Acknowledgements

Finally, I would like to thank my friends and family. I have met so many smart, talented, and passionate people in my time working at U of A, and I am especially thankful for Chris Fetterly and Rebecca Paliwoda. It is impossible to convey how much the friendships of Sarah Neufeld and Ashley Smith have enriched my life over the years. You two are more like family than friends, and have been the most perfect, fun, supportive, and encouraging people to surround myself with. A special thank you to the Neufeld, Scheifele, and Smith families for their love. And I have saved the best for last: thank you to my parents, Fred and Dolores, and my siblings, Amanda, Cherisse, and Theren. I dedicate my Thesis to you, my achievements are your achievements and this would not have been possible without your fierce support and unconditional love.

Table of Contents

List of Tables

xiii

List of Figures

List of Abbreviations and Acronyms

Amber	*assisted model building with energy refinement*
ASC	*apparent surface charge*
CAB	*cabazitaxel*
CC	*coupled cluster*
CCSD(T)	*coupled cluster with single, double, and perturbative triple excitations*
CI	*configuration interaction*
CM	*classical mechanics*
cryo-EM	*cryo-electron microscopy*
CS	*cyclostreptin*
DXL	*docetaxel*
FF	*force field*
FMO	*fragment molecular orbital*
GB	*generalized Born*
GDP	*guanosine diphosphate*
GMPCPP	*guanylyl-(alpha, beta)-methylene-diphosphonate; a GTP analogue*
GPU	*graphical processing unit*
GTP	*guanosine triphosphate*
HDX MS	*hydrogen-deuterium exchange mass spectrometry*
HF	*Hartree Fock*
HPLC	*high performance liquid chromatography*
IUPAC	*International Union of Pure and Applied Chemistry*
LLM	*laulimalide*
MDR	*multidrug resistance*

MDR1	*multidrug resistance protein 1*
MM	*molecular mechanics*
MM/GBSA	*molecular mechanics generalized-Born surface area*
MPn	n^{th}*-order Møller-Plesset perturbation theory*
MP2	*second order Møller-Plesset perturbation theory*
MS	*mass spectrometry*
MS/MS	*tandem mass spectrometry*
MT	*microtubule*
NVT	*constant number of particles, volume, and temperature; canonical ensemble*
NPT	*constant number of particles, pressure, and temperature; isothermal-isobaric ensemble*
PCM	*polarizable continuum model*
Pgp	*P-glycoprotein pump*
QM	*quantum mechanics*
RMSD	*root-mean-square deviation*
RMSF	*root-mean-square fluctuation*
SA	*surface area*
tacca	*taccalonolide*
TIPnP	*transferable intermolecular potential n point*
TXL	*paclitaxel*
vdW	*van der Waals*

List of Symbols

Å	*angstrom*
E	*energy*
$\hat{H}$	*The Hamiltonian operator*
G	*Gibbs free energy*
T	*kinetic energy*
$\hat{T}$	*kinetic energy operator*
T	*temperature*
V	*potential energy*
$\hat{V}$	*potential energy operator*
S	*entropy*
∇^2	*the Laplacian operator*
Ψ	*wavefunction*
$\boldsymbol{R}_A$	*nucleus A spatial coordinates*
$\boldsymbol{\zeta}_i$	*electron i coordinates, spatial and spin*
$\boldsymbol{r}_i$	*electron i coordinates, spatial*
$\psi(\boldsymbol{\zeta}_i)$	*spin orbital of electron i*
$\phi(\boldsymbol{r}_i)$	*spatial orbital of electron i*
$\chi_\mu(\boldsymbol{r_i})$	*basis function*
$\mathbf{D}$	*density matrix (FMO)*
$\mathbf{V}$	*environmental potential (FMO)*
ϵ_0	*permittivity of free space*
Δt	*time step*

Chapter 1

Introduction[*]

1.1 Scope

Microtubules, which segregate chromosomes during cell division, are targets for some of the most successful anticancer therapies in clinical use. A variety of antimitotic agents are known to bind to the tubulin protein within microtubules to alter the dynamicity of these structures. It is important to understand how these drugs interact with the protein and the mechanism by which they affect microtubule function. This will allow for the development of novel compounds with enhanced antimitotic properties.

A variety of microtubule-targeting compounds are in clinical and preclinical development. However, it is unknown how some of these agents interact in the binding sites on tubulin on a local scale, as well as how these agents affect tubulin on a global scale through allosteric effects. The work presented in this Thesis uses computational modeling to determine how antimitotic agents work and and what makes these agents successful. Specifically, molecular mechanics combined with molecular dynamics is used to study the structure and explore the dynamic behaviour of ligand–tubulin complexes. In addition, noncovalent interactions that govern ligand–tubulin binding are studied using a fully-quantum mechanical model.

1.2 Microtubules as a target for cancer chemotherapies

1.2.1 Microtubule structure, function, and dynamics

1.2.1.1 Function

A microtubule (MT) is a key component of the cytoskeleton, which plays important roles in cell structure, cell motility, cell signalling and transport, and the separation of chromosomes during cell division. For example, MTs form cilia and flagella, which are responsible for cell motility. They also bind with MT-associated proteins like the motor proteins kinesin and dynein, which are responsible for the intracellular transport of organelles and protein complexes.[5–10]

It is the role MTs play in cell division that makes these structures a target for cancer chemotherapies.[11] At the beginning of mitosis,[12,13] chromatin condenses into chromosomes and MTs, which originate from centrosomes, begin to organize for cell division. In the metaphase step of mitosis, chromosomes are aligned along the metaphase plate with MTs attached to the kinetochores on each chromosome (Figure 1.1). Subsequently, in anaphase the chromosomes are broken apart and the MTs move each sister chromatid to their respective centrosome at the poles of the cell. In order for the separation of chromosomes to occur, a cell cycle checkpoint known as the M-checkpoint must be met between metaphase and anaphase, which ensures all chromosomes are aligned on the metaphase plate and the MTs are attached to each kinetochore.[14] If this checkpoint is not met, the cell will enter a state of prolonged mitotic arrest.[15] From here, cell death may occur or the cell may enter a polyploid state. Antimitotic agents bind to MTs and alter the ability of MTs to grow and shrink, thereby influencing MT attachment to kinetochores and separation of chromosomes during mitosis. The goal of anticancer agents is to target MTs in cancerous cells and inhibit their ability to separate chromosomes during cell division, causing cancer cell death.[16–19]
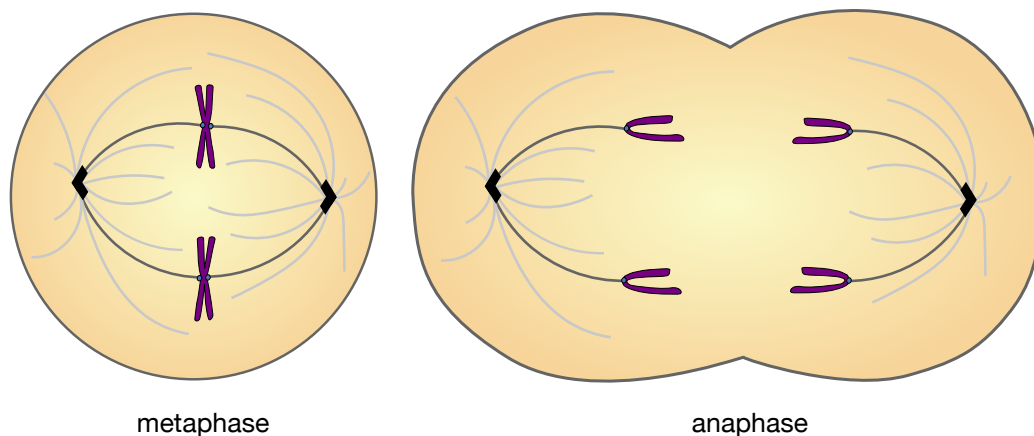
Figure 1.1: *An illustration of metaphase and anaphase in mitosis. In mitosis, the chromosomes (purple) are aligned along the metaphase plate and their kinetochores (blue) are attached to MTs (grey), which are anchored to centrosomes (black) at the poles of the cell. In anaphase, the chromosomes separate and MTs shrink to pull each of the sister chromatids towards its respective centrosome.*

1.2.1.2 Structure

MTs are hollow cylinders comprised of the tubulin protein, specifically α- and β-tubulin units that exist as an $\alpha\beta$-tubulin heterodimer in the cell (Figure 1.2(a)).[20–22] The interior of the MT is known as the lumen. Within the MT, the heterodimers are arranged linearly in a head-to-tail fashion known as a protofilament (Figure 1.2(b)). These protofilaments are aligned in a parallel arrangement, resulting in a polar MT with an α-tubulin-capped end and a β-tubulin-capped end (Figure 1.2(c,d)). Commonly, 13 protofilaments comprise the circumference of a MT,[23] which has an exterior diameter of 25 nm, an interior diameter of 15 nm, and can grow up to 10 μm long in the cell.[16] The arrangement of $\alpha\beta$-tubulin heterodimers in the MT wall primarily adopts a B lattice formation (Figure 1.2(c)), where lateral contacts occur between homologous tubulin monomers.[24] However, when the 1st protofilament meets the 13th protofilament, a seam is present where the $\alpha\beta$-tubulin heterodimers are arranged in an A lattice configuration characterized by heterologous lateral contacts (Figure 1.2(d)).[24]

The three-dimensional structures of MTs and tubulin have been obtained using methods such as cryo-electron microscopy (cryo-EM),[25,26] as well as electron and X-ray crystallography.[27] Atom coordinates are commonly deposited in the Protein Data Base (PDB) and given a unique identification code, making these structures easily
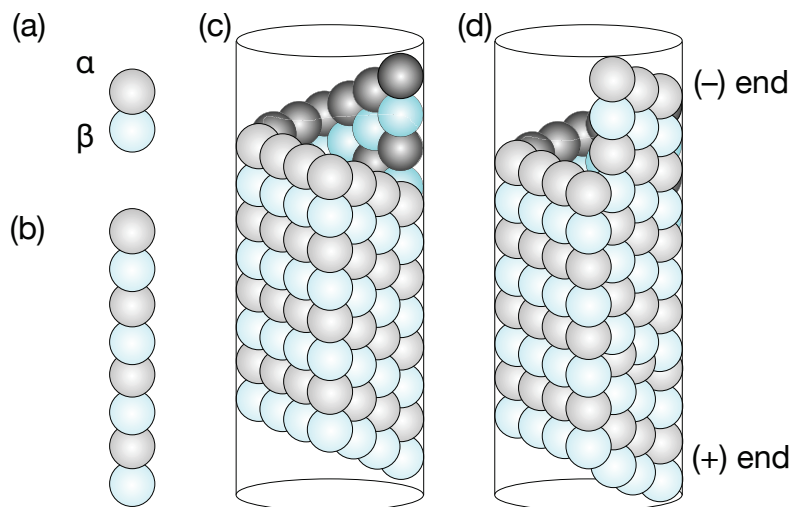
Figure 1.2: *An illustration of the structure and components of a MT, including (a) an αβ-tubulin heterodimer, (b) a tubulin protofilament, and (c,d) a MT. Tubulin within a MT is primarily arranged in (c) a B lattice configuration, where tubulin monomers engage in homologous lateral contacts. A 90° clockwise rotation of the MT in (c) results in image (d), showing the seam where the 1st protofilament meets the 13th protofilament and the A lattice configuration is present, involving heterologous lateral contacts.*

accessible. Cryo-EM has been used to obtain the structures of MTs with resolutions between 30 Å and 5 Å.[24,28–31] This method is beginning to surpass the quality provided by X-ray crystallography, where ligand–protein coordinates have recently been obtained at near atomic resolution (2.2 Å) by cryo-EM.[32,33] Higher-resolution models of MTs have also been obtained by combining cryo-EM data for a MT and docking a high-resolution structure of tubulin obtained from crystallography.[24,29–31] High-resolution crystallographic structures of tubulin have been challenging to obtain since tubulin forms MTs rather than crystals. However, two approaches have been used to obtain structural information about tubulin (Figure 1.3). The first uses zinc ions to induce the formation of two-dimensional tubulin sheets. This results in heterodimers that have a straight conformation, as observed in MTs, but the protofilaments in the zinc-induced sheets are arranged in an antiparallel direction, unlike found in MTs (Figure 1.3(a)). The second approach employs the stathmin-like domain of the RB3 protein to bind to tubulin heterodimers and promote crystallization, which results in a curved heterodimer conformation (Figure 1.3(b)). To further complicate the structural determination of tubulin, MT-stabilizing agents are commonly used to promote
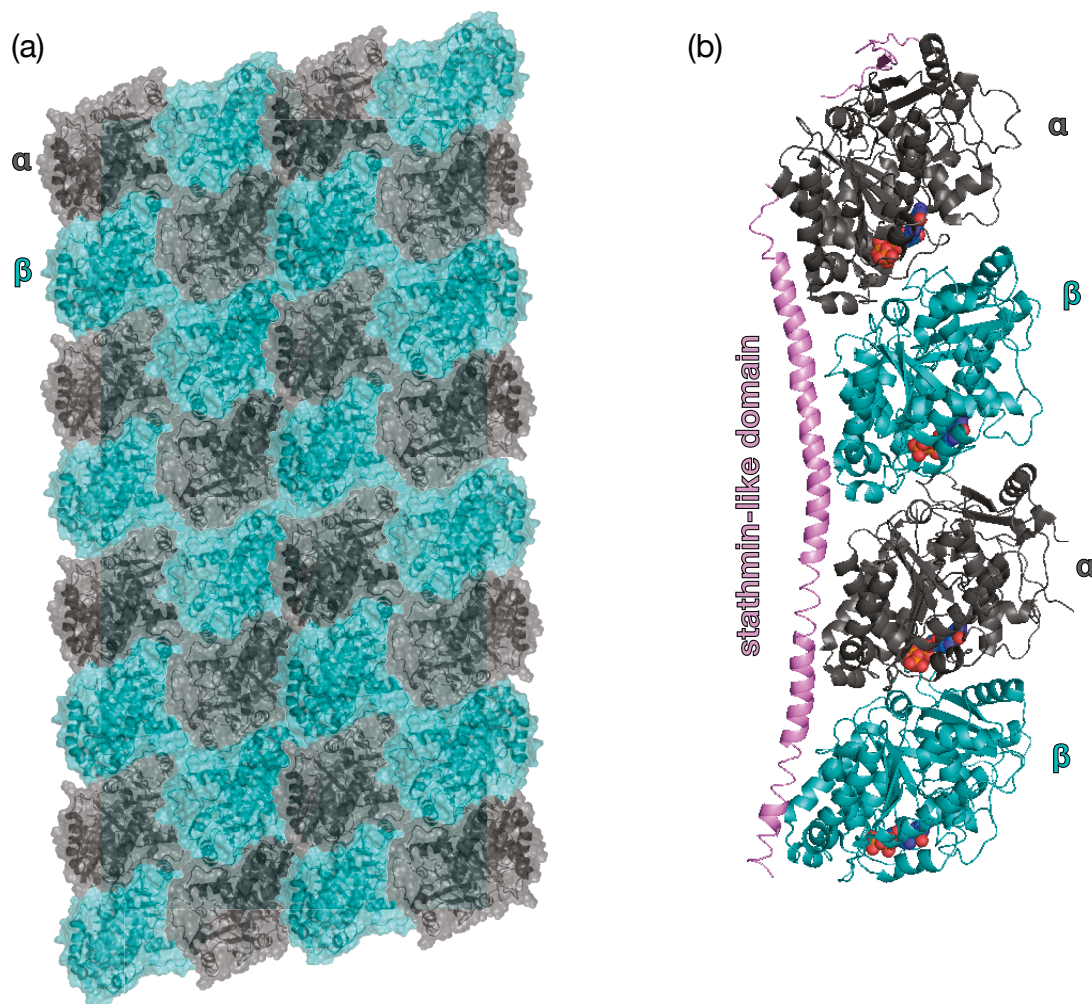
Figure 1.3: *Tubulin structures obtained by (a) electron diffraction of antiparallel zinc-induced sheets and (b) X-ray diffraction of a complex containing $\alpha\beta$-tubulin heterodimers bound to the stathmin-like domain of the RB3 protein in the 1SAO crystal structure.[34] Nucleotide cofactors are shown in space-filling mode.*

polymerization of sheets and MTs. Therefore, there is little experimental data regarding the structure of $\alpha\beta$-tubulin heterodimers in the apo (ligand- or drug-free) or stathmin-free form.

Although structural information about the $\alpha\beta$-tubulin heterodimer was obtained in conjunction with information about drug–$\alpha\beta$-tubulin heterodimer complexes, most notably the taxanes in crystal structures 1TUB[35] and 1JFF[36] (Table 1.1), valuable information about the structure of $\alpha\beta$-tubulin has been obtained. The first crystallographic studies obtained low resolution structures of tubulin that were unable to differentiate the α- and β-tubulin units[37,38] given the 40 % sequence identity between

the two proteins.[39] Higher resolution structures (3.7 Å for 1TUB,[35] 3.5 Å for 1JFF,[36] Table 1.1) definitively distinguished between the tubulin monomers, and identified the secondary (2°) structures of the proteins. Specifically, helices (denoted with an H), sheets (denoted with an S), and loops (defined as the protein backbone components between helices and sheets) were identified. The 10–24 residue C-terminal tail of the tubulin monomers, which is polyanionic and highly disordered, could not be resolved.[35,36] This tail features many post-translational modifications and is directed away from the surface of MTs, playing a role in MT assembly and interactions with MT-associated proteins.[39–45] In 1JFF[36] residues in the α-tubulin loop between H1 and S2 (denoted α:H1–S2) could not be resolved. Each tubulin monomer is divided into an N-terminal domain (the N-terminus to S6), an intermediate domain (H6 up to H11), and a C-terminal domain (H11 to the C-terminus). Each monomer also has a core helix, H7. Docking a high-resolution crystal structure[35] to a cryo-EM MT structure[24] identified the lateral contacts within a MT are primarily formed between S7–H9 in one monomer, and H1–S2 and H3 in the adjacent monomer. One important distinction between α- and β-tubulin is the presence of eight additional residues in α:S9–S10 occupying a region that corresponds to a ligand binding site (specifically the taxane binding site) on β-tubulin. An important secondary structure is also defined: β:S7–H9 is named the M-loop, or microtubule loop, and it is proposed to be the secondary structure responsible for determining the interprotofilament angle and therefore the number of protofilaments in a MT.[36]

Table 1.1: *Select experimental structures of MTs and tubulin available from the Protein Data Bank.*

PDB ID	Drug	Binding Site	Details	Experiment	Resolution (Å)	Year	Ref.
			Microtubule structures				
2XRP	apo	-	doublecortin-stabilized MT	cryo-EM	8.2	2010	30
3J6E	apo	-	GMPCPP-stabilized MT	cryo-EM	4.7	2014	31
3J6F	apo	-	GDP-MT	cryo-EM	4.9	2014	31
3J6G	paclitaxel	luminal taxane	GDP-MT	cryo-EM	5.5	2014	31
			Destabilizing agents bound to $\alpha\beta$-tubulin heterodimers				
1Z2B	vinblastine	vinca	zinc-induced sheets	electron diffraction	4.1	2005	46
4EB6	vinblastine	vinca	stathmin-like domain complex	X-ray diffraction	3.5	2012	47
1SA0	colchicine	colchicine	stathmin-like domain complex	X-ray diffraction	3.5	2004	34
4O2A	colchicine	colchicine	stathmin-like domain complex	X-ray diffraction	2.2	2014	48
4O2B	BAL27862	colchicine	stathmin-like domain complex	X-ray diffraction	2.5	2014	48
3UT5	ustiloxin	vinca	stathmin-like domain complex	X-ray diffraction	2.7	2012	47
4TV8	maytansine	maytansine	stathmin-like domain complex	X-ray diffraction	2.1	2014	49
4TV9	PM060184	maytansine	stathmin-like domain complex	X-ray diffraction	2.0	2014	49
4TUY	rhizoxin F	maytansine	stathmin-like domain complex	X-ray diffraction	2.1	2014	49
			Stabilizing agents bound to $\alpha\beta$-tubulin heterodimers				
1TUB	docetaxel	luminal taxane	zinc-induced sheets	electron diffraction	3.7	1998	35
1JFF	paclitaxel	luminal taxane	zinc-induced sheets	electron diffraction	3.5	2001	36
1TVK	epothilone A	luminal taxane	zinc-induced sheets	electron diffraction	2.9	2004	50
4I50	epothilone A	luminal taxane	stathmin-like domain complex	X-ray diffraction	2.3	2013	51
4I4T	zampanolide	luminal taxane	stathmin-like domain complex	X-ray diffraction	1.8	2013	51
4O4H	laulimalide	laulimalide/peloruside	stathmin-like domain complex	X-ray diffraction	2.1	2014	52
4O4J	peloruside A	laulimalide/peloruside	stathmin-like domain complex	X-ray diffraction	2.2	2014	52

Each tubulin subunit within the heterodimer contains a nucleotide binding site that binds guanosine nucleotides (Figure 1.3(b)). The locations of these sites were identified by crystal structure data,[35,36] photocrosslinking studies,[53–55] and mutational studies.[56] On the α-tubulin subunit, this site is located at the interdimer interface and is non-exchangeable. Therefore the nucleotide exists only in an unhydrolyzed form as guanosine triphosphate (GTP). In contrast, the nucleotide site on β-tubulin is located at the longitudinal interface on the exterior of the protein and is exchangeable. Before polymerization, the free tubulin heterodimers contain GTP bound to β-tubulin. However, polymerization into MTs results in this site being located at the longitudinal interdimer interface contacting α-tubulin, where GTP may be hydrolyzed to guanosine diphosphate (GDP). This hydrolysis is responsible for the change between growing and shrinking MTs, which allows MTs to generate force and carry out their required functions, such as separating chromosomes during cell division.

1.2.1.3 Dynamic instability

The propensity of a MT to stochastically switch between periods of dramatic growth and shrinkage is known as dynamic instability,[57] and is necessary for the functioning of MTs. This is related to GTP hydrolysis. MT lattices with heterodimers containing GTP–β-tubulin are stable, while heterodimers containing GDP–β-tubulin are destabilized. During polymerization, heterodimers containing a GTP–β-tubulin unit are added to the MT. Subsequently, GTP hydrolysis occurs, resulting in a heterodimer containing a GDP–β-tubulin unit.[58] Heterodimers containing GDP–β-tubulin favour dissociation and depolymerization. Whether a MT is in a state of growth (rescue) or shrinkage (catastrophe) depends on a delicate balance between polymerization and hydrolysis.

As discussed in Section 1.2.1.2, MT structures have a polarity where the α-tubulin end is known as the (−) end and the solvent-exposed β-tubulin end is known as the (+) end (Figure 1.2). There are greater changes in length at the (+) end than the (−) end,[16] since the (−) end is anchored to centrosomes during mitosis.

During polymerization, $\alpha\beta$-tubulin containing GTP–β-tubulin binds to the (+) end of the MT, where the exchangeable nucleotide site located on the longitudinal inter-

dimer interface is initially solvent exposed (Figure 1.4(a)). Upon the addition of more $\alpha\beta$-tubulin heterodimers, the GTP unit bound to β-tubulin comes into contact with residues from the longitudinal surface of the α-tubulin unit, which complete the binding pocket and provide the residues necessary to hydrolyze GTP to GDP,[24] releasing 52 kJ mol^{-1}.[40] This hydrolysis is associated with a conformational change in $\alpha\beta$-tubulin,[31] which can either be constrained by the surrounding MT lattice to allow for polymerization to continue, or destabilize the lattice to cause depolymerization. The path taken depends on whether a GTP cap (a series of heterodimers containing GTP–β-tubulin) is present on the (+) end.[59] In the presence of the stabilizing GTP cap, the conformational change that results upon the hydrolysis of GTP to GDP will be constrained by the MT lattice, storing energy within the MT and allowing polymerization to continue (Figure 1.4(b)). This occurs when the rate of polymerization is greater than the rate of GTP hydrolysis. Experiments suggests that a (+) end cap of one to three layers of heterodimers containing GTP–β-tubulin will stabilize MTs.[59] Alternatively, the absence of a GTP cap exposes the unstable MT core of heterodimers containing GDP–β-tubulin,[59] which destabilizes the MT lattice and leads to depolymerization (Figure 1.4(c)). This occurs when the rate of hydrolysis is greater than the rate of polymerization. During depolymerization, lateral contacts break and dissociation occurs with characteristic "ram horns"[60] as protofilaments twist and curl outwards(Figure 1.4(c)).[61] It is important to note that GTP hydrolysis is not required for MT polymerization, but is required for dynamic instability. As evidence for this, the use of unhydrolyzable GTP analogues such as GMPCPP allow MTs to polymerize, but no dynamic instability is observed.[62]

1.2.2 Antimitotic agents targeting microtubules

Antimitotic agents are one of the most successful classes of cancer chemotherapies available, suggesting MTs are an excellent cancer target.[16] Interestingly, many MT targeting agents are naturally derived, or based on the structure of naturally-derived compounds (Figure 1.5). These compounds bind to the β-tubulin subunits, and there are six distinct binding sites currently known (Figure 1.6). MT targeting agents may be categorized into MT destabilizing agents, which inhibit MT polymerization at high concentrations, and MT stabilizing agents, which promote MT polymerization
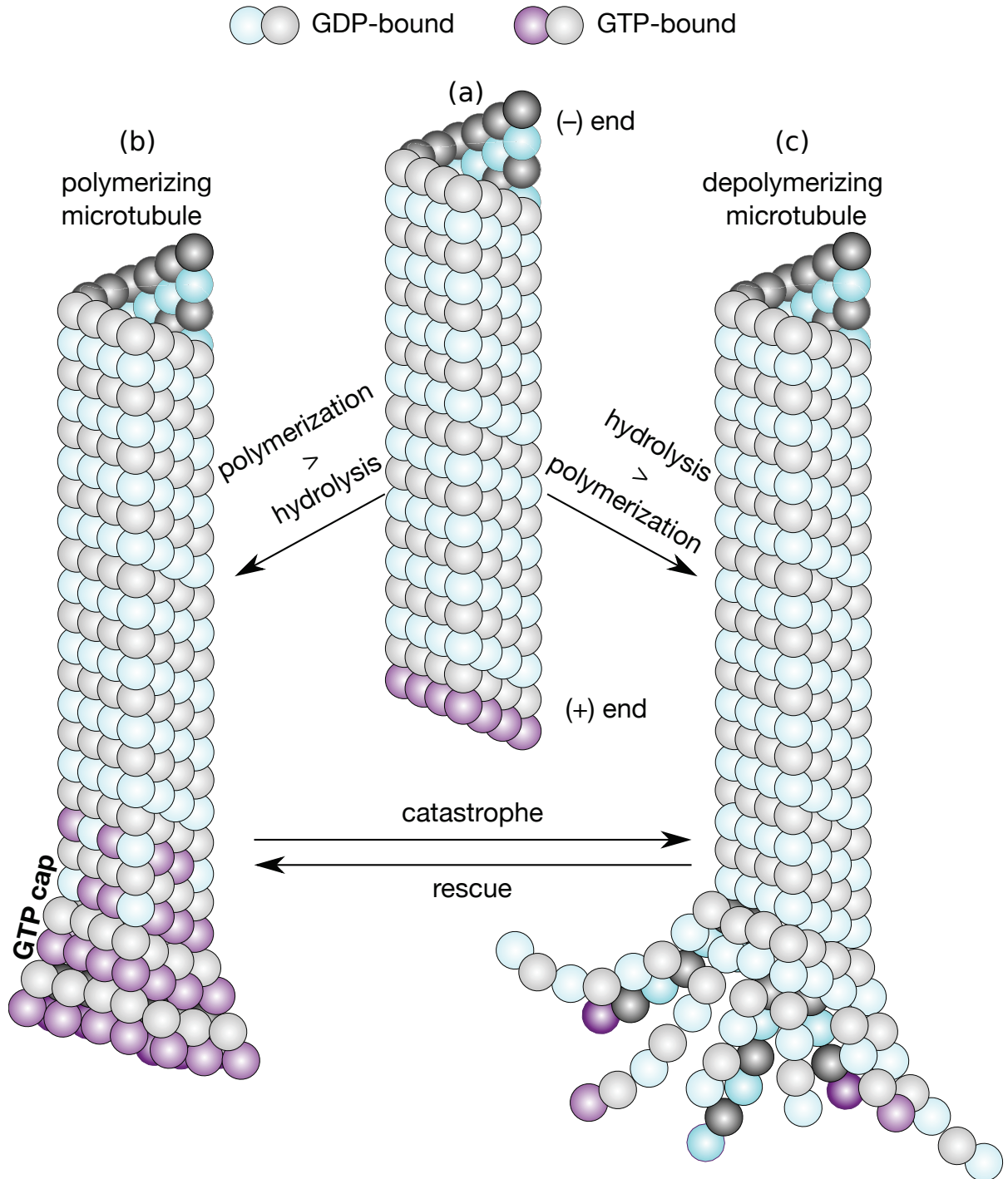
Figure 1.4: *An illustration of the dynamic instability of MTs related to the hydrolysis of GTP–β-tubulin (purple) to GDP–β-tubulin (cyan). (a) The addition of an αβ-tubulin heterodimer containing GTP–β-tubulin may lead to (b) polymerization if the rate of heterodimer addition is greater than the rate of GTP hydrolysis, resulting in GTP cap, or (c) depolymerization if the rate of hydrolysis is greater than the rate of heterodimer addition.*

at high concentrations. At clinically-relevant drug concentrations, all compounds have the same effect in which they exert their cytotoxic effects by altering the dynamic instability of MTs.[16,63]

1.2.2.1 Microtubule destabilizing agents

Several classes of drugs are known to destabilize MTs at high concentrations, which include the *Vinca* alkaloids and colchicine. The *Vinca* alkaloids were first isolated in the 1950s from leaves of periwinkle, *Vinca rosea*,[64] and their antitumour activity established.[65] In 1968, it was determined that the *Vinca* alkaloids targeted tubulin as an antimitotic agent.[66,67] Vinblastine (Figure 1.5) is cytotoxic in nanomolar concentrations (Table 1.2)[68] and may bind to the β-tubulin unit within soluble dimers of $\alpha\beta$-tubulin, or to MTs. The *Vinca* alkaloids bind with high affinity to the (+) end of MTs, but may also bind with lower affinity to the lattice.[69–72] The *Vinca* alkaloid binding domain is located at the longitudinal interdimer interface (Figure 1.6); when bound to the MT (+) end the *Vinca* alkaloids block polymerization (Figure 1.7(a)), whereas binding to the MT lattice creates a wedge between $\alpha\beta$-tubulin heterodimers to induce a curved protofilament conformation. The *Vinca* alkaloids also disrupt tumor vasculature.[17] Crystal structures are available for vinblastine–tubulin complexes (1Z2B[46] and 4EB6,[47] Table 1.1). Other agents like ustiloxins also bind to the *Vinca* alkaloid domain, and a crystal structure is available (3UT5, Table 1.1).[47]

Four *Vinca* alkaloids have been approved for clinical use in Canada. Vinblastine and vincristine were approved for use in the 1960s, while vindesine and vinorelbine were approved for use in the 1990s. These agents are used to treat a variety of cancers, including cancers of the breast, uterus, cervix, and testicles, as well as melanoma and leukemia.[73]

Colchicine (Figure 1.5) is isolated from the saffron plant, *Colchicum autumnale*.[74] Colchicine binds to free $\alpha\beta$-tubulin heterodimers, which may then be incorporated into MTs.[74] The 1SAO crystal structure of colchicine bound to $\alpha\beta$-tubulin (Table 1.1) revealed that colchicine binds at the intradimer interface (Figures 1.6 and 1.7(b)) and displaces β:H7–H8.[34] This induces a curved MT conformation,[34] unlike the straight conformation that $\alpha\beta$-tubulin adopts within the MT lattice.

Colchicine is cytotoxic in low nanomolar concentrations, but less effective than
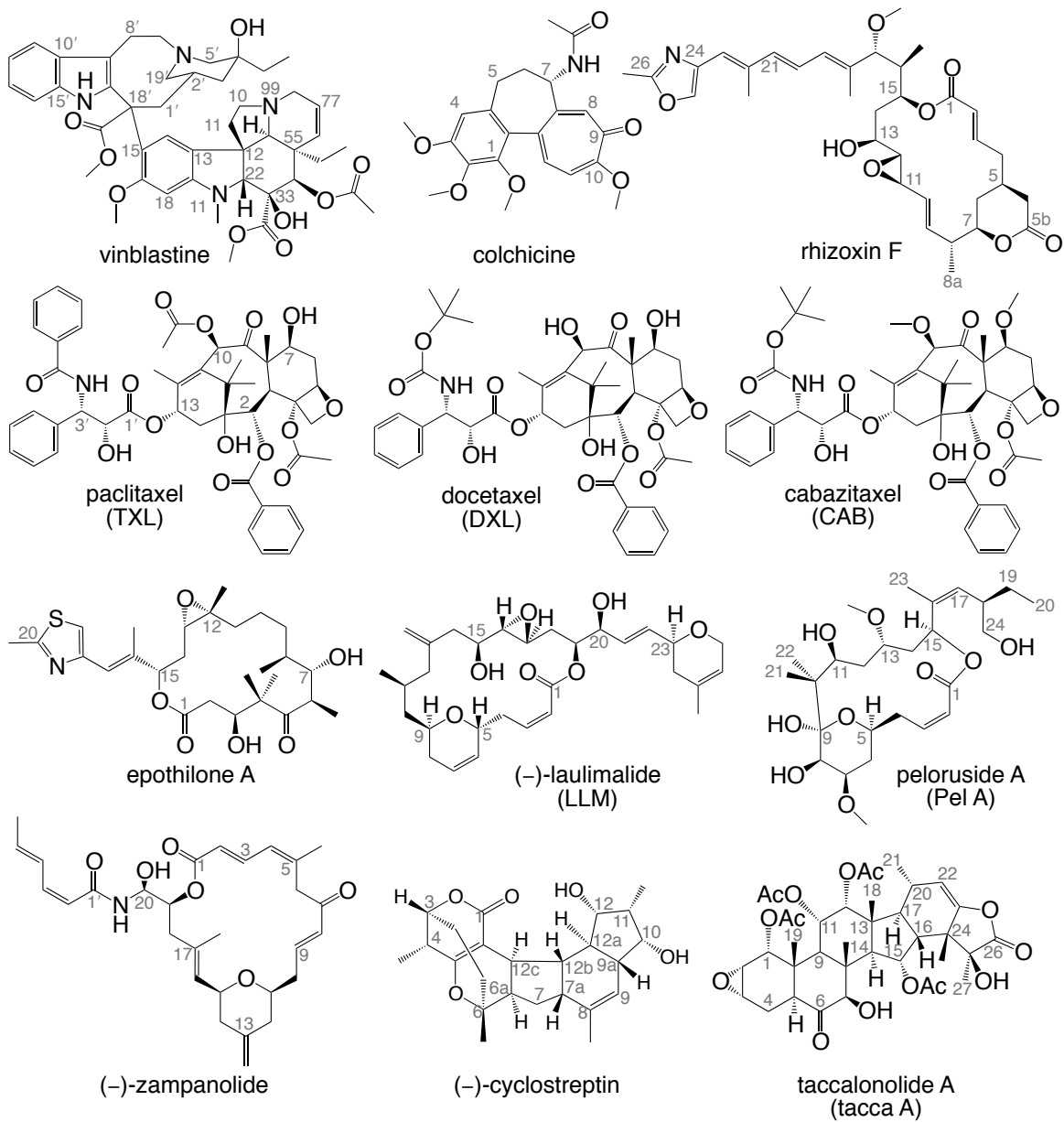
Figure 1.5: *The structure and numbering of MT-targeting agents, which bind to β-tubulin.*
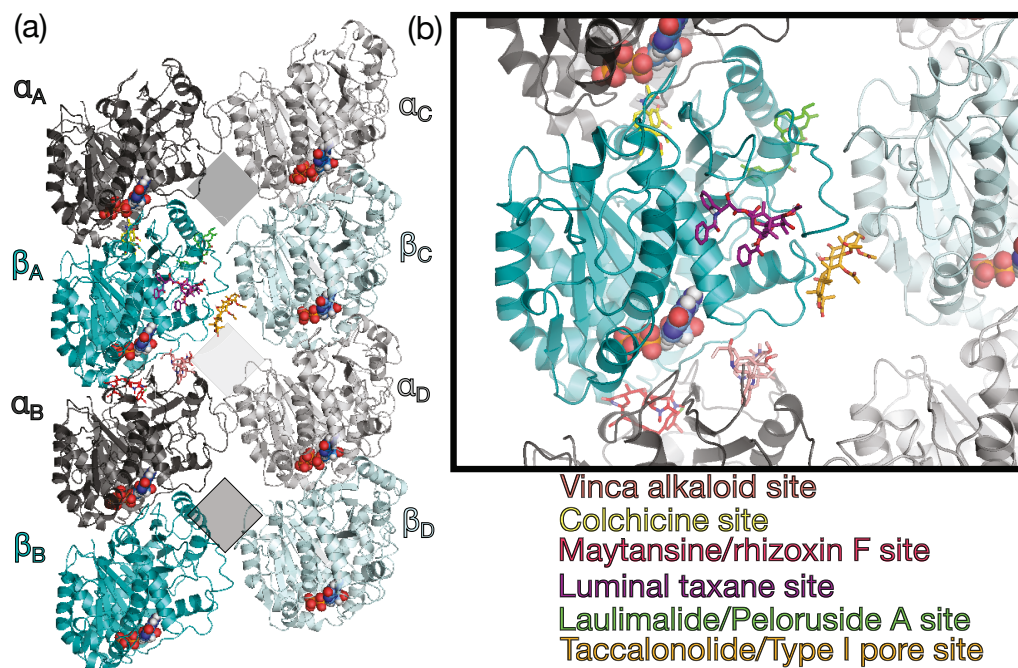
Figure 1.6: *An illustration of (a) two adjacent tubulin protofilaments and (b) β-tubulin illustrating the binding sites of different ligands and nucleotide cofactors, viewed from the MT lumen (interior). Guanosine nucleotides are indicated in space-filling mode. In (a) the MT protofilament, the type I pore is indicated with a light grey square and type II pores are indicated with a dark grey square. Colchicine (yellow) binds to the colchicine domain located at the longitudinal intradimer interface. Vinblastine (pink) binds to the Vinca alkaloid domain at the longitudinal interdimer interface. Rhizoxin F (red) binds to a recently-identified site also at the longitudinal interdimer interface. Paclitaxel (purple) binds to the luminal taxane binding site. Laulimalide (green) binds to the laulimalide/peloruside A binding site at the lateral interdimer interface between protofilaments. Taccalonolide AF (orange) covalently bonds to β-tubulin at a site in the type I pore.*
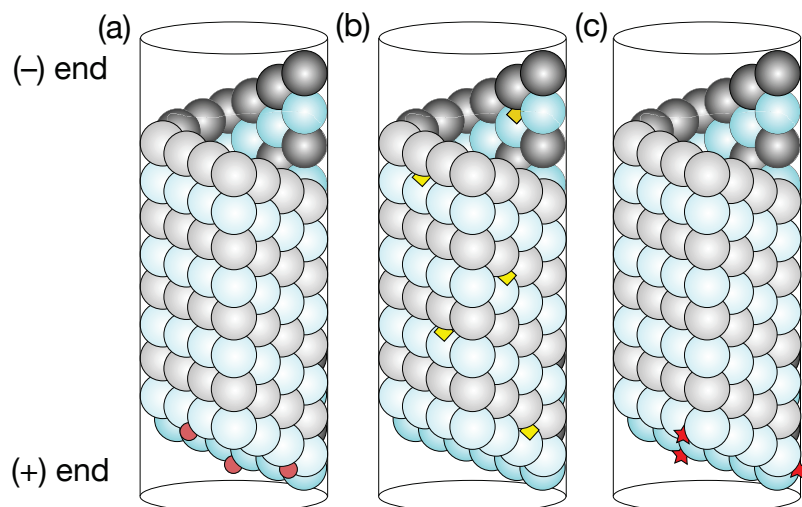
Figure 1.7: *An illustration of the binding sites of MT-destabilizing agents (a) vinblastine (Vinca alkaloid domain), (b) colchicine (colchicine domain), and (c) rhizoxin F (a newly-reported domain).*

vinblastine (Table 1.2). Colchicine was used for many years to treat gout, and was clinically approved in the US for this treatment in 2009,[74] but has not been successful in the treatment of cancer due to its small therapeutic window. However, the ability of this compound to target tumour angiogenesis and vasculature, while also evading common resistance mechanisms, has motivated researchers to derivatize this compound.[74] Related compounds are currently being examined in preclinical and clinical trails,[74] and crystal structures of some compounds bound to the colchicine domain of $\alpha\beta$-tubulin have been obtained.[48,75,76]

Recently, a new tubulin binding site was discovered with the crystallization of MT-destabilizing agents maytansine (4TV8), PM060184 (4TV9), and rhizoxin F (4TUY, Table 1.1, Figure 1.5).[49] Although these compounds interfere with vinblastine binding, this site is in a structurally-distinct location.[49] These agents bind at the longitudinal interdimer interface, but away from the *Vinca* alkaloid domain and adjacent to the exchangeable nucleotide site (Figures 1.6 and 1.7(c))

Table 1.2: *Cytotoxicity (IC$_{50}$, nM) of select MT-targeting agents acting on different cell lines.*[a]

Drug	1A9[b,c]	MDA-MB-435[d,e]	HeLa[d,f]	P388[g,h]	P388/TXL[g,i]
colchicine			12.2 ±1.0[68]		
vinblastine			6.85 ± 0.02[68]		
paclitaxel	1.0 ± 0.4[77]	1.02 ± 0.25[78]	1.63 ± 0.15[68]		
docetaxel	0.4 ± 0.2[77]		0.58 ± 0.03[68]	0.079 ± 0.004[79]	0.188 ±0.022[79]
cabazitaxel				0.041 ± 0.017[79]	0.024 ± 0.015[79]
epothilone A	4.1 ± 1.0[77]		0.53 ±0.03[68]		
epothilone B	1.2 ± 0.3[77]				
laulimalide		5.74 ±0.58[78]			
isolaulimalide		1970 ±97[78]			
cyclostreptin	40 ± 5[77]				
taccalonolide A			594 ± 4.3[68]		
taccalonolide AI			47 ± 3[80]		
taccalonolide AI-epo			0.88 ± 0.01[80]		

[a] IC$_{50}$ is half of the maximum inhibitory concentration for growth inhibition.; [b] Determined by an MTT assay measuring mitochondrial reductase activity.; [c] Human ovarian cancer cell line.; [d] Determined by a sulforhodamine B assay measuring cell protein.; [e] Human melanoma cell line.;[81] [f] Human cervical cancer cell line.; [g] Determined by a neutral red assay measuring lysosome activity.; [h] Mouse leukemia cell line.; [i] A paclitaxel-resistant cell line derived from P388.

15

1.2.2.2 The taxanes and taxane-domain binders

The taxanes are the most well-known and best understood class of MT-targeting agents.[82,83] They are also the most successful class of MT-targeting agents, with three taxanes, paclitaxel (TXL), docetaxel (DXL), and cabazitaxel (CAB), currently in clinical use. The taxanes feature a common tetracyclic baccatin core with a side chain at C13, but differ in functional group modifications at three sites (Figure 1.5). The C3′ position of TXL contains a benzyl amide moiety, while C7 and C10 feature hydroxyl and acetyloxy groups, respectively. DXL features a C3′-t-butyl carbamide ester, and a hydroxyl group at C10. CAB features the same C13 side chain as DXL, but is substituted with methoxy groups at the C7 and C10 positions.

The first taxane studied in the literature, TXL (Figure 1.5), is derived from the Pacific yew tree (*Taxus* genus). Its structure and cytotoxic activity against tumours was identified in 1971.[84] In 1979, the biological target of TXL was identified when it was determined that TXL worked by promoting the assembly of MTs,[85] and resulted in MT bundles and abnormal mitotic spindles in cells.[86] Initially, a lack of availability slowed the progress of TXL in preclinical studies.[86] TXL was isolated from the bark of the yew tree, which only yielded small quantities while also killing the tree.[83] Eventually, a semisynthetic process was developed from the baccatin species, which could be harvested in large quantities from the needles of the yew tree.[87] Phase I clinical trials began in 1984, and TXL was approved for clinical use in 1992 in Canada and the US for the treatment of ovarian cancer.[83] Currently, paclitaxel (Taxol) is administered to treat ovarian, breast, non-small cell lung cancer, as well as Kaposi's sarcoma.[82] Paclitaxel is also approved to be administered in an albumin-stabilized nanoparticle formulation, which circumvents the poor solubility of TXL and decrease systemic side effects.[88] Nanoparticulate drug delivery also provides a means of preferentially targeting tumour cells.[89,90]

TXL, like many cancer chemotherapies, is prone to resistance. Semisynthetic taxanes have been developed to provide an alternative to TXL and are in clinical use. Docetaxel (Taxotere), approved in 2006 in Canada and the US, is used to treat non-small cell lung cancer, as well as breast, prostate, stomach, head, and neck cancers.[17] Most recently, cabazitaxel (Jevtana) was approved in the US (2010) and

Canada (2011) to treat metastatic hormone-refractory prostate cancer. CAB has low affinity for the P-glycoprotein efflux pump that is implicated in drug resistance and is administered once treatments with DXL are ineffective.[18,91] The taxanes are cytotoxic in low and sub-nanomolar concentrations (Table 1.2). In some drug-sensitive cell lines such as A2780 (human ovarian cancer) and MCF-7 (human breast cancer), TXL has been reported to be more potent than DXL,[92] while other cell lines such as 1A9 (human ovarian cancer) and HeLa (human cervical cancer) indicate DXL is superior,[68,77] and CAB is superior to DXL in the sensitive P388 (mouse leukemia) cell line (Table 1.2).[79] However, in resistant cell lines, DXL is superior to TXL[92] while CAB is superior to DXL,[79] particularly in P-glycoprotein expressing cell lines. DXL also has greater solubility than TXL.[82] In addition to antimitotic activity, the taxanes are angiogenic.[19]

The location of the taxane binding site on $\alpha\beta$-tubulin heterodimers has been the subject of many studies. Photoaffinity labelling studies were the first to indicate the residues involved in the binding of taxanes to β-tubulin.[93–95] Subsequently, a series of electron crystallography studies by the Nogales group[35–38] definitively identified the taxane binding site (Figures 1.6 and 1.8). Zinc-induced sheets in an antiparallel protofilament arrangement were crystallized with TXL and resolved to 6.5 Å,[37] and then to 4 Å.[38] Although electron density corresponding to the taxane was visible near interprotofilament contacts, the inability to differentiate between the α- and β-tubulin units meant the receptor could not be identified. However, this did support previous studies, which determined that TXL binds to $\alpha\beta$-tubulin stoichiometrically.[96] A structure with a resolution of 3.7 Å was obtained with the 1TUB[35] crystal structure containing DXL and further improved in the 1JFF[36] crystal structure resolved at 3.5 Å with TXL in the taxane binding site (Table 1.1). The taxane binding site was located on the β-tubulin unit, in contact with secondary structures β:H1, β:H6–H7, β:H7, β:S7, the M-loop, and β:S9–S10 (Figure 1.8(b)). Although the baccatin core of TXL was well defined, the C2-, C3′, and N′-phenyl groups (Figure 1.5) were poorly resolved. By docking 1TUB to cryo-EM MT data, it was determined that the taxane binding site was located in the MT lumen (Figure 1.8(a,b)).[24]

Once the taxane binding site was identified in the MT lumen, researchers wondered how the taxanes gained access to this site. Interestingly, taxanes have negligible
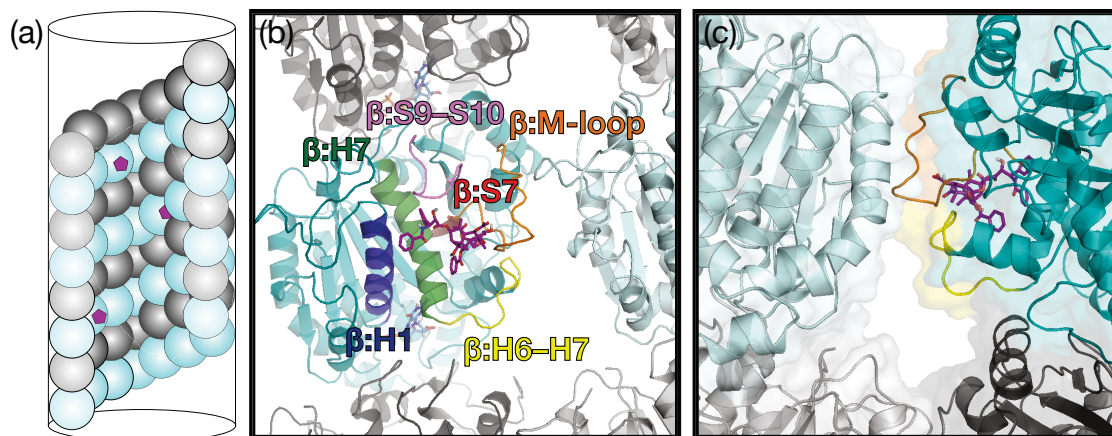
Figure 1.8: *An illustration of (a,b) the luminal taxane binding site as viewed from the MT lumen and (c) the intermediate binding region in the type I pore as viewed from the MT exterior. TXL (purple) binds near the indicated secondary structures in the lumen.*

affinity for free $\alpha\beta$-tubulin heterodimers,[97] preferring to bind to $\alpha\beta$-tubulin within MTs or zinc-induced sheets, suggesting an important structural difference between these systems that is important for taxane binding. It was initially suggested that TXL could gain access to the lumen by entering at the ends of the MT.[98] However, it is now accepted that TXL enters the lumen through the MT wall, as determined by studies using fluorescently-labeled taxanes,[99] as well as supported by the result that taxane binding could be blocked by the binding of agents to the type I pore (cyclostreptin, Section 1.2.2.4).[100] The binding of taxanes was determined to involve a two-step process:[101] First, the taxanes bind to an intermediate binding site in the MT wall and in the second step they bind to the luminal site. The intermediate binding site was identified by molecular modeling studies using docking calculations[102,103] and molecular dynamics simulations.[102,104] Although its exact location differed slightly between the different studies, the intermediate binding site region was found to be located in the the type I pore and forms upon the rearrangement of β:H6–H7, which is accessible to the bulk solution (Figure 1.8(c)). Interestingly, the intermediate and luminal binding sites are separated by the M-loop, and computational exploration of the transition from the intermediate to luminal binding site found the M-loop conformation changes to facilitate the movement of TXL into the luminal site.[102,103] Since taxane binding to $\alpha\beta$-tubulin is stoichiometric,[96] binding at the luminal and

intermediate sites is mutually exclusive.

The mechanism by which TXL stabilizes MTs has been the subject of several studies. TXL can promote MT formation from heterodimers containing GDP–β-tubulin.[96] It is known that upon binding TXL displaces residues in the M-loop and it was proposed that this moves the M-loop towards the adjacent tubulin unit to stabilize MTs by enhancing lateral contacts, particularly with β:H1–S2, β:H3, and β:H2–S3.[24,30,105] TXL is now believed to impart MT stability by allosterically reversing the conformational changes to $\alpha\beta$-tubulin that occur upon the hydrolysis of GTP to GDP in β-tubulin.[31,105] Therefore, it is expected that conformations of GTP-bound tubulin and TXL-bound tubulin are similar. The conformation of the apo $\alpha\beta$-tubulin heterodimer, with either GTP or GDP bound to β-tubulin, has been examined,[76,80,106–111] with comparatively fewer studies considering the effects of taxanes.[31,105,112] Tubulin heterodimer curvature is not greatly affected by GTP hydrolysis or taxane binding, where GTP-tubulin, GDP-tubulin, and TXL-bound tubulin are intrinsically curved and display flexibility that allows them to occupy a continuum of conformations ranging from bent to straight.[76,80,109] Local and global structural changes that occur within $\alpha\beta$-tubulin upon TXL binding to MTs have been identified.[31,112] Hydrogen-deuterium exchange (HDX) mass spectrometry (MS) detected structural changes in both the α- and β-tubulin units.[112] In HDX MS, acidic protons in the solute exchange with deuterium in the solvent, where solvent-exposed regions of the protein receptor will have higher deuterium incorporation than unexposed regions. By comparing a protein in its holo (ligand-bound) and apo forms, a ligand binding site can be identified, as well as other structural changes, based on the decreased deuterium incorporation in certain regions. Most recently, high-resolution MT structures have indicated that lateral contacts play a passive role in MT stability and are not substantially affected by TXL binding, which instead stabilizes MT by increasing longitudinal contacts and easing conformational strain.[31] HDX MS experiments also found that DXL has an effect on longitudinal, rather than lateral, tubulin interactions.[113]

Some structural analogues of the taxanes, and their effects on tubulin and MTs, have been studied using *in vitro*, *in vivo*, and *in silico* methods in order to understand the role of functional group modifications on the effectiveness of the taxanes.[92,114]

19

Although TXL has been the subject of an overwhelming number of studies and DXL to a much lesser extent, there has been little work examining the interaction between CAB and tubulin. Among the three clinically approved taxanes, there are some known differences in the effects of these drugs on MTs. DXL binds to tubulin with up to three times the affinity (K_a) of TXL and it has a greater effect on MT assembly than TXL.[115] CAB and DXL perform similarly in MT stabilization and tubulin assembly experiments,[79] indicating these are better MT stabilizing agents than TXL. While natural MTs typically have 13 protofilaments, TXL binding decreases this number to 12, while DXL binding results in MTs with 13 or 14 protofilaments.[116,117] Early studies proposed that the M-loop acts as a hinge that determines the number of protofilaments in a MT.[24] More recently, computational modeling also implicated the M-loop in determining protofilament number, which was related to the degree to which the C7- and C10-substituents displaced the M-loop from the taxane binding site and changed the interprotofilament angle.[92,117]

Despite what is known about the binding of taxanes to MTs, particularly TXL, it is still unclear how the taxanes stabilize MTs. Though their structures differ, the three clinically-approved taxanes (TXL, DXL, and CAB) are known to stabilize MTs and are effective in clinical use. Of particular interest is how the binding of the taxanes to β-tubulin results in an allosteric effect in the $\alpha\beta$-tubulin heterodimer to stabilize MTs. Chapter 5 applies computational methods using classical force fields and molecular dynamics simulations to determine the effects of these three taxanes on tubulin and insight is gained into the origin of the allosteric effects of taxane binding to tubulin. These taxane–tubulin complexes are also studied using quantum mechanics in Chapter 7, to gain additional information about taxane–tubulin interactions that is not available from computational methods based on classical mechanics.

Other agents are also known to bind to the taxane binding site.[18] The epothilones (for example epothilone A, Figure 1.5) were originally isolated from the myxobacterium *Sorangium cellulosum* and were found to stabilize MTs.[115,118] Competitive binding studies initially indicated that taxanes and epothilones bind to the same site,[119] and this was illustrated by zinc-induced tubulin sheets in the 1TVK crystal structure in 2004 (Table 1.1).[50] The epothilones, particularly epothilone B, can be easily obtained[120] and have greater solubility than TXL in water.[121] Furthermore,

epothilones were shown to be more effective than TXL in multidrug resistant cell lines,[119,122] though less effective in sensitive cell lines (Table 1.2).[77] Semisynthetic epothilone analogues are showing particular promise as cancer chemotherapies. Izabepilone (Ixempra), which began clinical development in 1999, was approved for the treatment of taxane-resistant breast cancer in 2007 in the US,[123] and other analogues are currently in clinical trials. Discodermolide, isolated from the marine sponge *Discodermia dissoluta*, also binds to the taxane binding site to stabilize MTs, but interestingly this compound works synergistically with TXL.[124] This is because TXL binds closer to the M-loop while discodermolide binds closer to β:H1–S2.[125] Despite its ability to promote MT assembly more effectively than TXL[126] and its efficacy in resistant cell lines,[127] this compound was unsuccessful in clinical trials.[17] Other compounds such as cyclostreptin, dactylolide, and zampanolide can bind in the taxane binding site through a covalent bond, and will be discussed in Section 1.2.2.4.[18]

1.2.2.3 Laulimalide and peloruside A

Laulimalide (LLM) is a macrolactone derived from the marine sponge *Cacospongia mycofijiensis*,[128–130] while peloruside A (Pel A) is a macrolactone isolated from the marine sponge *Mycale hentscheli* (Figure 1.5).[131] Both compounds have cytotoxic activity in the nanomolar range (Table 1.2).[78,132] These compounds are antimitotic agents currently undergoing preclinical development.

LLM and Pel A stabilize MTs in a fashion similar to TXL, promoting the assembly of $\alpha\beta$–tubulin heterodimers into MTs.[18,78,133,134] However, Pel A has been shown to be less potent in promoting MT assembly than LLM and TXL.[134–136] Exposure of cells to LLM was found to cause mitotic arrest in breast carcinoma and the onset of apoptosis.[78] Similarly, Pel A was found to induced mitotic arrest in lung cancer cell lines.[137] Although TXL was found to have lower IC_{50} values than LLM and Pel A in drug-sensitive cell lines,[78,135] LLM and Pel A are superior in TXL-resistant cell lines[133,135] and multidrug-resistant cell lines that overexpress the P-glycoprotein.[78,133,135] Furthermore, synergetic effects were observed in tubulin assembly with the co-administration of taxanes, as well as other taxol-domain binding agents and LLM.[134,136,138,139] This synergy and ability to overcome resistances is indicative of the potential of LLM and Pel A as chemotherapeutic agents.

The information about LLM and Pel A binding was initially elucidated from competitive binding assays of drugs with known binding sites. It was determined that LLM does not inhibit TXL binding, and that LLM and TXL could bind to $\alpha\beta$-tubulin heterodimers in stoichiometric quantities simultaneously,[133] indicating that LLM does not occupy the taxane binding site. Further work also indicated that both Pel A and LLM did not compete with TXL binding, but did compete with each other,[135,136] indicating that LLM and Pel A bind to the same or an overlapping site. Further identification of the LLM and Pel A binding sites proved challenging, and it was reported that it was not possible to create zinc-induced tubulin sheets with LLM.[140]

In 2006, based on the results of blind docking calculations using NMR-determined solution structures of Pel A, it was proposed that the binding site of Pel A was located on α-tubulin, contacting α:H7.[141] However, this was incorrect. Ultimately, a collaborative effort using HDX MS, blind docking, and molecular dynamics calculations correctly identified the LLM/Pel A binding site.[113,142] In 2008, HDX MS and blind docking calculations identified the Pel A binding site on β-tubulin near β:H9–H9′, β:H9′, β:H9′–S8, β:S8, β:H10, and β:H10–S9,[113] and in 2010 the LLM binding site was confirmed to be in the same location (Figure 1.9(a–c)).[142] This site is removed from the taxane site and located near the lateral interface between heterodimers in protofilaments, and therefore LLM and Pel A are in contact with two adjacent β-tubulin units within the MT lattice (Figure 1.6 and 1.9(a,b)). Interestingly, HDX MS studies also identified a region of decreased solvent exposure corresponding to β:H3 and β:H3–S4 in the adjacent β-tubulin unit (Figure 1.9(b)), which indicates these structures also form part of the LLM/Pel A binding site, though this was not discussed in the text.[142] Molecular dynamics simulations of Pel A-$\alpha\beta$-tubulin[113] and LLM-$\alpha\beta$-tubulin[142] complexes (Figure 1.9(c)) identified key residues involved in drug binding. Nguyen *et al.*[143] also computationally examined LLM and Pel A binding to β–tubulin, and identified a binding mode unique from that reported by Huzil *et al.*[113] and Bennett *et al.*,[142] which differs in the bound drug conformation and specific interactions with residues.

The above studies were instrumental in identifying the previously-unknown LLM and Pel A binding sites.[113,142] The associated computational work provided atomic-

resolution structures that could be used to better understand binding at this new site, and applied in the development of LLM and Pel A analogues. However, the LLM/Pel A site on β-tubulin is somewhat unique since, unlike the colchicine and taxane domains, it is in contact with multiple protein heterodimers within the MT. Furthermore, the HDX MS results suggest there may be important binding contributions from the adjacent β-tubulin unit via β:H3 and β:H3–S4.[142] The above computational models were limited to a single $\alpha\beta$-tubulin heterodimer[142] or β-tubulin.[143] To obtain dynamical, atomic-resolution insight into this binding site in a MT environment, it is necessary to utilize an extended computational model. The Tuszynski group has been particularly interested in LLM, and therefore as part of my PhD work I examined LLM binding to MTs using an extended protein model consisting of two adjacent $\alpha\beta$-tubulin heterodimers. These results were published[1] and are detailed in Chapter 2.

As the research presented in Chapter 2 was completed, a crystal structure became available for Pel A (4O4J) and LLM (4O4H, Table 1.1) bound to tubulin (Figure 1.9(d,e)).[52] These complexes show the compounds form contacts with β:H9, β:H9–H9′, β:H10, and β:H10–S9, highlighting the same pocket previously identified.[113,142] The LLM pose present in the crystal structure[52] differs from that determined by MD simulations reported by Bennett *et al.*[142] using a single $\alpha\beta$-tubulin heterodimer (Figure 1.9(c) vs. (e)), and also the pose identified in Chapter 2 using two adjacent $\alpha\beta$-tubulin heterodimers. The crystal structures were obtained with the compounds bound to the β-tubulin unit within an $\alpha\beta$-tubulin heterodimer that forms a complex with the stathmin-like protein RB3 and tubulin tyrosine ligase (similar to Figure 1.3(b)). However, the adjacent $\alpha\beta$-tubulin heterodimer that would be present within the MT lattice is absent. Recognizing the importance of considering this LLM pose in the context of the MT lattice, the researchers who obtained the crystal structure[52] also performed a fit of this LLM-bound $\alpha\beta$-tubulin heterodimer to cryo-EM reconstructions of a MT.[24,30] Although this representation did not allow for the relaxation of protein–protein or additional drug–protein interactions, information about the proximity of LLM to the adjacent tubulin unit was obtained. Specifically, lateral interactions with β:H3 were proposed, as suggested by the HDX MS results[142] and also reported in Chapter 2. However, it is important to consider LLM in a MT-
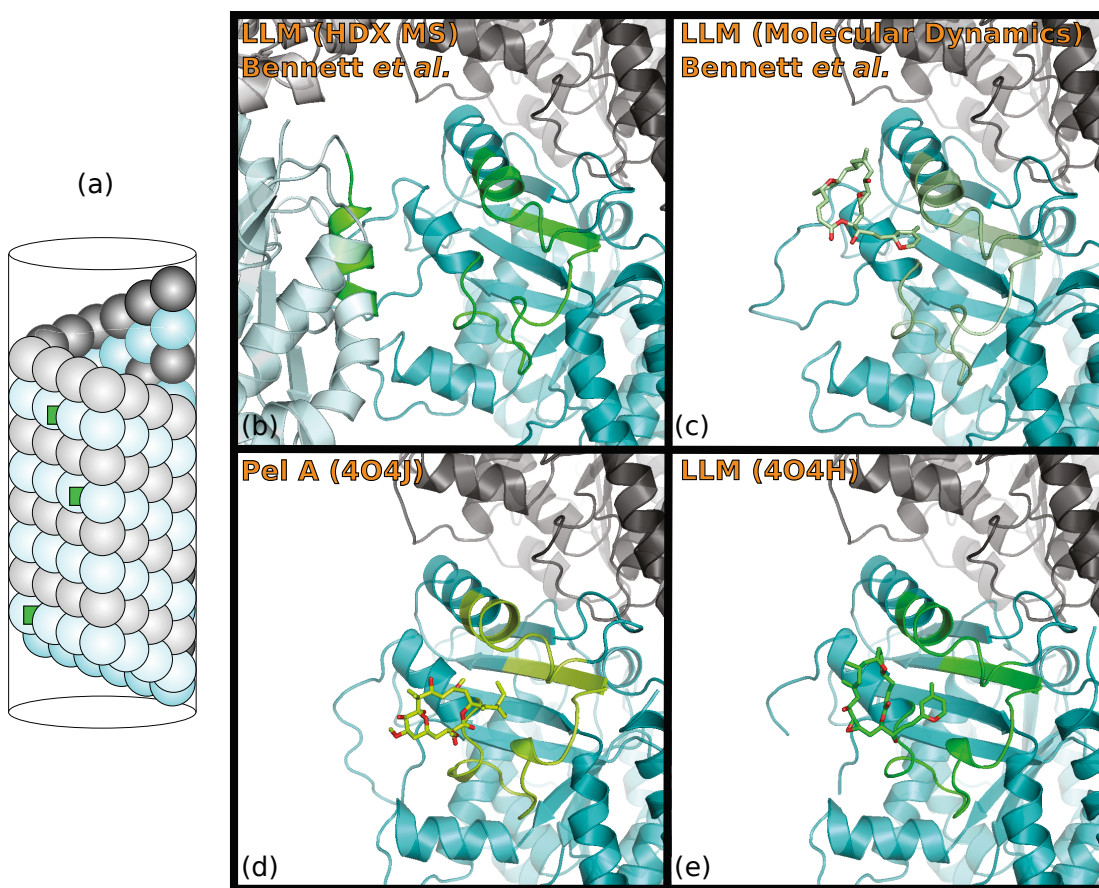
Figure 1.9: *(a) An illustration of the laulimalide/peloruside A binding site. (b) The lateral interdimer interface indicating the residues (in green) affected by laulimalide and peloruside A binding, as determined by HDX MS.[113,142] (c) The laulimalide binding pose as determined computationally by Bennett et al..[142] (d) The peloruside A binding pose in the 4O4J crystal structure.[52] (e) The laulimalide binding pose in the 4O4H crystal structure.[52] Panels (b–e) are viewed from the MT exterior.*

like environment that includes structural relaxation and dynamics. Therefore, using the LLM pose provided in the crystal structure, LLM binding between $\alpha\beta$-tubulin heterodimers was reexamined with classical mechanics and molecular dynamics, the results of which are detailed in Chapters 3 and 4.

Despite the ability of LLM to work synergistically with taxane-domain binders,[134] its potency in drug-resistant cell lines,[78,133,144,145] and anti-angiogenic properties,[146] *in vivo* experiments found both relatively small inhibition of tumour growth, as well as toxic effects by LLM.[144] Furthermore, LLM is prone to acid-catalyzed degradation into isolaulimalide, which is less potent by over two orders of magnitude (Table 1.2).[78] Therefore, it became a priority to find LLM analogues with improved efficacy and

stability, decreased toxicity, and that can be easily synthesized. This has proven challenging since all studies published to date regarding the efficacy of LLM analogues, which have been modified at the C2–C3, C15, C16–C17, C20, and C23 positions (Figure 1.5), show these novel analogues to be less potent than LLM,[145,147–152] and it is unknown how structural modifications alter the LLM binding mode to tubulin, making the rational design of LLM analogues challenging.

Substantial work has been conducted by a variety of groups to develop, synthesize, and evaluate structural analogues of LLM. Of notable interest is the work by the Mooberry group and their collaborators.[145,150,152,153] Some of these analogues are computationally-examined in Chapter 3 and have been published.[2] Gallagher and coworkers have synthesized a variety of LLM analogues, and evaluated their cytotoxicities.[151] Compounds related to LLM have also been proposed by Prof. Dennis Hall at the University of Alberta, which are structurally unique from other derivations based on the LLM framework. These compounds from the Gallagher and Hall groups are examined computationally in Chapter 4. By computationally examining LLM and LLM analogues in a MT model, characteristics of the effective LLM analogues can be identified. This will allow for the development of a LLM–tubulin pharmacophore, which is described by IUPAC as "the ensemble of steric and electronic features that is necessary to ensure the optimal supramolecular interactions with a specific biological target structure and to trigger (or to block) its biological response".[154] It is also a goal for this information to be used in the future to computationally predict the efficacy of newly-proposed LLM analogues, aiding in the rational drug design process and accelerating preclinical investigations of LLM.

1.2.2.4 Compounds that covalently bond to tubulin

In 2000, cyclostreptin (Figure 1.5) was isolated from the actinobacteria *Streptomyces* genus, and determined to have nanomolar antitumor activity (Table 1.2)[77] via an antimitotic mechanism.[155,156] Cyclostreptin was noted to behave uniquely compared to other MT-stabilizing agents, such as TXL. Cyclostreptin only weakly promoted tubulin assembly, but also bound strongly to MTs and competitively inhibited TXL binding.[157] Cyclostreptin-containing MTs also disassemble more slowly than TXL-stabilized MTs at low temperatures.[157] Although TXL was more effective than cy-

clostreptin in sensitive cell lines, cyclostreptin is very effective in resistant cell-lines.[157]

This unique behaviour was explained when it was discovered that cyclostreptin irreversibly binds to tubulin.[77,100] Cyclostreptin was the first MT targeting agent found to form a covalent bond to tubulin, and the first taxane-domain binder found to bind to dimeric tubulin (a dimer of heterodimers).[18] Cyclostreptin binds to tubulin stoichiometrically, and high performance liquid chromatography (HPLC) coupled to tandem MS (MS/MS) was used to determine that cyclostreptin covalently bonds to β:Thr220 (β:H6–H7) or β:Asn228 (β:H7) in MTs *in vitro* and *in vivo*, and these residues are located in the type I pore and luminal taxane site, respectively (Figure 1.10).[100] When cyclostreptin bonds to dimeric or oligomeric tubulin, it is less common and only at β:Thr220.[100] No crystal structure is currently available for the cyclostreptin–tubulin complex and MS/MS did not identify the connectivity of the ligand–protein crosslink, though the lactone and strained C2–C17-olefin (Figure 1.5) sites have been proposed.[100,158] The covalent bonding of this ligand explained several important observations about cyclostreptin-stabilized MTs, such as their cold stability and the higher temperatures required for cyclostreptin to induce MT assembly.[100] Furthermore, covalent bonding of cyclostreptin to MTs decreases intracellular drug concentrations, thereby reducing the efflux of this compound by the P-glycoprotein pump (Pgp).[159] It was also found that β-tubulin is the primary target of cyclostreptin, indicating the reduced tendency of this compound to engage in off-target interactions.[159]

The antimitotic activity of the taccalonolides is also due to covalent bonding to tubulin. The taccalonolides, a class of hexacyclic compounds naturally isolated from plants in the *Tacca* genus (Figure 1.5),[160–166] are a relatively new class of agents that have been under preclinical investigation as cancer chemotherapies, though total synthesis of these compounds is not available.[167] While not all taccalonolides have shown cytotoxic activity, some have antiproliferative activity at subnanomolar concentrations (Table 1.2)[68,80,168] and stabilize MTs.[169]

Preclinical studies by Mooberry and coworkers have shown that the taccalonolides are particularly promising antimitotic agents,[68,80,167–178] addressing many of the issues associated with taxane resistance. The taccalonolides are effective in cells that overexpress Pgp and in cells having single point mutations in the luminal taxane site.[169]

26

They have also shown enhanced efficacy in cells expressing the βIII-tubulin isotype,[68] which is associated with resistance in cancerous cells (see Section 1.2.3.1).[179,180] Although the taccalonolides have lower potencies than taxanes *in vitro*, they were more potent than the taxanes during *in vivo* antitumor trials.[68,172]

Much work has been done to determine how the taccalonolides interact with MTs. The taccalonolides have been found to work synergistically with the laulimalides, indicating these compounds interact at non-overlapping sites.[176] Taccalonolides were found to inhibit the binding of taxanes, but taxanes do not affect taccalonolide binding.[176] Further experiments revealed that once taccalonolides were bound to MTs, they could not be removed under denaturing conditions,[176] indicating covalent bonding was present. This was confirmed when MS/MS indicated that the taccalonolides covalently bond to β-tubulin in a segment of residues containing β:214–232, which involves β:H6–H7 and β:H7 in the type I pore and luminal site.[176] This is also the range of residues that cyclostreptin (see above) and zampanolide (β:Asn228 and β:His229 in the luminal site)[51,181] are known to covalently bond to (Figure 1.10). MS/MS could not identify the residues to which the ligand–protein crosslink occurs or the connectivity,[176] and no crystal structure is available for taccalonolide–tubulin complexes. However, reactivity is associated with the lactone, since removal of this functionality stopped taccalonolide activity.[175] HDX MS experiments probed the allosteric effects of taccalonolide binding to determine that taccalonolides stabilize lateral interprotofilament contacts, largely in α-tubulin.[176]

In addition to the above-mentioned drug candidates, zampanolide and its enantiomer dactylolide are known to bond to residues in the luminal taxane site.[18] There is a crystal structure available for zampanolide bound to a stathmin-stabilized $\alpha\beta$-tubulin heterodimer (4I4T, Table 1.1).[51] T138067 is a destabilizing agent known to bond in the colchicine site.[74]

1.2.3   Resistance

Anticancer drugs may become less effective due to the tendency of cells to develop resistance mechanisms that combat the effect of the drug. Common mechanisms of resistance pertaining to antimitotic compounds are discussed below.[182,183]
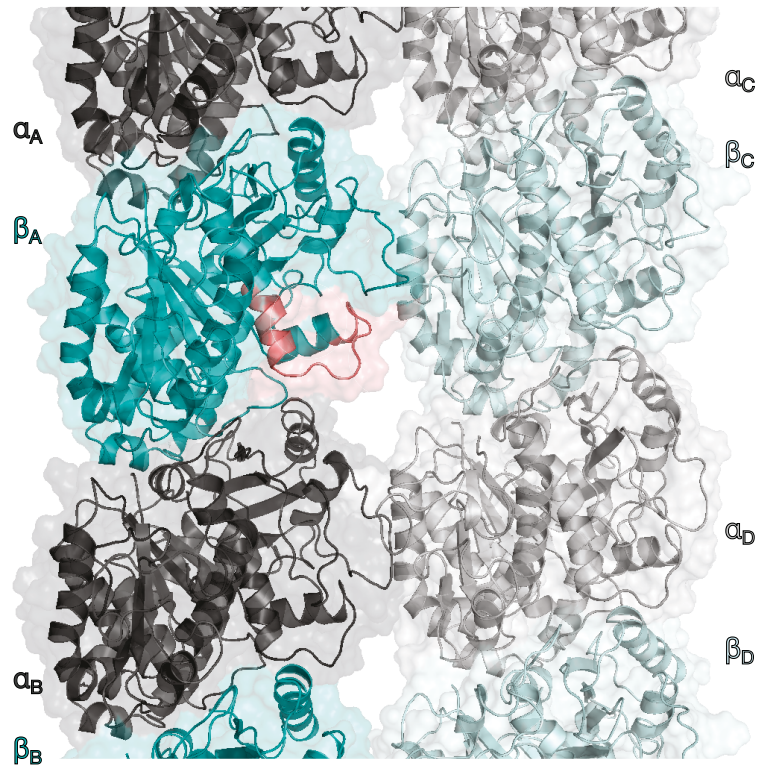
Figure 1.10: *The luminal taxane site (purple) and the pore site (orange) at which cyclostreptin is known to covalently bond to MTs. The residues β:214–232, to which the taccalonolides are known to covalently bond to, are indicated in pink. Viewed from the MT lumen.*

1.2.3.1 Tubulin isotype expression

Proteins such as tubulin exist in multiple forms encoded by different genes, known as isotypes.[39] As a result, there may be amino acid substitutions in the protein, which do not affect the ability of the protein to perform its normal function. In humans, there are six main α-tubulin isotypes and ten main β-tubulin isotypes (βI, βIIa, βIIb, βIII, βIVa, βIVb, βV, βVI, βVII, and βVIII).[184] 80–95 % sequence identity is observed among tubulin isotypes and the greatest variation is in the C-terminal tail.[44,184,185] βI is the most common isotype in both normal and cancerous cells.[186] Using homology modeling, structures have been obtained for the human β-tubulin isotypes.[184,185]

MT assembly was found to be affected by the tubulin isotypes present.[187] It is believed that cells may respond to changes in MT dynamics by altering tubulin isotype expression.[39,184,188] Alterations in cellular isotype expression have also been associated with resistant cell lines.[188,189] For example, increased levels of βII-tubulin were found in TXL-resistant cell lines and tumours.[179,190] βIII expression has also been associated with resistance to tubulin-targeting agents.[191] Drugs that preferentially bind to βII and βIII isotypes may increase the target specificity of antimitotic agents, preferentially affecting cancerous tissue over normal tissue.

Some residue alterations were identified between the isotypes in the known drug binding sites.[184] Within the luminal taxane site, six residues varied among the isotypes though this site was very similar in all isotypes. A Ser275Ala (M-loop) substitution was present in βIII, and an Arg359Trp (β:S9–S10) substitution was observed in βVII, while five substitutions were observed for βVI.[184] The colchicine binding site contains seven residues that show variation among the isotypes, with five isotypes containing substitutions.[184] The *Vinca* alkaloid domain involves four residues substitutions in three β-tubulin isotypes.[184]

The greatest variation in these three binding sites occurs for the βVI, βVII and βVIII isotypes, and no variations occur in the taxane, colchicine or *Vinca* alkaloid binding sites for βI, βII and βIV.[184] This makes it difficult to target the increased βII and βIII expression in cancerous tissues. However, the βIII Ser275Ala substitution located in the M-loop is also in contact with taxanes at the intermediate binding site. Therefore, taxane analogues have been designed to enhance interactions with

β:Ala275 in order to preferentially target the βIII-tubulin that is expressed in cancerous tissue.[102,192] Interestingly, vinblastine most strongly affects βII-tubulin,[193] though there are no residue substitutions found in the *Vinca* alkaloid domain of βII.[184] This points to the importance of investigating allosteric effects in drug–tubulin interactions and MT formation, rather than solely considering interactions within the drug binding site, which has been discussed in the literature.[188] Comparing the isotype sequences[184] to the computationally-determined LLM binding pose (Chapters 3 and 4) shows three substitutions in the LLM binding sites of βII- and βIII-tubulin. Of these, the conservative βII Ala298Ser substitution may be important since β:Ala296 forms a water-mediated hydrogen bond with LLM.

1.2.3.2 Tubulin point mutations

Point mutations in $\alpha\beta$-tubulin heterodimers have been implicated in the resistance of cells lines to MT-targeting agents. However the role of point mutations in the development of resistances in the clinic is less understood,[194] since it is difficult to differentiate between residue changes that results from gene expression or point mutations.

Point mutations are commonly found in the βI-tubulin present in cells resistant to MT-stabilizing agents.[183] Known mutations are detailed extensively in the literature.[180,188,195–202] For example, β:Thr274Ile, β:Arg282Gln, and β:Gln292Glu mutations have been associated with TXL and epothilone resistances, where the first two mutations are located in the luminal taxane site and the site of the third mutation facilitates lateral interdimer interactions.[195–197,199,200] In the absence of MT-targeting agents, these mutations decrease MT stability. Computational examinations of these mutations indicate varying effects on tubulin, which include changes localized to the taxane binding site such as changes in pocket volume, weakening of ligand binding, and changes in M-loop conformation, and well as more delocalized changes such as alterations in tubulin structure and increased tubulin flexibility.[203] Alternatively, cells resistant to an epothilone analogue showed mutations like β:Ala231Thr affect MT stability, but not drug binding.[199] Modifications to α-tubulin have also been associated with TXL resistance.[198,202]

Tubulin sequences have been obtained for the yew tree, the natural source of

TXL.[204] MTs formed from yew tree tubulin must be resistant to the effects of TXL, and may provide clues as to how TXL-resistant tubulin, involving either changes in isotype expression or point mutations, affects TXL efficacy. Yew tree tubulin and human tubulin share 80 % sequence identity, and 65 % of the differences between β-tubulin sequences are found on the surface of the protein, with most occurring in the lumen.[204] 18 residue substitutions are located in the luminal taxane binding site and eight residue substitutions were found in the type I pore, which is greater than the variation found among human isotypes.[204] Computations showed that each of the luminal site substitutions decreased TXL affinity.[204] A correlation was also found between the location of residue substitutions and regions that had been previously reported as having a change in mobility upon TXL binding,[105] which includes structures both near to and removed from the taxane binding site.

1.2.3.3 Multidrug resistance via the P-glycoprotein pump

Multidrug resistance (MDR) is a problem that plagues the efficacy of anticancer agents, including MT-targeting agents. One of the biggest contributors to MDR involves the Pgp, also known as multidrug resistance protein 1 (MDR1), which is an efflux pump that removes foreign substances from cells. Resistances associated with high levels of the Pgp are found in both clinical use and cell studies, as well as in tumours with intrinsic (untreated cells) and acquired (after treatment) resistances, and in tissues that undergo relapse.[205]

Many naturally-occuring and synthetic MT-targeting agents are substrates for and effluxed by Pgp. To address the problem of drug efflux by Pgp efflux, Pgp inhibitors have been developed to be coadministered with the drug.[205] Alternatively, studies have began to search for new anticancer agents with reduced affinity for the Pgp. Epothilones are not substrates for the Pgp,[182] and drugs like CAB and LLM have been shown to be more effective in multidrug resistant cell lines than TXL due to reduced affinity for the Pgp.[79,133,150] Covalently-bonding agents also have reduced efflux by the Pgp due to low intracellular drug concentrations.[159]

1.3 Computational methods

When applying computational chemistry to tackle a problem, a balance between accuracy and efficiency must be considered. Efficient methods based on classical mechanics are well-suited to study the structure of a variety of large biological systems, as well as their dynamics. However, these methods are unable to account for quantum phenomena that may be necessary to understand the system of interest. The application of more accurate quantum chemical methods to biological macromolecules has traditionally been prohibitively expensive. Fortunately, recent advances in quantum methods now make it possible to apply quantum mechanics to larger systems. Methods based on classical mechanics have been applied in Chapters 2–5, while methods based on quantum mechanics have been applied in Chapters 6 and 7.

Examining the behaviour of a system as it evolves in time provides important information about biological systems. Molecular dynamics (MD) simulations allow for the motion of atoms to be taken into account under different conditions (pH or temperature, for example) to calculate the time-averaged values of certain properties (energy, for example). In this Thesis, MD is combined with classical mechanics to examine ligand–protein binding (Chapters 2–5).

The methods listed above are appropriate for studying the structure and electronic properties of ligand–protein complexes. However, pharmacokinetic effects (how the body affects the drug) and toxicity are also important factors in understanding a drug and in the future design of novel agents. Therefore, calculations have been employed to predict the absorption, distribution, metabolism, excretion and toxicity (ADMET) properties of agents that are in preclinical development (Chapters 3 and 4).

The following sections will summarize the computational approaches applied in this Thesis.

1.3.1 Classical mechanics and molecular mechanics

Classical mechanics is the study of motion according to Newton's Laws of Motion. Within classical mechanics, a particle has a defined trajectory with a known position and momentum at any given time. The application of classical mechanics to study molecular systems, known as molecular mechanics (MM), is appealing due to the sig-

nificantly reduced computational cost of classical descriptions of molecules. However, since these microscopic systems are inherently quantum in nature and this governs the properties of the system, parameterization of molecular mechanics methods is required.

In molecular mechanics, the potential energy of a given system is described classically according to a force field. A simple atomistic force field may be described as:

$$V_{MM} = \sum^{bonds} V_{bond} + \sum^{angles} V_{angle} + \sum^{dihedrals} V_{dihedral} + \sum_{i<j}^{atoms} V_{ij,vdW} + \sum_{i<j}^{atoms} V_{ij,elec} \quad (1.1)$$

The potential (V_{MM}) is calculated as a sum of potentials between atoms, which includes both bonded (internal) and non-bonded terms. The bonded terms are contributions from bonds (V_{bond}), angles (V_{angle}), and dihedral angles ($V_{dihedral}$) between atoms. The non-bonded terms are pairwise contributions between atoms i and j, and include van der Waals (V_{vdW}) and electrostatic (V_{elec}) forces.

A variety of force fields are available, which differ in the functional form of each potential term in Equation 1.1 and in the parameterization. The Amber (assisted model building with energy refinement) series of force fields, designed for biological systems, is an atomistic force field that depends on the coordinates of the N atoms of a system and takes the following form:

$$V_{Amber} = \sum^{bonds} K_b(b - b_0)^2 + \sum^{angles} K_\alpha(\alpha - \alpha_0)^2 + \sum^{dihedrals} K_\phi[\cos(n\phi + \phi_0) + 1]$$
$$+ \sum_{i<j}^{N} (\frac{A_{ij}}{r_{ij}^{12}} - \frac{B_{ij}}{r_{ij}^6}) + \sum_{i<j}^{N} \frac{q_i q_j}{4\pi\epsilon_0 r_{ij}} \quad (1.2)$$

These terms correspond to those in Equation 1.1. The potential arising from bonded atoms is modeled harmonically and calculated using the variable b, which is the distance between bonded atoms, as well as the parameters K_b, related to the force constant, and b_0, related to the equilibrium bond length. The contributions from angles are also modeled harmonically, with a dependence on the variable α, the angle between bonded atoms, and the parameters K_α and α_0 representing force constants

33

and equilibrium angles, respectively. The contribution arising from dihedral angles is modeled as a continuous cosine function depending on the variable dihedral angle (ϕ), as well as the parameters relating to the rotation barrier (K_ϕ), equilibrium dihedral angle (ϕ_0), and phase (n). The nonbonded terms are summed over all distinct pairs of atoms, giving $\frac{1}{2}N(N-1)$ terms. The van der Waals (vdW) contribution is dependent on the variable r_{ij}, which is the distance between atoms i and j in the system, and parameters A_{ij} and B_{ij}, which are related to sizes of atoms i and j. The electrostatic contribution also depends on the variable r_{ij}, as well as the charges on atoms i and j (q_i and q_j, respectively) and the permittivity of free space (ϵ_0). Parameters may be based on data from experiment or quantum calculations. Since the nonbonded terms in Equation 1.2 are calculated in a pairwise fashion, the Amber force fields formally scale as N^2.

The Amber force field has been parameterized to describe biological systems, including proteins. The original version of the Amber force field, denoted ff94,[206] was developed in 1994. Since then, multiple reparameterizations of this force field have been developed to improve the accuracy of the potential energy function.[207] The ff99SB reparameterization improved the description of the protein backbone dihedral angles and secondary structures.[208] The ff12SB force field enhanced the description of protein backbone and side chain dihedral angles relative to ff99SB. During the course of this PhD research, the ff14SB force field was also released, which minimized the dependence of the protein side chain conformation on the backbone. The general Amber force field (GAFF) has also been developed to describe organic molecules,[209] such as ligands or drugs, and is compatible with the Amber force fields.

1.3.2 Quantum mechanics

The microscopic properties of systems are described by quantum mechanics (QM). QM-based methods, known as *ab initio* methods, are highly accurate and can be applied to study properties of systems that lie outside of CM, such as chemical reactions, excited states, and charge transfer. Unlike CM, a quantum particle does not have a well-defined position and momentum, and only the probability of finding a particle at a given position and momentum can be obtained. This probability may be determined from the wavefunction.

The first postulate of QM states that a quantum system is described by a wavefunction. By solving the Schrödinger equation, shown in Equation 1.3 in its time-independent nonrelativistic form, the wavefunction may be obtained.

$$\hat{H}(\mathbf{r}_1, \mathbf{r}_2, ...\mathbf{r}_n, \mathbf{R}_A, \mathbf{R}_B, ...\mathbf{R}_N)\Psi(\boldsymbol{\zeta}_1, \boldsymbol{\zeta}_2, ...\boldsymbol{\zeta}_n, \mathbf{R}_A, \mathbf{R}_B, ...\mathbf{R}_N) =$$
$$E\Psi(\boldsymbol{\zeta}_1, \boldsymbol{\zeta}_2, ...\boldsymbol{\zeta}_n, \mathbf{R}_A, \mathbf{R}_B, ...\mathbf{R}_N) \tag{1.3}$$

In this eigenvalue equation, the Hamiltonian operator $(\hat{H})$ is applied to the wavefunction (Ψ) to obtain the energy (E) and wavefunction. The wavefunction depends on the spatial $(\mathbf{r}_n = x_n, y_n, z_n)$ and spin (σ_n) coordinates of n electrons $(\boldsymbol{\zeta}_n = \mathbf{r}_n, \sigma_n)$, and the spatial coordinates of N nuclei $(\mathbf{R}_N = X_N, Y_N, Z_N)$ contained in the system of interest.

The Hamiltonian operator is the sum of potential $(\hat{V})$ and kinetic $(\hat{T})$ energy operators of electrons (el) and nuclei (nuc), and is defined in atomic units as:

$$\hat{H} = \hat{T}_{el} + \hat{T}_{nuc} + \hat{V}_{nuc-el} + \hat{V}_{nuc-nuc} + \hat{V}_{el-el} \tag{1.4}$$

$$\hat{H} = -\sum_i^n \frac{1}{2}\nabla_i^2 - \sum_A^N \frac{1}{2}M_A\nabla_A^2 - \sum_i^n\sum_A^N \frac{Z_A}{r_{iA}} + \sum_{A<B}^N \frac{Z_A Z_B}{r_{AB}} + \sum_{i<j}^n \frac{1}{r_{ij}} \tag{1.5}$$

Indices i and j run over n electrons while indices A and B run over N nuclei. This equation includes the nuclear mass (M_A), nuclear charge (Z_A), interparticle distances $(r_{iA}, r_{AB}, \text{ and } r_{ij})$, and Laplacian operator $(\nabla_i^2 = \frac{\partial^2}{\partial x_i^2} + \frac{\partial^2}{\partial y_i^2} + \frac{\partial^2}{\partial z_i^2})$.

Within a molecular system, the time scale of nuclear motion is much larger than the time scale of electronic motion, and therefore the nuclei are essentially stationary relative to the electrons. With this information, the Born-Oppenheimer approximation may be applied to simplify Equations 1.4 and 1.5 and obtain the electronic Hamiltonian $(\hat{H}_{el})$ and electronic wavefunction (Ψ_{el}):

$$\hat{H}_{el} = -\sum_i^n \frac{1}{2}\nabla_i^2 - \sum_i^n\sum_A^N \frac{Z_A}{r_{iA}} + \sum_{i<j}^n \frac{1}{r_{ij}} \tag{1.6}$$

$$(\hat{H}_{el} + V_{nuc})\Psi_{el}(\boldsymbol{\zeta}_1, \boldsymbol{\zeta}_2, ...\boldsymbol{\zeta}_n; \mathbf{R}_A, \mathbf{R}_B, ...\mathbf{R}_N) = E_{el}\Psi_{el}(\boldsymbol{\zeta}_1, \boldsymbol{\zeta}_2, ...\boldsymbol{\zeta}_n; \mathbf{R}_A, \mathbf{R}_B, ...\mathbf{R}_N) \tag{1.7}$$

in which the nuclear kinetic energy (T_n) is zero, and the internuclear potential energy is a constant ($V_{nuc} = \sum_{A<B}^{N} \frac{Z_A Z_B}{\mathbf{r}_{AB}}$). Therefore, the electronic wavefunction (Ψ_{el}) depends explicitly on the electronic coordinates ($\boldsymbol{\zeta}_n$), and parametrically on the nuclear coordinates ($\mathbf{R}_N$). As a simplification, an n-electron wavefunction is expressed as a Hartree-Fock product of n one-electron wavefunctions, or spin orbitals $\psi(\boldsymbol{\zeta}_n)$. A spin orbital is expressed as a product of a spatial orbital ($\phi(\mathbf{r}_n)$) and a Pauli spin function (designated $\alpha(\sigma_n)$ or $\beta(\sigma_n)$). The n-electron wavefunction is written as a Slater determinant to enforce the antisymmetry requirement of the electronic wavefunction:

$$\Psi_{el}(\boldsymbol{\zeta}_1, \boldsymbol{\zeta}_2, ...\boldsymbol{\zeta}_n) = \frac{1}{[n!]^{1/2}} \begin{vmatrix} \psi_1(\boldsymbol{\zeta}_1) & \psi_1(\boldsymbol{\zeta}_2) & \cdots & \psi_1(\boldsymbol{\zeta}_n) \\ \psi_2(\boldsymbol{\zeta}_1) & \psi_2(\boldsymbol{\zeta}_2) & \cdots & \psi_2(\boldsymbol{\zeta}_n) \\ \vdots & \vdots & \ddots & \vdots \\ \psi_n(\boldsymbol{\zeta}_1) & \psi_n(\boldsymbol{\zeta}_2) & \cdots & \psi_n(\boldsymbol{\zeta}_n) \end{vmatrix} \tag{1.8}$$

The application of the electronic Schrödinger equation to a multi-electron system is nontrivial. This arises due to the electron-electron repulsion term, $\sum_{i<j}^{n} \frac{1}{\mathbf{r}_{ij}}$, in Equation 1.6, which depends on the simultaneous pairwise interactions between all electrons. In the simplest *ab initio* method, the Hartree-Fock (HF) method, electron repulsion is calculated as the interaction between one electron and the average field of all other electrons. Since the electron repulsion experienced by electron i depends on the positions of the other $n-1$ electrons, the Hartree-Fock equations must be solved self consistently. A set of trial spin orbitals $\{\psi_n\}$ is provided, and the HF equations are solved to obtain a new set of $\{\psi_n\}$. This continues until the spin orbitals are self-consistent with the field they generate. This process is known as a self-consistent field (SCF) method.

In order to apply the above equations to molecules, the molecular orbitals ($\phi_p(\boldsymbol{r}_i)$) must be expanded as a linear combination of K basis functions ($\chi_\mu(\boldsymbol{r_i})$):

$$\phi_p(\boldsymbol{r}_i) = \sum_{\mu=1}^{K} c_{\mu p} \chi_\mu(\boldsymbol{r_i}) \tag{1.9}$$

The coefficients, $c_{\mu i}$, are variational parameters that are varied until the SCF procedure has converged. In practice the basis functions, $\chi_\mu(\boldsymbol{r_i})$, are expressed as linear combinations of Gaussian functions ($\propto e^{\alpha r^2}$). These collections of atom-centered Gaussian functions comprise a basis set.

Since the HF theory only includes electron-electron repulsion in an average way, the motion of electrons is not correlated. Physically, this neglects the fact that electrons inherently avoid each other. As a result, the energy of a system predicted by the HF theory is too repulsive. Correlated methods like the nth-order Møller-Plesset (MPn) perturbation theory, configuration interaction (CI) and coupled-cluster (CC) theory improve upon the HF method by reducing the repulsion in the HF wavefunction. The MPn methods rely on perturbation theory to include electron correlation, while CI and CC methods express the electronic wavefunction (Ψ_{el}, Equation 1.8) as a linear combination of Slater determinants. However, the inclusion of electron correlation makes these methods more computationally expensive. While HF scales formally as K^4, where K is the number of basis functions, MP2 methods scale as K^5, and the gold-standard correlated method CCSD(T) scales at K^7.

1.3.2.1 The Fragment Molecular Orbital method

For macromolecular systems comprised of thousands of atoms, and many basis functions on each atom, the scaling of *ab initio* methods is prohibitively expensive. However, fragmentation methods provide a means of applying *ab initio* methods to large systems with near-linear scaling.[210,211] These methods partition a large molecular system into fragments, and perform a QM calculation on each fragment to obtain the wavefunction and properties of the fragments, which are then combined to obtain the properties of the macromolecule.[212,213] The computational speed of these methods is further enhanced due to their ability to be massively parallelized. In this Thesis, the Fragment Molecular Orbital (FMO) method has been used to apply quantum-chemical calculations to different systems, including macromolecular taxane–tubulin complexes.

The FMO method partitions a system into fragments, calculating the energy of a system as a sum of polarized fragment energies and many-body interaction energies. The polarized monomers are calculated self-consistently in a Coulomb field generated by the surrounding fragments to create a converged electrostatic potential, such that each fragment is polarized by its environment.[214] This is known as the monomer SCF. Subsequently, many-body contributions are calculated and added to the polarized monomer energies to obtain the total energy of the system, E^{FMO}. The many-body

contribution, summed over all M fragments, is commonly truncated after the dimer term to obtain the two-body FMO (FMO2) energy of the system (E^{FMO2}),[215] as shown in Equation 1.10.

$$E^{FMO2} = \sum_{i=1}^{M} E'_i + \sum_{i<j}^{M} (E'_{ij} - E'_i - E'_j) + \sum_{i<j}^{M} Tr(\Delta \mathbf{D}^{ij} \mathbf{V}^{ij}) \qquad (1.10)$$

E'_i is the energy of a polarized monomer and E'_{ij} is the energy of a polarized dimer. $Tr(\Delta \mathbf{D}^{ij} \mathbf{V}^{ij})$ is the interaction of the relaxed density change with the embedding electrostatic potential, where $\Delta \mathbf{D}^{ij}$ is the difference in the density matrix between a dimer ij and monomers i and j, and $\mathbf{V}^{ij}$ is the environmental potential from the surrounding fragments acting on the dimer ij.[216] Using E^{FMO2} the interaction energy of an M-body system, where $M > 2$, may be obtained:

$$\Delta E'^{FMO2} = E^{FMO2} - \sum_{i=1}^{M} E'_i \qquad (1.11)$$

From a two-body FMO calculation, the pair interaction energies between fragments i and j ($\Delta E'^{FMO2}_{ij}$) are also easily obtained:

$$\begin{aligned} \Delta E'^{FMO2}_{ij} &= E^{FMO2}_{ij} - E'_i - E'_j \\ &= (E'_{ij} - E'_i - E'_j) + Tr(\Delta \mathbf{D}^{ij} \mathbf{V}^{ij}) \end{aligned} \qquad (1.12)$$

The FMO2 method formally scales as M^2 for HF.[215] Improved scaling to M may be obtained[217–219] by using additional approximations that are applied by default in the FMO[214] code in the GAMESS package.[220] For fragments that are spatially separated, terms describing the electrostatic potential of the environment may be described using Mulliken atomic orbital populations and Mulliken charges, and dimer interactions may be approximated with an electrostatic interaction.[215] In the study of small systems, the FMO method scales poorer than general *ab initio* calculations, though the FMO method is faster for a HF calculation with $M > 10$.[217]

Trimer interactions may also be included in the many-body expansion of FMO:[215]

$$E^{FMO3} = E^{FMO2} + \sum_{i<j<k}^{M} [\Delta E'_{ijk} + \Delta E^{D}_{ijk}] \qquad (1.13)$$

$$\Delta E'_{ijk} = E'_{ijk} - E'_i - E'_j - E'_k - \Delta E'_{ij} - \Delta E'_{ik} - \Delta E'_{jk} \tag{1.14}$$

$$\Delta E^D_{ijk} = Tr(\Delta \mathbf{D}^{ijk}\mathbf{V}^{ijk}) - Tr(\Delta \mathbf{D}^{ij}\mathbf{V}^{ij}) - Tr(\Delta \mathbf{D}^{ik}\mathbf{V}^{ik}) - Tr(\Delta \mathbf{D}^{jk}\mathbf{V}^{jk}) \tag{1.15}$$

As in Equation 1.11, E^{FMO3} may be used to calculate the interaction energy within a system. For a system containing M fragments, where $M > 3$, the interaction energy is calculated as:

$$\Delta E'^{FMO3} = E^{FMO3} - \sum_{i=1}^{M} E'_i \tag{1.16}$$

Using FMO2, the pair interaction energy between fragments i and j in Equation 1.12 may be analyzed via the pair interaction energy decomposition analysis (PIEDA) scheme, into electrostatic (ΔE^{ES}_{ij}), exchange (ΔE^{EX}_{ij}) and dispersion (ΔE^{DI}_{ij}) contributions, with the remaining contributions being attributed to charge transfer (CT) and mixed interactions (ΔE^{CT+mix}_{ij}).[221]

$$\Delta E'^{FMO2}_{ij} = \Delta E'^{ES}_{ij} + \Delta E'^{EX}_{ij} + \Delta E'^{DI}_{ij} + \Delta E'^{CT+mix}_{ij} \tag{1.17}$$

The FMO method may also include implicit solvent using the Polarizable Continuum Model (PCM). The pairwise desolvation free energy (ΔG^{sol}_{ij}) may be included using PCM to obtain the pairwise quantum-mechanical free energy of binding, ΔG^{PCM}_{ij}:[222]

$$\Delta G^{QM}_{ij} = \Delta G^{PCM}_{ij} = \Delta E'^{FMO2}_{ij} + \Delta G^{sol}_{ij} \tag{1.18}$$

PCM solvation may be included in any QM calculation.[223–230] In this method, a cavity is made around the solute. The solute induces a potential on the cavity resulting in an apparent surface charge (ASC) that is calculated from the electron density of the solute. Since there is solute-solvent polarization, the ASCs are obtained self consistently. There is a unique aspect about applying PCM solvation to FMO calculations, due to the FMO many-body expansions,[231] where different (monomer, dimer, etc) solute densities may be used to calculate the cavity ASCs. The combination of the FMO method and PCM solvent is denoted as FMOn/PCM[m], where an n-body

expansion is used to obtain the total energy and an m-body density is used in the calculation of the ASCs in the cavity surrounding the solute, where n ≥ m. [231]

The simplest implementation is the one in which an FMO2 calculation is performed and ASCs are calculated using monomer densities (FMO2/PCM[1]). Here, PCM solvent is included in the monomer SCF calculation. Subsequently, dimer calculations are performed using the ASCs induced by the monomer densities. The use of dimer densities to calculate ASCs is more complicated and time consuming than PCM[1]. Most commonly, the FMO2/PCM[1(2)] method is employed: Following an FMO2/PCM[1] calculation, the ASCs are recomputed according to the two-body densities. Subsequently, the FMO2 calculation is repeated in a second iteration using the new ASCs in the monomer SCF and dimer calculations. In order to obtain full two-body effects in PCM, FMO2/PCM[2] continues this process until the ASCs induced by the two-body densities are self-consistent, which generally takes 7–9 interactions. [231] Since PCM[1(2)] offers the best compromise between accuracy and efficiency, this method is employed in the Thesis.

The FMO method has been used in this Thesis, with the FMO [214] code in the GAMESS package. [220] This method was first applied to examine benzene-containing systems in order to understand monomer polarization as calculated by the FMO method, which is detailed in Chapter 6 and also published. [4] Subsequently, the FMO method was used to obtain a fully quantum-mechanical examination of taxane–tubulin interactions, detailed in Chapter 7.

1.3.3 Molecular dynamics

Molecular dynamics (MD) simulations calculate the motion of atoms and molecules as a system evolves in time. To follow the motion of a classical system in which the potential is described by molecular mechanics (Section 1.3.1), Newton's second law may be used. For each particle, i, this law relates the force on the particle ($\mathbf{F}_i$), which is the negative of the gradient of the potential ($-\nabla_i V$), to its mass (m_i) and acceleration ($\ddot{\boldsymbol{q}}_i$):

$$\boldsymbol{F}_i = -\nabla_i V = m_i \ddot{\boldsymbol{q}}_i \qquad (1.19)$$

Each particle evolves through time according to these forces. In systems containing many atoms, the equations are solved numerically at discrete time intervals known as time steps (Δt). In order to resolve the motions of atoms, particularly high frequency motions such as bond vibrations, small femtosecond time steps are required. Simulations are carried out for millions of time steps. As the system evolves, the position and momentum of each atom is collected at every time step to create a trajectory spanning nanoseconds to milliseconds, which may be subsequently analyzed.

1.3.3.1 The computational details of MD simulations

The application of classical MD simulations to a ligand–protein complex containing thousands of atoms involves many details. The procedure used in this Thesis is summarized below.

Drug molecules were described using the GAFF force field,[209] and parameters were derived with the ANTECHAMBER module of AmberTools. Nucleotide parameters for GDP and GTP were obtained from the literature[232] to supplement the Amber force field. Protein components were described with the Amber ff12SB or ff14SB force field, refinements of the ff99SB force field,[208] the details of which are included in the AmberTools Reference Manual. Explicit solvent was added using the transferable intermolecular potential 3 point (TIP3P) water model.[233] Specifically, the complex was solvated in a truncated octahedral box of pre-equilibrated TIP3P solvent extending 21 Å from the solute. Sodium and chloride ions were added to neutralize the system and obtain a physiologically-relevant ion concentration of 0.1 M. Ion parameters (compatible with TIP3P water) were taken from the work of Joung and Cheatham.[234,235] For computational efficiency, non-bonded terms were calculated within a 10 Å cutoff, while long-range electrostatics were calculated with the particle-mesh Ewald method.[236–238] For further efficiency, the SHAKE algorithm was utilized during simulations,[239] which restrains bonds involving hydrogen atoms to facilitate the use of a larger time step.

Using Amber 12[240] or Amber 14[241] GPU-enhanced code,[242–244] simulations were performed using periodic boundary conditions and Langevin dynamics. Each system studied underwent minimizations, followed by heating from 0 K to 300 K with the canonical ensemble (constant NVT (number of particles, volume, temperature)) and

density equilibration with the isothermal-isobaric ensemble (constant NPT (number of particles, pressure, temperature)). Subsequently, production data was collected. The minimizations, heating, and density equilibration steps differ for each system studied and are therefore specified in the Appendix (Appendices A–D) for the corresponding Chapter (Chapters 2–5). To verify the quality of each simulation, energy conservation was confirmed. The mass-weighted root mean square deviation (RMSD, calculated with respect to the structure at 0 ns) of ligand and protein atoms were calculated to determine the point at which the simulation was structurally equilibrated, and properties of the equilibrated system were calculated.

1.3.3.2   Calculating binding with the MM/GBSA method

To calculate the binding energy between two subsystems within a complex, the Molecular Mechanics/Generalized Born Surface Area (MM/GBSA) method was used.[245,246] In this approach, ligand–receptor coordinates are obtained from the explicitly-solvated trajectory (single-trajectory approach), but explicit solvent and ions are replaced with implicit generalized-Born solvation for computational efficiency. The MM/GBSA-calculated Gibbs binding free energy ($\Delta G^{MM/GBSA}$) is defined as the difference in Gibbs free energy between the complex ($G_{\text{complex}}^{MM/GBSA}$), and the receptor ($G_{\text{receptor}}^{MM/GBSA}$) and ligand ($G_{\text{ligand}}^{MM/GBSA}$):

$$\Delta G^{MM/GBSA} = G_{\text{complex}}^{MM/GBSA} - G_{\text{receptor}}^{MM/GBSA} - G_{\text{ligand}}^{MM/GBSA} \tag{1.20}$$

For each of these species, the Gibbs energy is calculated using the force field energy (V_{MM}), a solvation component (G_{sol}), the temperature (T), and the entropy (S):

$$G^{MM/GBSA} = V_{MM} + G_{sol} - \text{T}S \tag{1.21}$$

where V_{MM} is the force field potential obtained from Equation 1.1 and G_{sol} is the solvation contribution defined as $G_{sol} = G_{GB} + G_{SA}$, which is a sum of electrostatic contributions (derived from the generalized Born model) and non-electrostatic contributions (derived from the surface area), respectively.

To further analyze ligand–receptor interactions classically, pairwise contributions

may be obtained and decomposed into contributing forces:

$$\Delta G_{ij}^{CM} = \Delta G_{ij}^{MM/GBSA} = \Delta E_{ij}^{int} + \Delta E_{ij}^{vdw} + \Delta E_{ij}^{elec} + \Delta G_{ij}^{GB} + \Delta G_{ij}^{SA} \qquad (1.22)$$

The first three terms are obtained from the force field potential (Equation 1.1), where the internal (int) term includes bond, angle, and dihedral terms. The last two terms are obtained from the solvent contributions. These pairwise contributions are not additive, and therefore the sum of the pairwise contributions in Equation 1.22 is not equal to the total classical binding free energy in Equation 1.20 ($\sum \Delta G_{ij}^{MM/GBSA} \neq \Delta G^{MM/GBSA}$). Nevertheless, pairwise decomposition provides significant insight into ligand–residue contributions to ligand–protein binding.

The mmpbsa.py[247] protocols in AmberTools were utilized to perform MM/GBSA calculations, analyzing 100 frames per nanosecond. The GBn formulation[246] was implemented along with newly-developed parameters[248] and mbondi3 radii, which when combined with ff12SB was recommended by the Amber developers to give the best results for proteins. The entropic contribution to binding was not included due to the computational demand associated with calculating this quantity for large systems. Therefore, the binding energies reported include only the V_{MM} and G_{sol} terms. However, since the V_{MM} and G_{sol} terms can be decomposed into pairwise ligand–residue contributions, these contributions are most important when identifying the relative importance of protein residues in ligand binding. Therefore, these results are not directly comparable to experimentally-determined binding affinities. However, MM/GBSA calculations using a single-trajectory approach have been shown to successfully rank the binding affinities of different ligands, which is more important in drug-design studies and this Thesis than the prediction of absolute affinities.[249]

1.3.4   ADMET properties

The computational methods discussed above are useful in studying the structure, energy, and dynamics of ligand–protein complexes. However, these methods neglect the processes by which the drug comes to meet its target (pharmacokinetics), as well as adverse effects (toxicity), which are important elements of clinical drug use.[250] In the drug discovery process, there are high rates of attrition in the late stages due to the difficulty in predicting these problems in earlier preclinical development.[251]

Therefore, it is important to know the absorption, distribution, metabolism, excretion and toxicity (ADMET) properties of drug candidates in preclinical development. *In silico* models have been developed for the prediction of ADMET properties.

In order to assess potential pharmacokinetic factors and toxicity issues, the AD-MET Predictor™ program[252] was used to evaluate the ADMET properties in Chapters 3 and 4. The 3D coordinates of select compounds were used as input since properties based on 3D descriptors are superior to lower-dimensional descriptors.[253] The following physiochemical and biopharmaceutical properties are reported: native water solubility (S+S_w), human jejunal effective permeability (S+P_{eff}), the likelihood of crossing the blood-brain barrier (S+BBB_Filter), the likelihood of P-glycoprotein efflux (S+Pgp_Substr) and the likelihood of P-glycoprotein inhibition (S+Pgp_Inh). To gauge toxicity, hERG potassium channel inhibition (TOX_hERG_Filter) related to cardiotoxicity, the likelihood of causing elevation in SGOT enzymes and adverse liver effects (TOX_SGOT) and the likelihood of causing elevation in SGPT enzymes and adverse liver effects (TOX_SGPT) are also considered. An overall descriptor of the ADMET properties is also included (ADMET_Risk), taking into account all descriptors calculated for a given molecule.

1.4   Thesis Overview

This Thesis uses molecular modeling, based on classical and quantum mechanics, to examine the binding of antimitotic agents to tubulin. Many agents are currently in preclinical development. However, in some instances there is limited information available regarding the interaction of these agents with the tubulin target, making the design of novel compounds with enhanced efficacy very challenging. Despite the clinical success of other antimitotic agents, the mechanism by which these agents exert their effects on tubulin is unknown. This Thesis presents the results of extensive studies of laulimalide and laulimalide analogues that are in preclinical development, as well as the clinically-approved taxanes, in order to better understand how antimitotic agents affect tubulin. This information may be used in the development of novel agents with enhanced antimitotic effects.

Using classical mechanics, the binding of laulimalide to tubulin is studied in a

MT-like environment (Chapter 2) based on the results of a previous computational study of this compound. Next, laulimalide is reexamined in a MT-like environment based on the newly-available crystal structure (Chapter 3), along with laulimalide analogues from the Mooberry group (Chapter 3), Gallagher group (Chapter 4), and Hall group (Chapter 4). From this work, variations in the activity of the laulimalide analogues are explained based on the binding pose of the compound and the ligand–tubulin interactions. A pharmacophore is identified for laulimalide, and is used to predict the activity of newly-proposed compounds.

The three clinically-approved taxanes are also investigated using classical mechanics and molecular dynamics (Chapter 5). Despite the many studies that have considered TXL, few studies have considered the other taxanes in clinical use, DXL and CAB. It is well-established that the taxanes exert their effect on MTs via an allosteric mechanism. For the first time, the work detailed in Chapter 5 explains how the local effect of binding to β-tubulin produces an allosteric effect in the tubulin heterodimer. This provides a metric for future drug design studies to predict the efficacy of taxane-domain binders.

Quantum mechanical methods, specifically the Fragment Molecular Orbital method, were applied to study non-covalent interactions related to ligand–protein binding. First, the FMO method was applied to study π–π interactions in benzene-containing systems and other small systems of biological interest (Chapter 6). This provided insight into the effect of monomer polarization in binding. The FMO method was also applied to study taxane–tubulin interactions (Chapter 7), which indicated that different information may be obtained from the use of quantum mechanical methods to study ligand–protein interactions than when using classical mechanics.

Chapter 2

The unique binding mode of laulimalide to two tubulin protofilaments[*]

2.1 Introduction

Laulimalide (LLM, Figure 2.1) is a MT stabilizing agent in preclinical development and discussed in Section 1.2.2.3. Experimental and computational studies were instrumental in the identification of the LLM binding site (Section 1.2.2.3),[113,142,143] which is located on β-tubulin between protofilaments. Therefore, LLM is in contact with two adjacent β-tubulin subunits within a MT. This Chapter presents the results of a computational model in which LLM is located between two adjacent $\alpha\beta$-tubulin heterodimers, and is the first study to consider LLM in this MT-like environment. The work detailed below begins from a previous computationally-determined LLM binding pose.

---

[*]A version of this Chapter was published in *Chemical Biology and Drug Design*, **2015**, *86*, 190–199.
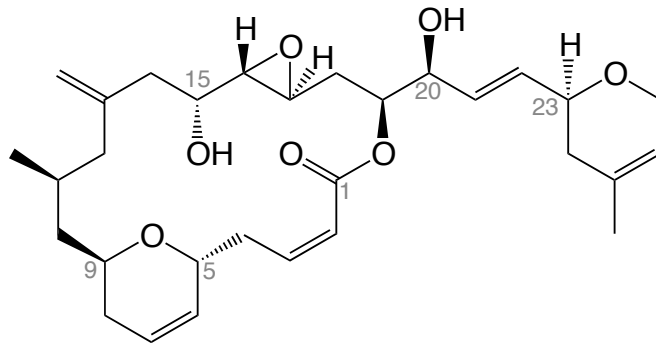
Figure 2.1: *Chemical structure and atomic numbering of (–)-laulimalide (LLM).*

2.2 Computational Details

The model utilized in this study contains two adjacent tubulin heterodimers with LLM bound between (Figure 2.2). The B-lattice configuration of these units was obtained from a high-resolution MT model by Fourniol *et al.* (PDB ID: 2XRP),[30] which combined cryo-EM data for a MT (resolved at 8 Å) with a high-resolution structure. The protein components utilized in this study were based on the 1JFF[36] crystal structure, where missing residues α:35–60 were overlayed from the 1TUB[35] crystal structure. This is essential since preliminary calculations found the omission of residues, though spatially removed from the binding site, can affect ligand–protein interactions. In the drug–protein model, apo $\alpha\beta$-tubulin (denoted $\alpha_1\beta_1$-tubulin, Figure 2.2) was overlayed onto 2XRP, and the LLM-bound $\alpha\beta$-tubulin (denoted $\alpha_2\beta_2$-tubulin, Figure 2.2), which was obtained from Bennett *et al.*,[142] was overlayed into the adjacent heterodimer. Since the model used in the present work takes tubulin heterodimers from 1JFF that are arranged in antiparallel protofilaments, and inserts them into a MT model with parallel protofilaments, substantial equilibration of the interdimer contacts is required (see Section 2.3, Results and Discussion).

All residues are discussed with respect to numbering in bovine α-tubulin isoform I-C (UniProt P81948) and β-tubulin isoform II-B (UniProt Q6B856), to maintain consistency with the report of Bennett *et al.*.[142] Hydrogen atoms were added using the tleap module of AmberTools, with all ionizable residues in a standard protonation state corresponding to a pH of 7.0. The four bound nucleotides, GTPs bound to the α-tubulins and GDPs bound to the β-tubulins, were also included.
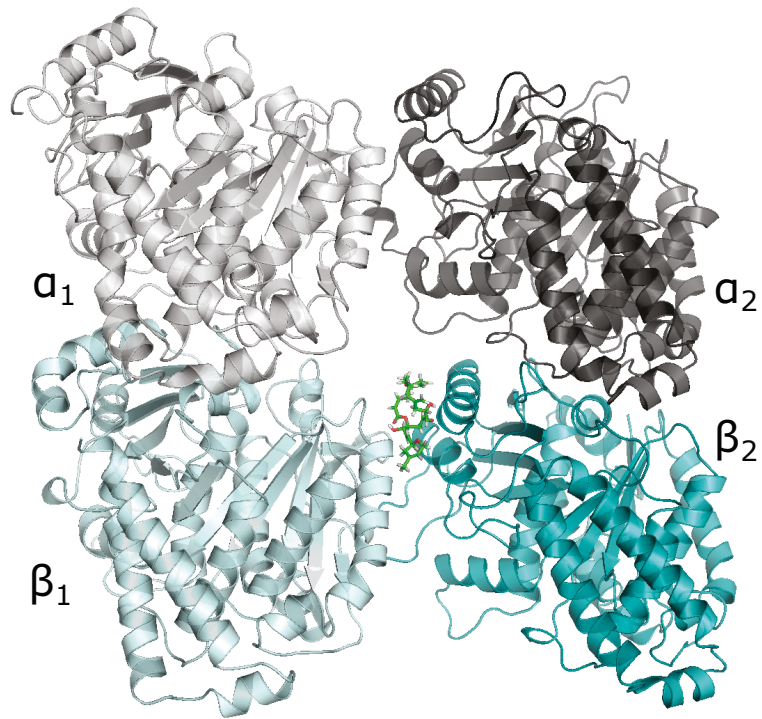
Figure 2.2: *Components of the LLM–tubulin model, including the ligand LLM (green), α-tubulin units (grey) and β-tubulin units (teal). Model was constructed from LLM bound to $\alpha_2\beta_2$-tubulin (dark), adjacent to $\alpha_1\beta_1$-tubulin (light) in a B-lattice configuration. Viewed from the exterior of the MT.*

MD simulations were performed using GPU-enhanced[242–244] Amber 12.[240] General details of the MD simulations performed in this Thesis may be found in Section 1.3.3.1 and details specific to this simulation may be found in Appendix A. The mass-weighted RMSD, calculated with respect to the structure at 0 ns, of the protein backbone atoms (Figure A1(a) in Appendix A), the binding site (Figure A1(b)), and the lateral contacts (Figure A1(c-f)), shows the system is structurally equilibrated after 45 ns. Therefore, the trajectory of the LLM–tubulin complex was analyzed over the final 90 ns. The seam between tubulin protofilaments is solvated, and therefore explicit solvent interactions play a role mediating LLM–tubulin and interprotofilament interactions, particularly hydrogen bonds (discussed below). Therefore, the twenty water molecules closest to LLM in every frame were retained for analysis. Crystallographic waters are also visible in 4O4H mediating LLM–tubulin interactions, emphasizing the importance of water in LLM binding.[52]

2.3   Results and Discussion

To obtain representative structures over the course of the 90 ns simulation, clustering analysis was performed with the hierarchical agglomerative algorithm,[254] where frames were clustered according to binding site similarity. Specifically, this similarity was measured based on the mass-weighted RMSD of the binding site atoms, which includes LLM, the 20 nearby water molecules and residues having atoms within 8 Å of LLM. The ideal number of clusters was selected based on a minimum in the Daves-Boulin Index and convergence of the ratio of the sum-of-squares regression to the sum-of-squares ratio.[254] Using these indices, the trajectory frames were partitioned into three clusters (Clusters A to C, Figure 2.3), and the representative structure (centroid) for each cluster was extracted (denoted as C–A to C–C). Clustering of the binding site without waters also identified the same three clusters, indicating the clustering to be solvent-independent. In an attempt to rank the importance of each cluster, simulations were continued to 180 ns (Figure A2). From 130–180 ns, Cluster C was adopted, which indicates Cluster C is dominant. Although results for all three Clusters are presented and discussed, emphasis is placed on Cluster C since it is most dominant over the course of 180 ns and also persists at the end of the simulation.
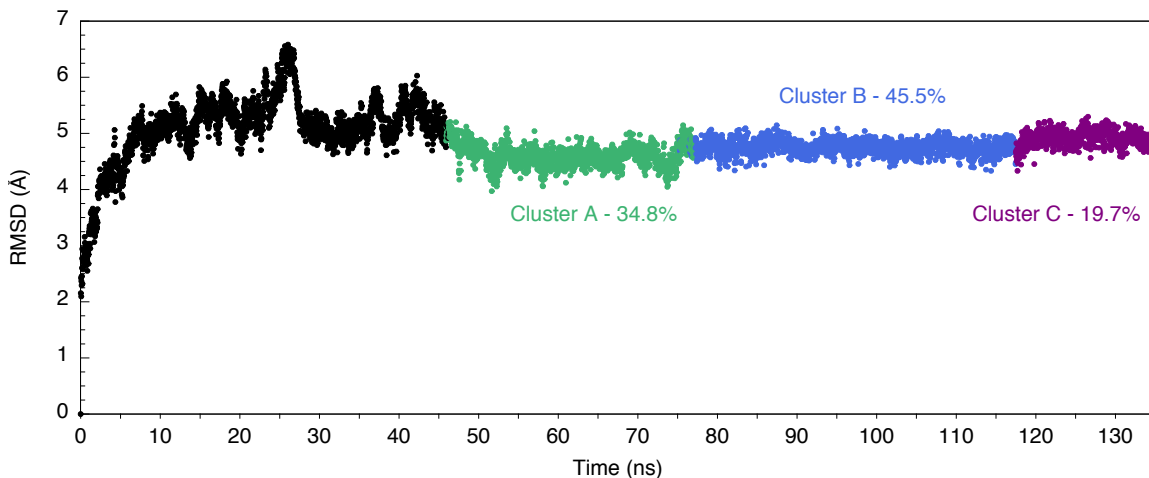
Figure 2.3: *Mass-weighted RMSD (Å) of the binding site atoms, coloured according to cluster, with occupancy indicated. Equilibration is shown in black. The binding site includes LLM, 20 water molecules and residues having atoms within 8 Å of LLM. Figure A2 identifies the same clusters over 180 ns.*

2.3.1 The laulimalide binding pose

The conformation of LLM was analyzed throughout the simulation, where it was determined that the LLM conformations in Clusters A and B are similar, while Cluster C offers a unique conformation of LLM (Figure A3). LLM in Cluster C differs most substantially from the rest of the simulation in the pseudorotations within the macrolactone ring (Figure A3). This conformational change in LLM is also evidenced by the change in the RMSD of its atoms (Figure A4), which coincides with the change in state from Cluster B to Cluster C at approximately 115 ns. Changes in binding that result from this conformational change are discussed below. The conformations of LLM determined in this study differ from those reported by Bennett *et al.*[142] which was used as a starting structure in the present work, from those determined by Thepchatri and coworkers in DMSO (Figure A3, Conf1–Conf21),[140] and that reported in the crystal structure (Figure A3, 4O4H).[52] Similarly, an RMSD comparison of the LLM conformation identified by Bennett *et al.*[142] also did not reveal a preference for any of the solution-state DMSO structures. Nguyen *et al.*[143] identified yet another unique conformation of tubulin-bound LLM than observed by Bennett *et al.*,[142] Thepchatri *et al.*,[140] Prota *et al.*,[52] or in this study, which features close contacts between the dihydropyran rings and an intramolecular hydrogen bond between the oxygen of

50

the dihydropyran side chain and the C15-hydroxyl group of the macrolactone ring. Hydrogen bond analysis of this simulation (discussed in detail below) identified no such intramolecular hydrogen bond.

Throughout the simulation, LLM maintained its position in contact with β_2:H9 and β_2:H10 (Figures 2.4, A5, and A6), as previously reported, though is not in close proximity to β_2:H9′ (greater than 9 Å). Contacts are also observed with β_1:H1′–S2, β_1:H3, and β_1:H3–S4 from the adjacent tubulin unit. This is supported by mass shift perturbation data that found a negative mass shift corresponding to residues in β_1:H3 and β_1:H3–S4.[142] Although Prota et al.,[52] using their LLM–tubulin model fit to cryo-EM reconstruction of a MT, predicted LLM to be in close proximity to H3,[52] the interactions with β_1:H1′–S2 and β_1:H3–S4 were not observed in that model. The dynamic model in the present work shows that the LLM side chain is directed towards β_1:H3 and the exterior of the MT, while the C1-carbonyl group is directed towards β_1:H1′–S2 and the MT lumen. LLM interacts most closely with the β_2 unit, where the oxygen of the dihydropyran side chain, as well as the macrolactone C15-hydroxyl, C16–C17-epoxide and C13-methylene, are tightly bound to β_2. In contrast, the remainder of LLM is solvated, suggesting interactions with LLM are of a polar nature.

2.3.2 Hydrogen bond interactions

The hydrogen bonds between LLM and tubulin residues were analyzed from 45–135 ns (Table 2.1), and contacts between LLM and protein components investigated (Figures 2.4 and A5). As mentioned above, many contacts were water mediated. Therefore, hydrogen bonds were analyzed while including the 20 water molecules closest to LLM in every frame. Since the binding arrangements, including hydrogen bonds, changed over the course of the simulation as the complex transitions between different clusters, hydrogen bonds were analyzed for each cluster (Table 2.1).

Within LLM, an intramolecular hydrogen bond is present between the C20-hydroxyl and the C1-carbonyl (occupancy > 53 %) throughout Clusters A and B (45–107.5 ns), where both these substituents are also solvent exposed. This intramolecular hydrogen bond was also observed by Bennett et al..[142] During this time, the C20-hydroxyl group may also occupy a hydrogen bond with β_2:Gln291 either directly (< 8 %) or
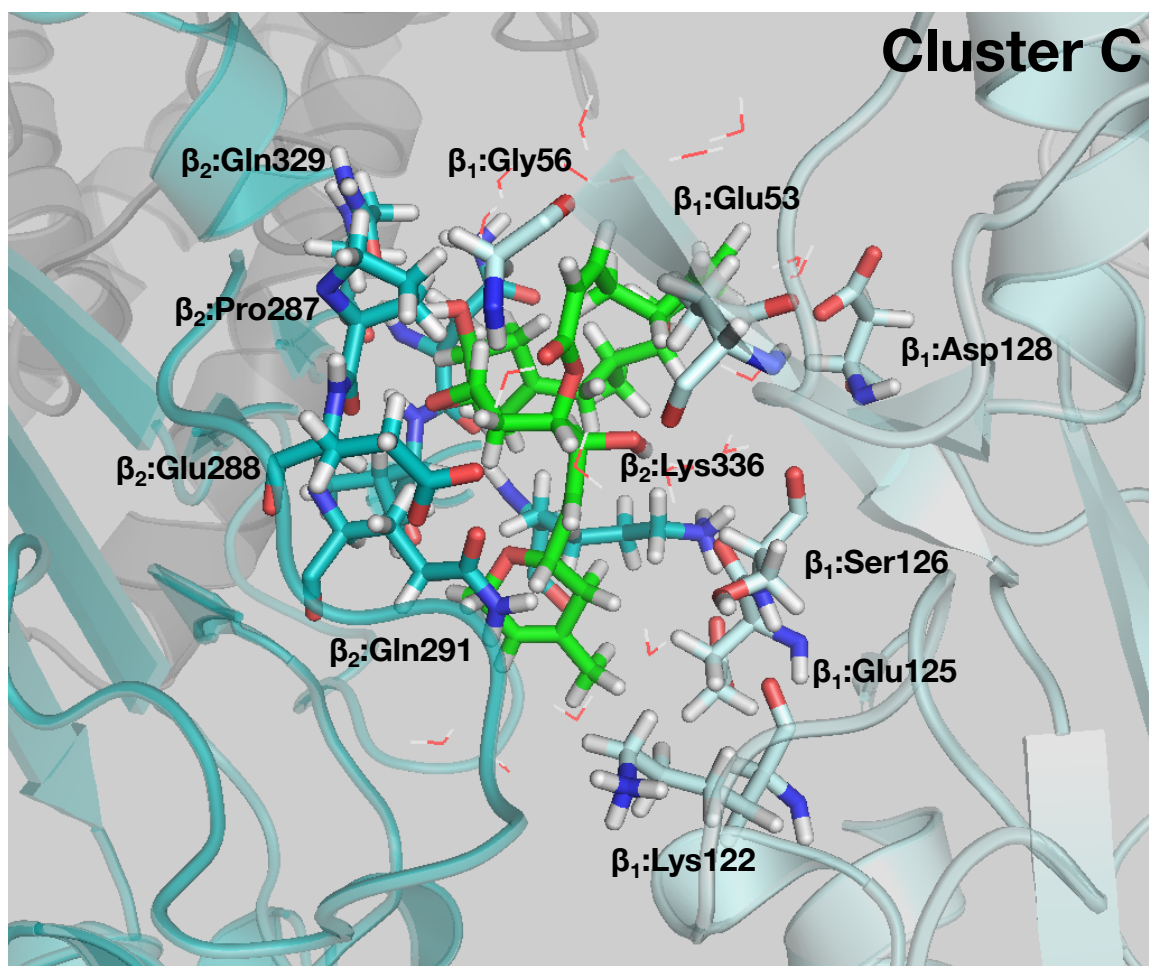
Figure 2.4: *A representative illustration of LLM (green) binding to β_1-tubulin (light cyan) and β_2-tubulin (teal) in Cluster C, as viewed from the MT lumen. Residues β_1:Glu53, β_1:Gly56, β_1:Lys122, β_1:Glu125, β_1:Ser126, β_1:Asp128, β_2:Pro287, β_2:Glu288, β_2:Gln291, β_2:Gln329, and β_2:Lys336 are shown in stick mode. Twenty binding-site waters are shown in line mode. Illustrations for the remaining clusters are included in Figure A5. Corresponding videos of the LLM binding site for each cluster are available online in the Supporting Information for the published version[1] of this Chapter (Videos S1–S3).*

Table 2.1: *Hydrogen bond occupancy (in percent) of various hydrogen bonds through-out the course of the simulation.*

Hydrogen Bond[a]	Cluster A	Cluster B	Cluster C	Average
C20-hydroxyl				
C1-carbonyl	55.7	53.2	0.1	43.6
β_2:Gln291	7.5	4.0	-	4.4
*β_2:Gln291	19.0	7.8	1.6	10.5
*β_2:Glu288, β_1:Gln291	1.8	0.1	-	0.7
β_1:Glu53	1.4	6.1	64.2	15.9
*β_1:Glu53	11.0	23.1	17.0	17.7
C1-carbonyl				
C20-hydroxyl	55.7	53.2	0.1	43.6
*β_2:Glu288	19.9	9.5	32.4	17.6
*β_1:Gly56	5.2	2.0	-	2.7
*β_1:Gly56, β_2:Glu288	5.2	1.5	31.4	8.7
C15-hydroxyl				
C16–C17-epoxide	2.0	3.0	1.3	2.3
β_2:Gln329	21.5	11.6	45.0	21.6

* Indicates a solvent-mediated hydrogen bond. The code in AmberTools identifies single bridging water molecules, and will not include instances where multiple water molecules bridge an interaction.; [a] Hydrogen bond defined as having heavy atoms within 3.0 Å and 135° ≤ ∠(donor–H···acceptor) ≤ 180°.

mediated by water (> 19 %), or in a water-mediated interaction with β_2:Gln291 and β_2:Glu288 (> 2 %). From 117.5–135 ns, (Cluster C), the intramolecular hydrogen bond is broken and the C20-hydroxyl instead forms a hydrogen bond with β_1:Glu53 of the adjacent tubulin unit, which may (17 %) or may not (64 %) be water mediated (Table 2.1).

The C1-carbonyl forms hydrogen bonds to the protein in a water-mediated fashion. As mentioned above, this carbonyl is engaged in an intramolecular hydrogen bond from 45 ns to 107.5 ns, while also interacting with β_2:Glu288 and β_1:Gly56. When this intramolecular interaction breaks in Cluster C, the carbonyl acts as an acceptor in a water-mediated interaction with β_1:Gly56 and β_2:Glu288.

The conformational change undergone by LLM when moving from Cluster B to Cluster C is also accompanied by a change in binding, with LLM moving closer to the β_1 unit. Specifically, the macrolactone dihydropyran moves away from β_2:Asn332 in β_2:H10 and towards β_1:H3 and β_1:H3–S4. There is also a movement of the dihydropyran side chain away from β_2:H9 and towards β_1:H3. The remaining substituents only

undergo a slight shift in positions relative to the protein. This explains why, upon changing state from Cluster B to Cluster C, LLM forms hydrogen bonds with β_1, and the side chain C20-hydroxyl group interacts with β_1:Glu53.

The C15-hydroxyl engages in hydrogen bonds throughout the simulation. An intramolecular interaction is occasionally observed between this hydroxyl and the C16–C17-epoxide. Otherwise, this polar group acts as a hydrogen bond donor to β_2:Gln329, located on β_2:H10. From 45–107.5 ns, the hydroxyl interacts with the side chain of β_2:Gln329 (occupancy < 21 %, Table 2.1), while the conformational change in LLM in Cluster C results in the hydroxyl group interacting with the backbone of β_2:Gln329 (occupancy = 45 %, Table 2.1). It is important to note that, unlike what was previously reported in MD simulations,[142] this group does not hydrogen bond to β_2:Asn337, which is buried further into the protein than β_2:Gln329. This previous study also observed that β_2:Asn337 resided at the entrance to a cavity in tubulin that housed the dihydropyran side chain of LLM.[142] Residues β_2:Phe294, β_2:Arg306, β_2:Asn337 and β_2:Tyr340 (Figure A6) were proposed to reorganize upon LLM binding to form this cavity. It was also reported that a polar contact between β_2:Arg306 and the dihydropyran moiety of the side chain was present.[142] However, in the present simulations, the large average distances between the dihydropyran side chain and β_2:Arg306 (19.6 Å), as well as the C15-hydroxyl and β_2:Asn337 (11.4 Å) indicate the LLM side chain is not in close enough proximity to occupy such a cavity (Figure A6). The addition of the adjacent β_1-tubulin in this model causes LLM not to bind as deep into β_2-tubulin. Therefore, rather than occupy a position recessed in a cavity, the dihydropyran side chain prefers a position in close proximity to β_1-tubulin, particularly β_1:H3, and interacts with solvent. Such information cannot be obtained using unrelaxed drug–protein models.[52]

No significant hydrogen bonds to the protein were observed for the oxygens of the dihydropyran moieties, the macrolactone ring-bound O1, or the C16–C17-epoxide moiety. However, numerous hydrogen bonds to solvent are observed for the macro-lactone dihydropyran. The oxygen of the side chain dihydropyran also forms hydrogen bonds with water, though to a lesser extent, while the methyl group is in close proximity to a salt bridge formed between β_1:Glu125 and β_2:Lys336. The C16–C17-epoxide moiety is oriented towards β_2 between H9 and H10, and is not exposed to solvent,

though does not engage in hydrogen bonds. The ring-bound O1 of the enolate is directed to the interior of the macrolactone ring and is also inaccessible to solvent.

2.3.3 Analysis of the binding free energy

To quantify the interaction between LLM and $(\alpha\beta\text{-tubulin})_2$, binding was evaluated with the MM/GBSA method according to Equations 1.20 and 1.21, neglecting entropy (Table A1). Pairwise ligand–residue contributions were also obtained according to Equation 1.22 (Figure 2.5, Table A1). Binding was analyzed for each of the clusters, as well as the entire 90 ns simulation. The largest binding contributions come from the β_2 subunit, where summing the (nonadditive) pairwise contributions involving the β_2 unit indicates its large contribution (-146.4 kJ mol^{-1}) to the total binding (-127.1 kJ mol^{-1}). The strongest interactions occur with β_2:Gln329 (-23.7 kJ mol^{-1}), which interacts with the macrolactone C15-hydroxyl via hydrogen bonds, and β_2:Gln291 (-19.0 kJ mol^{-1}), which interacts with the C20-hydroxyl via hydrogen bonds. In addition, large contributions are observed from β_2:Pro287 (-15.2 kJ mol^{-1}), β_2:Asn332 (-17.3 kJ mol^{-1}), β_2:Val333 (-15.1 kJ mol^{-1}), and β_2:Lys336 (-15.6 kJ mol^{-1}) (Figure A5). These strong-binding residues also have the largest correlations in motion with LLM throughout the simulation. The reported binding energies also support the structural arguments above that no cavity is formed to hold the LLM side chain (Figure A6). The less-recessed position of the drug results in some interaction of LLM, primarily the side chain, with β_2:Phe294 and β_2:Asn337 (Figure A6), having a notable strength (-3.8 to -7.3 kJ mol^{-1} and -3.3 to -5.6 kJ mol^{-1}, respectively), whereas β_2:Arg306 (up to -0.5 kJ mol^{-1}) and β_2:Tyr340 (up to -0.8 kJ mol^{-1}) have minimal contributions to binding (Figure 2.5, Table A1).

In addition to the calculated binding to β_2, contributions from β_1 (-33.4 kJ mol^{-1}, Table A1) were found. The primary stabilization from β_1 comes from β_1:Glu53 (-11.7 kJ mol^{-1}), which forms hydrogen bonds to the C20-hydroxyl in Cluster C (-28.0 kJ mol^{-1}). Notable energetic contributions also arise from β_1:H1′–S2, β_1:H3, and β_1:H3–S4 (Table A1).
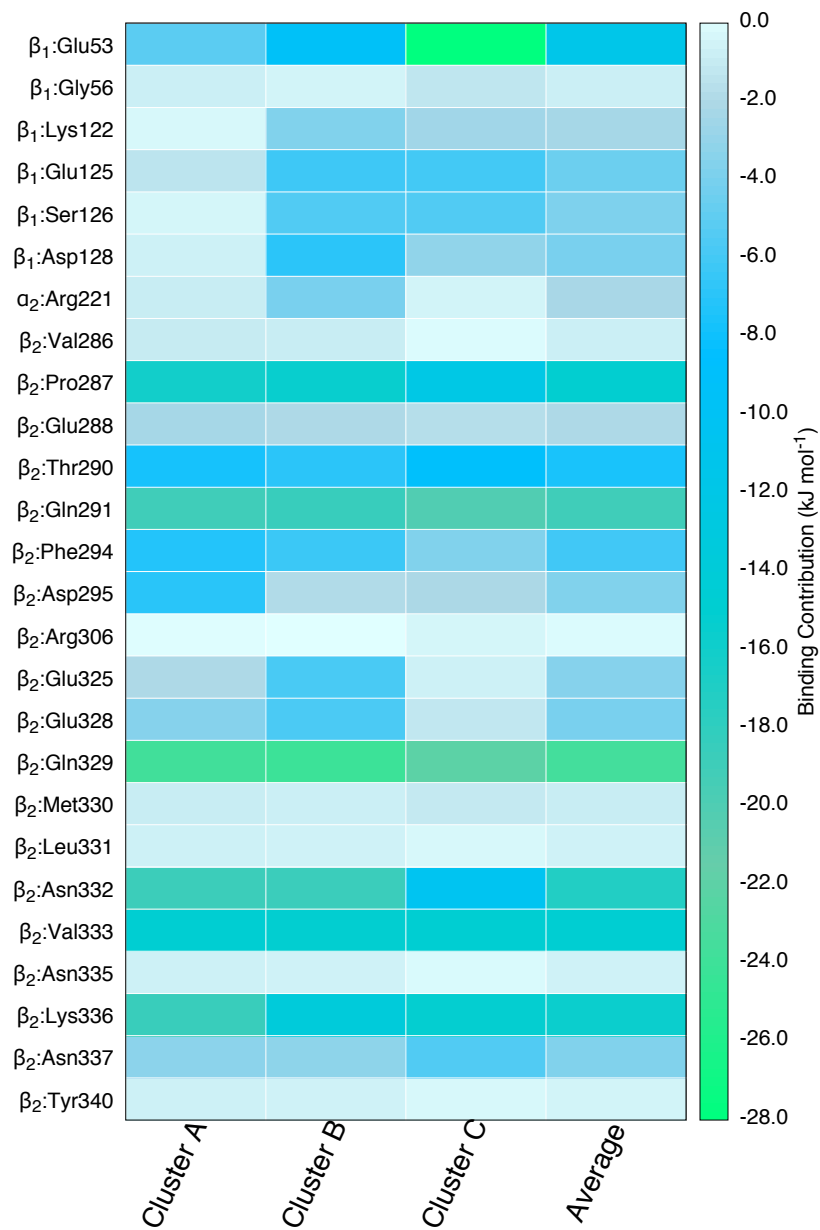
Figure 2.5: *MM/GBSA pairwise binding free energy (kJ mol^{-1}) between select binding-site residues and LLM. Calculated according to Equation 1.22, neglecting the entropy component. Data included in Table A1.*

2.3.4 Microtubule stabilization

Overall, the strongest binding of LLM occurs in Cluster B (-136.4 kJ mol^{-1}, Table A1). This is due to increased interactions between LLM and β_1 (-38.8 kJ mol^{-1}, Table A1), particularly from β_1:H1$'$–S2 (-12.9 kJ mol^{-1}), β_1:H3 (-5.0 kJ mol^{-1}), and β_1:H3–S4 (-20.3 kJ mol^{-1}), involving β_1:Glu53, β_1:Lys122, β_1:Glu125, β_1:Ser126, and β_1:Asp128 (Figure 2.5). Binding interactions in Cluster C strengthen for β_2:Glu53 and β_2:Gln291, but weaken for residues in H10 (Table A1). The binding of LLM to tubulin varies by a maximum of 28.4 kJ mol^{-1} throughout the clusters (Table A1), indicating all three of the reported binding modes are accessible to LLM. However, given the strong binding observed for Cluster B, and the dominance of Cluster C up to 180 ns, these clusters are likely to be the most important for describing LLM binding.

2.3.5 A crystal structure comparison

The binding mode of LLM reported here differs from the crystal structure 4O4H (Figure 2.6).[52] The crystal structure finds LLM, particularly the side chain, binds deeply in a pocket involving residues from β:H9, β:H9–H9$'$, β:H9$'$, β:H9$'$–H10, β:H10, β:H10–S9. Prota et $al.$[52] report the C20-hydroxyl group forms hydrogen bonds with Asp295 and Ser296 in H9 (Asp297 and Ser298 in Prota et $al.$[52]). However, the computations find this group breaks hydrogen bonds with β_2:S7–H9 and β_2:H9 (Clusters A and B) and instead forms a hydrogen bond with β_1:Glu53 of the adjacent β-tubulin subunit (Cluster C). Although no hydrogen bond to the C1-carbonyl group is observed in the crystal structure, simulations show a hydrogen bond with β_1:Gly56. These specific interactions with β_1-tubulin emphasize the structural effect of the adjacent tubulin unit on LLM–protein contacts, and the importance of its explicit inclusion when studying LLM–MT interactions. In contrast with the crystal structure, no hydrogen bonds to the dihydropyran oxygens are observed. In the simulations, the addition of an adjacent β_1-tubulin unit resulted in LLM not binding as deep into β_2-tubulin, and observed a migration of LLM towards the adjacent unit to increase contacts with β_1-tubulin. It is hypothesized that the addition of an adjacent protein unit to this crystal structure complex to better mimic the MT will have an effect on

57
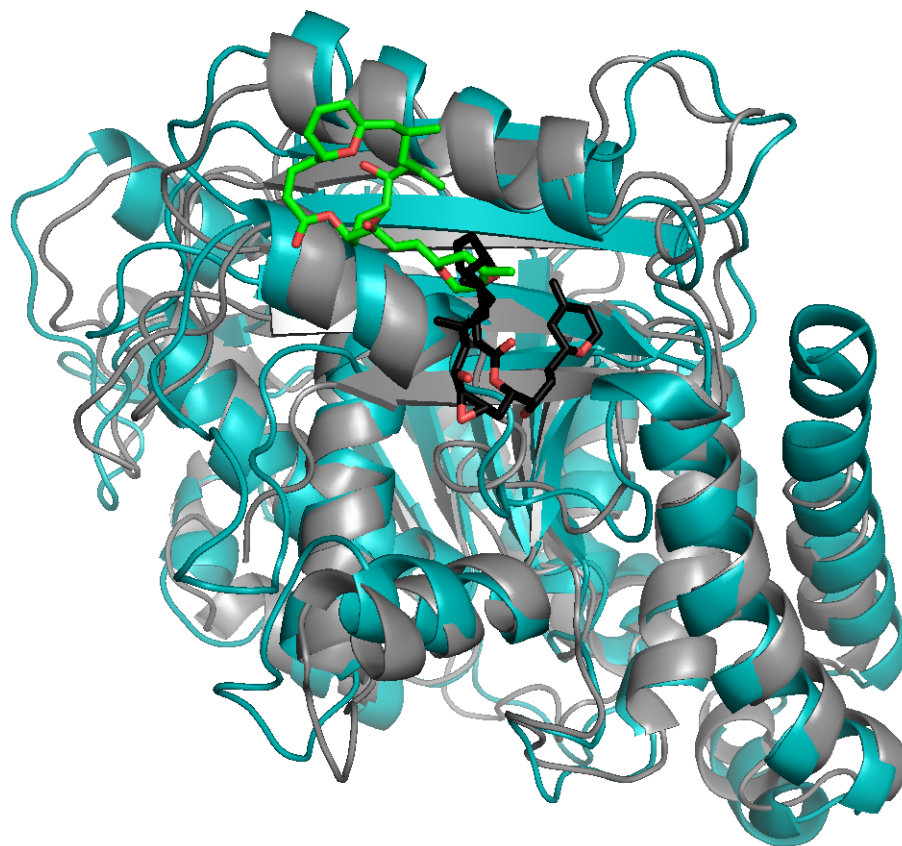
Figure 2.6: *An overlay of protein backbone atoms to compare the binding modes obtained by simulations in this Chapter and the 4O4H crystal structure. The LLM–β_2-tubulin complex from the representative structure of Cluster C is indicated in teal/green, with LLM between β:H10 (top) and β:H9 (bottom). The LLM–β-tubulin complex from 4O4H is indicated in grey/black.*

the crystal structure pose and should be considered in future MD studies.

LLM is known to stabilize MTs. In the absence of LLM, lateral contacts between adjacent tubulin protofilaments in a B-lattice involve β:H9 and β:H10 in one subunit with β:H3 and β:H4 in the adjacent unit.[36] Results show that LLM interacts strongly with β_1:H3, β_2:H9 and β_2:H10. LLM binding also causes the M-loop to expandc towards the adjacent β-tubulin unit, relative to LLM-free tubulin in the 1JFF crystal structure (Figure A7). LLM binding also stabilizes β_1:H1′–S2, which reorganizes its secondary structure to form β-sheets (Figure A7), thereby enhancing noncovalent interactions. The LLM–tubulin crystal structure also reveals structural differences in the M-loop, which becomes more helical and increases hydrogen bonding inter-

actions.[52] Structural changes to the M-loop have also been reported for drugs like taxanes.[105,117] The specific interactions and structural reorganization reported here may be related to the stabilizing effect LLM has on MTs, therefore explaining the mode of action of the drug.

2.4 Conclusions

MD methods provide a useful approach to acquire new, detailed information about the interactions between LLM and tubulin within a MT. An improved model of LLM binding is presented, which consists of LLM bound to β-tubulin located between two adjacent $\alpha\beta$-heterodimers. The explicit inclusion of an additional heterodimer better mimics the binding of LLM to MTs, where the LLM binding site lies between tubulin protofilaments. This model presents a unique binding mode for LLM, identifying different LLM–residue interactions than reported previously. This indicates the importance of using an explicit extended model when studying drugs located in MT pores, or interdimer interfaces. This is evidenced by the large structural changes observed in the LLM–tubulin binding mode upon the addition of an additional heterodimer.

As previously found,[142] LLM still binds near β_2:H9 and β_2:H10, which is in agreement with the available crystal structure. In addition to this, contacts between LLM and β_1:H1′–S2, β_1:H3, and β_1:H3–S4 from the adjacent heterodimer are identified, which is supported by mass shift perturbation experiments and unavailable in the crystal structure. The presence of the additional heterodimer has a major structural effect, causing LLM not to bind so deeply to β_2-tubulin, which results in the side chain of LLM lying closer to β_1-tubulin rather than residing in a cavity on β_2-tubulin as previously reported. Simulations also show that LLM is solvent exposed and engages in many water-mediated interactions with tubulin.

LLM participates in substantial hydrogen bonds with tubulin, as well as solvent. In addition to the hydrogen bonds that LLM forms with the β-tubulin to which it is bound (β:Gln291, β:Gln288, β:Gln329), key residues from the adjacent unit also engage in hydrogen bonds with the drug (β:Glu53, β:Gly56). Although the majority of the binding free energy is attributed to the β_2-tubulin unit (particularly

β:Gln329, β:Glen291, β:Asn332, β:Lys336, β:Gln291 and β:Val333), an important energetic contribution does arise from the adjacent unit (particularly β:Glu53, β:Lys122, β:Glu125, β:Ser126 and β:Asp128). The identification of these new contacts provides an enhanced understanding of LLM binding. These contacts, including the important solvent-mediated interactions identified here, must be accounted for in future derivatizations and optimizations of this drug. Chapters 3 and 4 consider LLM analogues in this extended protein model, while also taking into account the newly-available crystal structure pose.

Structural changes are observed upon the binding of LLM that may explain its role in stabilizing MTs. The MD simulations show the M-loop adopts an expanded conformation closer to the adjacent tubulin heterodimer when LLM binds. In addition, LLM binding causes β:H1$'$–S2 to reorganize its secondary structure to form β-sheets, which is a more energetically-favourable arrangement than loops.

Chapter 3

Analysis of the binding mode of laulimalide to microtubules: Establishing a laulimalide–tubulin pharmacophore[*]

3.1 Introduction

Experimental studies have synthesized and tested a variety of structural analogues of LLM in an attempt to improve the efficacy of this compound and avoid the degradation of LLM to isolaulimalide (isoLLM, Figure 3.1), discussed in Section 1.2.2.3.[145,147–152] However, this has proven challenging since all these compounds are less effective than LLM itself.

LLM analogues that avoid degradation to isoLLM have been synthesized and studied by the Mooberry group and their collaborators.[145,150,152,153] Modifications were made at the C16–C17-epoxide and C20-hydroxyl to remove the reactive groups, as well as to the C2–C3-alkene that resulted in a change in the macrocycle conformation to alter orbital alignment between the reactive C16–C7-epoxide and C20-hydroxyl, thereby preventing isoLLM formation.[150] Five LLM analogues, C16–C17-des-epoxy laulimalide (LA1), C20-methoxy laulimalide (LA2), C2–C3-alkynoate laulimalide (LA3), C16–C17-des-epoxy, C20-methoxy laulimalide (LA4), C2–C3-alkynoate, C16–C17-des-epoxy laulimalide (LA5, Figure 3.1),[150,152] have been synthesized and studied. Results show that LA1 and LA2 are more stable than and have simi-

lar cellular effects to LLM, while having decreased cytotoxicity relative to LLM but greater toxicity than isoLLM (Table 3.1).[152,153] Furthermore, LA1 and LA2 work more synergistically with TXL than LLM does.[138] LA4 is less cytotoxic than, but has similar cellular effects to LLM, LA1, and LA2, retaining activity in resistant cell lines,[152] while LA3 and LA5 have markedly-reduced cytotoxicity than LLM and affect the cell differently than other MT stabilizers.[152]

Following the completion of the work presented in Chapter 2, a crystal structure (4O4H,[52] Table 1.1) was released with LLM bound to tubulin. This structure contained an LLM–$\alpha\beta$-tubulin complex bound to the stathmine-like domain of the RB3 protein and tubulin tyrosine ligase. Although this provided valuable information about the binding mode of LLM, it is not representative of the MT environment since the LLM binding site is located between protofilaments contacting two β-tubulin units. Using the newly-available crystallographic data and MD simulations with extended MT models, the binding of LLM, isoLLM, and these five LLM analogues to tubulin were studied. With this information, an understanding may be gained as to how structural modifications affect LLM binding to tubulin, and these properties may be related to the experimentally-observed toxicity. This will aid in the development of strategies for derivatizing LLM in future studies.
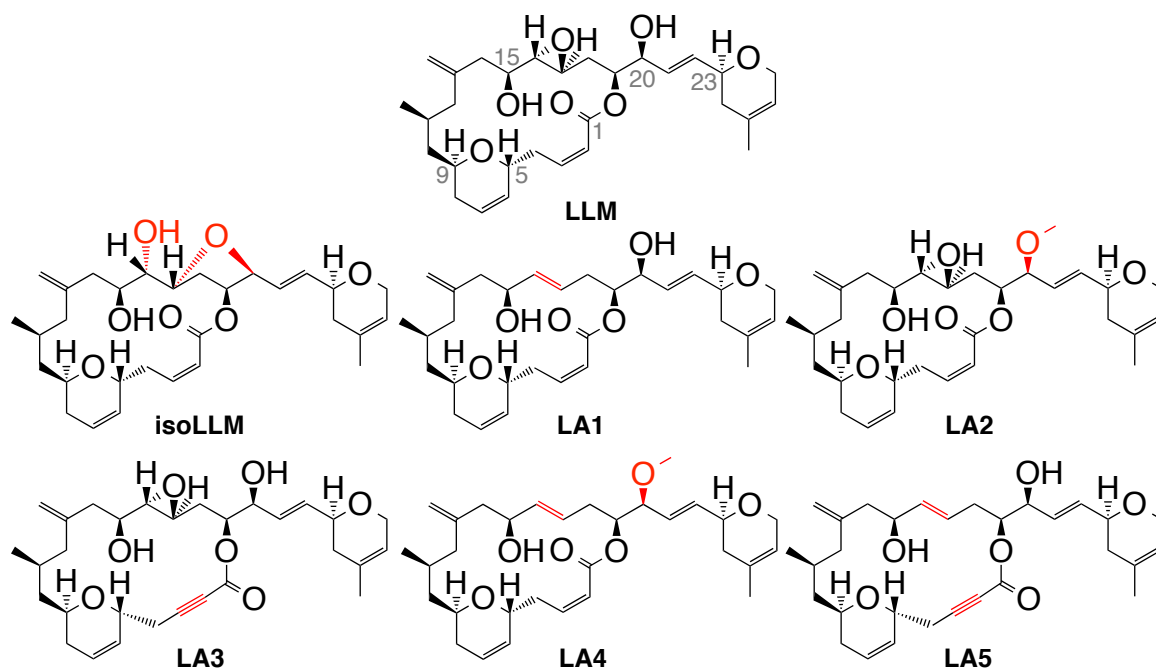
Figure 3.1: *The chemical structure and numbering of (−)-laulimalide (LLM), its degradation product isolaulimalide (isoLLM), and analogues LA1 to LA5.*[152,153] *Fragments in red indicate modifications.*

63

Table 3.1: *Cytotoxicity (IC_{50}, μM) of the various LLM analogues acting on different cell lines.*

Compound	Cell Line						
	HeLa[150(a)]	MDA-MB-435[150(b)]	NCI/ADR[150(c)]	1A9[152(d)]	PTX10[152(e)]	PTX22[152(f)]	A8[152(g)]
LLM	-	0.0057 ± 0.0006[78]	-	-	-	-	-
isoLLM	-	1.97 ±0.097[78]	-	-	-	-	-
LA1	0.10 ± 0.01	0.12 ± 0.004	0.37 ± 0.007	0.189 ± 0.018	0.353 ± 0.053	1.22 ± 0.16	0.625 ± 0.13
LA2	0.18 ± 0.014	0.24 ± 0.009	0.47 ± 0.052	0.45 ± 0.027	0.862 ±0.105	1.76 ± 0.09	0.531 ± 0.032
LA3	2.20 ± 0.84	2.50 ± 0.29	13.7 ± 0.34	-	-	-	-
LA4	5.86 ± 0.85	4.41 ± 0.58	22.0 ± 2.5	10.9 ± 1.23	10.3 ± 1.65	9.68 ± 2.41	11.6 ± 3.4
LA5	18.3 ± 4.0	16.5 ± 2.5	25.4 ± 3.0	-	-	-	-

[a] Human cervical cancer cell line, drug sensitive.; [b] Human melanoma cell line,[81] drug sensitive.;
[c] A multidrug resistant cell line with a high level of P-glycoprotein expression derived from the MCF-7 human breast cancer cell line.;
[d] Human ovarian cancer cell line.; [e] TXL-resistant cell line derived from the 1A9 human ovarian cancer cell line.; [f] TXL-resistant cell line derived from the 1A9 human ovarian cancer cell line.; [g] Epothilone A-resistant cell line derived from the 1A9 human ovarian cancer cell line.

3.2 Computational Details

LLM binding was examined using the crystal structure pose in 4O4H, with LLM located between two adjacent $\alpha\beta$-tubulin heterodimers (Figure 3.2). Protein and nucleotide coordinates were taken from the end of a 135 ns simulation reported in Chapter 2 and the LLM pose was taken from the 4O4H crystal structure, following the addition of hydrogen atoms and optimization with PM6 in Gaussian 09.[255] The pre-equilibrated protein model was used, rather than develop a new model based on the higher-resolution 4O4H coordinates, since substantial structural equilibration (45 ns) is necessary to stabilize the lateral contacts between tubulin heterodimers. The coordinates of isoLLM and the LLM analogues (LA1 to LA5) were also optimized with PM6 using constraints to retain a conformation similar to the crystal structure pose, and then inserted into the heterodimer model in the same position as LLM. The heterodimers were also simulated in the apo form by removing LLM.

MD simulations were performed using GPU-enhanced[242–244] Amber 14.[241] General details of the MD simulations performed in this Thesis may be found in Section 1.3.3.1 and details specific to this simulation may be found in Appendix B. Production data was collected for 90 ns. The mass-weighted RMSD of the protein components, calculated with respect to the structure at 0 ns, showed each system was structurally equilibrated after 20 ns (Figure B1). Therefore, the final 70 ns portion of the simulation was analyzed, and the data reported below. All residues are discussed with respect to the numbering in bovine α-tubulin isoform I-C (UniProt P81948) and β-tubulin isoform II-B (UniProt Q6B856), as was reported in Chapter 2.

Binding within the LLM–$(\alpha\beta$-tubulin$)_2$ complex was evaluated using a single-trajectory approach with the MM/GBSA method. The binding within the complexes was evaluated two different ways: (1) ligand–tubulin binding, where the ligand was defined as one unit, and the protein–nucleotide complex was treated as the second unit; and (2) interdimer binding, where the $\alpha_1\beta_1$-tubulin and associated nucleotides were treated as one unit, and the ligand–$\alpha_2\beta_2$-tubulin complex and associated nucleotides were treated as the second unit.
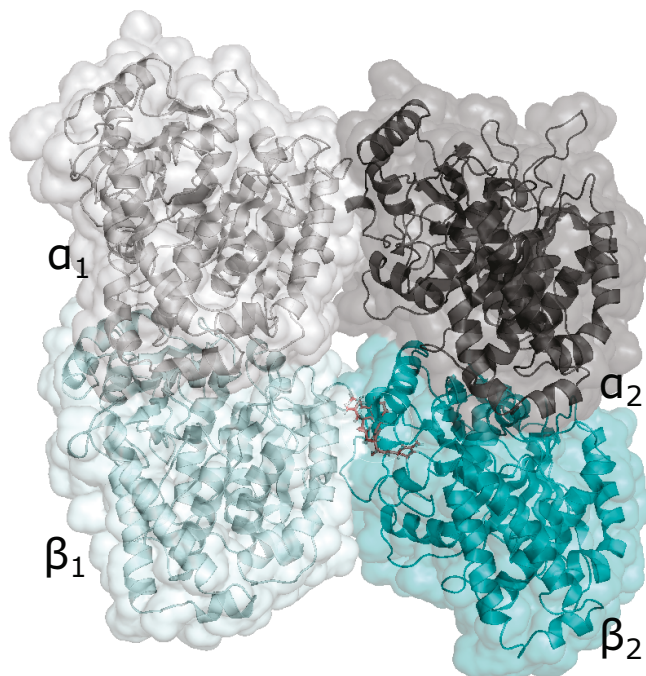
Figure 3.2: *Components of the LLM–tubulin model, including LLM (red), α-tubulin units (grey) and β-tubulin units (teal). Model was constructed from LLM bound to $\alpha_2\beta_2$-tubulin (dark), adjacent to $\alpha_1\beta_1$-tubulin (light) in a B-lattice configuration. Viewed from the exterior of the MT.*

3.3   Results and Discussion

3.3.1   Laulimalide binding in a LLM–($\alpha\beta$-tubulin)$_2$ model

3.3.1.1   Local effects

During the simulations of the LLM–($\alpha\beta$-tubulin)$_2$ complex, LLM retained a conformation similar to that found in the crystal structure (Figure 3.3(a, b)), which is stabilized by an intramolecular hydrogen bond between the C1-carbonyl and C15-hydroxyl (Table 3.2). This is in contrast to the intramolecular hydrogen bond observed between the C1-carbonyl and C20-hydroxyl in previous LLM poses[142] and Chapter 2. The presence of the $\alpha_1\beta_1$-tubulin heterodimer adjacent to the LLM binding pocket causes LLM to rotate slightly and bind more deeply into β_2-tubulin than what was observed for the crystal structure (Figure 3.3(c, d)), so that the LLM side chain is directed into β_2-tubulin. Low root-mean squared fluctuation (RMSF) values for LLM atoms (less than 0.66 Å) indicate the drug is rigid within the binding site (Figure B2). The pose identified in this Chapter is different from the poses identified by previous MD sim-

ulations using a LLM–$(\alpha\beta$-tubulin$)^{142}$ model and the LLM–$(\alpha\beta$-tubulin$)_2$ model in Chapter 2 (Figure B3) since the C23-dihydropyran is further from β_2:H9 and β_2:H10 and closer to β_2:H9–H9′, β_2:H9′, β_2:S8 and β_2:H10–S9′ in this Chapter.
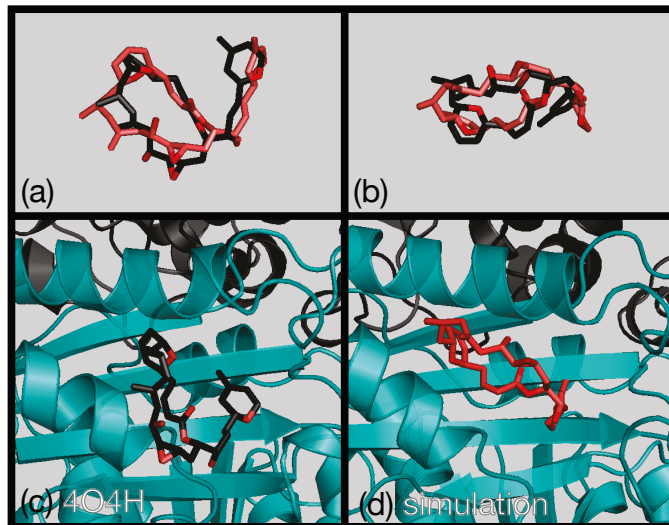
Figure 3.3: *A comparison of the conformations of LLM obtained from the 4O4H crystal structure (black)[52] and the simulation (red) viewed from different angles: panel (b) shows the system on panel (a) viewed from the bottom. The LLM binding site is shown both (c) in the crystal structure and (d) from the simulation, with LLM located between β_2:H9 (bottom helix) and β_2:H10 (top helix) in panels (c, d).*

A comparison to the apo model shows the binding of LLM widens the separation between β_2:H9 and β_2:H10, and pushes β_1:H3 away from β_2-tubulin (Figure 3.4(a, h)). LLM also displaces residues in the binding pocket up to 5.5 Å, namely β_2:Gln291, β_2:Phe294, β_2:Asp295 and β_2:Gln329, as well as β_1:Glu125 from the adjacent heterodimer (Figure B4(a,b)). In the pocket, the macrolactone binds closely to helices β_2:H9 and β_2:H10, with the C5–C9-dihydropyran near β_2:H9 and the C15-hydroxyl near β_2:H10 (Figure 3.3(d)). The C13-methylene and C16–C17-epoxide are directed towards β_1:H3, which LLM interacts with in a water-mediated fashion, evidenced by the solvation of the epoxide (Table 3.2, 43 %). The C11-methyl is directed towards β_1:H3–S4 and the MT type II pore that contains solvent. While the C1-carbonyl and C15-hydroxyl engage in an intramolecular hydrogen bond, the C1-carbonyl simultaneously engages in a direct hydrogen bond with the β_2:Asn337 side chain (35 %, Table 3.2), while the C15-hydroxyl does not interact with the protein. Neither the C1 site nor the C15 site of LLM are solvated (Table 3.2).

The C23-dihydropyran is near β_2:H9–H9′, β_2:H9′, β_2:S8, and β_2:H10–S9′, with solvent also located in this region. The oxygen of the C23-dihydropyran is slightly solvated (Table 3.2, 33 %) while hydrogen bonds between the C20-hydroxyl and solvent are prominent (Table 3.2, up to 75 %). Both these solvated species interact with β_2-tubulin through water-mediated hydrogen bonds. The C23-dihydropyran and the C20-hydroxyl interact with the backbone carbonyl of β_2:Phe294 (Table 3.3, 56 %), and the C20-hydroxyl may alternatively interact with the β_2:Asp304 side chain (Table 3.3, 21 %).

The β_2:Asn337 $N_{\delta2}$–H_1···LLM C1-carbonyl and the β_2:Phe294 O···water···LLM C20-hydroxyl hydrogen bonds are the only specific and directional interactions that take place between LLM and tubulin. As observed in Chapter 2,[1] and indicated by crystallographic water molecules,[52] the solvent plays an important role in the binding of LLM between tubulin protofilaments. Non-directional interactions also have important contributions to LLM binding. The olefin present in the C23-dihydropyran is important for drug activity, and it has been suggested this may be due to a C-H–π interaction between this moiety and binding-site residues.[145] The simulations performed in this work show π–π interactions are present between the C25–C26 olefin and different aromatic residues in the binding site, where β_2:Phe294, β_2:Tyr310, β_2:Tyr340, β_2:Phe341 and β_2:Phe367 engage in a π–π motif (Figure B5). The C25–C26-olefin maintains close contacts with the aromatic rings of β_2:Tyr310 (4.1 Å) and β_2:Phe367 (5.7 Å), and the vdW component of the interaction between these aromatic residues and LLM provides an estimation that these π–π interactions contribute $\sim$31 kJ mol^{-1} to the binding of LLM. It is interesting that π–π interactions provide such stability to LLM binding since the modification of the C23-dihydropyran to an aryl group reduced potency (analogue LA16 from Mooberry *et al.*[145]) despite the fact that this would maximize the strength of the π–π interactions. However, it is possible that this decreased toxicity could be explained by the restricted flexibility in the side chain, and therefore poorer binding to MTs, due to the conjugation between the C21–C22-olefin and an aromatic group at C23.

MM/GBSA calculations using a single-trajectory approach have been shown to successfully rank the binding affinities of different ligands.[249] Calculations indicate that LLM binds to ($\alpha\beta$-tubulin)$_2$ with a strength of -196.6 $\pm$ 12.7 kJ mol^{-1} (Ta-

ble 3.4), which is stronger than the binding mode previously found for LLM in Chapter 2 (-127.1 $\pm$ 17.3 kJ mol^{-1}). The affinity calculated in the present work is comparable in strength to the binding of taxanes to tubulin in Chapter 5. Through per-residue decomposition of this binding energy, the sources of stabilization in LLM–($\alpha\beta$-tubulin)$_2$ binding have been calculated (Figure 3.5, Table B1). The most significant stabilization comes from β_2:Gln291 (-21.6 kJ mol^{-1}), β_2:Phe294 (-25.6 kJ mol^{-1}), β_2:Lys336 (-18.4 kJ mol^{-1}), and β_2:Asn337(-26.6 kJ mol^{-1}). β_2:Phe294 engages in a water-mediated hydrogen bond and π–π interactions with LLM, while β_2:Asn337 directly hydrogen bonds to LLM. Interactions between LLM and β_2:Gln291 or β_2:Lys336 are less direct. β_2:Gln291 is near the C5–C9-dihydropyran, while the cationic β_2:Lys336 side chain spans closely along LLM from the C11-methyl to the C16–C17-epoxide. Smaller stabilizing contributions are also provided by β_1:Lys122, β_1:Glu125, β_2:Thr290, β_2:Tyr310 (π–π), β_2:Gln329, and β_2:Val333 (Figure B4, Table B1). LLM interacts stronger with the β_2-tubulin subunit than the β_1-tubulin unit (-203.7 kJ mol^{-1} vs. -40.1 kJ mol^{-1}, Table B1), with β_2:H9 (-66.6 kJ mol^{-1}), β_2:H10 (-50.6 kJ mol^{-1}), and β_2:H10–S9 (-40.0 kJ mol^{-1}) providing greater stability than β_1:H3 (-19.1 kJ mol^{-1}) and β_1:H3–S4 (-19.6 kJ mol^{-1}).
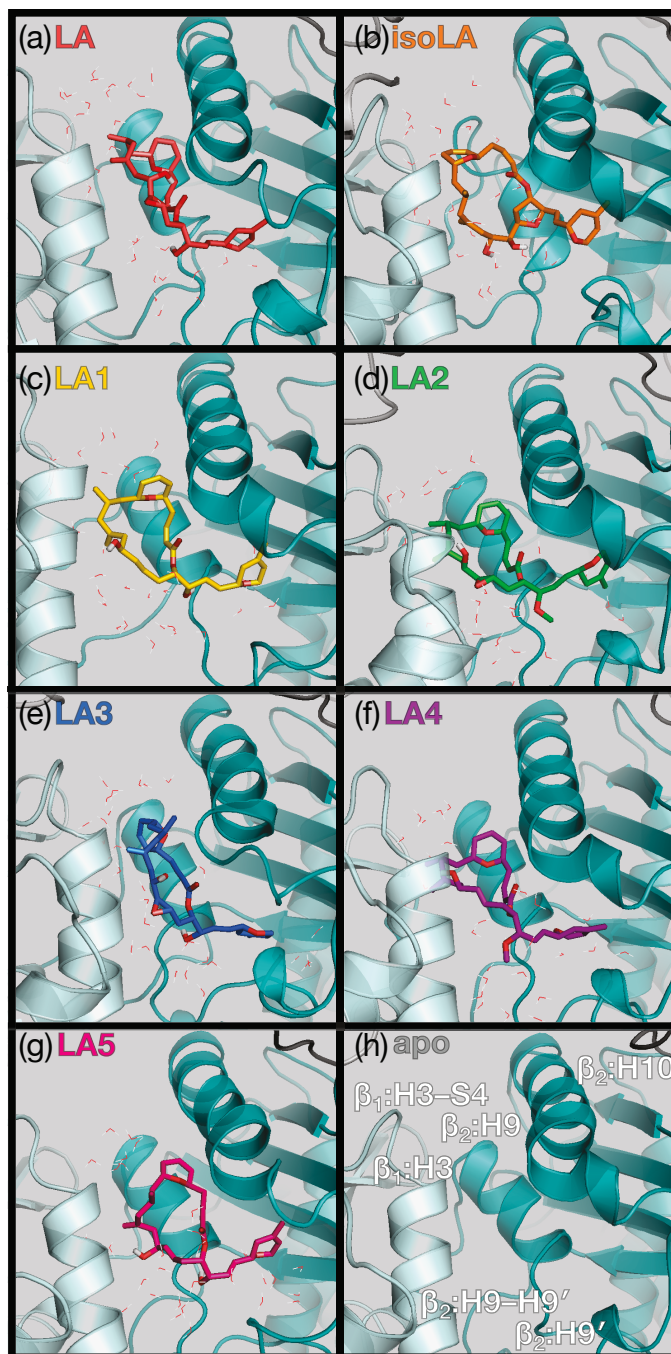
Figure 3.4: *The LLM poses within the binding site located between β_1-tubulin (light cyan) and β_2-tubulin (teal). Viewed along the lateral interface from the (+) end of the MT.*

Table 3.2: *Ligand–tubulin and ligand–solvent hydrogen-bond occupancy (%) over 70 ns.*

Acceptor[a]	Donor[a]	LLM	isoLLM	LA1	LA2	LA3	LA4	LA5
LLM C1-carbonyl	LLM C15-hydroxyl	60.0	-	-	10.9	-	-	-
LLM C1-carbonyl	β_2:Asn337 $N_\delta 2$–H_1	34.9	-	54.7	49.1	-	27.0	-
LLM C1-carbonyl	β_2:Asn337 $N_\delta 2$–H_2	-[b]	15.0	-	-	-	-	-
LLM C5–C9-dihydropyran	β_2:Gln329 $N_{\epsilon 2}$–H_1	-	-	-	-	21.0	-	-
β_1:Lys122 O	LLM C15-hydroxyl	-	-	-	-	-	20.3	-
β_1:Ser124 O_γ	LLM C15-hydroxyl	-	-	-	-	-	19.9	-
β_1:Glu125 O	LLM C15-hydroxyl	-	-	-	12.7	-	-	-
β_2:Phe294 O	LLM C15-hydroxyl	-	-	-	-	-	-	11.9
β_2:Asp295 $O_{\delta 1}$	LLM C15-hydroxyl	-	35.8	-	-	-	-	-
β_2:Asp295 $O_{\delta 2}$	LLM C15-hydroxyl	-	12.3	-	-	-	-	-
LLM C15-hydroxyl	β_1:Ser124 O_γ–H	-	-	-	-	-	16.6	-
LLM C15-hydroxyl	β_2:Asn337 $N_\delta 2$–H_1	-	-	-	-	13.9	-	-
β_2:Phe294 O	LLM C20-hydroxyl	-	-	23.1	—[c]	91.9	—	80.7
LLM C23-dihydropyran	β_2:Tyr310 O_η–H	-	-	-	-	-	-	29.6
LLM C1-ester	water	-	-	12.9	13.3	25.1	-	-
LLM C1-carbonyl	water	-	67.4	-	17.3	63.1	-	53.4
LLM C5–C9-dihydropyran	water	-	45.2	37.1	-	-	-	-
LLM C15-hydroxyl	water	-	64.8	16.2	12.7	36.1	21.1	63.3
water	LLM C15-hydroxyl	-	40.4	55.6	30.5	54.6	-	64.9
LLM C16–C17-epoxide	water	42.6	—	-	55.4	53.2	-	-
LLM C16-hydroxyl	water	—	54.2	—	—	—	—	—
water	LLM C16-hydroxyl	—	65.2	—	—	—	—	—
LLM C20-hydroxyl/ tetrahydrofuran/methoxy	water	75.4	32.2	65.8	63.7	33.7	69.6	60.6
water	LLM C20-hydroxyl	74.3	-	43.4	-	-	—	-
LLM C23-dihydropyran	water	32.9	44.4	58.3	-	-	-	26.6

[a] Hydrogen bond defined as having heavy atoms within 3.0 Å and $135° \leq \angle(\text{donor–H}\cdots\text{acceptor}) \leq 180°$. Occupancies > 10 % are reported.; [b] Indicates an occupancy < 10 %.; [c] Not applicable.

Table 3.3: *Water-mediated ligand–tubulin hydrogen-bond occupancy (%) over 70 ns.*

Hydrogen bond[a]	LLM	isoLLM	LA1	LA2	LA3	LA4	LA5
β_1:Asp118$\cdots$LLM	-	-	-	-	21.2 (C16–C17)	-	34.4 (C15)
β_1:Arg121$\cdots$LLM	-	12.7 (C15) 10.7 (C15)	-	-	14.1 (C15, C16–C17)	-	-
β_1:Lys122$\cdots$LLM	-	-	-	-	-	-	-
β_1:Glu125$\cdots$LLM	-	-	-	13.9 (C15)	-	-	-
β_2:Gln291$\cdots$LLM	-	-	-	-	17.3 (C1)	-	-
β_2:Phe294$\cdots$LLM	55.7 (C20, C23)	21.6 (C15, C16)	47.2 (C20, C23)	22.8 (C1, C20)	-	53.4 (C1, C20, C23)	-
β_2:Asp295$\cdots$LLM	-	-	-	-	-	-	12.1 (C15)
β_2:Ala296$\cdots$LLM	-	9.3 (C23)	-	10.5 (C1, C20)	-	-	-
β_2:Cys303$\cdots$LLM	21.2 (C20)	-	-	-	-	-	-
β_2:Asp304$\cdots$LLM	-	-	-	-	-	-	-
β_2:Lys336$\cdots$LLM	-	36.9 (C1)	-	-	25.2 (C15)	-	22.3 (C1)
β_2:Asn337$\cdots$LLM	-	-	11.5 (C15)	-	-	-	-
β_2:Tyr340$\cdots$LLM β_2:Phe294$\cdots$	-	-	-	-	-	-	-
β_2:Ala296$\cdots$LLM	-	-	-	14.5 (C1, C20)	-	-	-

(a) Hydrogen bond defined as having heavy atoms within 3.0 Å and $135° \leq \angle(\text{donor–H}\cdots\text{acceptor}) \leq 180°$. Occupancies > 10 % are reported. Atoms in brackets indicate sites engaged in water-mediated interactions.

Table 3.4: *MM/GBSA-calculated binding free energy (kJ mol^{-1}).[a]*

	LLM	isoLLM	LA1	LA2	LA3	LA4	LA5	apo
Ligand–tubulin binding	-196.6 ±12.7	-160.3 ±19.4	-187.9 ±15.4	-180.2 ±14.9	-194.7 ±15.9	-192.7 ±16.9	-205.3 ±20.0	-
Relative ligand–tubulin binding[b]	0.0	36.3	8.6	16.4	1.8	3.9	-8.7	-
Interdimer binding	-183.8 ±30.1	-158.1 ±46.4	-192.3 ±34.4	-117.1 ±33.3	-173.0 ±38.8	-168.1 ±40.4	-114.5 ±34.0	-223.8 ±43.4
Relative interdimer binding[b]	0.0	25.7	-8.5	66.7	10.8	15.7	69.3	-40.0

[a] $\Delta G^{MM/GBSA}$, Equations 1.20 and 1.21, neglecting entropy.;   [b] Binding energy relative to LLM.

3.3.1.2   Global effects

The binding of LLM to a tubulin heterodimer significantly weakens the lateral interdimer interactions (-183.8 kJ mol^{-1} for LLM, -223.8 kJ mol^{-1} for apo, Table 3.4). Although these calculated values are larger than the latest experimental measurements of the free energy of dissociation of lateral interactions in MTs,[256] they provide a semiquantitative comparison for this model. The calculation indicates that the stabilization of MTs by LLM does not occur in the lateral interdimer contacts, and also that the stabilization induced by LLM binding must be significant enough to overcome this weakening of lateral contacts. The weakening of lateral contacts upon LLM binding agrees with experimental HDX MS evidence that Pel A, which binds to the same site as LLM, weakens lateral contacts at β:H1–S2 and to a lesser extent, in the M-loop.[113] These effects of LLM and Pel A on MTs differ from that of TXL, which recent experimentally-determined MT structures show exerts a stabilizing effect on MTs by increasing longitudinal interdimer contacts, with little effect on lateral interactions.[31]

Pairwise decomposition of the lateral interdimer interaction energies (Tables 3.5 and B2, Figure B6) indicates interdimer contacts are generally weakened in the presence of LLM. A major contributor to this is the elimination of contacts between

73
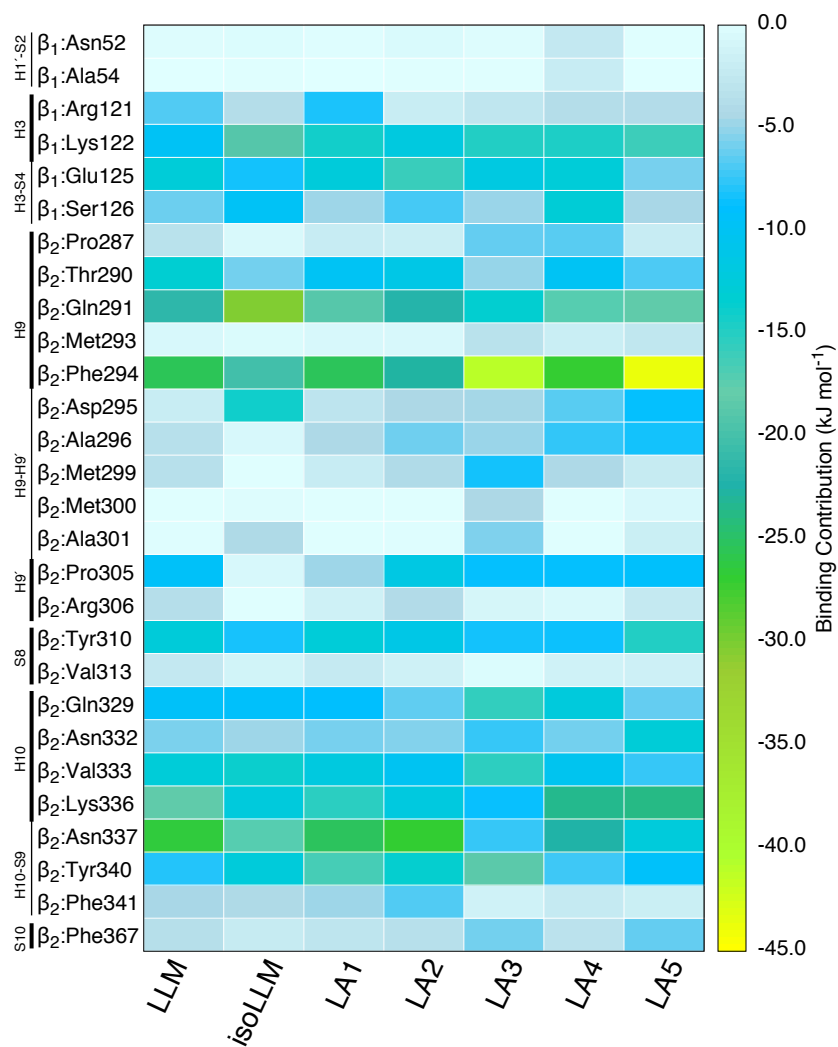
Figure 3.5: *MM/GBSA pairwise binding free energy (kJ mol^{-1}) between select binding-site residues and the laulimalides. Calculated according to Equation 1.22, neglecting the entropy component. Data included in Table B1.*

β_1:Asp88 and β_2-tubulin. The salt bridges β_1:Lys122$\cdots\beta_2$:Glu288 and β_1:Lys122$\cdots$ β_2:Gln291 are largely eliminated upon LLM binding and reduce stability by 41.2 kJ mol^{-1}, and these residues instead interact favourably with LLM by -32.1 kJ mol^{-1} (Table 3.5). Many of these weakened lateral contacts correspond to residues in the M-loop (residues 270–286), but not β:H1–S2 (residues 12–67) as reported for Pel A.[113] Although the model in the present work does not find a weakening of contacts in β_1:H1–S2, it is possible that LLM affects lateral contacts through residues in β_2:H1–S2 via an allosteric mechanism that cannot be captured by this model. LLM strengthens the β_1:Glu125$\cdots\beta_2$:Lys336 interaction as LLM binding alters the direction of the β_2:Lys336 side chain to enhance its interaction with β_1:Glu125. These two residues also have a strong interaction with LLM. Interestingly, LLM binding also has an effect on lateral contacts between α-tubulin subunits (Table B2). Most notably, α_1:Gln35$\cdots\alpha_2$:Tyr282, α_1:Glu55$\cdots\alpha_2$:Lys338, and α_1:Glu90$\cdots\alpha_2$:Arg215 interactions are weakened while α_1:Lys60$\cdots\alpha_2$:Glu284 is strengthened (Table 3.5).

Table 3.5: *Changes in interdimer interactions upon LLM binding.*

Pairwise Interaction[a]	apo $\Delta G_{ij}^{MM/GBSA}$[b] (kJ mol^{-1})	apo Occupancy[c] (%)	LLM $\Delta G_{ij}^{MM/GBSA}$[b] (kJ mol^{-1})	LLM Occupancy[c] (%)	$\Delta\Delta G_{ij}^{MM/GBSA}$[d] (kJ mol^{-1})
β_1:Asp88$\cdots\beta_2$:Ser275	-13.6	23	-0.2	0	+13.4
β_1:Asp88$\cdots\beta_2$:Gln280	-13.3	29	-2.1	4	+11.2
β_1:Lys122$\cdots\beta_2$:Glu288	-31.7	65	-0.9	0	+30.8
β_1:Lys122$\cdots\beta_2$:Gln291	-16.0	27	-5.6	8	+10.4
β_1:Lys122$\cdots$LLM	—[e]	—	-10.0	0	-10.0
β_2:Glu288$\cdots$LLM	—	—	-0.5	0	-0.5
β_2:Gln291$\cdots$LLM	—	—	-21.6	0	-21.6
β_1:Glu125$\cdots\beta_2$:Lys336	-27.1	23	-38.5	70	-11.4
β_1:Glu125$\cdots$LLM	—	—	-12.8	0	-12.8
β_2:Lys336$\cdots$LLM	—	—	-18.4	0	-18.4
α_1:Gln35$\cdots\alpha_2$:Tyr282	-14.4	47	-1.7	0	+12.8
α_1:Glu55$\cdots\alpha_2$:Lys338	-10.2	16	-0.8	0	+9.4
α_1:Glu90$\cdots\alpha_2$:Arg215	-24.5	43	-11.0	18	+13.5
α_1:Lys60$\cdots\alpha_2$:Glu284	-8.2	5	-33.2	46	-25.0

[a] All pairwise interdimer interactions are included in Figure B6 and Table B2.; [b] Calculated according to Equation 1.22.; [c] The occupancy of hydrogen bonds and salt bridges is defined as having heavy atoms within 3.0 Å.; [e] Not applicable.
[d] A positive value indicates a decrease in stability upon LLM binding.;

The M-loop is an important secondary structure in MTs that is involved in lateral tubulin contacts. The crystal structure of LLM bound to a tubulin heterodimer[52] showed an increase in the ordering and stabilization of the M-loop and C-terminus of β:H9. However, the simulations presented here show that the M-loop in β_2-tubulin remains disordered. The C-terminal portion of the M-loop also becomes more flexible upon LLM binding (Figure B7), which is consistent with the experimentally-observed increase in M-loop solvation and weakening of lateral contacts in MTs observed upon Pel A binding.[113] In the model used in the present work, the incorporation of an adjacent β_1-tubulin unit results in β_1:H1′–S2, β_1:H2′–H2″, and β_1:H2″ interacting with the M-loop. LLM binding also causes the M-loop to extend further from β_2-tubulin (Figure 3.6(a)), as also observed in Chapter 2. Since the M-loop acts as a hinge to determine the number of protofilaments in a MT,[24] where expansion of the M-loop leads to fewer protofilaments in a MT, LLM binding may alter this property.

Upon LLM binding, β_1:H1′–S2 near the binding site adopts greater sheet character than in apo tubulin (calculated on the basis of backbone atom positions[257]), as was observed in Chapter 2.[1] This is accompanied by a slight decrease in the RMSD of these residues relative to apo tubulin (Figure B7). Greater sheet character is also observed in residues removed from the binding site (β_1:S5–H5, β_1:S6–H6, and the C-terminus of β_1:S9–S10), while increased helical character is found in β_1-tubulin (H1–H1′, H2–H2′, H2′–H2″, and the N-terminus of H6–H7). In β_2-tubulin near the LLM binding site, β_2:H9, β_2:H9′ and β_2:H10 become more helical.

LLM binding causes the β-tubulin units to move apart while the α-tubulin units come closer together (Figure 3.6(b,c)). Although this may be related to the decreasing strength of interdimer interactions upon LLM binding, there is no direct correlation between the degree to which interdimer binding is weakened (Table 3.4) and the magnitude of the shift (Figure 3.6(b,c)). With the greater separation of the β-tubulin units, the intradimer interface at the MT pore comes closer, as evidenced by the decreased distance between β_2:H10 and α_2:H6 (Figure 3.6(d)). Within a MT, it is likely that lattice constraints will dampen these shifts. It is possible that these shifts manifest in such a way that LLM binding returns $\alpha\beta$-tubulin to a GTP-like state, as recently observed for cryo-EM structures of TXL bound to MTs.[31] Longitudinal expansions are also observed, relative to the apo model, for α:H10 in both

heterodimers and β:S5–H5 in β_2-tubulin (Figure 3.6(e-g)).

3.3.2   Characteristics of the laulimalide analogues

LLM is the most effective drug considered in this work, with IC_{50} values in the low nanomolar range (5.7 nM for MDA-MB-435 cells, Table 3.1),[78] while decomposition to isoLLM decreases effectiveness by nearly three orders of magnitude to give low micromolar toxicity (Table 3.1).[78] Analogues LA1 and LA2 have intermediate toxicity, with IC_{50} values between 100 nM and 240 nM in drug-sensitive cell lines, which offers a substantial improvement in potency over isoLLM.[152] Although LA4 is less cytotoxic than LA1, LA2, and isoLLM, the analogues LA1, LA2, and LA4 have similar biological effects to LLM and retain their activity against drug-resistant cell-lines.[152] In contrast, LA3 and LA5 are much less potent and have different cellular effects than LLM and other MT stabilizers; it was proposed that these differences may be due to the reactive alkynoate in these compounds.[152] While cytotoxicity data indicate the most potent analogues, the potency is not necessarily an indicator of the magnitude of drug–protein interactions or the MT-stabilizing ability of compounds. Therefore, ADMET properties are considered, and correlations between LLM–tubulin interactions and cytotoxicity are carefully noted below, though measurements of MT assembly would be a preferred metric to compare to computational models of drug–tubulin interactions.
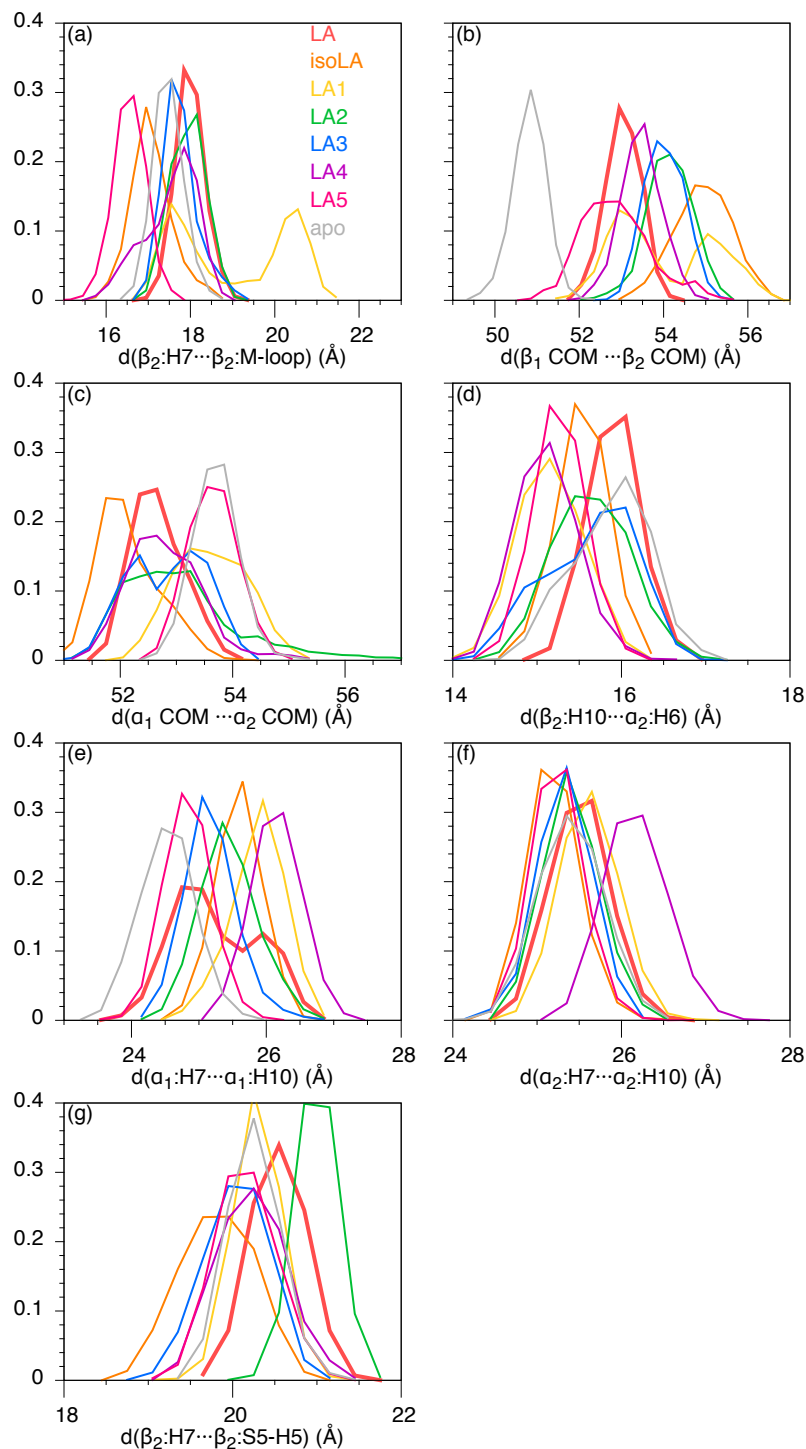
Figure 3.6: *A probability distribution of distances (Å) between important structural elements in ($\alpha\beta$-tubulin)$_2$. Distances are calculated with respect to the centres of mass (COM) of the indicated structures over the last 70 ns of the simulations. The central helix, H7, was selected as reference point. The colour legend is indicated in the figure and the data for LLM is shown with a bold line.*

Table 3.6: *Calculated ADMET properties of TXL and the LLM analogues.*

Property	TXL	LLM	isoLLM	LA1	LA2	LA3	LA4	LA5
S+S$_w$ (mg/mL)	0.020	0.300	0.362	0.177	0.112	0.378	0.053	0.215
S+P$_{eff}$ (cm^{-1}/s $\times$ 10^4)	0.21	0.88	1.06	1.22	1.50	0.8	1.99	1.15
S+Pgp_Substr	Yes (95%)	Yes (95%)	Yes (95%)	Yes (95%)	Yes (95%)	Yes (95%)	Yes (95%)	Yes (95%)
S+Pgp_Inh	Yes (97%)	Yes (78%)	Yes (83%)	Yes (97%)	Yes (78%)	Yes (78%)	Yes (97%)	Yes (97%)
S+BBB_Filter	Low	High	High	High	High	High	High	High
TOX_hERG_Filter	No (95%)	No (95%)	No (95%)	No (82%)	No (82%)	No (82%)	No (82%)	No (82%)
TOX_SGOT	Normal (73%)	Elevated (75%)	Elevated (75%)	Elevated	Elevated (75%)	Elevated (71%)	Elevated	Elevated (75%)
TOX_SGPT	Elevated (93%)	Elevated	Elevated	Elevated	Elevated	Elevated (98%)	Elevated	Elevated
ADMET_Risk	10.03	6.63	6.02	7.53	8.39	6.64	9.12	6.93

3.3.2.1   ADMET properties

ADMET properties were calculated for the LLM series, as well as the clinically-approved drug, TXL (Table 3.6). The laulimalides studied in the present work show low solubility and intestinal permeability (S+S$_w$ and S+P$_{eff}$, respectively, Table 3.6), but neither of these properties correlate with cytotoxicity (Table 3.1). Calculations predict that both TXL and laulimalides are likely to be effluxed by (S+Pgp_Substr) and inhibit (S+Pgp_Inh) the P-glycoprotein pump (Pgp) associated with multidrug resistance. However, LLM was shown to be more effective than TXL in multi-drug resistant cell-lines,[78,133] due to the ability of LLM to evade efflux by Pgp,[78] and the laulimalide analogues are not substrates for Pgp.[150] Therefore, the predicted ADMET properties for the laulimalides regarding Pgp are not experimentally validated and caution is urged to researchers examining this ADMET property. Predicted values for solubility, intestinal permeability, and drug interactions with Pgp indicate low bioavailability for the laulimalides through oral administration, similar to what has been established for TXL.[258] ADMET calculations predict that all the laulimalides are likely to penetrate the blood-brain barrier (S+BBB_Filter) making neurotoxicity a concern, as is hepatotoxicity (high levels of SGOT (TOX_SGOT) and SGPT (TOX_SGPT) enzymes), but not cardiotoxicity (TOX_hERG_Filter, related to inhibition of potassium channels). All laulimalide compounds are predicted to have high risk (ADMET_Risk, Table 3.6), where 10 % of drugs in the World Drug Index have ADMET_Risk > 6.5.[252] However, TXL has a greater risk than all laulimalides, which indicates that the laulimalides may still be successful drug candidates if they attain an acceptable efficacy-to-toxicity ratio. There is little variability in the results presented in Table 3.6 for LLM and its analogues, and therefore ADMET properties cannot explain the relative cytotoxic effects observed for these compounds (Table 3.1). The binding of these agents to ($\alpha\beta$-tubulin)$_2$ is considered next.

3.3.2.2   Cytotoxicity and binding affinity are not correlated

There is no correlation between the strength of drug binding and cytotoxicity (Tables 3.1 and 3.4), with the strongest binding occurring for LA5. The strong binding observed for LA3 and LA5 results from substantial interactions with β_2:H9, largely

from β_2:Phe294. (Table 3.1). Experimental studies of tubulin targeting agents,[77] along witj the study of the taxanes presented in Chapter 5,[3] indicate a similar lack of correlation between cytotoxicity and binding affinity. Tubulin-targeting agents act allosterically on tubulin, and therefore binding affinity is not an appropriate metric of efficacy. Additionally, no correlation is found between the strength of lateral contacts and cytotoxicity, with all LLM analogues weakening the lateral interdimer interaction (Tables 3.1, 3.4 and S4).

3.3.2.3 A unique conformation of isolaulimalide

The acid-catalyzed degradation of LLM to isoLLM results in a substantial decrease in potency. Structurally, this decomposition causes a large conformational change in the ligand (Figure B8), in both the macrocycle and the side chain: the macrocycle moves away from β_2:H10 and towards β_2:H9, while the side chain binds deeper into β_2-tubulin (Figure 3.4(b)). As a result, the C15-hydroxyl breaks the intramolecular hydrogen bond with the C1-carbonyl and moves away from β_2:H10 to form a hydrogen bond with the β_2:Asp295 side chain in β_2:H9–H9′, while the C1-carbonyl forms a hydrogen bond with the β_2:Asn337 side chain in β_2:H10–S9 (Figure 3.5, Tables 3.2 and 3.3). The isoLLM tetrahydrofuran ring and C16-hydroxyl are heavily solvated, along with the C15-hydroxyl and the C23-dihydropyran that are in close proximity (Figure B4(b)).

3.3.2.4 Modification of the C2–C3-alkene

The goal in the design of LA3 and LA5 was to change the conformation of LLM so that the C16–C17-epoxide and C20-hydroxyl could not react to form isoLLM.[150] This conformational change substantially affects the binding of these two analogues to the LLM binding site ((Figures 3.4(e, g) and B4). The C5–C9-dihydropyran is oriented towards β_2:H10 and the C20-hydroxyl of both LA3 and LA5 forms a direct hydrogen bond to the backbone carbonyl of β_2:Phe294 (Table 3.2), resulting in substantial stabilization (Figure 3.5). In contrast, for LLM, LA1, LA2, and LA4, the C20 site engages with the backbone of β_2:Phe294 in a water-mediated fashion (Table 3.3) and the C5–C9-dihydropyran is directed towards β_2:H9. Although there is a π-containing bond present at C2–C3 in all the compounds considered here, only the C2–C3-alkyne

in LA3 and LA5 moves towards the π-ring of β_2:Phe294 to engage in a π–π interaction and cause LA3 and LA5 to bind deep into β_2-tubulin, while the C2–C3-alkene in LLM, LA1, LA2, and LA4 does not participate in specific interactions with the protein. These differences reveal two important insights into LLM binding. First, the importance of the enolate is in providing an active macrocycle conformation rather than as part of the pharmacophore, a question that has been posed in previous literature.[151] In fact, the presence of an alkyne at C2–C3 results in the addition of a pharmacophore element. Second, the deep binding of LA3 and LA5, associated with a C2–C3$\cdots\beta_2$:Phe294 interaction, is accompanied by weaker interactions with β_1-tubulin (Figure 3.5, Table B1), while the more effective analogues have increased contact with β_1-tubulin (Figure 3.5, Tables 3.2, 3.3, and B1). Similar to LA3 and LA5, isoLLM binds deep into the binding pocket and forms a direct hydrogen bond between the C1-carbonyl and the β_2:Asn337 side chain, as well as C15-hydroxyl and the β_2:Asp295 side chain (Tables 3.2). Interestingly, this deep binding mode does not decrease the extent of the separation of the β-tubulin units (Figure 3.6(b)), since LA3 and LA5 have intermediate separations of the β-tubulin units relative to the other compounds.

3.3.2.5 Modification of the C16–C17-epoxide

The C16–C17-epoxide moiety was replaced with an alkene (LA1) to remove a reactive group, preventing the formation of isoLLM.[150] However, the presence of the C16–C17-epoxide is correlated with the excellent cytotoxicity of the parent molecule since LA1 exhibits decreased potency (Table 3.1) relative to LLM. LA1 adopts a different macrocycle conformation from LLM that breaks the intramolecular hydrogen bond between the C1-carbonyl and C15-hydroxyl (Figure B8). As a result the C15 site moves away from β_2:H10 and towards β_1:H3 and β_1:H3–S4 (Figure 3.4 and S4). In the LLM species, the epoxide does not engage in specific interactions with the protein and is heavily solvated (43-55 %, Table 3.2). Since it appears the epoxide doesn't have a large contribution to binding, it likely contributes to a macrocycle conformation that is important for LLM activity.

3.3.2.6 Modification of the side chain

In all instances, the C20 site is solvated, though only weakly solvated for isoLLM and LA3. Replacing the C20-hydroxyl (LLM) with a C20-methoxy (LA2) does not substantially change the macrolactone conformation (Figures 3.4, S4, and S8), but causes a change in the water-mediated hydrogen-bond pattern. Instead of interacting with β_2:Phe294 and β_2:Asp304, the methoxy group in LA4 interacts with β_2:Phe294 and β_2:Ala296 with lower frequencies (Table 3.3). Other modifications to the C20 site have also been studied.[151] While replacing the C20-hydroxyl with a methoxy or acetyloxy group decreases activity, substitution of the C20 site with a bulky *tert*-butyldimethylsilyl ether makes the analogue inactive.[151] It was proposed that perhaps bulky substituents could not be accommodated at this site,[151] however the simulations show that the C20 position is highly solvated (Table 3.2) in the seam between the protofilament. Since the C20-hydroxyl in LLM switches between forming water-mediated hydrogen bonds with β_2:Phe294 and β_2:Asp304, it is possible that a bulky group is unable to allow for the presence of multiple hydrogen bond partners at the C20 site. It may also be required that a hydrogen bond-donor be present at this site.

Replacing the C20-hydroxyl with a C20-methoxy group in LA2 results in a similar reduction in potency as replacing the C23-dihydropyran with a C23-cyclohexene (LA18 of Mooberry *et al.*[145]). This indicates that the ability for β_2:Phe294 to interact with both these groups in LLM is important to activity. Therefore, future design of analogues should ensure that a hydrogen-bond donor is present at C20, and that any modifications to the C23-site in the side chain involve a π-containing system (though not an aryl group, as discussed in Section 3.3.1.1)[145] and an atom capable of forming a hydrogen bond. It is unknown whether the hydrogen-bond acceptor in the C23-dihydropyran is a necessary pharmacophore, or if a hydrogen bond donor could also form water-mediated hydrogen bonds to β_2:Phe294 at this site. The importance of β_2:Phe294 to LLM binding may be verified by mutational experiments.

3.3.2.7 Other structural effects

Previous experimental work found that LA4 had slightly different cellular effects than LLM, LA1, and LA2 for interphase MTs, and it was proposed that these differences

could be due to changes in the number of protofilaments.[152] The calculations of the M-loop expansion from β_2-tubulin show that the M-loop in LA4-$(\alpha\beta$-tubulin)$_2$ is more extended than in apo tubulin, can occupy a broad range of states (Figure 3.6(a)), and is highly flexible (Figure B7). However it is not significantly different from the behaviour of the M-loop when LLM, LA1, and LA2 are bound (Figure 3.6(a)), and therefore this does not account for the different cellular effects observed experimentally. Therefore, it is unlikely the number of protofilaments is responsible for the alternative cellular effects observed for LA4. Evidence to support this can also be found with other MT stabilizing agents, where the binding of different taxanes results in different numbers of protofilaments in MTs,[116,117] without causing different cellular effects.

The LLM analogues have similar effects on the global tubulin structure as observed for LLM (Figures 3.6), with the exception of the M-loop conformation (Figures 3.6(a) and S7), α_2:H10 expansion (Figure 3.6(f)), and β_2:S5–H5 expansion (Figure 3.6(g)). These last two metrics have recently been implicated with the longitudinal expansion of the interdimer interface upon taxane binding.[31] However, LLM has some effects on tubulin that differ from the taxanes. Nearly all the LLM analogues increase the separation between the tubulin heterodimers (Figure 3.6(b,c)), with the exception of the effects of LA1 and LA5 on the α-tubulin units. All the laulimalides considered here also decrease the distance between β_2:H10 and α_2:H6 (Figure 3.6(d)), and increase the expansion of the α_1:H10 (Figure 3.6(e)).

3.3.2.8 The importance of the intramolecular hydrogen bond

None of the analogues have significant retention of the intramolecular hydrogen bond that was present in LLM. Interestingly, LA2, the only analogue that is not modified at the C16–C17-epoxide or C2–C3-alkene and therefore retains a macrocycle conformation similar to LLM (Figure B8), slightly retains the intramolecular hydrogen bond (11 %, Table 3.2). In the absence of an intramolecular hydrogen bond, the C1-carbonyl in LA1, LA2, and LA4 interacts with the β_2:Asn337 side chain, while the C15-hydroxyl can engage in direct and water-mediated hydrogen-bonds, predominantly in β_1-tubulin (Tables 3.2 and 3.3). Unlike LLM, the C1-carbonyl

and C15-hydroxyl have some solvent exposure in the analogues. Interestingly, the more effective LA1, LA2, and LA4 analogues are less solvated at these sites than the less effective isoLLM, LA3, and LA5 compounds (Table 3.2). The intramolecular C1-carbonyl···C15-hydroxyl hydrogen bond is likely important for activity, while solvent-exposure of these sites is correlated with reduced activity.

3.4   Conclusions

An improved model of the binding of LLM to MTs has been presented. π–π interactions are important contributors to LLM binding, where the C23-dihydropyran forms stabilizing contacts with β:Phe294, β:Tyr310, β:Tyr340, β:Phe341, and β:Phe367. Within the binding site, LLM forms an intramolecular hydrogen bond between the C1-carbonyl and the C15-hydroxyl. The C1-carbonyl also forms a direct hydrogen bond with β:Asn337, and the side chain groups form water-mediated hydrogen bonds with β:Phe294 and β:Asp304. Otherwise, the drug is highly solvated. Interestingly, LLM binding weakens the interdimer interactions, indicating LLM affects MTs differently than the taxanes.

The binding modes of the less-potent LLM analogues were identified to determine the binding features responsible for the success of the parent drug candidate. No correlations were found between the experimentally-observed cytotoxicity and the ligand–tubulin binding energy, interdimer binding energy, or ADMET properties. Several important structural correlations were determined. Retention of the LLM macrocycle conformation appears important for LLM activity, where both the C16–C17-epoxide and the C2–C3-alkene, as well as the intramolecular hydrogen bond between the C1-carbonyl and C15-hydroxyl contribute to the conformation. Retention of this hydrogen bond is correlated with high activity (LLM), while breaking the intramolecular interaction results in intermediate activity (LA1, LA2, LA4) and heavy solvation of these two sites provides poor activity (isoLLM, LA3, LA5). The less-potent analogues were found to bind more deeply into the binding pocket, forming a direct, strong hydrogen bond at the C20-hydroxyl with the β:Phe294 backbone carbonyl and minimizing interactions with the adjacent β-tubulin unit. In contrast, the more potent LLM analogues had larger binding contributions from the adjacent

β-tubulin unit. Within the side chain, several important pharmacophores were identified. It is important to have a π-containing system at C23 so that it may engage with the π-containing residues in the binding site. Furthermore, a hydrogen bond donor at C20 is important for participating in water-mediated hydrogen bonds with the β:Phe294 backbone, and to a lesser extent with β_2:Asp304. It may be important for this group to be small rather than bulky so that it can exchange between interacting with these two nearby residues. Similarly, a group capable of forming water-mediated hydrogen bonds to β:Phe294 is also important in the C23 position, although this work does not determine if an acceptor is required at this site, as was present in all LLM analogues considered in this study, or if a hydrogen-bond donor may also suffice.

The direction of the C11-methyl into the MT pore provides a potential site for future modifications to be made that may enhance the interaction between LLM and tubulin. Side chains from β:Asn52 and β:Asp128 in the adjacent β-tubulin unit, and from β:Gln291 in the LLM binding site are near C11 (6–8 Å). Only one study has considered a modification at the C11-site in which the methyl group was replaced with a hydrogen, decreasing LLM activity by an order of magnitude.[153] It is possible that larger groups may be tolerated at this site and enhance the interaction with the adjacent β-tubulin unit, while being far enough away from the C1 and C15 sites that modifications will not interrupt the intramolecular hydrogen bond.

Additional data regarding the ability of each of these drug candidates to induce MT polymerization (the critical concentration of tubulin required for MT assembly in the presence of each drug) will allow for further conclusions to be drawn about how this class of agents promotes MT formation and stability.

Chapter 4

Understanding and predicting laulimalide analogue efficacy

4.1 Introduction

Gallagher and coworkers synthesized a variety of LLM analogues, which are cyto-toxic at concentrations ranging from the low nanomolar concentrations of the original LLM (2.3 ±0.2 nM), to micromolar concentrations. Inversion of the stereocenter at C15 leads to poorer potency (176 ± 15 nM; compound 35 in Gallagher *et al.*;[151] denoted LLM-15R in Figure 4.1). The most promising analogue, (15*R*)-acetyloxy-(–)-laulimalide (compound 29 in Gallagher *et al.*;[151] denoted LLM29 in Figure 4.1), was potent in the low nanomolar range (23 ± 2 nM). In contrast, several compounds were found to be ineffective, for example (15*R*)-methoxy-(–)-laulimalide (compound 32 in Gallagher *et al.*;[151] denoted LLM32 in Figure 4.1).

In addition to the analogues synthesized and evaluated by Gallagher, the group of Prof. Dennis Hall at the University of Alberta has designed several new LLM analogues (Figure 4.1, SVH1 and SVH4). These compounds feature changes to the C23-dihydropyran and simplifications of the macrolactone ring. This addresses degradation by eliminating the problematic epoxide moiety that causes isoLLM formation.

The work presented in Chapter 3 is expanded upon by examining the analogues of Gallagher and coworkers,[151] which contains the most potent analogue (LLM29) next to LLM, as well as the analogues proposed by Hall and coworkers. From this information, characteristics of the effective LLM analogues will be identified, with a focus on the newly-developed pharmacophore presented in Chapter 3, and use this
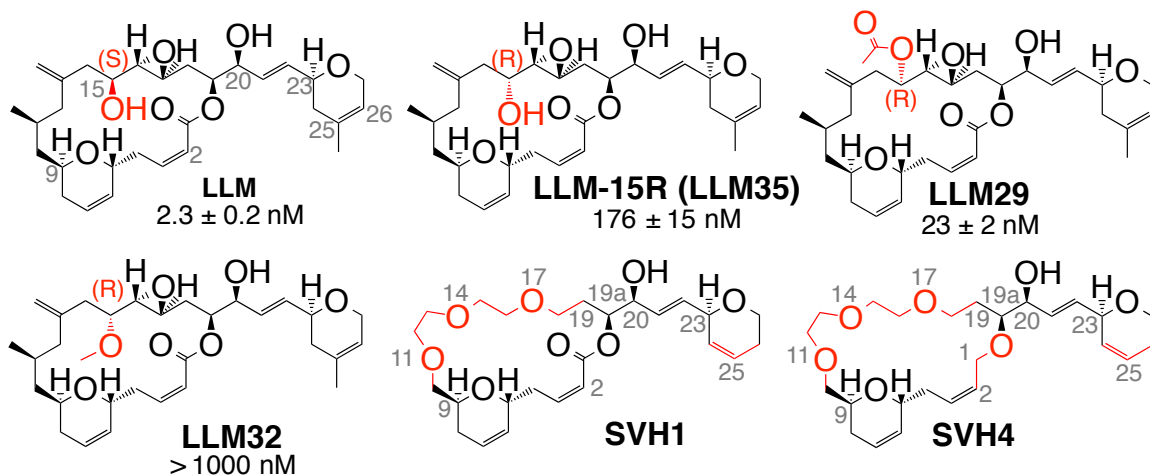
Figure 4.1: *The chemical structure, numbering and stereochemistry of the naturally-derived (−)-laulimalide (LLM), its diastereomer (15R)-(−)-laulimalide (LLM-15R), as well as analogues (15R)-acetyloxy-(−)-laulimalide (LLM29), (15R)-methoxy-(−)-laulimalide (LLM32), SVH1, and SVH4. Cell growth inhibition (IC$_{50}$) is indicated for the drug-sensitive MD-MB-435 human melanoma cell line when available.[151] Fragments in red indicate modifications.*

information to predict the potency of the proposed LLM analogues.

4.2 Computational Details

Using the model and procedures described in Chapter 3, LLM analogues from the Gallagher and Hall groups were examined (Figure 4.2). MD simulations were performed using GPU-enhanced[242–244] Amber 14.[241] General details of the MD simulations performed in this Thesis may be found in Section 1.3.3.1 and details specific to this simulation may be found in Appendix C. For each simulation, the mass-weighted RMSD of the protein components was calculated, with respect to the structure at 0 ns, to ensure the system was structurally equilibrated (Figure C1). For LLM, LLM-15R, SVH1, and SHV4, the system was equilibrated after 20 ns, and production data was collected from 20 ns to 90 ns. For LLM29 and LLM32, conformation changes required the simulations be extended. For LLM29, a conformational change occurred around 70 ns (Figure C1(c)), and analysis was performed on the structures from 76 ns to 155 ns, for a total of 79 ns. In the case of LLM32, 40 ns of structural equilibration was required due to a shift in the lateral contacts (Figure C1(d)), and production data was collected from 34 ns to 110 ns for a total of 76 ns. All residues are discussed
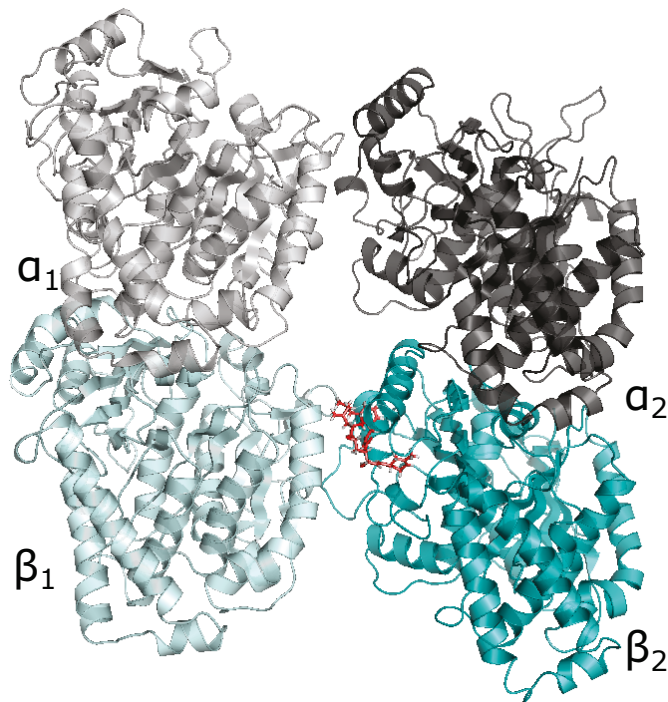
Figure 4.2: *The computational model combining protein and nucleotide coordinates from a previous study[1] and the LLM pose from 4O4H.[52] LLM (red) is bound to the $\alpha_2\beta_2$-tubulin heterodimer, and adjacent to the $\alpha_1\beta_1$-tubulin heterodimer. Image shown is as viewed from the MT exterior.*

with respect to the numbering in bovine α-tubulin isoform I-C (UniProt P81948) and β-tubulin isoform II-B (UniProt Q6B856), as reported in Chapters 2 and 3.

4.3 Results and Discussion

4.3.1 Binding of laulimalide analogues to a ($\alpha\beta$-tubulin)$_2$ model

Structural changes to the LLM analogues result in different conformations and binding poses than those found for LLM (Figure 4.3). For LLM29 and LLM32, modifications at C15 eliminate the potential for an intramolecular hydrogen bond between the C15-hydroxyl and C1-carbonyl in LLM (Table 4.1). Inversion of the stereochemistry at C15 (LLM-15R) also breaks this intramolecular hydrogen bond and decreases potency. Elimination of the intramolecular hydrogen bond alters the binding pose of the compound, where the LLM analogues undergo a conformational change in the macrocycle that moves C15 away from β_2:H10 and towards β_1:H3 while also solvating this site (17.2–54.4 %, Table 4.1) in the seam between the protofilaments.

90

For LLM-15R and LLM32, the macrolactone dihydropyran moves away from β_2:H10 (Figure 4.3(b,d)). In contrast, the C1-ester to the C5–C9-macrolactone of LLM29 are in positions similar to that observed for LLM (Figure 4.3(c)), which is correlated with the increased cytotoxicity of LLM29 observed experimentally. However, it is worth noting that LLM and LLM29 adopt similar binding motifs to LA1 and LA2 in Chapter 3,[2] but LA1 and LA2 have cytotoxicities[150,152] that are an order of magnitude greater than that of LLM29. In order to further understand the effect of these compounds on MTs, and to fully exploit the power of computational models of ligand–protein complexes in the design of LLM analogues, it will be necessary to obtain MT-assembly data for LLM and its analogues. Such experiments are more relevant to the study of drug–tubulin binding than relative cytotoxicities. For LLM-15R, LLM29, and LLM32 there are variations in the position of the side chain relative to LLM as the C23-dihydropyran binds less deeply into the binding pocket, moving away from β_2:S8 and β_2:S10, and towards β_2:H10–S9 (Figures 4.3 and C2). This is evident from the increase in separation between the C23-dihydropyran, and β_2:Tyr310 (β_2:S8) or β_2:Phe367 (β_2:S10) as the analogues move towards β_2:Tyr340 (β_2:H10–S9) at the seam between protofilaments (Figure 4.4).

The SVH1 and SVH4 analogues are greatly modified with respect to the natural LLM compound (Figure 4.1). To first ensure that the modifications to these compounds do not affect their preference for the LLM binding site, docking calculations were performed with the MOE program.[259] Both blind docking to β-tubulin, and targeted docking to the LLM binding site indicated the most populated and highest-affinity poses occurred in the LLM binding site for both compounds. Furthermore, the best docking poses also resembled the conformations obtained by MD simulations. MD simulations indicated SVH1 and SVH4 exhibit changes in the binding pose relative to LLM (Figure 4.3(e,f)). Surprisingly, the binding mode of SVH1 resembles that of LLM29; while C11 to C17 are directed towards β_2:H3 and solvated (Table 4.1), the C1-ester to the C5–C9-macrolactone retain a position between β_2:H9 and β_2:H10 (Figure 4.3(e)). In contrast, removing the ester functionality when going from SVH1 to SVH4 significantly alters the binding of the compound. SVH4 adopts a collapsed conformation with the dihydropyran moieties in close proximity (Figure 4.3(f)). In this pose, the macrocycle is away from β_2:H9 and β_2:H10, and is instead positioned

91
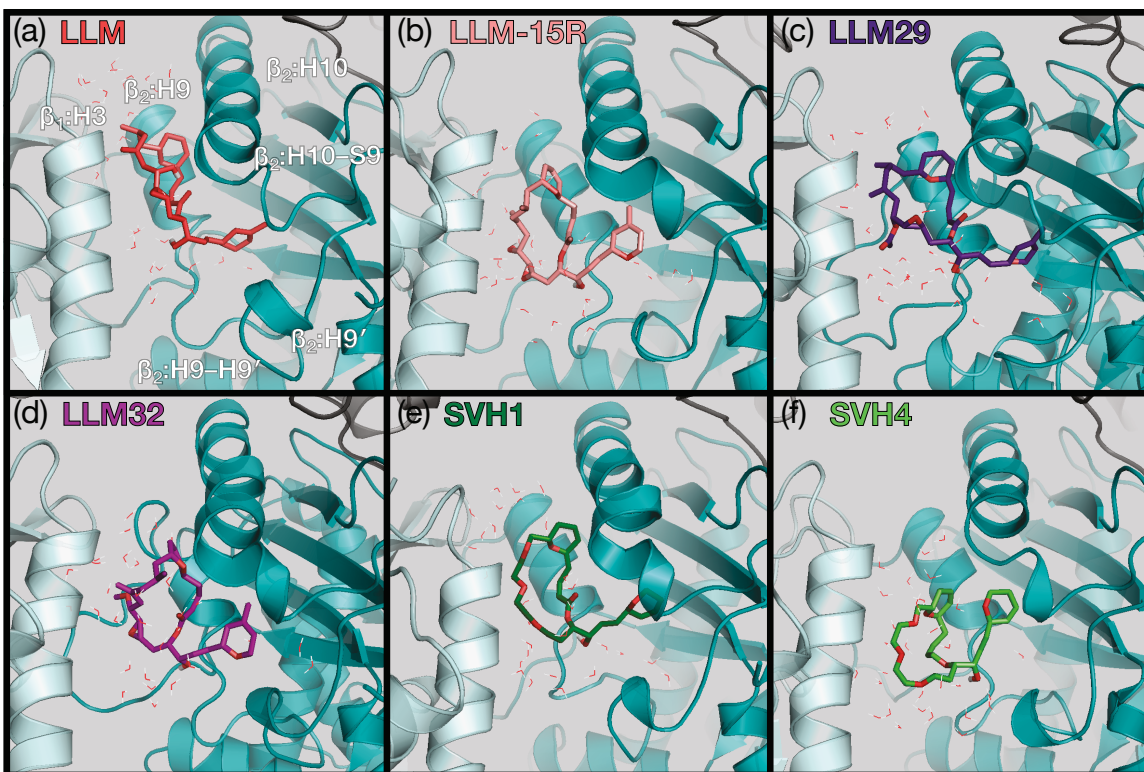
Figure 4.3: *An illustration of the LLM poses in the binding pocket located at the seam between β_1-tubulin (cyan) and β_2-tubulin (teal). The compounds are in contact with helices β_1:H3, β_2:H9, and β_2:H10. 30 binding site water molecules are shown in stick mode.*

in the seam between the protofilaments, which displaces β_1:H3 away from β_2-tubulin. The C23-dihydropyran is still located in the binding site, but is slightly displaced towards β_2:H10–S9 as observed for all the modified compounds.

Table 4.1: *Ligand–tubulin and ligand–solvent hydrogen-bond occupancy (%) throughout the equilibrated trajectories.*

Acceptor[a]	Donor[a]	LLM	LLM-15R	LLM29	LLM32	SVH1	SVH4
LLM C1-carbonyl	LLM C15-hydroxyl	60.0	-	-	-	-	-
LLM C1-carbonyl	β_2:Asn337 $N_{\delta2}$	34.9	-	51.4	-	77.5	-
LLM C5–C9-dihydropyran	β_2:Asn337 $N_{\delta2}$	-[b]	56.0	-	61.6	-	-
β_2:Gln291 $O_{\epsilon1}$	LLM C15-hydroxyl	-	18.5	-	-	-	-
LLM C15-hydroxyl	β_2:Gln291 $N_{\epsilon2}$	-	-	-	23.8	-	-
C15-ether	β_2:Gln291 $N_{\epsilon2}$	-	-	-	-	-	-
β_2:Asp295 $O_{\delta2}$	LLM C20-hydroxyl	-	65.0	-	-	-	-
β_2:Phe294 O	LLM C20-hydroxyl	-	-	-	15.3	67.9	-
LLM C20-hydroxyl	β_2:Ala296 N	-	21.9	-	12.8	-	-
LLM C23-dihydropyran	β_2:Asn337 $N_{\delta2}$	-	-	-	-	42.1	-
LLM C1-ether	water	-	-	-	-	11.3	71.7
LLM C1-carbonyl	water	-	89.6	37.6	86.0	22.8	-
LLM C5–C9-dihydropyran	water	-	-	-	-	43.6	56.9
LLM O11	water	—[c]	—	—	—	29.3	25.7
LLM O14	water	—	—	—	—	39.4	56.5
LLM O17	water	—	—	—	—	46.5	41.9
water	LLM C15-hydroxyl	-	54.4	—	—	—	—
LLM C15-hydroxyl	water	-	42.5	—	—	—	—
LLM C15-carbonyl	water	—	—	46.7	—	—	—
LLM C15-ether	water	—	—	-	17.2	—	—
LLM epoxide	water	42.6	77.1	47.8	79.6	—	—
water	LLM C20-hydroxyl	74.3	13.9	55.9	52.3	-	72.6
LLM C20-hydroxyl	water	75.4	43.7	66.2	39.6	37.2	68.4
LLM C23-dihydropyran	water	32.9	46.5	50.9	58.4	-	43.7

[a] Hydrogen bond defined as having heavy atoms within 3.0 Å and $135° \leq \angle(\text{donor–H}\cdots\text{acceptor}) \leq 180°$. Occupancies > 10 % are reported. Atoms in brackets indicate sites engaged in water-mediated interactions.; [b] Indicates an occupancy < 10 %.; [c] Not applicable.
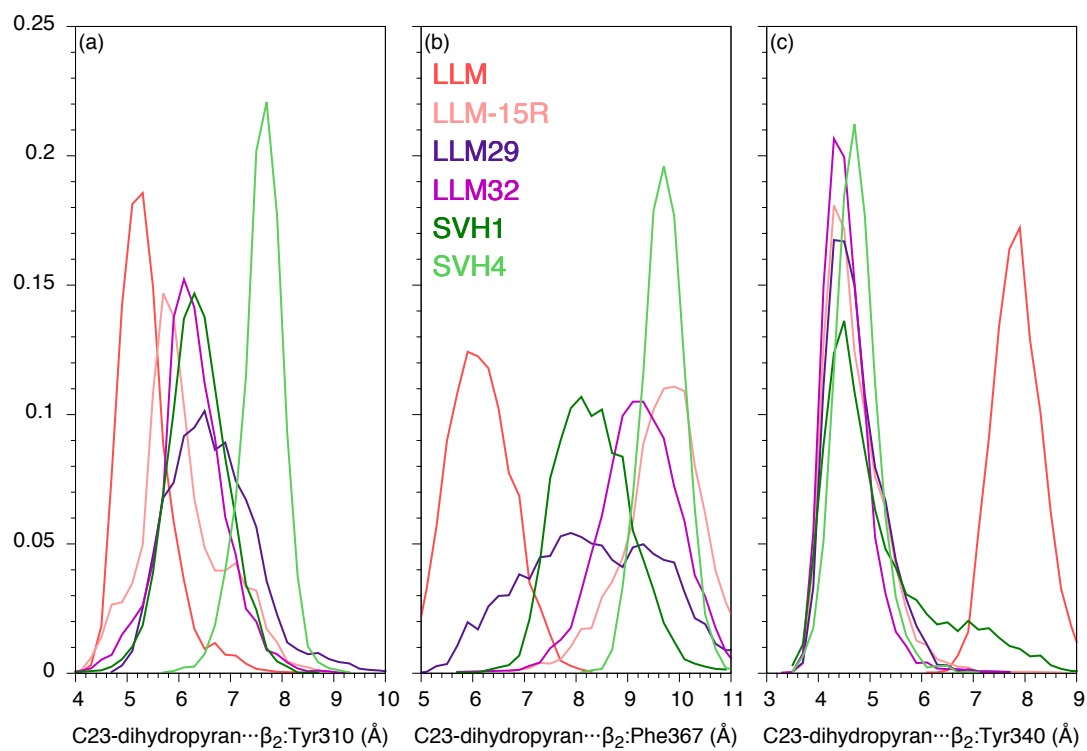
Figure 4.4: *A probability distribution of the distances (Å) between the side chain dihydropyran and residues in the LLM binding site, illustrating the deep binding of LLM near β_2:Tyr310 and β_2:Phe367, and the shallow binding of the analogues near β_2:Tyr340. An illustration of these residues is shown in Figure 4.6.*

Table 4.2: *Water-mediated ligand–tubulin hydrogen-bond occupancy (%) throughout the equilibrated trajectories.*

Hydrogen Bond[a]	LLM	LLM-15R	LLM29	LLM32	SVH1	SVH4
β_1:Asp88$\cdots$LLM	-	26.4 (C16–C17)	-	-	-	-
β_2:Gln291$\cdots$LLM	-	-	25.8 (C1-ether, C20)	-	-	-
β_2:Phe294$\cdots$LLM	55.7 (C20, C23)	17.1 (C23)	37.2 (C20, C23)	45.5 (C20, C23)	-	-
β_2:Asp295$\cdots$LLM	-	20.0 (C20)	-	17.2 (C20)	-	-
β_2:Asp304$\cdots$LLM	21.2 (C20)	-	-	-	-	-
β_2:Asn332$\cdots$LLM	-	-	-	-	-	-
β_2:Asn337$\cdots$LLM	-	44.1 (C1, C23)	-	69.6 (C1)	-	-
β_2:Tyr340$\cdots$LLM	-	-	-	-	-	-
β_1:Arg121$\cdots\beta_2$:Asn337$\cdots$LLM	-	21.9 (C1)	-	-	-	-
β_2:Gln291$\cdots\beta_2$:Phe294$\cdots$LLM	-	-	10.5 (C20)	-	-	-
β_2:Asn332$\cdots\beta_2$:Asn337$\cdots$LLM	-	-	-	-	-	-
β_2:Asp295$\cdots\beta_2$:Ala296$\cdots$LLM	-	-	-	-	-	17.6 (C20, C23)

(a) Hydrogen bond defined as heavy atoms within 3.0 Å and $135° \leq \angle(\text{donor–H}\cdots\text{acceptor}) \leq 180°$. Occupancies > 10 % are reported. Atoms in brackets indicate sites engaged in water-mediated interactions.

Alterations in binding poses affect hydrogen bond contacts with the LLM analogues (Tables 4.1 and 4.2, Figure C2). In addition to an intramolecular hydrogen bond between the C1-carbonyl and C15-hydroxyl, LLM simultaneously forms a hydrogen bond between the C1-carbonyl and the β_2:Asn337 side chain. Water-mediated interactions also occur between the LLM side chain, and β_2:Phe294 and β_2:Asp304, where the C20-hydroxyl is highly solvated, and the C16-C17-epoxide and the C23-dihydropyran are lightly solvated.

The unique conformation adopted by SVH4 results in different ligand–tubulin contacts (Tables 4.1 and 4.2) and different sources of stabilization (Figures 4.5 and C2, Table C1) compared to the other LLM analogues. This compound is largely solvated in the LLM binding pocket and forms no direct hydrogen bonds to tubulin (Table 4.1). Only one notable hydrogen bond is present in a water-mediated fashion between residues β_2:Asp295 and β_2:Ala296, and the side chain (18 %, Table 4.2). Compared to the other compounds studied, SVH4 has the weakest binding to $\alpha\beta$-tubulin (Table 4.3). This involves the smallest contribution from β_2-tubulin to stability, but one of the largest contributions from β_1-tubulin (Table C1). This is primarily due to favourable interactions with β_1:H3, specifically ionic β_1:Asp118 and β_1:Arg121 (Figure 4.5), when the collapsed macrocycle displaces β_1:H3.

Greater similarities in binding poses are found between the remaining analogues and LLM. None of the analogues are stabilized by an intramolecular hydrogen bond, and instead the C1-carbonyl and C15-substituent are solvated (Table 4.1). This was also observed with other LLM analogues in Chapter 3 and this intramolecular hydrogen bond was proposed to be an important contributor to activity.[2] As the C15 side of the macrolactone ring opens up away from β_2:H10 and towards β_1:H3, interactions with residues in β_2:H10, such as the cationic β_2:Lys336, decrease (Figure 4.5). The C1-carbonyl in LLM-15R, LLM29, LLM32, and SVH1 retains some interaction with β_2:Asn337 in β_2:H10–S9, that is either direct or water-mediated (Tables 4.1 and 4.2). The absence of the C1-carbonyl in SVH1 eliminates interactions with β_2:Asn337, leading to the collapsed structure. Therefore, it appears the C1-carbonyl$\cdots\beta_2$:Asn337 interaction is important for stabilizing the ligand. The interactions between LLM-15R, LLM29, LLM32, and SVH1 and tubulin can be further subdivided based on the common poses adopted by LLM-15R and LLM32, and

LLM29 and SVH1, as evident in both ligand–tubulin contacts (Tables 4.1 and 4.2) and sources of stabilization (Figure 4.5 and Table C1). For example, both LLM29 and SVH1 engage in direct interactions with β_2:Asn337, while the less-cytotoxic LLM-15R and LLM32 form water-mediated interactions with this residue. The less cytotoxic LLM-15R and LLM32 analogues also form a stabilizing direct hydrogen bond between the C15-site and β_2:Gln291 (Table 4.1). This occurs as the macrolactone of LLM-15R and LLM32 binds less deeply into β_2-tubulin and moves away from β_2-tubulin, causing interactions with β_2:Thr290 and β_2:Gln329 to decrease (Figure 4.5).

The side chain in the LLM analogues adopts a slightly different position in the binding pocket than the one observed for LLM (Figure 4.3), but is solvated for all compounds studied (Table 4.1). As the C23-dihydropyran moiety moves away from β_2:S8 and β_2:S10, and towards β_2:H10–S9 for the analogues, the C20-hydroxyl moves closer to β_2:H9–H9'. This increases the number of direct and water-mediated hydrogen bonds between the side chain of the LLM analogues and residues β_2:Phe294, β_2:Asp295, and β_2:Ala296 (Tables 4.1 and 4.2). This also increases the relative contribution of these residues to binding compared to that for LLM (Figure 4.3).

In addition to hydrogen bonds between the ligand and surrounding protein and/or solvent, the olefin in the C23-dihydropyran ring engages in π–π-interactions with the protein (Figure 4.6). The side chain in all analogues adopts a range of positions within the binding site that differ from those found for LLM (Figure 4.6(a)). For all the analogues, there is a decreases in the distance between the side chain heterocycle and the aromatic ring of β_2:Tyr340 that is located at the edge of the binding pocket (Figure 4.6(b–f)), while also increasing the affinity of the drug for β_2:Tyr340 (Figure 4.5). This movement is accompanied by an increase in the distance between the side chain dihydropyran in the analogues and residues β_2:Tyr310 and β_2:Phe367 that are located deep in the binding pocket (Figure 4.4(a,b)), as well as a lower affinity of the ligand for these residues (Figure 4.5). This shows the side chain dihydropyran in the analogues binds less deeply into β_2-tubulin. For LLM29, the side chain occupies a broad range of states (Figure 4.4), while the side chain of SVH4 has different interactions with the π-containing residues that are a result of its unique conformation (Figure 4.6).

The only side chain modification considered in this study involves the alteration

of the C23-dihydropyran in SVH1 and SVH4 (Figure 4.1). Although SVH1 and SVH4 still contain a C23-dihydropyran moiety, it is without a methyl group and involves a different location of the double bond (Figure 4.1). While SVH4 adopts a very different conformation from LLM and the other analogues, SVH1 is very similar to LLM29, and the SVH1 side chain engages in similar interactions with the π-containing residues as the LLM-15R, LLM29, and LLM32 analogues (Figures 4.4 and 4.6). Therefore, it appears that this side chain modification does not significantly affect LLM analogue binding. This modification retains all the essential side chain pharmacophore elements proposed in Chapter 3,[2] which include a hydrogen bond donor (C15), an additional hydrogen-bond participant (in the C23-ring) and a π-containing system (in the C23 ring). Most importantly, this alteration shows that variability in the location of the π-system is tolerated, which is not surprising given the nonspecific nature of π–π-interactions and the abundance of π-containing residues in this binding pocket.

In Chapter 3,[2] it was found that the least potent (micromolar) analogues had deeply-bound side chains, resulting in high affinities for β_2-tubulin and low affinities for β_1-tubulin. In contrast, all the analogues with submicromolar potency examined in this Chapter and Chapter 3 bind less deeply to β_2-tubulin, have lower affinities for β_2-tubulin, but variable affinities for β_1-tubulin relative to LLM (Table C1). LLM lies in an intermediate position between these two extremes with a balanced affinity for both β_1- and β_2-tubulin, and it is possible that such an intermediate conformation leads to ligands with high activity. Although the nonspecific π-π interactions that occur between the C23-side chain and the β_2-tubulin binding site may facilitate a variety of binding motifs, the intermediate pose associated with the natural LLM appears to be the most effective.

The ligand–protein MM/GBSA binding energy calculations indicate that LLM binds strongest to the tubulin heterodimers (-197 kJ mol^{-1}), illustrating the balance of interactions between β_1- and β_2-tubulin discussed above. Binding strength decreases as LLM > LLM29 > SVH1 $\approx$ LLM-15R > LLM32 >> SVH4 (Table 4.3). Although this trend correlates with the known cytotoxicities for the synthesized compounds (Figure 4.1), Chapter 3 showed that relative ligand–tubulin binding strength is not an indicator of cytotoxicity.[2] LLM and all the analogues considered in this Chapter and Chapter 3 cause the distance between α-tubulin to decreases and the distance
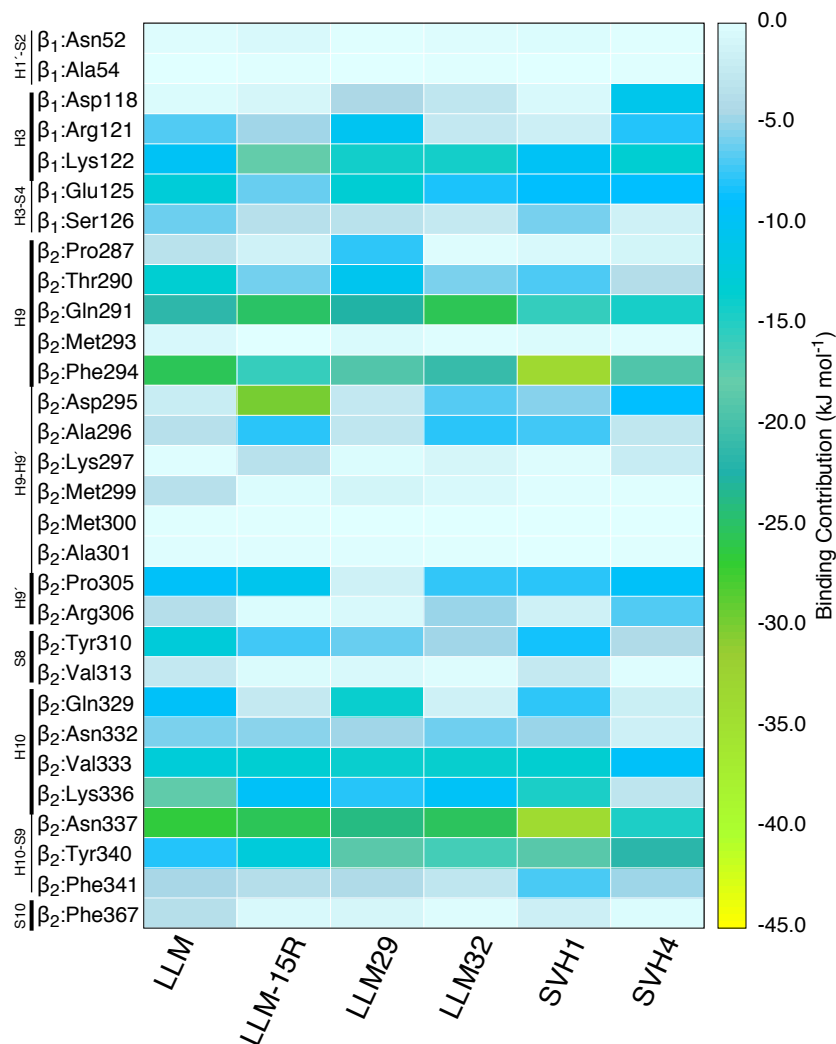
Figure 4.5: *Residue contributions to the ligand–tubulin MM/GBSA binding energy (kJ mol^{-1}). Data included in Table C1.*

between β-tubulin to increase.

The lateral interdimer interactions are destabilized, with SVH4 having the largest destabilizing effect and LLM-15R having the smallest effect (Table 4.3). Interestingly, the similar binding poses observed for LLM, LLM29, and SVH1 result in a comparable energetic effect on the lateral contacts. Pel A, which binds to the same site as LLM, destabilizes lateral contacts.[113] This is unique from the effects of the taxanes on MTs, which enhance longitudinal contacts but have little effect on lateral contacts.[31]

Table 4.3: *MM/GBSA-calculated binding free energy (kJ mol^{-1}).*[a]

	LLM	LLM-15R	LLM29	LLM32	SVH1	SVH4	apo
Ligand–tubulin binding	-196.6 ±12.7	-171.4 ±21.0	-178.8 ±17.4	-148.5 ±17.9	-174.3 ±15.3	-123.7 ±17.4	- -
Relative ligand–tubulin binding[b]	0.0	25.1	17.8	48.1	22.2	72.9	-
Interdimer binding	-183.8 ±30.1	-215.2 ±43.6	-182.9 ±16.9	-151.8 ±33.9	-184.6 ±39.7	-141.3 ±35.0	-233.8 ±43.4
Relative interdimer binding[b]	0.0	-31.4	0.9	32.0	-0.8	42.5	-40.0

[a] $\Delta G^{MM/GBSA}$, Equations 1.20 and 1.21, neglecting entropy.; [b] Binding energy relative to LLM.
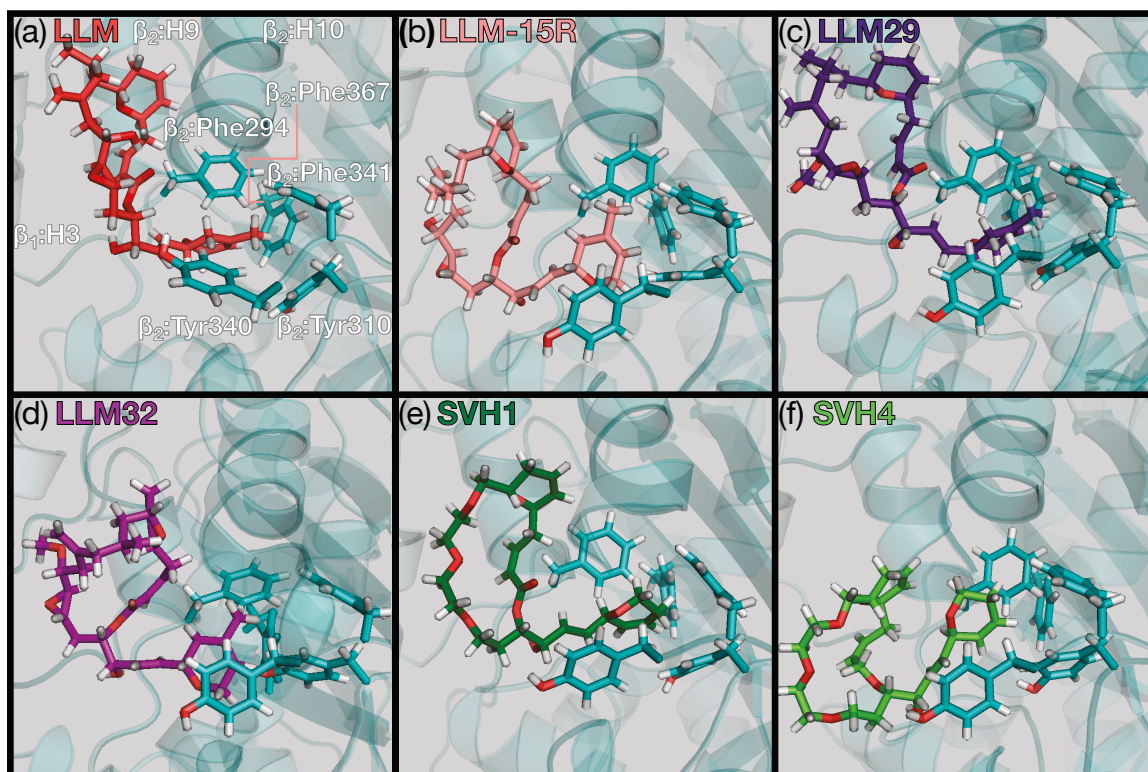
Figure 4.6: *An illustration of the π–π-interactions present in the LLM binding pocket, located at the seam between β_1-tubulin (cyan) and β_2-tubulin (teal).*

4.3.2 Distinguishing the laulimalide analogues

4.3.2.1 ADMET properties

The ADMET properties were evaluated for TXL, LLM, and the LLM analogues (Table 4.4). All compounds considered have low solubility (S+S$_w$), though the proposed SVH1 compound shows improved solubility. Intestinal permeability (S+P$_{eff}$) is also problematic. Although the ADMET properties considered here examine the likelihood of the compounds to be effluxed by (S+Pgp_Substr) and inhibit (S+Pgp_Inh) the Pgp, LLM has been shown to evade Pgp efflux[78] and therefore it is likely these reported values are inaccurate. However, the lower value of S+Pgp_Inh predicted for SVH4 may indicate this compound is less likely to evade Pgp efflux. The compounds considered in this Chapter are likely to be neurotoxic, as evidenced by their predicted ability to cross the blood-brain barrier (BBB, S+BBB_Filter). They are also predicted to be hepatotoxic based on high levels of SGOT and SGPT (TOX_SGOT and TOX_SGPT, respectively), but should have low cardiotoxicity (based on the inhibition of potassium channels, TOX_hERG_Filter). The ADMET_Risk property is calculated to determine overall toxicity, where 10 % of drugs in the World Drug Index have ADMET_Risk values greater than 6.5.[252] While TXL has the greatest risk, LLM and its isomer LLM-15R have intermediate risks. The most potent analogue, LLM29 has a greater risk than LLM, which may be detrimental for this agent if it is further pursued as a therapeutic agent. The LLM32 analogue has similar toxicity to LLM29. Interestingly, the proposed SVH1 and SVH4 analogues have the lowest predicted toxicity of all the compounds considered in this Chapter and Chapter 3.[2]

Table 4.4: *Calculated ADMET properties of TXL and the LLM analogues.*

Property	TXL	LLM	LLM-15R	LLM29	LLM32	SVH1	SVH4
S+S$_w$ (mg/mL)	0.020	0.300	0.297	0.068	0.091	1.720	0.805
S+P$_{eff}$ (cm^{-1}/s $\times$ 10^4)	0.21	0.88	0.88	1.10	1.42	1.21	1.72
S+Pgp_Substr	Yes (95%)	Yes (95%)	Yes (95%)	Yes (95%)	Yes (95%)	Yes (95%)	Yes (95%)
S+Pgp_Inh	Yes (97%)	Yes (78%)	Yes (78%)	Yes (72%)	Yes (78%)	Yes (83%)	No (61%)
S+BBB_Filter	Low	High	High	High	High	High	High
TOX_hERG_Filter	No (95%)	No (95%)	No (95%)	No (95%)	No (82%)	No (95%)	No (95%)
TOX_SGOT	Normal (73%)	Elevated (75%)	Elevated (75%)	Elevated (75%)	Elevated (82%)	Elevated	Elevated
TOX_SGPT	Elevated (93%)	Elevated	Elevated	Elevated	Elevated	Elevated	Elevated
ADMET_Risk	10.03	6.63	6.63	8.52	8.57	5.39	5.39

4.3.2.2 Binding properties

The intramolecular hydrogen bond between the C1-carbonyl and the C15-hydroxyl in LLM is not retained by any of the analogues. A modification as simple as the inversion of the stereocenter at C15 breaks this hydrogen bond and results in substantially lower potency. The important intramolecular hydrogen bond creates a specific macrocycle conformation that is likely a major contributor to the superior potency of the parent compound. Elimination of this hydrogen bond results in increased solvation of the LLM analogues, and a movement of the C15-site and C16–C17-epoxide away from β_2:H10 and towards β_1:H3. The hydrogen bond between the C1-carbonyl and β_2:Asn337 also appears to be important, where direct hydrogen bonds are correlated with increased potency (LLM, LLM29), and water-mediated hydrogen bonds are correlated with decreased potency (LLM-15R, LLM32).

A large stabilization results from the π-π-interactions between the LLM side chains and β_2-tubulin. Based on the similarities in the poses of LLM, LLM29, and SVH1, it is concluded that modifications of the side chain as observed in the SVH1 and SVH4 analogues have little structural or energetic effect on LLM analogue binding, and modification of the location of the π-containing system in the C23-ring appears to be well tolerated. A variety of poses are observed in the side chains of the LLM analogues that range from deeply bound (LA3 and LA5 in Chapter 3) to shallow binding with β_2-tubulin. This is likely due to the nonspecific nature of π–π interactions and the abundance of π-containing residues in the binding site. The parent LLM compound adopts an intermediate location between deep and shallow binding modes resulting in significant interactions with both β_1- and β_2-tubulin, which may be important to the mechanism of action of this compound.

The binding of the newly-proposed analogues SVH1 and SVH4 indicates that SVH1 shows promise as a MT-targeting agent similar to LLM and its analogues. Despite the structural similarity of SVH1 and SVH4, SVH1 adopts LLM-like poses while SVH4 adopts a collapsed conformation, engaging in few direct interactions with and having low affinity for ($\alpha\beta$-tubulin)$_2$. Furthermore, SVH4 may have a decreased ability to evade Pgp efflux. Together, this suggests that SVH4 will not behave similarly to natural LLM in its effects on MTs. In contrast, the conformation of SHV1

resembles that of the most potent LLM analogue, LLM29, while also engaging in direct interactions with β_2:Asn337. SVH1 is predicted to have decreased adverse effects as indicated by ADMET toxicity calculations. Therefore, SVH1 merits experimental synthesis and evaluation as an alternative to LLM.

4.4 Conclusions

The binding of several LLM analogues to tubulin has been computationally examined within a MT-like environment. Both experimentally-examined and newly-proposed analogues were considered to build upon the LLM pharmacophore model previously developed in Chapter 3, as well as evaluate the predictive ability of the model used.

A specific macrocycle conformation is present for the parent LLM compound, which is governed by an intramolecular hydrogen bond between the C1-carbonyl and the C15-hydroxyl. None of the analogues studied retain this intramolecular hydrogen bond or macrocycle conformation, which may account for the reduced potency of the analogues that have been observed experimentally. An abundance of nonspecific π-π interactions in the binding site near the dihydropyran side chain allow for a variety of ligand poses to be adopted by the compounds, which results in variations in how deep or shallow these ligands interact within the binding site. The parent compound was found to occupy an intermediate position between the β-tubulin heterodimers, which results in highly stabilizing contributions from both β-tubulin units that may be key to the superior potency of this compound. Despite the structural differences between the compounds, and the differences in their binding modes, all the compounds studied here weaken the lateral interdimer interface, which is distinct from the mechanism of action of the taxanes.

Computational models provide a means of efficiently screening compounds in rational drug design, while providing information about ligand–protein complexes at an atomistic level. Novel LLM analogues have been evaluated to determine if their interactions with tubulin mimic the binding of LLM. These compounds feature significant modifications to the macrocycle and additional changes to the side chain. This computational model of LLM binding to tubulin finds the SVH1 analogue to be particularly promising. SVH1 is LLM-like in its binding mode and behaves simi-

larly to the most potent LLM analogue, LLM29, which is only an order of magnitude less potent than LLM. The side chain modifications present in these new compounds contain the elements of the pharmacophore previously proposed in Chapter 3 for the LLM side chain, and the calculated binding mode indicates that side chain modifications are tolerated. In contrast, the related compound, SVH4, adopts a collapsed conformation within the ligand binding site that is unique from the other analogues studied, and the model presented here predicts that this compound will not behave similarly to LLM.

Chapter 5

Elucidating the mechanism of action of the clinically-approved taxanes: A comprehensive comparison of local and allosteric effects[*]

5.1 Introduction

The most well-studied MT targeting agent is paclitaxel (TXL), a naturally-derived taxane. This compound is currently in clinical use, along with the taxanes docetaxel (DXL) and cabazitaxel (CAB, Figure 5.1). As discussed in Section 1.2.2.2, the taxanes stabilize MTs by binding to β-tubulin at a site contacting β:H1, β:H6–H7, β:H7, β:S7, the M-loop, and β:S9–H10 located in the lumen of the MT.[35,36] The mechanism by which the taxanes stabilize MTs has been the subject of many studies. The most recent experimental work indicates that TXL allosterically reverses the conformational changes to $\alpha\beta$-tubulin that occur upon the hydrolysis of GTP to GDP in β-tubulin[31,105] through increasing longitudinal contacts and easing conformational strain, rather than through lateral contacts with the M-loop.[31]

Despite the ability of TXL, DXL, and CAB to similarly stabilize MTs, there are known differences in the effects of these compounds on MTs. DXL has a greater affinity for tubulin and greater effect on MT assembly than TXL,[115] while CAB and

---
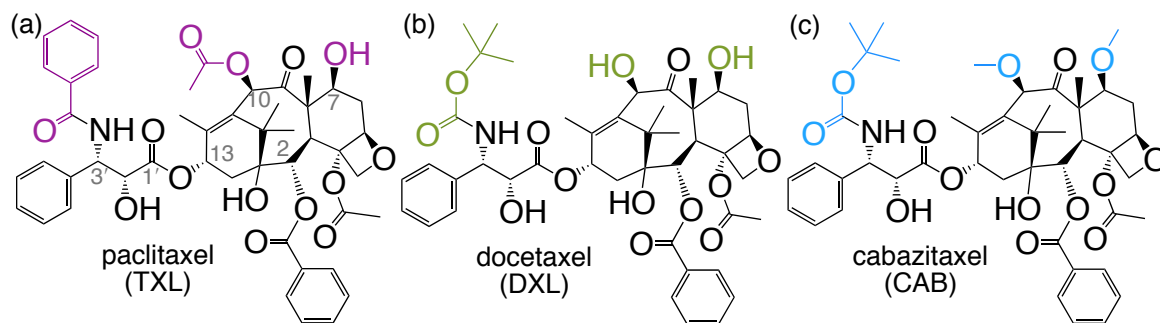
Figure 5.1: *The chemical structure and numbering of (a) paclitaxel, (b) docetaxel, and (c) cabazitaxel highlighting functional group modifications to the taxane framework.*

DXL perform similarly in MT stabilization and tubulin assembly experiments.[79] TXL binding decreases the number of MT protofilaments from 13 to 12, while DXL binding results in MTs with 13 or 14 protofilaments.[116,117] This change in protofilament number has been attributed to changes in the M-loop, which acts as a hinge to determine the number of protofilaments in a MT,[24] which has recently been proposed to be affected by the C7- and C10-substituents of the taxane.[92,117]

This Chapter examines the effects of the three clinically-approved taxanes on $\alpha\beta$-tubulin by using molecular mechanics and MD simulations to compare the binding of TXL, DXL, and CAB. Usually when designing drugs, emphasis is placed on the strength of drug–protein binding to predict drug efficiency with studies correlating binding or inhibition constants to IC_{50} values.[260] However, certain tubulin-binding agents only show a weak correlation between IC_{50} cytotoxicity and the free energy of binding.[77] In addition to such correlations neglecting pharmacokinetics, in the case of tubulin-binding agents that allosterically affect the protein, binding affinity alone cannot fully account for the effect of the drug on the protein. Therefore, more appropriate metrics of taxane efficacy are established in this study. The effects of taxane binding to tubulin on both a local (binding site) and global (allosteric) scale are considered. Similarities between these drugs may hint at a common mechanism of the taxanes.

5.2 Computational Details

Atomistic MD simulations were performed to identify differences in binding between TXL, DXL, and CAB. The TXL–$\alpha\beta$-tubulin complex is based on the 1JFF crystal structure[36] involving TXL bound to an $\alpha\beta$-tubulin heterodimer in zinc-induced sheets, where missing residues α:35–60 were overlaid from the 1TUB crystal structure.[35] Hydrogen atoms were added to the protein using the tleap module of Amber-Tools, where the protonation states of ionizable residues at a pH of 7 were determined by PROPKA.[261] In addition to the protein and drug, the GTP and Mg^{2+} bound to the α-tubulin, as well as the GDP bound to the β-tubulin, were included. To obtain the analogous DXL–tubulin and CAB–tubulin complex, modifications to TXL were made at the C7, C10, and C3′ sites, and the coordinates were optimized using PM6 in Gaussian 09.[255] Simulations of apo tubulin were carried out by removing the taxane.

MD simulations were performed using GPU-enhanced[242–244] Amber 12.[240] General details of the MD simulations performed in this Thesis may be found in Section 1.3.3.1 and details specific to this Chapter may be found in Appendix D. Analysis of the mass-weighted RMSD of the protein C_α atoms (Figures D1–D3) showed the ligand–protein complexes were structurally equilibrated after 10 ns. Therefore, the final 37.5 ns of the simulation were analyzed, and the results of this analysis are discussed below. In the discussion of results, the residues are referenced using the numbering and secondary structures as reported in the 1JFF crystal structure[36] In this structure, there are discontinuities in the numbering of the β-tubulin unit, compared to the α-tubulin unit, and therefore this numbering is slightly different from the numbering in bovine α-tubulin isoform I-C (UniProt P81948) and β-tubulin isoform II-B (UniProt Q6B856) used in Chapters 2–4.

5.3 Results and Discussion

5.3.1 Local effects of taxane binding

First, the local effects of the binding of TXL, DXL, and CAB to β-tubulin are considered by examining the binding site. Throughout the simulations, the taxanes adopt similar, rigid conformations of the baccatin core, the C2-phenyl, the C7, and C10

substituents (Figure 5.2). This is reflected by the low RMSF of the drug atoms (Figure D4) in these groups. However, the taxanes differ in the C13 side chain rigidity. The C3′-phenyl and N′-benzyl amide of TXL are rigid throughout the simulation (RMSF less than 1.09 Å), with the N′-substituent directed towards β:H1 and the lumen, and the C2′ directed into the binding pocket towards β:H7, resembling the bioactive T-Taxol geometry previously reported.[262] Corresponding RMSFs for DXL show larger fluctuations (up to 2.80 Å). DXL adopts two distinct conformations throughout the simulation that differ in the C13 side chain conformation, particularly the $\angle$(N′-C3′-C2′-C1′) dihedral (Figure D5). The first conformer (DXL–C1) exists in the time intervals from 10–23.8 ns and 37.3–47.5 ns (Figure D5), involves the close proximity of the C2-phenyl and C3′-t-butyl carbamide ester ($\angle$(N′-C3′-C2′-C1′) $\approx$ 70°), and resembles the conformation of TXL. Alternatively, the second conformer (DXL–C2) is occupied from 23.8–37.3 ns with close contacts between the C2-phenyl and C3′-phenyl ($\angle$(N′-C3′-C2′-C1′) $\approx$ 110–160°). DXL–C1 is in agreement with the NMR-determined pre-release conformation of DXL bound to tubulin, while DXL–C2 is similar to conformations previously found to exhibit low affinity for the luminal binding site in docking studies.[114] Therefore, it is likely that DXL–C1 is the biologically-active conformation of DXL, which is present during 64 % of the simulation and also persists for up to at least 67.5 ns in extended simulations (Figure D5). The C13 side chain of CAB is highly mobile (RMSF up to 3.26 Å) with the C3′ and N′ substituents occupying a range of positions in the binding site. In general, the N′ side chain of CAB is closer to the protein towards β:H1, rather than towards the lumen as observed for TXL and DXL. The conformation of CAB switches between two states: CAB–C1 ($\angle$(N′-C3′-C2′-C1′) $\approx$ 60–100°) has the C2-phenyl and N′-t-butyl carbamide ester in close proximity (similar to TXL and DXL–C1), while CAB–C2 ($\angle$(N′-C3′-C2′-C1′) $\approx$ 160–200°) has the C2-phenyl and C3′-phenyl in close proximity. CAB–C2 is distinct from DXL–C2 (Figure 5.2) and resembles the "hydrophobic collapse" of TXL and DXL observed in solution,[263] with the C3′-phenyl group oriented in a direction similar to that of the N′ substituents of TXL and DXL–C1 within the binding site. Extension of the simulations of CAB by an additional 20 ns (Figure D5) shows the drug primarily occupies the conformation found in CAB–C2, and this structure will be discussed in the present work. Although DXL and CAB have the same C13 side
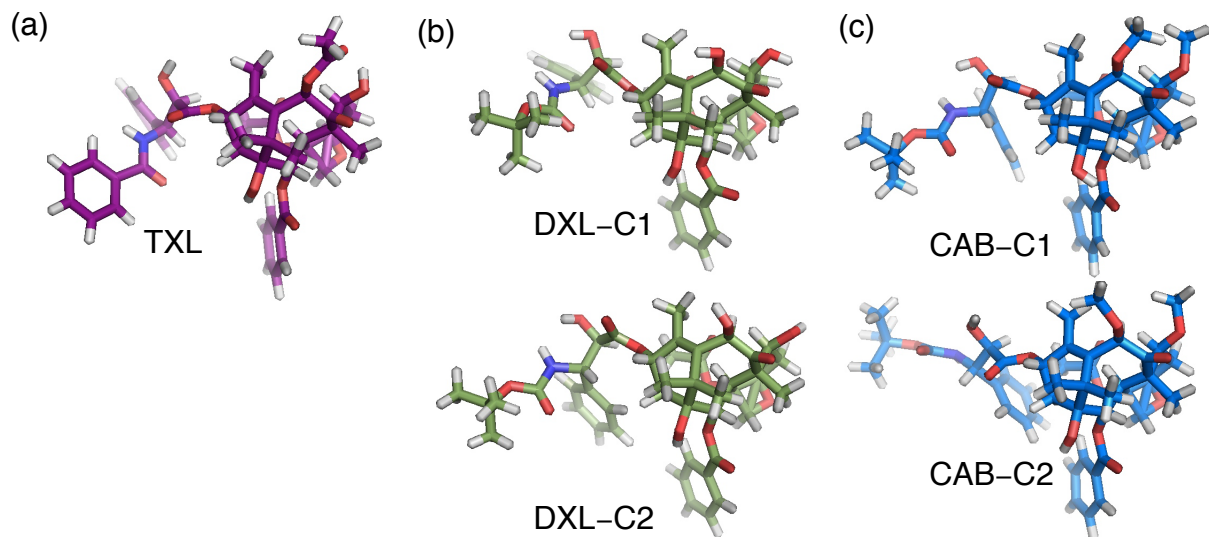
Figure 5.2: *A comparison of the conformations of (a) TXL, (b) DXL, and (c) CAB taken from snapshots during the simulations, where atom coordinates have been overlaid.*

chain, DXL does not collapse, which points to an important role that the C7 and C10 substituents play in maintaining a hydrophilic conformation of the drug.

The rigidity of TXL binding coincides with an abundance of π–π interactions (Figure D6). The three phenyl rings of TXL interact with β:His229 (β:H7) and β:Phe272 (M-loop). Although generally weaker in strength than hydrogen bonds, π–π interactions provide structural support for TXL binding. Previous work proposed the insertion of β:His229 between the C2- and C3′-phenyl of TXL prevents collapse of the drug.[262] The present study shows β:His229, located near the exterior of the binding pocket, is close to the C2-phenyl of TXL and equidistant to the N′- and C3′-phenyl groups (Figure D7(a–c)). In the interior of the binding pocket, β:Phe272 is close to the C3′-phenyl but further from the N′- and C2-phenyl groups (Figure D7(d–f)). Therefore, both β:His229 and β:Phe272 play an important role in stabilizing the conformation of TXL. Mutations to β:Phe272[195] are known to confer TXL resistance and support this finding. Also in support of the importance of β:His229 and β:Phe272 is the experimental finding that yeast tubulin, which is normally resistant to the effects of TXL, may be susceptible to the effects of TXL by introducing several point mutations that include the introduction of β:His229 and β:Phe272.[264] Despite the missing aromatic ring at N′, DXL–C1 maintains contacts with β:His229, but slight

variations are observed for DXL–C2 (24–37 ns). Alternatively CAB–C2 interactions with β:His229 differ at the C3′-phenyl, much like DXL–C2. Interactions between β:Phe272 and either DXL or CAB are different from those observed when TXL is bound, indicating that these clinically-approved taxanes have similar effects on β:H7 (β:His229) but variable effects on the M-loop via β:Phe272.

Hydrogen bonds play an important role stabilizing the taxanes in the luminal binding site. Both conformers of DXL engage in significantly more hydrogen bonds with the protein than TXL and CAB (Figure 5.3 and Table D1). Some of this increase is due to the hydrogen-bond donor abilities at the C7 and C10 positions of DXL relative to TXL or CAB. Interestingly, hydrogen bonds to DXL also increase at unmodified sites: the C1-hydroxyl, the oxetane oxygen, the C9-carbonyl, the C1′-carbonyl, the N′–H, and N′-carbonyl. These observed changes in drug–protein interactions indicate that in the case of TXL, π–π interactions are important in stabilizing the conformation of the drug, while for DXL, hydrogen bonds stabilizes the drug in the binding site. Since both these interactions are weaker for CAB, it adopts a collapsed structure.
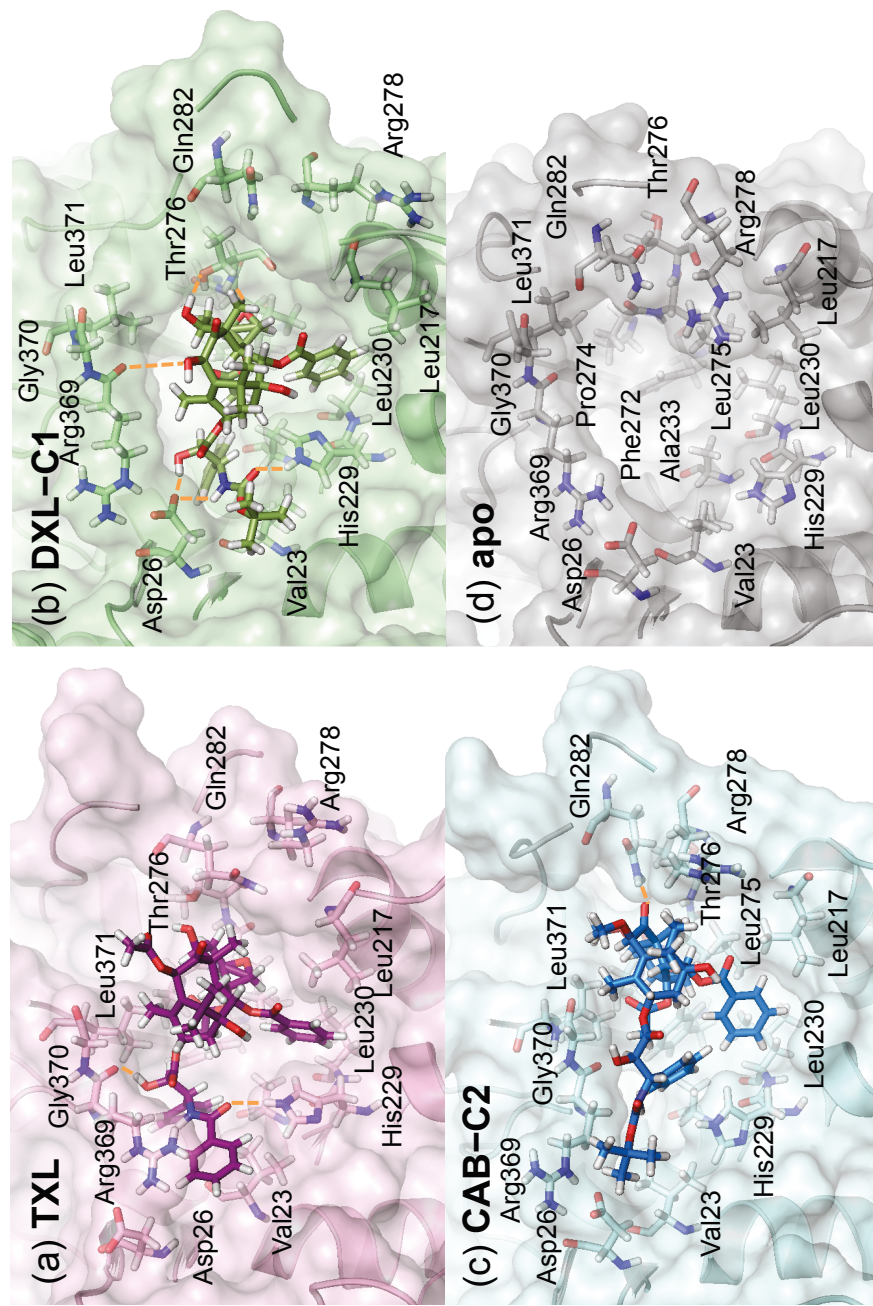
Figure 5.3: *The binding site of (a) TXL, (b) DXL, and (c) CAB, as well as this region in (d) apo tubulin taken from the end of the 47.5 ns simulation. The taxane and select residues are indicated in stick mode, hydrogen bonds are indicated with dashed orange lines. Corresponding videos of the taxane binding site are available online in the Supporting Information for the published version[3] of this Chapter (Videos S1–S3).*

An intramolecular hydrogen bond occurs between the C1-hydroxyl and C2-carbonyl, more prominent for CAB (when CAB–C2 is present, a hydrogen bond exists 49 % of the time) and TXL (25 %) than DXL (DXL–C1, 17 %). The most dominant hydrogen bond occurs between the C2′-hydroxyl of TXL and the backbone oxygen of β:Arg369 (83 %). For DXL (specifically, DXL–C1), the β:Arg369 backbone carbonyl shifts to interact with the C10-hydroxyl (18 %), resulting in the C1′-carbonyl being in close proximity to the β:Arg369 side chain. This makes the C2′-hydroxyl of DXL available to form a hydrogen bond with the β:Asp26 side chain (up to 52 %), which is also in position to interact with the N′–H of DXL (up to 49 %). There is no hydrogen bond between β:Asp26 and TXL. Neither β:Arg369 nor β:Asp26 form significant hydrogen bonds with CAB (Table D1), which are displaced by the N′ side chain of CAB when it is directed towards β:H1. Since the C2- and C3′-phenyl groups of CAB adopt a collapsed state, this alters the position of the C13 side chain in such a way that the C3′-t-butyl moiety is wedged between the C2′-hydroxyl and N′–H of CAB, and β:Asp26 and β:Arg369. Although β:Asp26 engages in water-mediated hydrogen bonds with CAB (9 %), it does so to a much lesser extent than with TXL (up to 22 %) and DXL (up to 18 %).

Additional notable hydrogen bonds between β:Thr276 and DXL occur, both direct (to the oxetane oxygen (16 %) or C7-hydroxyl (19 %) and water mediated (25 %). Interestingly, while β:Thr276 is evolutionarily conserved in all known human β-tubulin isotypes[188] and mutations to β:Thr276 are known to confer resistance to TXL, there are very few hydrogen bonds (direct or water-mediated) observed between β:Thr276 and TXL. This supports the views that β:Thr276 instead plays an important role in taxane binding to the intermediate binding site,[102] or by modifying (opening) the M-loop conformation.[203] In addition to its important role in π–π stacking interactions, β:His229 also forms hydrogen bonds with DXL (directly via N′-carbonyl, 49 %; water mediated, 10 %) and TXL (directly via N′-carbonyl, 5 %; water mediated, 16 %), but not with CAB–C2. β:Gln282 forms direct hydrogen bonds with the C9-carbonyl of DXL–C1 (up to 12 %) and CAB–C2 (up to 15 %), as well as the C7-methoxy of CAB–C2 (up to 12 %), but engages primarily in water-mediated hydrogen bonds with TXL (38 %). Several residues (β:Arg320, β:Arg329,β:Gly370, and β:Ser374) engage with the taxanes exclusively through water-mediated hydrogen bonds, which

are more common for DXL than TXL or CAB (Table D2).

Hydrogen bonds with β:Arg284 are only observed at the C9-carbonyl of the short-lived DXL–C2 species. This is in contrast to previous work that found β:Arg284 forms hydrogen bonds with the C10-methoxy of TXL, though these bonds were not found with DXL.[92] Given the transient nature of DXL–C2, hydrogen bonds with β:Arg284 are likely insignificant and do not play a direct role in the mechanism of taxane-induced stabilization of MTs considering that β:Arg284 interdimer hydrogen bonds are important in MT stability[265] and the taxane$\cdots\beta$:Arg284 hydrogen bonds would destabilize the MT lattice. It is worth pointing out that β:Arg284 is conserved across human β-tubulin isotopes[188] and mutations to this residue decrease MT stability.[196]

TXL and DXL (both DXL–C1 and DXL–C2) engage in many hydrogen bonds, both with polar residues and solvent (Tables D1–D3). Conversely, CAB does not engage in many intermolecular hydrogen bonds. Not only are solvent interactions greater for the N′-, C7- and C10-substituents of TXL and DXL compared to CAB, but greater solvation also occurs for TXL and DXL at unmodified positions like the C9-carbonyl, C1′-carbonyl, C2′-hydroxy and the N′-carbonyl (Table D3). This provides further support for the "hydrophobic collapse" of CAB.

The increased number of hydrogen bonds to DXL is reflected in the calculated binding free energy of interaction (Table D4), which is the strongest for DXL (for DXL–C1, -198.4 kJ mol^{-1}, Table D4). TXL also binds to tubulin strongly (-182.5 kJ mol^{-1}), while binding of CAB is much weaker (for CAB–C2, -151.6 kJ mol^{-1}). This is in qualitative agreement with DXL and TXL binding affinities reported in the literature.[115] Both DXL and CAB have similar ability to induce MT formation,[79] which is greater than the ability of TXL. *In vivo* cytotoxicity experiments find TXL superior in drug-sensitive cell lines while DXL and CAB are more effective in resistant cell lines, possibly due to differences in drug interactions with the P-glycoprotein efflux pump. Therefore, there is no correlation between binding affinity, and taxane-induced MT assembly or IC$_{50}$ values.

Although these binding free energies neglect entropy, they allow for the binding to be decomposed into pairwise per-residue contributions (Figure 5.4, Table D4). β:Asp26 and β:Arg369 have the largest contributions to DXL–C1 and TXL binding, respectively (up to -47 kJ mol^{-1}), while the strongest pairwise residue$\cdots$CAB–C2
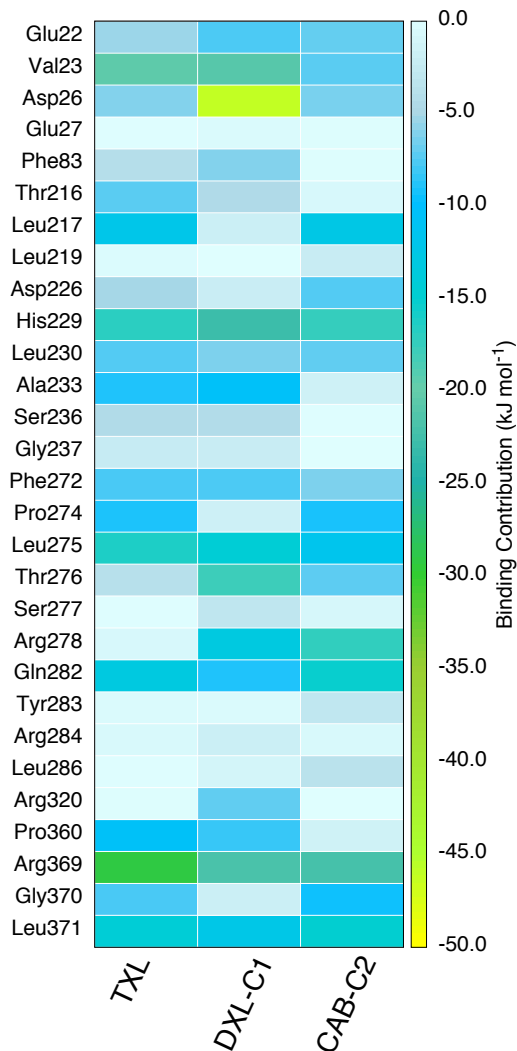
Figure 5.4: *MM/GBSA pairwise binding free energy (kJ mol^{-1}) between select binding-site residues and the taxanes. Calculated according to Equation 1.22, neglecting the entropy component. Data included in Table D4.*

interactions contribute to binding by -22 kJ mol^{-1}. It is worth noting that the conformers of DXL and CAB that dominate the simulation (DXL–C1 and CAB–C2) provide the most stable binding with $\alpha\beta$-tubulin (Table D4).

The binding of TXL and CAB to β-tubulin decreases flexibility of the M-loop, as evidenced by the smaller standard deviation in C$_\alpha$ RMSD (Figure 5.5), while DXL binding maintains the M-loop flexibility observed in apo tubulin. Coarse-grained studies of vibrational modes also found TXL reduced M-loop flexibility.[266] No significant changes in the helical character of the M-loop were observed upon taxane binding. Residues in the C-terminal portion of the M-loop (β:Tyr283 to β:Val288)

are closest to CAB, followed by DXL and then TXL. For CAB binding, the M-loop excludes solvent to directly contact the C7 and C10 substituents. The direction of the N′ side chain of CAB towards β:H1 moves the baccatin ring closer to the M-loop than what is observed for TXL (Figure 5.6 (a)), and pushes the M-loop out from tubulin. Conversely, the baccatin region of TXL and DXL–C1 is not as enveloped by the M-loop and is further from the baccatin ring of these drugs (Figure 5.6 (a, c)). This is supported by the hydrogen bond data (Tables D1–D3), where interactions between the baccatin ring and the M-loop are more direct for CAB than DXL and TXL (see β:Gln282, for example). Similar results regarding solvation have been observed for taxane analogues in the MT pore, where polar substituents at C7 and C10 interact with solvent and non-polar substituents interact with the protein.[117] Interestingly, the structure of DXL–C2 also has close contacts between the C7 and C10 substituents, and the M-loop.

Prior to taxane binding, the M-loop is in a contracted conformation at the taxane binding site. In this form, the M-loop does not have a significant energetic (hydrogen bond) contribution to the lateral contacts in a MT.[265] Upon binding, the M-loop side chains are displaced out from β-tubulin and towards the adjacent subunit to adopt a more expanded conformation (Figure 5.6 (b, c)). Given that these three taxanes affect the M-loop to varying degrees, this indicates that the common mechanism of action of the taxanes is not exerted through the M-loop, but rather through other factors. This finding support recent work suggesting lateral contacts play a passive role in MT stability and the energy contribution of lateral contact is constant in the presence and absence of TXL binding, whereas TXL binding increases longitudinal contacts and eases conformational strain.[31]

Although the above discussion and an experimentally-obtained TXL–MT structure[31] propose that the mechanism of action of the taxanes is not exerted through the M-loop stabilizing lateral contacts, the taxanes still have a structural effect on MTs through the M-loop. Lateral contacts in the MTs hold dimers apart.[31,267] While natural MTs contain 13 protofilaments, TXL binding decreases this number to 12, and DXL binding results in MTs with 13 or 14 protofilaments.[116] This has been related to the compression or expansion of the M-loop, where an expanded M-loop conformation results in a larger angle between protofilaments and fewer protofilaments in a MT.

Calculations show the largest M-loop expansion for TXL and a smaller expansion for CAB, while the M-loop in DXL-bound and apo tubulin have similar expansions (Figure 5.6 (b, c)). This supports the experimentally-observed decrease in protofilaments in TXL–MTs compared to DXL–MTs, and a similar number of protofilaments in DXL–MTs and apo MTs.[116] Previous studies considering many taxane analogues have implicated the size of C7 and C10 substituents in determining the M-loop expansion.[92,117] A correlation is found between the C10 substituent size and the M-loop expansion. However, the present work also implicates hydrophobicity as a factor, since this determines the proximity of the baccatin ring to the M-loop, where a movement of the CAB N′-substituent towards β:H1 (at the opposite end of the taxane from the M-loop) pushes CAB towards the M-loop and the loop away from tubulin.

5.3.2   Global effects of taxane binding

TXL has an allosteric effect on the $\alpha\beta$-tubulin heterodimers, and changes in both the α- and β-tubulin units have been identified upon TXL binding.[112] A recent cryo-EM structure of TXL bound to MTs has shown a change in longitudinal contacts and easing of strain relative to drug-free MTs.[31] Specifically, a translation of the α-tubulin intermediate domain (α:H6–H7 to the end of α:S10, residues 216–381) towards the (–) end of the MT lattice and away from the lumen is observed, as well as an expansion at the longitudinal interdimer contacts that reverses the compaction observed in MTs upon the hydrolysis of GTP to GDP. The computational heterodimer model sufficiently captures some of these effects, as discussed below.

5.3.2.1   Global changes to β-tubulin

In the β-tubulin subunit, changes in structure outside the taxane binding site can be isolated between the holo and apo forms of tubulin (Figures 5.5 and 5.7). Near the taxane binding site, β:H6–H7 and β:S9–H10 move towards the drug, while the M-loop and N-terminal end of β:H1 are displaced by taxane binding (Figure 1.8). Further from the binding site, there is a movement of the middle portion of β:H1–H1′ and β:H6 towards the drug. The flexibility of β:H1–H1′ decreases upon taxane binding (residues 27–46 in Figure 5.5, residues 27–48 in 1JFF numbering) and adopts greater helical character, with a larger effect for DXL and CAB than for TXL. Taxane binding
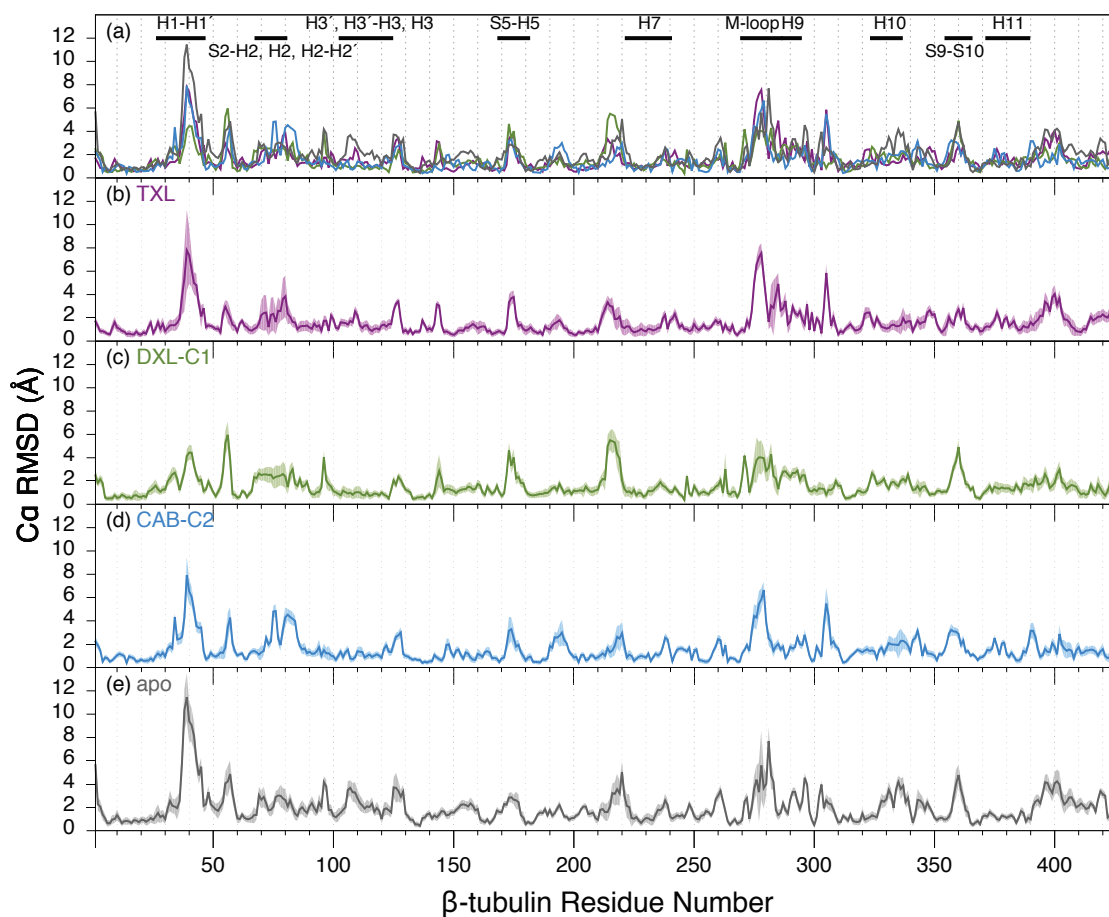
Figure 5.5: *The average mass-weighted RMSD of the C_α atoms for each β-tubulin residue, with the standard deviation shaded to indicate flexibility. (a) Superposition of all systems is shown, followed by (b) TXL–tubulin (purple), (c) DXL–tubulin (green), and (d) CAB–tubulin (blue) complexes, as well as (e) apo (grey) tubulin. Important secondary structures are indicated. The residues for the β-tubulin model are numbered consecutively. Therefore, residues 1–42 in the figure correspond to residues 1–42 in 1JFF, residues 43–358 in the figure correspond to residues 45–360 in 1JFF, and residues 359–427 in the figure correspond to residues 369–437 in 1JFF. Results for the different conformers are shown in Figure D8.*
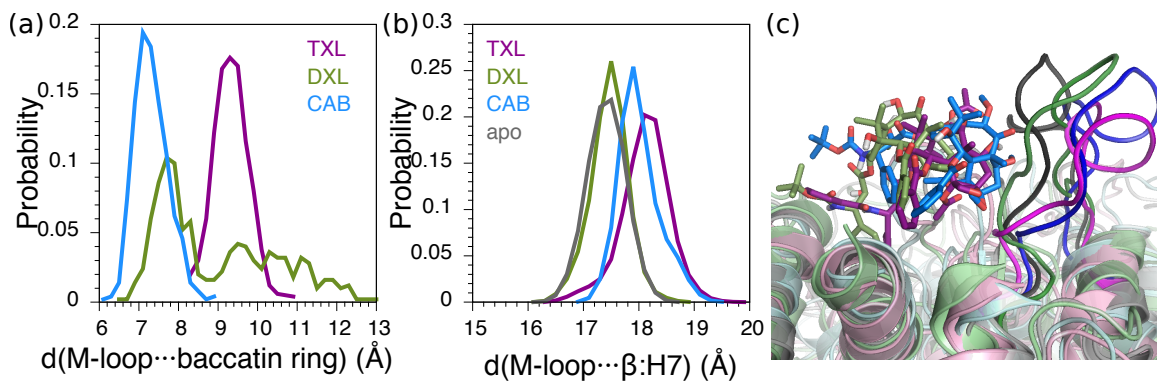
Figure 5.6: *The conformation of the M-loop for TXL- (purple), DXL-C1- (green), CAB–C2- (blue) and apo (grey) tubulin showing the distance between the M-loop, and (a) the baccatin ring and (b) β:H7, as well as (c) an illustration of the binding site with the M-loop highlighted. Distances are calculated with respect to the centres of mass (COM) of the indicated structures over the last 10 ns of the simulations.*

decreases flexibility in β:H3′, β:H3′–H3, β:H3 (residues 103–124 in Figure 5.5, residues 105–126 in 1JFF numbering), where DXL- and CAB-bound heterodimers have greater helical character than observed for TXL-bound and apo tubulin. In general, taxane binding induces greater helical character in many secondary structures of tubulin, including β:H7 and β:H10.

5.3.2.2 Global changes to α-tubulin and intermediate domain translation

Changes in α-tubulin occur upon taxane binding. Interestingly, previous computational work determined that conformational changes to α-tubulin upon GTP hydrolysis could not be found in a heterodimer model, but required an expanded model.[110] However, the present work shows that heterodimer models capture some of the allosteric changes that occur upon taxane binding to β-tubulin, and this may also be the case for the binding of other drugs to β-tubulin. Overall, larger fluctuations from the starting simulation structure are observed for α-tubulin than β-tubulin (Figure D2). Similar to β-tubulin, greater helical character is observed in the α subunit for α:H1–S2, α:H2, α:H5, α:H8, as well as for α:H3, α:H3–H3′, and α:H3′, which are oriented longitudinally along the α subunit to form a single large helix. The induction of greater helical character to both the α- and β-tubulin units may be related to the increasing experimental evidence[31,267,268] supporting the stiffening of protofilaments upon taxane binding. The extension of α:H1–S2 from α-tubulin is
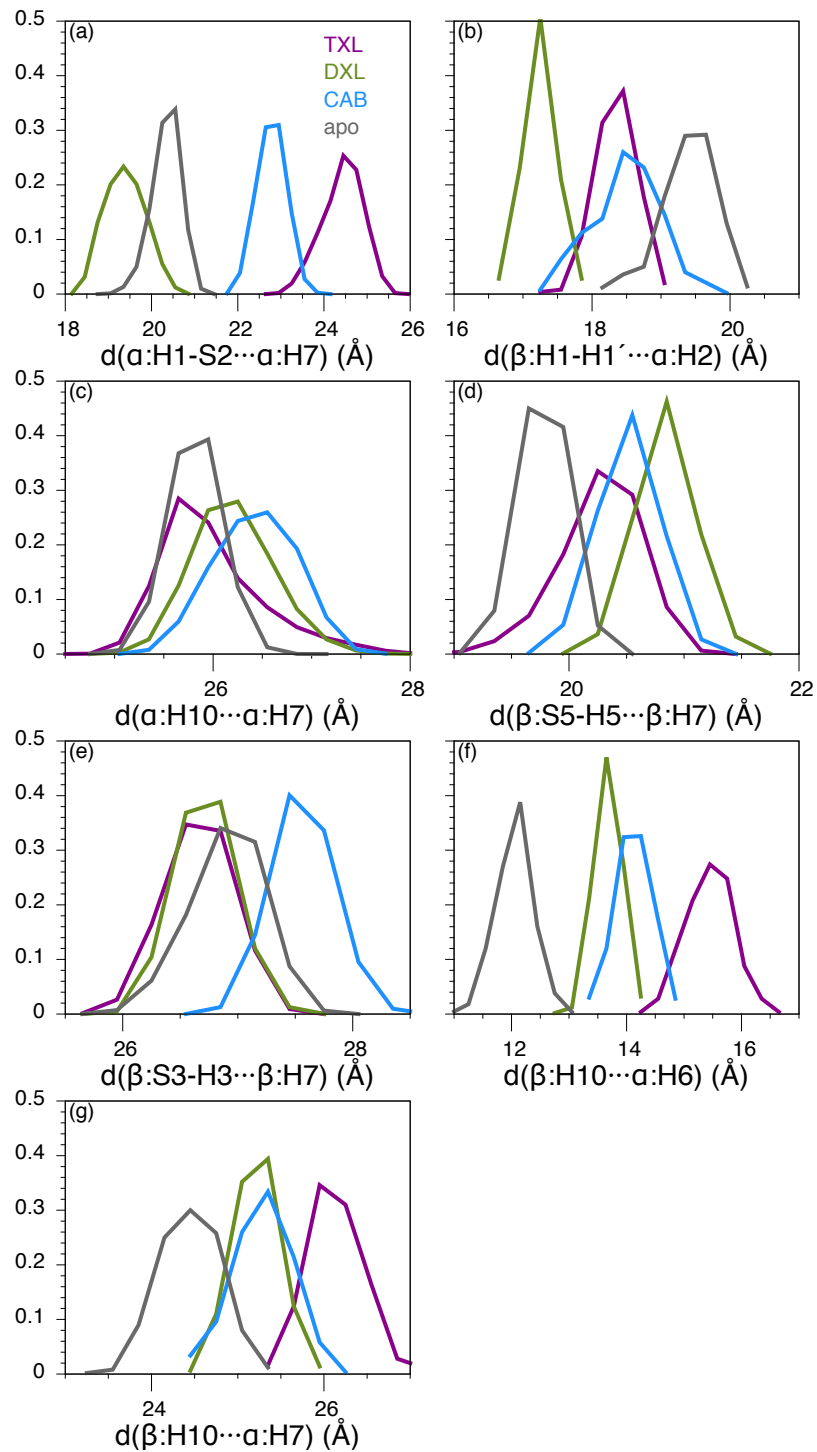
Figure 5.7: *A probability distribution of distances (Å) between important secondary structures in αβ-tubulin. Distances are calculated with respect to the centres of mass (COM) of the indicated structures over the last 10 ns of the simulations. The central helix, H7, was selected as the reference point. The colour legend is indicated in the figure.*

also affected, where both TXL and CAB binding result in a more extended conformation, while DXL binding has the opposite effect (Figures 5.7(a) and 5.8). This loop is particularly extended and flexible when TXL binds, which coincides with the loop being disordered and unresolved in the 1JFF crystal structure of TXL-tubulin zinc-induced antiparallel sheets.[36] The increased flexibility of α:H1–S2 upon TXL binding was verified as significant (rather than an artefact of the simulations or starting structure used) by running two additional simulations for TXL: (1) beginning the TXL–$\alpha\beta$-tubulin simulation from a different random seed, and (2) using the protein conformation generated at the end of the CAB–$\alpha\beta$-tubulin simulation and inserting TXL. Similar increases in flexibility of α:H1–S2 have been reported elsewhere for TXL-[266] and GTP-bound tubulin.[110] The extention of α:H1–S2 does not correlate with MT assembly, and therefore is not implicated in the mechanism of actions of the taxanes. This extension does, however, correlate with the extension of the M-loop, indicating that α:H1–S2 may also affect the interprotofilament angle and play a role in determining the number of protofilaments in a MT.

A translation of the α-tubulin intermediate domain is observed (Figure 5.9), similar to the translation[31] and rotation[110] of α-tubulin previously reported. The most significant shifts occur for α:H6, α:H7, and α:H8 as these structures move away from the lumen, with a greater shift observed for DXL, followed closely by CAB, and then TXL. The relative magnitudes of these shifts correlate with the increase in MT polymerization that occurs in the presence of these drugs and is supported by differences in solvation of α:H8, α:H8–S7, and α:S7 in MTs upon TXL binding as determined by HDX MS.[112] A less significant translation is visible for α:H10. In the same direction as this translation, α:H2 moves towards β-tubulin to decrease the distance between this secondary structure and β:H1–H1' (Figure 5.7 (b)), which indicates there is also an expansion at the intradimer interface upon taxane binding. The translation of the α-tubulin intermediate domain and movement of secondary structures at the intradimer interface may also be interpreted as a bend in the $\alpha\beta$-tubulin heterodimers. However, it is believed bending motions would be dampened by the confines of the MT lattice, and instead manifest as translations.[31]
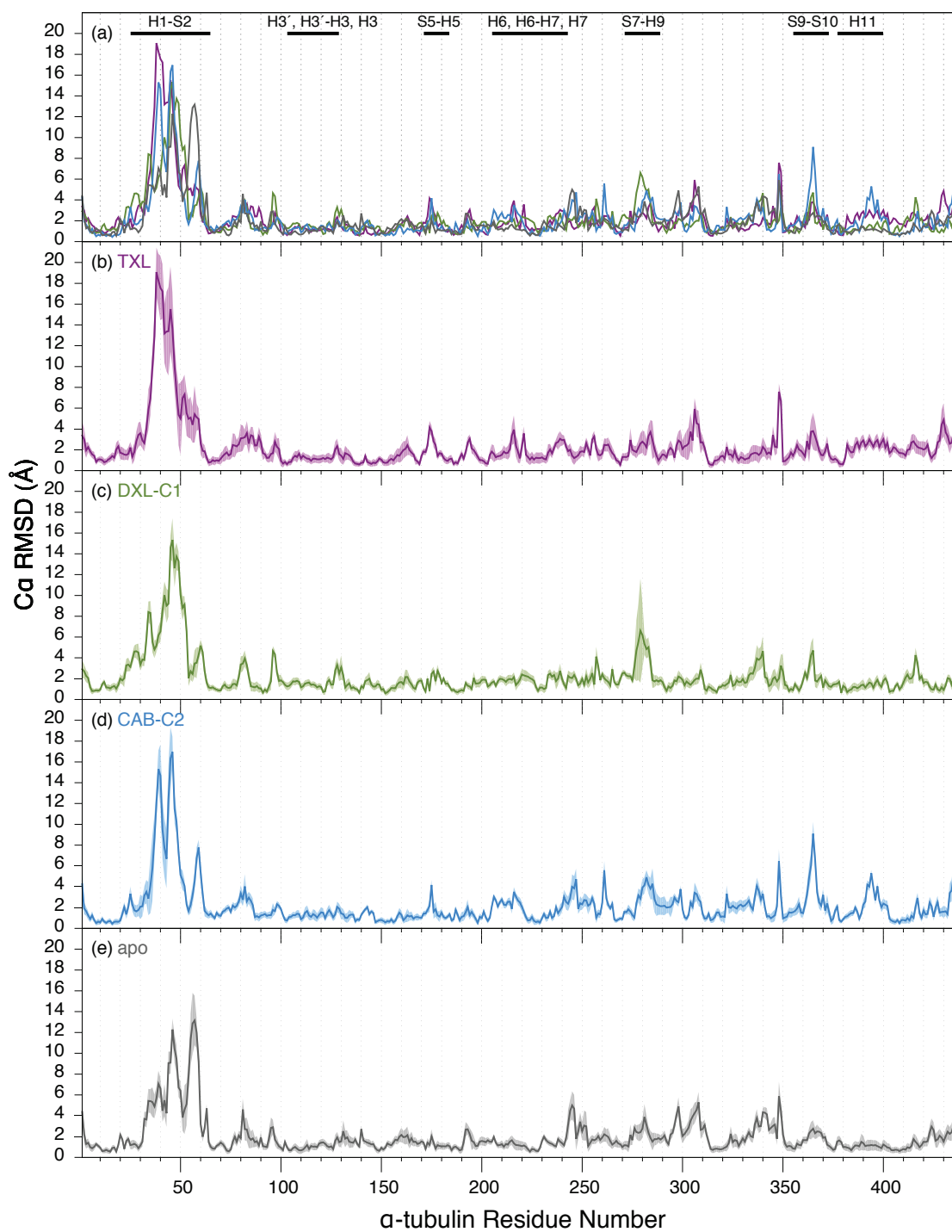
Figure 5.8: *The average mass-weighted RMSD of the C_α atoms for each α-tubulin residue, with the standard deviation shaded to indicate flexibility. (a) Superposition of all systems is shown, followed by (b) TXL–tubulin (purple), (c) DXL–tubulin (green), and (d) CAB–tubulin (blue) complexes, as well as (e) apo (grey) tubulin. Important secondary structures are indicated. Results for the different conformers are shown in Figure D9.*
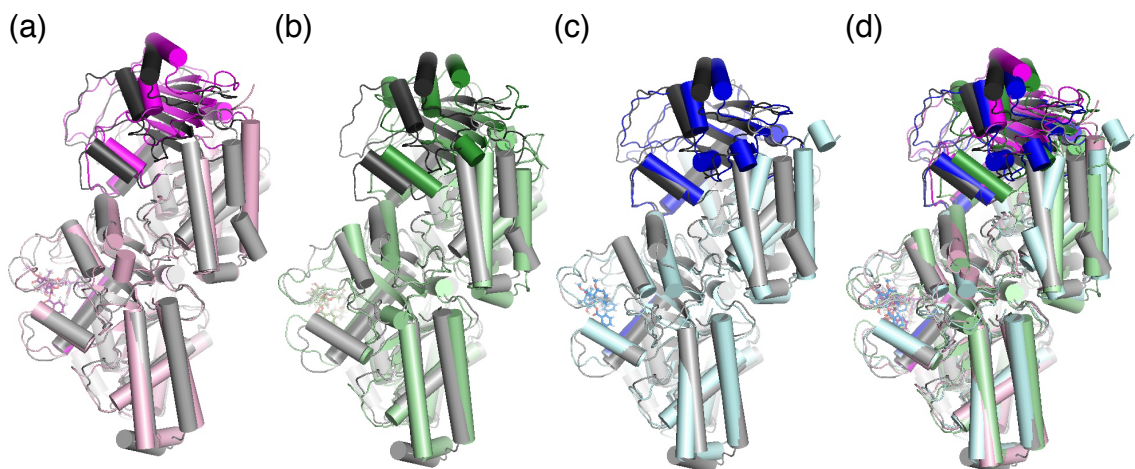
Figure 5.9: *The translation of the intermediate domain of α-tubulin, compared to apo (grey) αβ-tubulin, when αβ-tubulin is bound to (a) TXL (purple), (b) DXL (green) and (c) CAB (blue). A superposition of the β-tubulin unit (bottom) atoms of all four systems is shown in (d). The α-tubulin intermediate domain and β:H7 are highlighted. Structures taken from the end of the 47.5 ns simulations. The M-loop is directed outside of the plane of the page, with the taxane binding site and MT lumen on the left.*

5.3.2.3 Longitudinal expansion

Longitudinal expansions have been found to be more readily observed in heterodimer models, rather than extended protofilament models.[110] The small translation of α:H10 discussed above results in a movement of this helix away from α-tubulin (Figure 5.7 (c)), and corresponds to an expansion of the protein at the interdimer interface within a MT. An expansion of β:S5–H5 (β:T5) is also observed (Figure 5.7 (d)), in agreement with other studies,[31,110] though no expansion is observed for β:S3–H3′ (β:T3; Figure 5.7 (e)) as was reported by Alushin *et al.*[31] Interestingly, within a MT, β:S5–H5 forms longitudinal contacts with α:H10, α:H10–S9, and α:S9, which have the most substantial decrease in solvent exposure in MTs upon TXL binding.[112] The observed shifts in protein secondary structure provide further support for the importance of these secondary structures in enhancing MT stability upon taxane binding. Taxane binding also moves β:H11, β:H11′, and β:H12, as previously reported.[31]

5.3.2.4 The allosteric effect on $\alpha\beta$-tubulin heterodimers

With MT binding agents, allosteric effects are known to play a role in altering the stability of MTs. However, it is unclear how the binding of a taxane to β-tubulin results in allosteric changes to α-tubulin. The results of these MD simulations allow for the effect of taxane binding to be traced across the tubulin heterodimer. Two distinct pathways are observed (Figure 5.10).

In the first pathway, taxane binding results in a movement of β:S9–S10 towards the taxane. This loop interacts with portions of the C13 side chain, and is also in close proximity to the C7 and C10 positions, making its conformation sensitive to modifications at each of these positions. Decreases in β:S9–S10 flexibility upon TXL binding have been reported.[266] Changes in β:S9–S10 disrupt β:S8–H10 (near α:H6 and α:H7), β:H9, and β:H10 (near α:H6, α:H6–H7, and α:H7). Further, the N-terminal end of β:H10 moves towards the intradimer interface to disrupt the α-tubulin intermediate domain, and also becomes more helical. As a result, α:H6 and α:H7 and other secondary structures in α-tubulin are moved away from the lumen and β:H10 (Figure 5.7 (f, g)) to create an overall translation of the α-tubulin intermediate domain. Interestingly, the movements of β:H9 and β:H10 towards the intradimer interface coincide with the greatest change (decrease) in solvent exposure in MTs upon TXL binding, as observed in HDX MS studies.[112] It is important to note that the site that binds LLM and Pel A is in contact with β:H9 and β:H10,[1,52,142] indicating that both taxanes and LLM/Pel A may stabilize MT through these secondary structures. In support of this, the results in Chapter 3 showed LLM binding displaces β:H10 towards α-tubulin.

The second pathway begins with the C13 side chain interacting with the C-terminal region of β:H1. Residues of β:H1 are displaced towards the intradimer interface by the C13 side chain of the taxane. The degree of this displacement varies depending on the nature of the side chain and the conformation of the drug. For DXL, β:Asp26 forms a hydrogen bond with the C2′-hydroxyl and N′–H to displace these residues. When CAB binds, the collapsed structure causes the C13 side chain to bend away from the lumen and towards β:H1. Alternatively, TXL binding causes the N′-phenyl group to displace residues on β:H1. The importance of β:H1 is supported by mutations to
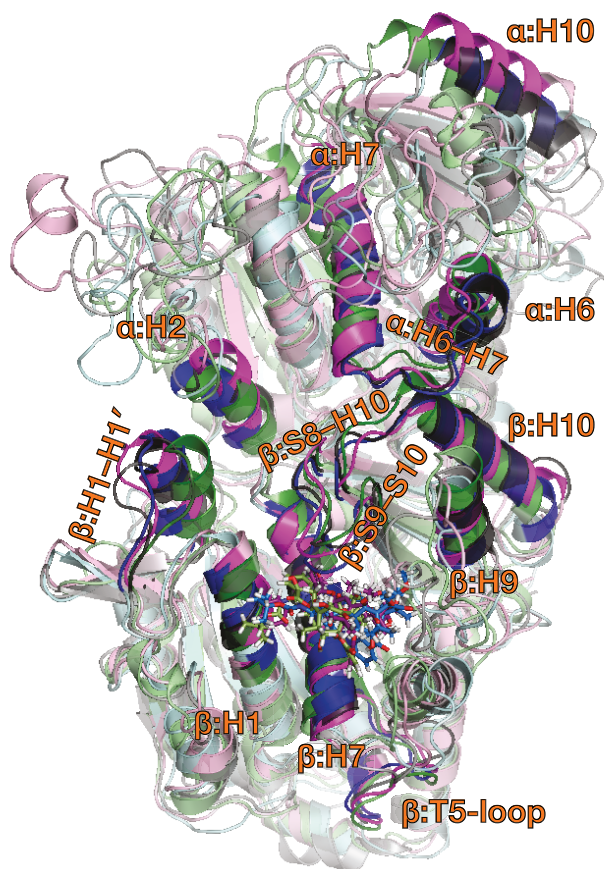
Figure 5.10: *An overlay of the coordinates of holo (TXL (purple), DXL (green), CAB (blue)) and apo (grey) tubulin, highlighting various structures proposed to be responsible for the allosteric changes in α-tubulin.*

β:Asp26 in yew tree tubulin.[204] Regardless of the mechanism of β:H1 displacement, the central portion of β:H1–H1′ moves towards the taxane, where decreases in flexibility of this structure have been reported for TXL binding,[266] while the C-terminal end of β:H1–H1′ moves towards the intradimer interface and α-tubulin. This results in a decreased distance between this structure and α:H2 (Figure 5.7 (b)), coinciding with the movement of the α-tubulin subunit away from the lumen as observed for the translation described above.

5.4 Conclusions

Using MD simulations, atomic-level insight was gained into the effect of the three clinically-approved taxanes, paclitaxel, docetaxel and cabazitaxel, on the $\alpha\beta$-tubulin

heterodimer. Both paclitaxel and docetaxel were found to adopt a conformation similar to the T-Taxol conformation previously reported, while cabazitaxel adopts a collapsed structure, despite docetaxel and cabazitaxel having the same C13 side chain. Both paclitaxel and docetaxel interact with the protein via hydrogen bonds, while cabazitaxel does not. Both β:Asp26 and β:Arg369 engage in significant hydrogen bonds with paclitaxel and docetaxel, and have significant contributions to their binding. Although docetaxel and cabazitaxel exhibit tubulin assembly effects superior to paclitaxel, cabazitaxel has substantially weaker binding to tubulin. These taxanes also have variable effects on the M-loop and lateral interactions. Therefore, in the case of the taxanes, binding affinity and the enhancement of lateral contacts do not correlate with assembly power or IC_{50}. Despite these differences, all three agents: (1) effectively stabilize MTs to alter MT dynamics and (2) are clinically approved.

The MD simulations detailed in this Chapter have shown that taxane binding not only affects β-tubulin where the binding site resides, but also α-tubulin. The results of Alushin et $al.$ have been confirmed,[31] where the simulations have shown translations of the α-tubulin intermediate domain and expansions of the interdimer interface upon taxane binding to increase longitudinal interactions. In addition, an increase in helical character in both α- and β-tubulin was observed that is related to a stiffening of protofilaments upon taxane binding. Structural changes in the intradimer interface that occur upon taxane binding were also identified. It is proposed that β:H1–H1′, β:H9, and β:H10 are of particular importance in transferring the effect of taxane binding in β-tubulin to an allosteric effect in α-tubulin. Both β:H9 andβ:H10 are also directly involved in binding at the LLM/Pel A binding site. Therefore, future studies examining novel taxane analogues should consider the effect that the drug candidate has on β:H9 and β:H10 as a predictive indicator for the ability of the drug to promote MT formation.

Alushin et $al.$ concluded that the mechanisms of MT-stabilizing agents should be examined in a MT-like environment.[31] However, even using the relatively small model reported in this paper, important effects were observed in the tubulin heterodimer that correlate with those observed experimentally in the MT lattice.[31] This indicates that models consisting of a single heterodimer may be capable of capturing important local and allosteric effects of taxane binding, and that computationally-efficient preliminary

studies examining drug candidates binding to the taxane binding site may still utilize this limited-size model, which may serve as a basis for future large-model studies.

Chapter 6

The Fragment Molecular Orbital method and understanding monomer polarization[*]

6.1 Introduction

The Fragment Molecular Orbital (FMO) method facilitates the application of quantum methods to large systems. However, before applying the FMO method to study ligand–protein interaction, it is important to develop an understanding of how this method works on small systems. Of particular interest is understanding the polarization of fragments by their surroundings through the monomer SCF, and how the FMO method for evaluating interaction energies differs from other approaches.

Noncovalent interactions are important contributors to the structure and stability of molecular complexes, such as ligand–protein assemblies. However, accurate determination of these interactions within large assemblies presents a computational challenge, particularly with *ab initio* methods.[269,270] Approaches such as the FMO method have been developed to perform accurate computations on macromolecules by structurally decomposing large assemblies into computationally-manageable fragments,[214] and is discussed in Section 1.3.2.1. This method has been successfully applied to a variety of problems,[217,270] including the investigation of protein mutations in a system containing over 36 000 atoms.[271] Given its promise and applications in the literature, it is important to understand how the FMO method varies from other approaches of quantifying noncovalent interactions, before applying the FMO

method to study noncovalent interactions in large molecular systems.

The supermolecular approach is the most popular for examining the strength of noncovalent interactions in small systems, where the interaction energy is calculated as the difference in energy between the complex and its constituents.[272] This approach may even be extended to calculate many-body interactions. For example, in a simple tetramer not only can the total interaction energy be calculated, but also two-, three- and four-body contributions, allowing additivity to be investigated. However, with such an approach, effects like monomer polarization are implicitly included in the interaction energy, rather than explicitly calculated.[217]

The FMO method has two advantageous features in regard to noncovalent interactions: (1) the ability to study noncovalent interactions in large molecular systems; and (2) the explicit calculation of monomer polarization. Therefore, the goal of this study is to understand the role monomer polarization plays in noncovalent interactions and how FMO results differ from those obtained using a supermolecular approach. This will allow the FMO method to be applied with confidence in studies that examine noncovalent interactions in ligand–protein systems, or other macromolecules.

This Chapter applies the FMO method to quantify π–π interactions in benzene systems. The benzene geometries of interest have been previously studied in the literature.[273–275] In addition, these molecular clusters are noncovalently bound and therefore do not require the fragmentation of bonds, which will allow the interactions to also be evaluated using a supermolecular approach. Furthermore, it is expected that the benzene monomers will experience little polarization from the surrounding benzene molecules since the electrostatic component of these interactions is small.[276] Results from these test systems provide a measure of the minimum polarization one may expect in noncovalently-bound systems. Ultimately, the present work will offer insight into the effect of monomer polarization within larger systems, as well as an enhanced understanding of the FMO method.

6.2 Computational Details

Structures of the benzene-containing dimers, trimers, and tetramers were obtained from the literature.[273,274] For brevity, the dimer geometries in this work have been
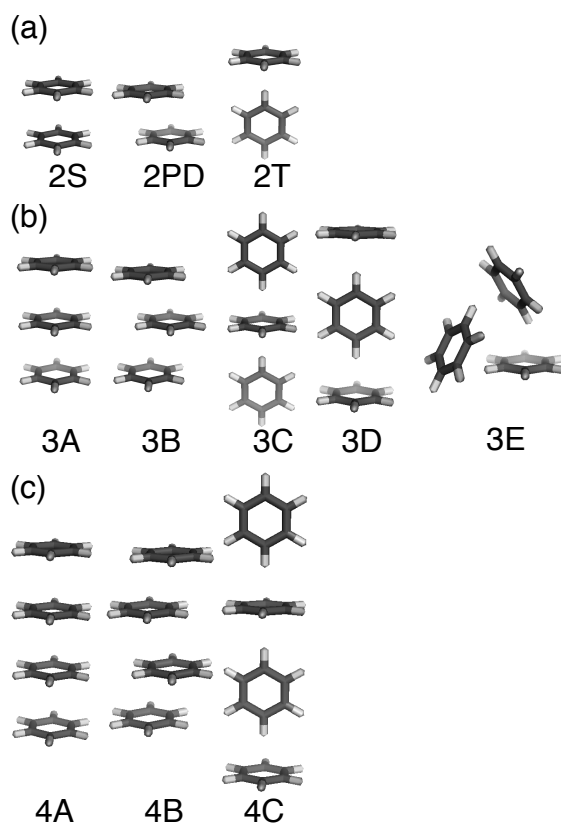
Figure 6.1: *Geometry and naming of the benzene (a) dimers, (b) trimers, and (c) tetramers, where fragments are numbered from top to bottom.*

renamed from those of Sinnokrot *et al.*[273] according to the following: 2S = dimer S; 2PD = dimer PD; 2T = dimer T. Similarly, the trimer and tetramer geometries in this work have been renamed from Tauer *et al.*:[274] 3A = trimer S; 3B = trimer D; 3C = trimer T2; 3D = trimer T1; 3E = trimer C; 4A = tetramer S; 4B = tetramer PD; 4C = tetramer T.

Binding energies were first evaluated at MP2/6-31G(d,p) using a supermolecular approach for an M-body system (ΔE^{sup}):

$$\Delta E^{sup} = E(M) - \sum_{i=1}^{M} E_i \tag{6.1}$$

where $E(M)$ is the energy of the M-body system and E_i is the energy of an isolated monomer.

Interaction energies were also evaluated with the FMO method at the MP2/6-31G(d,p) level of theory, designated FMO-MP2/6-31G(d,p). This comparative study examines the ability of FMO-MP2 to reproduce MP2 energies with the same basis set. Although it is well known that MP2/6-31G(d,p) is not the most accurate approach for calculating π–π interaction energies,[269] this method was chosen with the ultimate goal of studying ligand–protein interactions, where a balance between computational efficiency and accuracy will be necessary.

As discussed in Section 1.3.2.1, the FMO method calculates fragment energies self-consistently in a Coulomb field generated by surrounding fragments to create a converged electrostatic potential, such that each fragment is polarized by its environment.[214] The polarization is the sum of both destabilizing (due to mutual polarization) and stabilizing (due to electrostatic interactions between polarized charge distributions) components. However, in molecular clusters, the stabilizing component is equal to the negative of two times the destabilizing component, resulting in the total polarization being related to the negative of the destabilization component.[219] Therefore, polarization discussed in the present work refers to only the destabilization component. Subsequently, interfragment interactions are calculated and added to the polarized monomer energies to obtain the total energy of the M-body system, E^{FMO}. In this Chapter, FMO2 (E^{FMO2}) and FMO3 (E^{FMO3}) energies are evaluated.

Interaction energies were evaluated from the FMO-calculated energy of the system

in two ways, which differ subtly in their interpretation. In one case, binding was evaluated with respect to the isolated monomers in their free states:[222]

$$\Delta E^{FMO} = E^{FMO} - \sum_{i=1}^{M} E_i \qquad (6.2)$$

This energy represents the change in stability of the isolated monomers upon complex formation and is similar to the supermolecular approach in Equation 6.1. Alternatively, interaction energies were evaluated with respect to the polarized monomers:

$$\Delta E'^{FMO} = E^{FMO} - \sum_{i=1}^{M} E_i' \qquad (6.3)$$

This represents the interaction between monomers within their current environment, and it is this quantity that is reported by the FMO method in the GAMESS package. Equation 6.3 is analogous to Equations 1.11 and 1.16.

The FMO2 results were further probed by examining the various contributions to the interaction energies using the Pair Interaction Energy Decomposition Analysis (PIEDA) scheme, which decomposes $\Delta E_{ij}'^{FMO2}$ for monomers i and j (also Equation 1.17):

$$\Delta E_{ij}'^{FMO2} = \Delta E_{ij}'^{ES} + \Delta E_{ij}'^{EX} + \Delta E_{ij}'^{DI} + \Delta E_{ij}'^{CT+mix} \qquad (6.4)$$

The default implementation of FMO employs approximations for calculating interfragment interaction energies.[214,217–219] For fragments that are spatially separated, terms describing the electrostatic potential of the environment may be described using Mulliken atomic orbital populations and Mulliken charges, and dimer interactions may be approximated with an electrostatic interaction. The FMO calculations in this Chapter are performed both with (ΔE_{approx}^{FMO}, $\Delta E_{approx}'^{FMO}$) and without (ΔE_{full}^{FMO}, $\Delta E_{full}'^{FMO}$) these approximations. Specifically, approximations corresponding to the RESPPC, RESDIM and RCORSD keywords were disabled, as well as RITRIM for FMO3 calculations.[217] All calculations were performed using the FMO code[214] in the GAMESS-US (Version October 2010 R1) program.[220] The program Facio was used to prepare input files and analyze output.[277,278]

Table 6.1: *MP2/6-31G(d,p) benzene dimer interaction energies (kJ mol^{-1}).*

	Dimer[a]		
	2S	2PD	2T
ΔE^{sup}[b]	-9.8	-14.3	-13.7
ΔE^{FMO2}_{approx} [c,d]	-9.8	-14.3	-13.7
$\Delta E'^{FMO2}_{approx}$ [c,e]	-8.4	-14.5	-15.1
ΔE^{FMO2}_{full} [d,f]	-9.8	-14.3	-13.7
$\Delta E'^{FMO2}_{full}$ [e,f]	-8.4	-14.5	-15.1

[a] Geometries shown in Figure 6.1.;   [b] Calculated according to Equation 6.1.;
[c] FMO results with default approximations.;
[d] Calculated with respect to isolated monomers according to Equation 6.2.;
[e] Calculated with respect to polarized monomers according to Equation 6.3.;
[f] FMO results obtained without approximations.

6.3   Results and Discussion

6.3.1   Benzene dimers

Initially, benzene-containing dimers were considered. FMO2 will provide exact results for dimer systems since pairwise interactions are the only many-body interactions that exist in dimers. The interactions energies are calculated with the supermolecular approach and FMO2 (with and without approximations) in Table 6.1 (ΔE^{sup}, ΔE^{FMO2}_{approx}, and ΔE^{FMO2}_{full}). The small interfragment distances in the benzene dimers are within the cutoffs for the FMO method, and therefore the interaction is explicitly evaluated and the implementation of approximations has no effect for these systems. Table 6.1 shows identical results from the supermolecular approach and FMO, indicating FMO2 provides exact MP2/6-31G(d,p) energies for these systems.

The FMO treatment of the benzene dimers reveals small polarization of the monomers ($<$ 1 kJ mol^{-1}, Table E1). Therefore, the binding energies calculated with respect to the polarized monomers ($\Delta E'^{FMO2}_{approx}$ and $\Delta E'^{FMO2}_{full}$) differ slightly compared to that calculated with respect to the isolated monomers (ΔE^{FMO2}_{approx} and ΔE^{FMO2}_{full}). This originates from whether monomer polarization is included in the reported binding energy. For example, calculations for dimer 2T show $\Delta E^{FMO2}=$ -13.7 kJ mol^{-1} and $\Delta E'^{FMO2}=$ -15.1 kJ mol^{-1} with a difference of -1.4 kJ mol^{-1}. However, Fragment 1 is polarized (destabilized) by 0.55 kJ mol^{-1} while Fragment 2

is polarized (destabilized) by 0.92 kJ mol^{-1} (Table E1), for a total monomer desta-bilization of 1.47 kJ mol^{-1}. Therefore, binding energies calculated with respect to isolated monomers (ΔE^{sup} and ΔE^{FMO2}) inherently include the energy difference re-sulting from monomer polarization, whereas binding energies calculated with respect to the polarized monomers ($\Delta E'^{FMO2}$) do not. These results for dimers clearly show the relationship between binding energies calculated with respect to isolated (ΔE^{sup} and ΔE^{FMO2}) and polarized ($\Delta E'^{FMO2}$) monomers. It should be noted that it is $\Delta E'^{FMO2}$ that is reported in the output for FMO calculations in GAMESS.

6.3.2 Benzene trimers

Next, benzene trimers were considered (Table 6.2). For such systems, FMO3 provides exact energies since it includes three-body interactions. This is illustrated in the binding results for FMO3 with respect to isolated monomers (ΔE^{FMO3}_{approx} and ΔE^{FMO3}_{full}) and the supermolecular approach (ΔE^{sup}), where minor discrepancies (< 1 kJ mol^{-1}) may be attributed to tighter convergence in FMO than in *ab initio* calculations. Small differences exist between the FMO2 energies and the MP2/6-31G(d,p) energies (up to 0.6 kJ mol^{-1}), where the use of approximations further increases these deviations (up to 1.1 kJ mol^{-1}). Unlike the dimers systems, the distances between non-nearest neighbour fragments (Fragments 1 and 3) in trimers 3A to 3D (Figure 6.1) fall outside the implemented cutoffs. The use of approximations leads to minimal deviations between ΔE^{FMO}_{full} and ΔE^{FMO}_{approx}, which are slightly larger for FMO2 than FMO3 (0.6 kJ mol^{-1} and 0.2 kJ mol^{-1}, respectively).

Within the benzene trimers, monomer polarization is as large as 2 kJ mol^{-1} in magnitude, which is greater than that observed for fragments within the dimers (Ta-ble E1). Larger polarization is observed for the middle fragment (Fragment 2, Ta-ble E1) in structures 3A–3D, which is engaged in two nearest-neighbour interactions. The largest polarizations are observed for 3E (Table E1), which is the only true three-body system (i.e. each monomer has two nearest-neighbour contacts). These results illustrate that the number of nearest-neighbour monomers influences the magnitude of the calculated monomer polarization.

Because polarization is present, differences arise between $\Delta E'^{FMO}_{full}$ and ΔE^{FMO}_{full}. For example, results for 3E show a difference in binding energy of 6.2 kJ mol^{-1} depend-

Table 6.2: *MP2/6-31G(d,p) benzene trimer interaction energies (kJ mol^{-1}).*

	Trimers[a]				
	3A	3B	3C	3D	3E
ΔE^{sup} [b]	-19.7	-29.4	-27.5	-26.9	-43.5
ΔE^{FMO2}_{approx} [c,d]	-19.3	-28.3	-26.9	-26.9	-43.2
$\Delta E'^{FMO2}_{approx}$ [c,e]	-16.4	-28.8	-29.6	-29.2	-49.2
ΔE^{FMO2}_{full} [d,f]	-19.6	-28.8	-27.1	-26.9	-43.2
$\Delta E'^{FMO2}_{full}$ [e,f]	-16.7	-29.4	-29.8	-29.2	-49.2
ΔE^{FMO3}_{approx} [c,d]	-19.6	-29.3	-27.5	-27.0	-43.4
$\Delta E'^{FMO3}_{approx}$ [c,e]	-16.7	-30.0	-30.2	-29.3	-49.4
ΔE^{FMO3}_{full} [d,f]	-19.8	-29.3	-27.5	-27.0	-43.4
$\Delta E'^{FMO3}_{full}$ [e,f]	-16.9	-30.0	-30.2	-29.3	-49.4

[a] Geometries shown in Figure 6.1.;   [b] Calculated according to Equation 6.1.;
[c] FMO results obtained with default approximations.;
[d] Calculated with respect to isolated monomers according to Equation 6.2.;
[e] Calculated with respect to polarized monomers according to Equation 6.3.;
[f] FMO results obtained without approximations.

ing on which monomer energies are used (ΔE^{FMO3} = -43.2 kJ mol^{-1} vs. $\Delta E'^{FMO3}$ = -49.4 kJ mol^{-1}, Table 6.2). This difference can be explained by the fragment polarization, which has a destabilizing effect of 2.0 kJ mol^{-1} for each monomer (Table E1). This indicates that the discrepancy between binding energies calculated with respect to isolated and polarized monomers increases with system size.

6.3.3 Benzene tetramers

In benzene tetramers, neither FMO2 nor FMO3 fully include the many-body interactions in these systems (Table 6.3). Comparing the FMO results calculated with respect to the isolated monomers (ΔE_{full}^{FMO2} and ΔE_{full}^{FMO3}) to the supermolecular binding energies (ΔE^{sup}) shows that the FMO2 results deviate (up to 0.5 kJ mol^{-1}) and can be improved by FMO3 (deviations up to 0.1 kJ mol^{-1}). The use of approximations tends to worsen results, with greater disagreement between ΔE_{full}^{FMO} and ΔE_{approx}^{FMO} being observed for FMO2 (deviations up to 2.3 kJ mol^{-1}) than FMO3 (deviations up to 0.3 kJ mol^{-1}).

The results for the benzene tetramers again illustrate that fragment polarization increases with system size. As observed for the trimers, the middle fragments (Fragments 2 and 3, Table E1) experience greater polarization, while the outer fragments are less affected. However, a comparison of monomer polarization between trimers and tetramers reveals a given fragment is most affected by the presence of a nearest neighbour, and less affected by next-nearest-neighbour fragments. For example, identical intermonomer geometries exist within trimer 3A and tetramer 4A. Within 3A, Fragment 2 is polarized by -1.4 kJ mol^{-1} from two nearest-neighbour fragments (Fragments 1 and 3). In comparison, within 4A, Fragment 2 is also polarized by -1.4 kJ mol^{-1}, but in the presence of two nearest-neighbour fragments (Fragments 1 and 3) and a next-nearest-neighbour fragment (Fragment 4). Therefore, a next-nearest-neighbour monomer has little influence on monomer polarization within these systems.

The tetramer binding energies differ depending on whether they are calculated with respect to isolated or polarized monomer energies. The differences reach 4.4 kJ mol^{-1}, reflecting the increased polarization of fragments within a tetramer. This discrepancy between binding energies calculated with respect to isolated and

Table 6.3: *MP2/6-31G(d,p) benzene tetramer interaction energies (kJ mol^{-1}).*

	Tetramer[a]		
	4A	4B	4C
ΔE^{sup}[b]	-29.6	-44.6	-40.9
ΔE^{FMO2}_{approx} [c,d]	-28.7	-42.3	-40.2
$\Delta E'^{FMO2}_{approx}$ [c,e]	-24.3	-43.2	-43.8
ΔE^{FMO2}_{full} [d,f]	-29.4	-43.5	-40.4
$\Delta E'^{FMO2}_{full}$ [e,f]	-25.0	-44.4	-44.1
ΔE^{FMO3}_{approx} [c,d]	-29.3	-44.4	-40.9
$\Delta E'^{FMO3}_{approx}$ [c,e]	-24.9	-45.4	-44.5
ΔE^{FMO3}_{full} [d,f]	-29.7	-44.5	-40.9
$\Delta E'^{FMO3}_{full}$ [e,f]	-25.3	-45.4	-44.5

[a] Geometries shown in Figure 6.1.;   [b] Calculated according to Equation 6.1.;
[c] FMO results obtained with default approximations.;
[d] Calculated with respect to isolated monomers according to Equation 6.2.;
[e] Calculated with respect to polarized monomers according to Equation 6.3.;
[f] FMO results obtained without approximations.
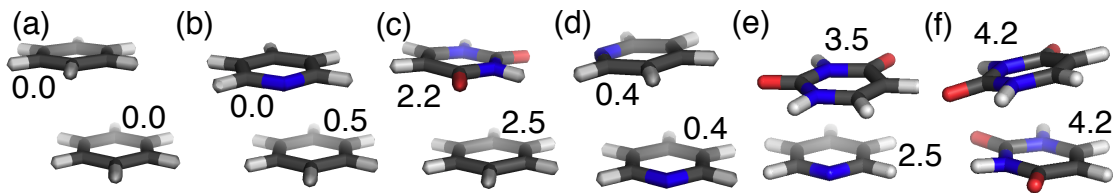
Figure 6.2: *A selection from the S66 database containing π–π interactions, including (a) benzene–benzene, (b) benzene–pyridine, (c) benzene–uracil, (d) pyridine–pyridine, (e) pyridine–uracil, and (f) uracil–uracil dimers. The FMO-calculated change in monomer energy upon polarization (kJ mol^{-1}) is indicated next to each monomer.*

polarized monomers increases with system size for two reasons: (1) as the number of nearest-neighbour contacts increases the magnitude of fragment polarization increases; and (2) as the number of polarizable fragments that contribute to the binding energy increases, the deviations can accumulate.

6.3.4 The S66 database and the effect of larger electrostatic contributions

The systematic study of the benzene-containing systems detailed above illustrates the effect of fragment polarization on binding energies for systems of increasing size in which the electrostatic components are small. However, similar effects on fragment polarization will also be observed for systems with larger electrostatic components, which will lead to discrepancies in the calculation of binding between either ΔE^{sup} or ΔE^{FMO}, and $\Delta E'^{FMO}$. Therefore, in addition to the above systems, a subset of the S66 database[279] was chosen to consider interactions with larger electrostatic contributions. Specifically, interactions in π–π dimers containing: (1) benzene–benzene, (2) benzene–pyridine, (3) benzene–uracil, (4) pyridine–pyridine, (5) pyridine–uracil, and (6) uracil–uracil were evaluated at their equilibrium geometries (Figure 6.2).[279] Although this test set also contains a stacked benzene–benzene dimer (Figure 6.2), its geometry differs from that of 2S (Figure 6.1). Differences between the electrostatic contribution to the interactions ($\Delta E'^{ES}$) for the benzene systems and the S66 subset can be found in the PIEDA results (Figures E2 and E3, Tables E2 and E3).

As found for the benzene dimers above, the calculated interaction energies of the S66 subset with respect to the isolated monomers (Table 6.4) show that the same en-

Table 6.4: *MP2/6-31G(d,p) dimer interaction energies (kJ mol^{-1}) of a select subset of the S66 database.*

	Subset of the S66 Database[a]					
	benzene–benzene	benzene–pyridine	benzene–uracil	pyridine–pyridine	pyridine–uracil	uracil–uracil
ΔE^{sup}[b]	-14.0	-17.3	-27.6	-20.1	-32.3	-46.9
ΔE^{FMO2}_{approx} [c,d]	-14.0	-17.3	-27.6	-20.1	-32.3	-46.9
$\Delta E'^{FMO2}_{approx}$ [c,e]	-13.9	-17.8	-32.4	-20.8	-38.2	-55.4
ΔE^{FMO2}_{full} [d,f]	-14.0	-17.3	-27.6	-20.1	-32.3	-46.9
$\Delta E'^{FMO2}_{full}$ [e,f]	-13.9	-17.8	-32.4	-20.8	-38.2	-55.4

[a] Geometries shown in Figure 6.2.; [b] Calculated according to Equation 6.1.;
[c] FMO results obtained with default approximations.;
[d] Calculated with respect to isolated monomers according to Equation 6.2.;
[e] Calculated with respect to polarized monomers according to Equation 6.3.;
[f] FMO results obtained without approximations.

ergy is obtained from both FMO2-MP2 and MP2, and approximations are not invoked for these small systems since interfragment distances are within the defined cutoffs. However, larger discrepancies are found when interaction energies are evaluated with respect to isolated (ΔE^{FMO2}) and polarized ($\Delta E'^{FMO}$) monomers than observed for the systems in Figure 6.1. These discrepancies range from 0.0 kJ mol^{-1} for the benzene–benzene dimer, up to 8.4 kJ mol^{-1} for the uracil–uracil dimer. Monomer polarization is greatest for the uracil homodimer (Figure 6.2(e)). These results illustrate that monomer polarization and discrepancies in binding energies will also increase in magnitude as the electrostatic contribution to the interaction increases.

6.4 Conclusions

This Chapter examined the π–π interaction energies of benzene-containing dimers, trimers, and tetramers, as well as a subset of the S66 database using both a supermolecular approach and the Fragment Molecular Orbital method. Results show that both MP2/6-31G(d,p) and FMO-MP2/6-31G(d,p) predict nearly identical absolute energies for the systems considered. Deviations may occur depending on whether the calculation of binding energies is performed with respect to isolated (ΔE^{FMO})

or polarized ($\Delta E'^{FMO}$) monomers. Deviations between these two values tend to increase as the number of monomers increases and the electrostatic contribution to the interactions increases. Therefore, caution is suggested in the direct comparison of binding energies reported in the FMO output in GAMESS ($\Delta E'^{FMO}$) and those calculated with respect to isolated monomers (ΔE^{FMO} or ΔE^{sup}). This is especially true for systems that are large and/or have substantial electrostatic contributions to interaction energy, since the magnitude of fragment polarization is greater in both these instances.

Chapter 7

A fully quantum-mechanical investigation of drug–protein interactions shows both attractive and repulsive contributions to binding

7.1 Introduction

Many computational studies have examined MTs in the context of understanding compounds that bind to tubulin and disrupt MT dynamics, which have employed classical mechanics (CM) and molecular dynamics (MD) to examine these systems. In order to computationally study quantum chemical phenomena, methods based on quantum mechanics (QM) must be applied to these macromolecular systems. Using QM, more complex problems may be considered in greater detail and with higher accuracy.

Quantum phenomena are particularly important to the structure and functioning of tubulin and MTs, making tubulin-containing systems interesting test cases for which to apply QM-based methods. For example, quantum channels of π-containing residues in tubulin have been modeled in relation to consciousness.[280] Quantum processes are also responsible for MT conductivity, which has potential applications to disease and cell proliferation.[281] Furthermore, some drugs, such as cyclostreptin[100] and zampanolide,[181] discussed in Section 1.2.2.4, covalently bond to tubulin, which requires QM-based methods to study the chemical reaction involved. Additionally,

accounting for change-transfer and polarization in drug–tubulin binding requires QM methods.

This Chapter examines the binding in drug–tubulin complexes using the Fragment Molecular Orbital (FMO) method. In particular, complexes between β-tubulin and the clinically-approved taxanes paclitaxel (TXL), docetaxel (DXL), and cabazitaxel (CAB) are considered (Figure 5.1), as taxanes are the most well-studied MT-targeting agents and represent some of the most successful chemotherapy drugs.[16] Descriptions of both taxane binding and taxane–residue interactions are compared between the FMO method (Section 1.3.2.1), and the classically-derived MM/GBSA method (Section 1.3.3.2). The objective of this work is to compare classical, specifically MM/GBSA, and quantum methods for evaluating ligand–protein binding.

7.2 Computational Details

Structures of drug–protein complexes were obtained from the end of the classical, explicitly-solvated MD simulations of $\alpha\beta$-tubulin–taxane complexes in Chapter 5. To decrease the size of the system for QM calculations, only the coordinates of the taxane–β-tubulin complexes, including GDP, were retained, while the α-tubulin subunit, solvent, and ions were removed. This resulted in three taxane–β-tubulin complexes as input for FMO calculations: (1) TXL–β-tubulin, (2) DXL–β-tubulin, and (3) CAB–β-tubulin. This truncation provides a model that captures the local effects of drug–protein interactions at an atomistic level of detail. Residue and fragment names are discussed with respect to the numbering of the 1JFF crystal structure,[36] as also reported in Chapter 5.

FMO2 calculations were performed on each of the three taxane–β-tubulin complexes in the gas phase with both HF/6-31G(d) and MP2/6-31G(d,p) methods, as well as in implicit solvent (water) with PCM[1(2)]-MP2/6-31G(d,p).[231] For the solvent-phase results, the dispersion contribution was taken from the gas-phase calculation. Pair interactions energies between the taxanes and protein fragments ($\Delta E_{ij}^{\prime FMO2}$) were calculated using Equations 1.12, which may be decomposed via Equations 1.17 and 1.18. Each complex was separated into 429 fragments, with the taxane defined as one fragment, GDP defined as one fragment, and 427 fragments corresponding to
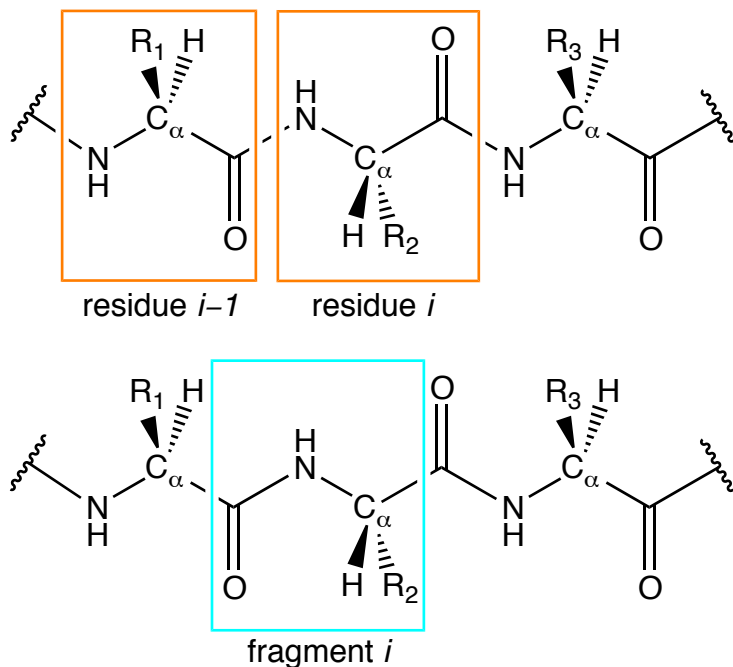
Figure 7.1: *The structure of the protein backbone, illustrating the difference in composition of an amino acid residue and a fragment defined by the FMO method.*

protein residues. Fragmentation must occur between sp^3-hybridized carbon atoms,[215] and therefore each residue was fragmented along the C_α–C bond of the protein backbone (Figure 7.1). It is important to note that this differs from the definition of a residue, since residues are partitioned along the amide bond. By definition, FMO fragment i contains the amine and C_α group of residue i, but the carbonyl group of residue $i-1$. For example, fragment GLY-370 contains the side chain and amine of residue β:Gly370 and the carbonyl of residue β:Arg369, and therefore the terms fragment and residue are not interchangeable. Each system contains over 6700 atoms and 68 000 basis functions. QM FMO[214] calculations were performed using GAMESS (Version May 2013 R1).[220] For increased computational efficiency, the approximations described in Section 1.3.2.1 were implemented using the default values in GAMESS.

For comparison, binding contributions were also obtained classically with the MM/GBSA method in Amber 12.[240,247] Pairwise taxane–residue contributions were calculated with Equation 1.22. However, unlike FMO, these pairwise contributions are not additive, and therefore the sum of the pairwise contributions is not equal to the total classical binding free energy ($\sum \Delta G_{ij}^{MM/GBSA} \neq \Delta G^{MM/GBSA}$, Equa-

tions 1.20 and 1.22). Neither FMO2 nor MM/GBSA calculations include an entropy contribution.

7.3 Results and Discussion

7.3.1 Classical binding energy: A comparison to Chapter 5

In Chapter 5[3] and also in Table F1, binding is reported for taxane–$\alpha\beta$-tubulin complexes over the course of a 47.5 ns simulation using the MM/GBSA method, which found that binding strength increases as CAB (-151.5 kJ mol^{-1}) < TXL (-182.5 kJ mol^{-1}) < DXL (-198.4 kJ mol^{-1}). The results from this Chapter differ from those in Chapter 5 in two important ways: (1) in the present work, calculations were performed on a single structure taken from the end of the simulation; and (2) the present work considers binding to β-tubulin monomer rather than the $\alpha\beta$-tubulin heterodimer. The α-tubulin subunit has no affect on the magnitude of taxane binding to the protein (Table F1), and therefore the differences in the MM/GBSA binding energies between the two Chapters are a result of using different structures. In the present work, the MM/GBSA binding energy increases as CAB (-142.8 kJ mol^{-1}) < DXL (-167.9 kJ mol^{-1}) < TXL (-197.5 kJ mol^{-1}). Compared to the results obtained with MD simulations in Chapter 5, both CAB–tubulin and DXL–tubulin binding weakens while TXL–tubulin binding strengthens. This coincides with a reduction of hydrogen bonds in the DXL– and CAB–tubulin complexes when only the end structure is considered, in contrast to using the data from the entire simulation. In the structures considered in this study, the TXL–β-tubulin complex has a hydrogen bond between the C2′-hydroxyl of TXL and the backbone carbonyl of β:Arg369 (fragment GLY-370). The DXL–β-tubulin complex involves hydrogen bonds between the C2′-hydroxyl of DXL and the side chain of β:Asp26, as well as between the N′-carbonyl of DXL and the β:His229 side chain. These contacts were also prominent in the taxane–$\alpha\beta$-tubulin simulation, but the less frequent hydrogen bonds from the DXL–$\alpha\beta$-tubulin trajectory are absent in the DXL–β-tubulin complex. The CAB–β-tubulin complex in the present study contains no CAB–tubulin hydrogen bonds, though several transient hydrogen bonds were observed throughout the simulated CAB–$\alpha\beta$-tubulin trajectory.

144

Table 7.1: *Taxane–β-tubulin binding energy (kJ mol^{-1}).*

Method	TXL	DXL	CAB
MM/GBSA	-197.5	-167.9	-142.8
HF/6-31G(d,p)	-165.8	-321.9	-222.8
MP2/6-31G(d,p)	-499.8	-613.1	-460.8
PCM[1(2)]-MP2/6-31G(d,p)	-378.6	-494.6	-277.5

7.3.2 Classical vs. quantum interaction energies

In general, full QM calculations on the taxane–β-tubulin complexes predict greater binding affinities than the MM/GBSA method, with the exception of the HF method applied to the TXL–β-tubulin. Both the QM and MM methods considerably overestimate the binding affinity of the drug to the protein relative to experimentally-determined binding affinities (-42 kJ mol^{-1}).[115] This trend is well-established in the literature, and indicates that the QM and MM methods are more appropriate for studying the rank order of ligand–protein binding rather than obtaining absolute binding free energies.[249] Full quantum calculations on the taxane–β-tubulin complexes show that DXL binds the strongest to β-tubulin, regardless of the method used. However, HF and MP2 predict different ranking of CAB and TXL, with MP2 calculating increasing binding as CAB < TXL < DXL, while the HF method finds TXL binding to be the least favourable (TXL < CAB < DXL).

Differences in binding between HF and MP2 indicate electron correlation plays an important role in taxane–β-tubulin binding. The inclusion of electron correlation results in a substantial increase in the affinity of the taxane for β-tubulin, which is readily observed when comparing the HF/6-31G(d,p) and MP2/6-31G(d,p) (Table 7.1). With the PCM[1(2)]-MP2/6-31G(d,p) method, electron correlation (ΔE^{DI}) contributes 86–88 % of the binding energy for TXL and CAB (Table 7.2), but substantially less for DXL binding (59 %). This difference may be explained by the taxane–β-tubulin contacts, where DXL binding involves more hydrogen-bonding interactions with the protein and therefore interactions are more electrostatic (ΔE^{ES}, 78 %) and less dispersion-dominated in nature. Alternatively, CAB adopts a collapsed structure and engages in fewer interactions with β-tubulin,[3] leading to a reduced affinity for β-tubulin. The electron correlation is a substantial contributor to TXL

145

Table 7.2: *Decomposition of the total binding energy (kJ mol^{-1}) obtained with PCM[1(2)]-MP2 and MM/GBSA for the taxane–β-tubulin complexes.*

PCM[1(2)]-MP2/6-31G(d,p)[a]	ΔG_{ij}^{QM}	ΔE_{ij}^{ES}	ΔE_{ij}^{EX}	ΔE_{ij}^{CT+mix}	ΔE_{ij}^{DI}	ΔG_{ij}^{sol}
TXL	-378.6	-240.9 (64%)	221.0 (-58%)	-81.1 (21%)	-334.0 (88%)	56.4 (-15%)
DXL	-494.6	-390.2 (79%)	263.9 (-53%)	-99.8 (20%)	-291.2 (59%)	22.6 (-5%)
CAB	-277.5	-215.0 (77%)	143.2 (-52%)	-59.2 (21%)	-238.0 (86%)	91.5 (-33%)

MM/GBSA[b]	$\sum \Delta G_{ij}^{CM\,(c)}$	ΔE_{ij}^{elec}			ΔE_{ij}^{vdW}	ΔG_{ij}^{sol}
TXL	-253.7	-72.7 (29%)			-139.2 (55%)	-41.9 (16%)
DXL	-240.9	-118.7 (49%)			-110.1 (46%)	-12.1 (5%)
CAB	-190.4	-66.1 (35%)			-104.7 (55%)	-19.5 (10%)

[a] PIEDA performed according to Equation 1.17; the force field terms as specified in Equation 1.22; [b] Decomposition performed according to [c] The sum of the pairwise taxane–residue contributions, not equivalent to $\Delta G^{MM/GBSA}$ provided in Table 7.1.

binding, supported by the observation in Chapter 5 that dispersion-dominated π–π interactions occur between the TXL side chain, which has an additional aromatic ring at N′ relative to DXL and CAB (Figure 5.1), and the protein side chains of β:His229 and β:Phe272. The importance of electron correlation in TXL binding also explains the low binding affinity calculated by the HF method (Table 7.1) discussed above. Quantum electronic effects such as dispersion are not sufficiently captured with classical mechanics, where the van der Waals component of the binding energy contributes 46–55 % to the total interaction energy of the three taxanes (Table 7.2). However, this contribution is still larger for TXL and CAB than DXL.

7.3.3 Binding contributions from secondary structures and fragments

The interactions between the taxanes and β-tubulin have been partitioned into the contributions from each protein secondary structure by summing the contributions from each fragment or residue within the structure (Table F2). The secondary

structures in the binding site, β:H1, β:H6–H7, β:H7, the M-loop, and β:S9–S10, stabilize all three of the taxanes, as calculated by both QM and CM methods. However, different secondary structures have a greater stabilizing effects on certain taxanes. The PCM[1(2)]-MP2 data shows that DXL is most stabilized by β:H1 (-248.1 kJ mol^{-1}) and β:H7 (-125.5 kJ mol^{-1}), while TXL is most stabilized by β:S9–S10 (-148.7 kJ mol^{-1}). CAB is stabilized by the M-loop (-193.2 kJ mol^{-1}), which coincides with the closer proximity of CAB to this structure found in Chapter 5, whereas TXL and DXL are further from the M-loop.[3] CM may also be used to rank the importance of secondary structures, and achieves similar rankings as PCM[1(2)]-MP2, despite predicting lower binding affinities. However, the QM methods identify repulsive interactions between the taxane and certain secondary structures or fragments. For example, with the PCM[1(2)]-MP2 method, CAB is repelled by β:H1–H1′, while TXL and DXL are stabilized by this structure. However, both β:H8 and β:S8 stabilize CAB while destabilizing TXL and DXL. Notably, the β:S9–S10 structure that strongly stabilizes TXL, and to a lesser extent CAB, has a destabilizing effect on DXL.

Pair interaction energies indicate which protein fragments contribute the most to taxane binding (Figure 7.2 and Table F3). To gain further insight into the nature of the taxane–β-tubulin interactions, the PCM[1(2)]-MP2 pair interaction energies can be decomposed according to Equation 1.17 (Figure 7.3 and Table F4). The majority of residues do not contribute to taxane binding, as visible in Figure 7.2, with 84–95 % of fragments contributing a magnitude of less than 5 kJ mol^{-1}. TXL binding is most stabilized by fragment GLY-370 (-82.5 kJ mol^{-1}). Due to the hydrogen bond that forms between the C2′-hydroxyl of TXL and and the backbone carbonyl of β:Arg369 that is present in fragment GLY-370. This interaction is largely electrostatic (ΔE_{ij}^{ES} = -87.2 kJ mol^{-1}, Figure 7.3), however hydrogen bonds are also accompanied by some of the largest $CT + mix$ contributions (ΔE_{ij}^{CT+mix} = -12.8 kJ mol^{-1}, Figure 7.3). Charge transfer contributions are not obtainable using CM methods. A large interaction is also present with fragment ARG-369 (-46.5 kJ mol^{-1}, large electrostatic and dispersion contributions) and LEU-275 (-41.0 kJ mol^{-1}, large dispersion contribution). HIS-229 provides stabilization to both TXL (-48.4 kJ mol^{-1}) and DXL (-64.7 kJ mol^{-1}). For both these taxanes, this interaction involves impor-

tant dispersion stabilization (ΔE_{ij}^{DI} = -31 kJ mol^{-1}), but a larger ES contribution to DXL binding due to the hydrogen bond that forms between the N′-carbonyl of DXL and the β:His229 side chain. The hydrogen bond between the C2′-hydroxyl of DXL and the side chain of β:Asp26 provides the largest stabilization (-170.7 kJ mol^{-1}), which is electrostatic in nature (ΔE_{ij}^{ES} = -183.2 kJ mol^{-1}) and also has the largest charge-transfer contribution (ΔE_{ij}^{CT+mix} -43.5 kJ mol^{-1}) observed for all fragments and taxanes (Figure 7.3). The magnitude of the interactions between CAB and the protein fragments are generally smaller, with the most notable stabilization arising from electrostatic contributions (Figure 7.3) in the M-loop fragments ARG-278 (-66.6 kJ mol^{-1}) and GLN-282 (-51.8 kJ mol^{-1}).

Repulsive taxane–fragment interactions up to 20.8 kJ mol^{-1} are also evident (Figures 7.2 and 7.3), both close to and distant from the taxane binding pocket. Most PCM[1(2)]-MP2 ligand–fragment interactions within the TXL–β-tubulin complex are attractive, while large repulsive contributions are calculated for DXL and CAB binding (Figure 7.2). LYS-19 (14.3 kJ mol^{-1}), ARG-320 (20.8 kJ mol^{-1}), and ARG-369 (16.1 kJ mol^{-1}) destabilize DXL binding at the PCM[1(2)]-MP2 level of theory. GLU-290 (15.3 kJ mol^{-1}), ASP-297 (14.2 kJ mol^{-1}), and GDP (18.0 kJ mol^{-1}) destabilize CAB binding (Figure 7.2 and Table F2). The majority of these destabilizing contributions occur with charged fragments and are a result of repulsive electrostatic and/or solvation terms (Table F3). Interestingly, the CAB–GDP interaction has an attractive electrostatic term, but an unfavourable solvation component (Table F3). In contrast, MM/GBSA predicts all taxane–residue interactions to either be attractive (50–56 % of residues) or have no contribution to taxane binding. In general, for values of $\Delta G_{ij}^{MM/GBSA}$ at or near zero, $\Delta E_{ij}^{elec} \approx -\Delta G_{ij}^{GB}$.

7.4   Conclusions

A fully quantum-mechanical description has been obtained for three complexes between β-tubulin, and each of three taxanes (paclitaxel, docetaxel, and cabazitaxel). Both uncorrelated (HF) and correlated (MP2) QM methods were used, and the effect of implicit solvent (PCM[1(2)]-MP2) was also considered. Variable ranking is found between the QM methods depending on whether the HF or MP2 method is used.
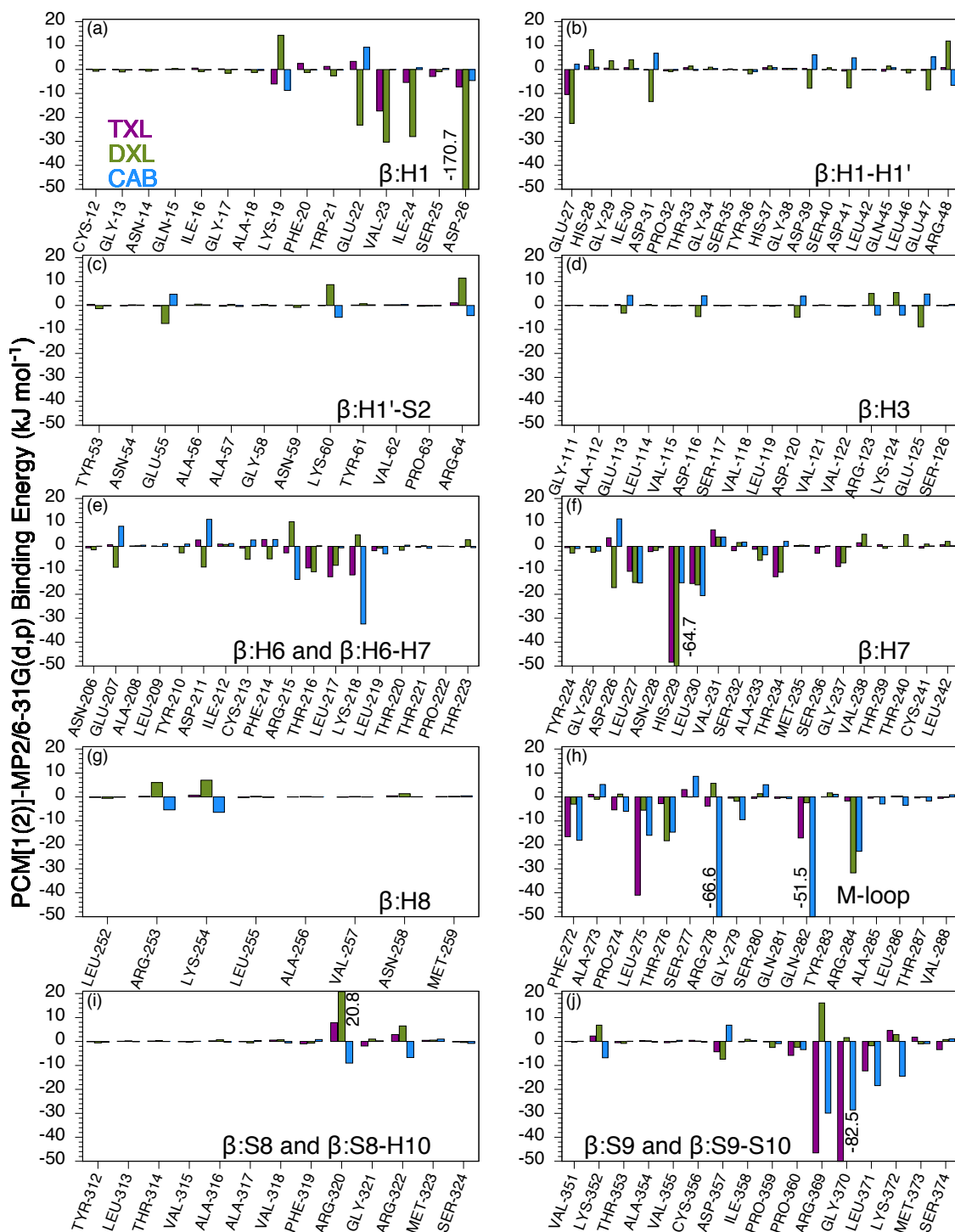
Figure 7.2: *PCM[1(2)]-MP2/6-31G(d,p) taxane–fragment binding energy ($\Delta E_{ij}^{\prime FMO2}$, kJ mol^{-1}) for select secondary structures in β-tubulin. Values included in Table F3.*

Figure 7.3: *PIEDA results for the PCM[1(2)]-MP2/6-31G(d,p) taxane–fragment binding energies ($\Delta E_{ij}'^{FMO2}$, kJ mol^{-1}) for select fragments in β-tubulin. Values included in Table F4.*

Electron correlation plays an important role in describing the dispersive interactions involved in taxane binding, contributing up to 88 % of the total interaction energy. The HF method under estimates the binding affinity of the drugs relative to the MP2 method. Therefore, correlated QM methods are necessary for describing drug–protein interactions. The addition of implicit solvent decreased the calculated MP2 binding energies, though maintains the ranking of taxanes. Therefore, when ranking these taxane–β-tubulin interactions, greater improvement is obtained upon the addition of electron correlation than after the addition of implicit solvent. The ranking of taxane affinity differs between the CM and QM methods, with the van der Waals component only contributing up to 55 % of the classically-calculated total interaction energy. This indicates the difference in forces captured by CM and the correlated QM methods.

QM and CM methods have identified contributions to taxane binding. Important contributions from secondary structures, namely β:H1, β:H6–H7, β:H7, the M-loop, and β:S9–S10, were confirmed. The classical MM/GBSA method calculated all pair-wise taxane–residue interactions to have either attractive or negligible contributions. However, the quantum-mechanical methods identified repulsive interactions between the taxanes and certain fragments or secondary structures that may be near or removed from the taxane binding site. This resulted from unfavourable electrostatic or solvation contributions to the interaction. The ability to identify repulsive drug–fragment interactions may provide a means to strengthen drug–protein interactions in rational drug design by introducing drug modifications that minimize that repulsive contributions. This should be of practical importance in derivatizing novel taxane analogues with not only improved binding profiles for tubulin, but also specifically and selectively binding to tubulin isotypes and mutants.[192]

Chapter 8

Conclusions

8.1 Summary of Thesis Research

The goal of this Thesis was to examine the interactions of antimitotic agents with tubulin, specifically MT stabilizing agents that include laulimalide and its analogues, as well as the clinically-approved taxanes. It is important to know how these compounds interact with tubulin on a local and global scale so that an understanding may be gained into the binding modes of these compounds and their allosteric effects on tubulin. This information is essential for the rational design of novel compounds with enhanced effects on tubulin.

Laulimalide–tubulin interactions were studied in Chapter 2 using an extended model, providing the first atomistic model of laulimalide in a MT-like environment. The MT environment altered the drug pose from what was previously obtained, establishing the importance of using an explicit extended model when studying drugs located between protofilaments. Specific laulimalide–residue interactions were identified, the importance of solvent was established, and important binding contributions were found from both tubulin heterodimers surrounding laulimalide.

The model presented in Chapter 2 was improved upon in Chapter 3 through the incorporation of an alternative pose for laulimalide that became available with the release of a crystal structure. The laulimalide binding mode was found to be characterized by an intramolecular hydrogen bond, direct and water-mediated ligand–tubulin hydrogen bonds, and π–π interactions. By also considering laulimalide analogues, which are less effective than laulimalide itself, the characteristics of the effective compounds were established. Greater cytotoxicity was observed for compounds that are

more weakly solvated and feature an intramolecular hydrogen bond, as well as a side chain with a hydrogen-bond donor, a π-containing system, and an additional hydrogen bond participant, which establishes a laulimalide pharmacophore that may be used in the design of novel laulimalide compounds.

The work presented in Chapter 3 was further expanded in Chapter 4 by considering additional laulimalide analogues and using the information presented in Chapters 3 and 4 to predict the ability of newly-proposed compounds to bind to tubulin in a laulimalide-like fashion. The importance of a specific macrocycle conformation was established, which is governed by an intramolecular hydrogen bond. This conformation is not retained by any of the laulimalide analogues examined in this Thesis, which may account for the reduced activity of the analogues with respect to the parent compound. An abundance of nonspecific π-π-interactions in the binding site near the dihydropyran side chain allow for a variety of side chain poses to be adopted, with the most effective compounds occupying an intermediate pose between the two heterodimers, having significant binding contributions from both heterodimers. Two newly-proposed laulimalide compounds were also computationally examined. One of these compounds may be particularly promising, exhibiting a laulimalide-like binding pose.

In Chapter 5, the interactions between each of the clinically-approved taxanes and $\alpha\beta$-tubulin were studied. Previously-used metrics, such as binding affinity and the enhancement of lateral tubulin interactions in MTs, did not correlate with the experimentally-observed ability of these taxanes to promote MT formation. Instead, for the first time, the work presented in this Thesis traced the effect of taxane binding from the binding site, through specific secondary structures on β-tubulin, namely H1–H1′, H9, and H10, which thereby alters contacts between α-tubulin and β-tubulin to induce an allosteric effect. Since the displacements of α:H10 and β:T5 correlate with the effect of the taxanes on MTs, this displacement should be used as a metric to predict the ability of taxanes to promote MT formation in future rational drug design strategies.

Quantum mechanical methods were also utilized in this Thesis with the Fragment Molecular Orbital method. However, before applying this method to study ligand–protein interactions, it was necessary to understand how it differs from other ap-

proaches of calculating noncovalent interactions. In Chapter 6, the Fragment Molecular Orbital method was applied to study π-π-interactions in benzene-containing systems, and other systems of biological interest. The polarization of fragments affects the interaction energies calculated via the Fragment Molecular Orbital method compared to a supermolecular approach, and these discrepancies increase as the number of fragments increases and as the electrostatic contribution to the interactions increases.

The Fragment Molecular Orbital method was next applied in Chapter 7 to study the interactions between each of the clinically-approved taxanes and β-tubulin. It was found that when ranking the affinity of the taxanes, the inclusion of electron correlation is more important than the inclusion of implicit solvent. Electron correlation represents the most substantial contribution to the binding energy. Additionally, quantum methods calculate some drug–residue interactions to be repulsive, whereas classical mechanics predicts all drug–residue interactions to be attractive or negligible (near zero). This may provide a means of identifying unfavorable interactions in rational drug design, and provide clues how to alter drug structure to maximize affinity for the target protein.

8.2   Future Work

Despite the extensive studies of laulimalide presented in Chapters 2 to 4, further work remains to be completed. All the laulimalide analogues that have been evaluated in the literature are less effective than the parent compound, which provides motivation to develop more effective laulimalide-like compounds. The novel compounds, SVH1 and SVH4, proposed in Chapter 4 have yet to be synthesized and evaluated. Future work should examine the cytotoxicity of these compounds, which in addition to potentially providing effective compounds, will provide a means of evaluating the predictive model presented in Chapter 4. Future computational and experimental work should also consider modifications of the laulimalide compound at the C11-site, as proposed in Chapter 3. This site is directed towards the adjacent β-tubulin unit, near several polar and charged residues, as well as the MT type II pore containing solvent. Modification at this site may provide a means of increasing the affinity of laulimalide for tubulin, while maintaining the active macrocycle conformation since

this site is removed from the C1- and C15-sites that form the intramolecular hydrogen bond.

In addition to the development of novel laulimalide-like compounds, it will be important to obtain MT assembly data for the laulimalides. Computational models of ligand–protein interactions are not directly comparable to the cytotoxicity experiments that are presented in the literature and discussed for laulimalide in Chapters 3 and 4. Instead, it is more appropriate to compare such models to MT assembly data like that reported for the taxanes in Chapter 5. With such data, it may be possible to establish a metric that may be used in computational models to predict the ability of agents that bind to the laulimalide/peloruside A binding site to affect tubulin. In order for computational models to be successful in rational drug design, appropriate comparisons between computations and experiments must be used.

Antimitotic agents continue to be promising compounds in anticancer applications and research. Furthermore, adverse toxic effects and the tendency for patients to develop resistances fuels the search for new anticancer drugs. In recent years, an abundance of structural information regarding ligand–tubulin compounds has become available. Specifically, crystal structures have been released for antimitotic compounds bound to $\alpha\beta$-tubulin, including the destabilizing agents maytansine (4TV8) and rhizoxin F (4TUY), as well zampanolide (4I4T) that covalently bonds to tubulin at the taxane site. These covalently-bonding agents are showing particular promise in preclinical studies since irreversible binding allows for the evasion of the P-glycoprotein pump. Other compounds such as cyclostreptin and the taccalonolides also covalently bond to tubulin, with some taccalonolides showing subnanomolar potencies. Therefore, much work remains to be done in order to understand how these compounds interact with and affect tubulin and to move these compounds and their analogues towards clinical use.

Bibliography

[1] Churchill, C. D. M.; Klobukowski, M.; Tuszynski, J. A. The unique binding mode of laulimalide to two tubulin protofilaments. *Chemical Biology & Drug Design* **2015**, *86*, 190–199.

[2] Churchill, C. D. M.; Klobukowski, M.; Tuszynski, J. A. Analysis of the binding mode of laulimalide to microtubules: Establishing a laulimalide–tubulin pharmacophore. *The Journal of Biomolecular Structure and Dynamics* **2015**, DOI: 10.1080/07391102.2015.1078115.

[3] Churchill, C. D. M.; Klobukowski, M.; Tuszynski, J. A. Elucidating the mechanism of action of the clinically-approved taxanes: A comprehensive comparison of local and allosteric effects. *Chemical Biology & Drug Design* **2015**, DOI: 10.1111/cbdd.12595.

[4] Churchill, C. D. M. The Fragment Molecular Orbital method and understanding monomer polarization. *Chemical Physics Letters* **2012**, *554*, 185–189.

[5] Howard, J. Molecular motors: structural adaptations to cellular functions. *Nature* **1997**, *389*, 561–567.

[6] Hirokawa, N. Kinesin and dynein superfamily proteins and the mechanism of organelle transport. *Science* **1998**, *279*, 519–526.

[7] Goldstein, L. S. B.; Yang, Z. H. Microtubule-based transport systems in neurons: The roles of kinesins and dyneins. *Annual Review of Neuroscience* **2000**, *23*, 39–71.

[8] Sharp, D. J.; Rogers, G. C.; Scholey, J. M. Microtubule motors in mitosis. *Nature* **2000**, *407*, 41–47.

[9] Schliwa, M.; Woehlke, G. Molecular motors. *Nature* **2003**, *422*, 759–765.

[10] Vale, R. D. The molecular motor toolbox for intracellular transport. *Cell* **2003**, *112*, 467–480.

[11] Fojo, T., Ed. *The role of microtubules in cell biology, neurobiology, and oncology*; Cancer drug discovery and development; Humana Press: Totowa, NJ, 2008.

[12] Berg, J. M.; Tymoczko, J. L.; Stryer, L. *Biochemistry*, 6th ed.; W.H. Freeman and Company: New York, 2007.

[13] Ruchaud, S.; Carmena, M.; Earnshaw, W. C. Chromosomal passengers: Conducting cell division. *Nature Reviews Molecular Cell Biology* **2007**, *8*, 798–812.

[14] Musacchio, A.; Salmon, E. D. The spindle-assembly checkpoint in space and time. *Nature Reviews Molecular Cell Biology* **2007**, *8*, 379–393.

[15] Zhou, J.; Panda, D.; Landen, J. W.; Wilson, L.; Joshi, H. C. Minor alteration of microtubule dynamics causes loss of tension across kinetochore pairs and activates the spindle checkpoint. *Journal of Biological Chemistry* **2002**, *277*, 17200–17208.

[16] Jordan, M. A.; Wilson, L. Microtubules as a target for anticancer drugs. *Nature Reviews Cancer* **2004**, *4*, 253–265.

[17] Dumontet, C.; Jordan, M. A. Microtubule-binding agents: A dynamic field of cancer therapeutics. *Nature Reviews Drug Discovery* **2010**, *9*, 790–803.

[18] Field, J.; Díaz, J. F.; Miller, J. The binding sites of microtubule-stabilizing agents. *Chemistry & Biology (Oxford, United Kingdom)* **2013**, *20*, 301–315.

[19] Field, J. J.; Waight, A. B.; Senter, P. D. A previously undescribed tubulin binder. *Proceedings of the National Academy of Sciences* **2014**, *111*, 13684–13685.

[20] Jordan, A.; Hadfield, J. A.; Lawrence, N. J.; McGown, A. T. Tubulin as a target for anticancer drugs: Agents which interact with the mitotic spindle. *Medicinal Research Reviews* **1998**, *18*, 259–296.

[21] Nogales, E.; Downing, K. H. In *The role of microtubules in cell biology, neurobiology, and oncology*; Fojo, T., Ed.; Cancer drug discovery and development; Humana Press: Totowa, NJ, 2008; pp 211–225.

[22] Nogales, E.; Alushin, G. Tubulin and microtubule structure: Mechanistic insights into dynamic instability and its biological relevance. *Comprehensive Biophysics* **2011**, *Volume 4: Molecular Motors and Motility*, 72–92.

[23] Chrétien, D.; Metoz, F.; Verde, F.; Karsenti, E.; Wade, R. H. Lattice defects in microtubules: Protofilament numbers vary within individual microtubules. *Journal of Cell Biology* **1992**, *117*, 1031–1040.

[24] Nogales, E.; Whittaker, M.; Milligan, R. A.; Downing, K. H. High-resolution model of the microtubule. *Cell* **1999**, *96*, 79–88.

[25] Auer, M. Three-dimensional electron cryo-microscopy as a powerful structural tool in molecular medicine. *Journal of Molecular Medicine* **2000**, *78*, 191–202.

[26] Moores, C. In *Introduction to electron microscopy for biologists*; Allen, T. D., Ed.; Methods in cell biology; Elsevier Academic Press Inc: San Diego, CA, 2008; Vol. 88; pp 299–317.

[27] Fujiyoshi, Y. Structural physiology based on electron crystallography. *Protein Science* **2011**, *20*, 806–817.

[28] Sosa, H.; Dias, D. P.; Hoenger, A.; Whittaker, M.; Wilson-Kubalek, E.; Sablin, E.; Fletterick, R. J.; Vale, R. D.; Milligan, R. A. A model for the nicrotubule–Ncd motor protein complex obtained by cryo-electron microscopy and image analysis. *Cell* **1997**, *90*, 217–224.

[29] Li, H.; DeRosier, D. J.; Nicholson, W. V.; Nogales, E.; Downing, K. H. Microtubule structure at 8 Å resolution. *Structure* **2002**, *10*, 1317–1328.

[30] Fourniol, F. J.; Sindelar, C. V.; Amigues, B.; Clare, D. K.; Thomas, G.; Perderiset, M.; Francis, F.; Houdusse, A.; Moores, C. A. Template-free 13-protofilament microtubule-MAP assembly visualized at 8 Å resolution. *Journal of Cell Biology* **2010**, *191*, 463–470.

[31] Alushin, G. M.; Lander, G. C.; Kellogg, E. H.; Zhang, R.; Baker, D.; Nogales, E. High-resolution microtubule structures reveal the structural transitions in $\alpha\beta$-tubulin upon GTP hydrolysis. *Cell* **2014**, *157*, 1117–1129.

[32] Bartesaghi, A.; Merk, A.; Banerjee, S.; Matthies, D.; Wu, X.; Milne, J. L. S.; Subramaniam, S. 2.2 Å resolution cryo-EM structure of β-galactosidase in complex with a cell-permeant inhibitor. *Science* **2015**, *348*, 1147–1151.

[33] Binshtein, E.; Ohi, M. D. Cryo-electron microscopy and the amazing race to atomic resolution. *Biochemistry* **2015**, *54*, 3133–3141.

[34] Ravelli, R. B. G.; Gigant, B.; Curmi, P. A.; Jourdain, I.; Lachkar, S.; Sobel, A.; Knossow, M. Insight into tubulin regulation from a complex with colchicine and a stathmin-like domain. *Nature* **2004**, *428*, 198–202.

[35] Nogales, E.; Wolf, S. G.; Downing, K. H. Structure of the $\alpha\beta$ tubulin dimer by electron crystallography. *Nature* **1998**, *391*, 199–203.

[36] Löwe, J.; Li, H.; Downing, K. H.; Nogales, E. Refined structure of $\alpha\beta$-tubulin at 3.5 Å resolution. *Journal of Molecular Biology* **2001**, *313*, 1045–1057.

[37] Nogales, E.; Grayer Wolf, S.; Khan, I. A.; Ludueña, R. F.; Downing, K. H. Structure of tubulin at 6.5 Å and location of the Taxol-binding site. *Nature* **1995**, *375*, 424–427.

[38] Nogales, E.; Wolf, S. G.; Downing, K. H. Visualizing the secondary structure of tubulin: Three-dimensional map at 4 Å. *Journal of Structural Biology* **1997**, *118*, 119–127.

[39] Ludueña, R. F. In *International review of cytology*; Kwang, W. J., Ed.; A survey of cell biology; Academic Press: Toronto, 1997; Vol. 178; pp 207–275.

[40] Desai, A.; Mitchison, T. J. Microtubule polymerization dynamics. *Annual Review of Cell and Developmental Biology* **1997**, *13*, 83–117.

[41] Westermann, S.; Weber, K. Post-translational modifications regulate microtubule function. *Nature Reviews Molecular Cell Biology* **2003**, *4*, 938–947.

[42] Tuszynski, J. A.; Carpenter, E. J.; Huzil, J. T.; Malinski, W.; Luchko, T.; Luduena, R. F. The evolution of the structure of tubulin and its potential consequences for the role and function of microtubules in cells and embryos. *International Journal of Developmental Biology* **2006**, *50*, 341–358.

[43] Janke, C.; Bulinski, J. C. Post-translational regulation of the microtubule cytoskeleton: mechanisms and functions. *Nature Reviews Molecular Cell Biology* **2011**, *12*, 773–786.

[44] Luchko, T.; Huzil, T. J.; Stepanova, M.; Tuszynski, J. Conformational analysis of the carboxy-terminal tails of human β-tubulin isotypes. *Biophysical Journal* **2008**, *94*, 1971–1982.

[45] Roll-Mecak, A. Intrinsically disordered tubulin tails: complex tuners of microtubule functions? *Seminars in Cell & Developmental Biology* **2015**, *37*, 11–19.

[46] Gigant, B.; Wang, C. G.; Ravelli, R. B. G.; Roussi, F.; Steinmetz, M. O.; Curmi, P. A.; Sobel, A.; Knossow, M. Structural basis for the regulation of tubulin by vinblastine. *Nature* **2005**, *435*, 519–522.

[47] Ranaivoson, F. M.; Gigant, B.; Berritt, S.; Joullié, M.; Knossow, M. Structural plasticity of tubulin assembly probed by Vinca-domain ligands. *Acta Crystallographica Section D* **2012**, *68*, 927–934.

[48] Prota, A. E.; Danel, F.; Bachmann, F.; Bargsten, K.; Buey, R. M.; Pohlmann, J.; Reinelt, S.; Lane, H.; Steinmetz, M. O. The novel microtubule-destabilizing drug BAL27862 binds to the colchicine site of tubulin with distinct effects on microtubule organization. *Journal of Molecular Biology* **2014**, *426*, 1848–1860.

[49] Prota, A. E.; Bargsten, K.; Díaz, J. F.; Marsh, M.; Cuevas, C.; Liniger, M.; Neuhaus, C.; Andreu, J. M.; Altmann, K.-H.; Steinmetz, M. O. A new tubulin-binding site and pharmacophore for microtubule-destabilizing anticancer drugs. *Proceedings of the National Academy of Sciences* **2014**, *111*, 13817–13821.

[50] Nettles, J. H.; Li, H.; Cornett, B.; Krahn, J. M.; Snyder, J. P.; Downing, K. H. The binding mode of epothilone A on α,β-tubulin by electron crystallography. *Science* **2004**, *305*, 866–869.

[51] Prota, A. E.; Bargsten, K.; Zurwerra, D.; Field, J. J.; Díaz, J. F.; Altmann, K.-H.; Steinmetz, M. O. Molecular mechanism of action of microtubule-stabilizing anticancer agents. *Science* **2013**, *339*, 587–590.

[52] Prota, A. E.; Bargsten, K.; Northcote, P. T.; Marsh, M.; Altmann, K.-H.; Miller, J. H.; Díaz, J. F.; Steinmetz, M. O. Structural basis of microtubule stabilization by laulimalide and peloruside A. *Angewandte Chemie International Edition* **2014**, *53*, 1621–1625.

[53] Hesse, J.; Thierauf, M.; Ponstingl, H. Tubulin sequence region β155–174 is involved in binding exchangeable guanosine triphosphate. *Journal of Biological Chemistry* **1987**, *262*, 15472–15475.

[54] Linse, K.; Mandelkow, E. M. The GTP-binding peptide of β-tubulin: Localization by direct photoaffinity labeling and comparison with nucleotide-binding proteins. *Journal of Biological Chemistry* **1988**, *263*, 15205–15210.

[55] Shivanna, B. D.; Mejillano, M. R.; Williams, T. D.; Himes, R. H. Exhangeable GTP binding site of β-tubulin: Identification of cystine 12 as the major site of cross-linking by direct photoaffinity labeling. *Journal of Biological Chemistry* **1993**, *268*, 127–132.

[56] Davis, A.; Sage, C. R.; Dougherty, C. A.; Farrell, K. W. Microtubule dynamics modulated by guanosine triphosphate hydrolysis activity of β-tubulin. *Science* **1994**, *264*, 839–842.

[57] Mitchison, T.; Kirschner, M. Dynamic instability of microtubule growth. *Nature* **1984**, *312*, 237–242.

[58] Weisenberg, R. C.; Deery, W. J.; Dickinson, P. J. Tubulin–nucleotide interactions during the polymerization and depolymerization of microtubules. *Biochemistry* **1976**, *15*, 4248–4254.

[59] Drechsel, D. N.; Kirschner, M. W. The minimum GTP cap required to stabilize microtubules. *Current Biology* **1994**, *4*, 1053–1061.

[60] Hoog, J. L.; Huisman, S. M.; Sebo-Lemke, Z.; Sandblad, L.; McIntosh, J. R.; Antony, C.; Brunner, D. Electron tomography reveals a flared morphology on growing microtubule ends. *Journal of Cell Science* **2011**, *124*, 693–698.

[61] Quiniou, E.; Guichard, P.; Perahia, D.; Marco, S.; Mouawad, L. An atomistic view of microtubule stabilization by GTP. *Structure* **2013**, *21*, 833–843.

[62] Hyman, A. A.; Salser, S.; Drechsel, D. N.; Unwin, N.; Mitchison, T. J. Role of GTP hydrolysis in microtubule dynamics: Information from a slowly hydrolyzable analog, GMPCPP. *Molecular Biology of the Cell* **1992**, *3*, 1155–1167.

[63] Nogales, E. Structural insights into microtubule function. *Annual Review of Biochemistry* **2000**, *69*, 277–302.

[64] Noble, R. L.; Beer, C. T.; Cutts, J. H. Role of chance observations in chemotherapy: Vinca Rosea. *Annals of the New York Academy of Sciences* **1958**, *76*, 882–894.

[65] Johnson, I. S.; Armstrong, J. G.; Burnett, J. P.; Gorman, M. Vinca alkaloids: A new class of oncolytic agents. *Cancer Research* **1963**, *23*, 1390–1427.

[66] Bensch, K. G.; Malawista, S. E. Microtubule crystals: A new biophysical phenomenon induced by Vinca alkaloids. *Nature* **1968**, *218*, 1176–1177.

[67] Bensch, K. G.; Malawista, S. E. Microtubular crystals in mammalian cells. *Journal of Cell Biology* **1969**, *40*, 95–107.

[68] Risinger, A. L.; Jackson, E. M.; Polin, L. A.; Helms, G. L.; LeBoeuf, D. A.; Joe, P. A.; Hopper-Borge, E.; Ludueña, R. F.; Kruh, G. D.; Mooberry, S. L. The taccalonolides: Microtubule stabilizers that circumvent clinically relevant taxane resistance mechanisms. *Cancer Research* **2008**, *68*, 8881–8888.

[69] Wilson, L.; Jordan, M. A.; Morse, A.; Margolis, R. L. Interaction of vinblastine with steady-state microtubules in vitro. *Journal of Molecular Biology* **1982**, *159*, 125–149.

[70] Toso, R. J.; Jordan, M. A.; Farrell, K. W.; Matsumoto, B.; Wilson, L. Kinetic stabilization of microtubule dynamic instability in vitro by vinblastine. *Biochemistry* **1993**, *32*, 1285–1293.

[71] Jordan, M. A.; Margolis, R. L.; Himes, R. H.; Wilson, L. Identification of a distinct class of vinblastine binding-sites on microtubules. *Journal of Molecular Biology* **1986**, *187*, 61–73.

[72] Singer, W. D.; Jordan, M. A.; Wilson, L.; Himes, R. H. Binding of vinblastine to stabilized microtubules. *Molecular Pharmacology* **1989**, *36*, 366–370.

[73] Rendine, S.; Pieraccini, S.; Sironi, M. Vinblastine perturbation of tubulin protofilament structure: a computational insight. *Physical Chemistry Chemical Physics* **2010**, *12*.

[74] Lu, Y.; Chen, J.; Xiao, M.; Li, W.; Miller, D. An overview of tubulin inhibitors that interact with the colchicine binding site. *Pharmaceutical Research* **2012**, *29*, 2943–2971.

[75] Dorleans, A.; Gigant, B.; Ravelli, R. B. G.; Mailliet, P.; Mikol, V.; Knossow, M. Variations in the colchicine-binding domain provide insight into the structural switch of tubulin. *Proceedings of the National Academy of Sciences* **2009**, *106*, 13775–13779.

[76] Barbier, P.; Dorléans, A.; Devred, F.; Sanz, L.; Allegro, D.; Alfonso, C.; Knossow, M.; Peyrot, V.; Andreu, J. M. Stathmin and interfacial microtubule in-

hibitors recognize a naturally curved conformation of tubulin dimers. *Journal of Biological Chemistry* **2010**, *285*, 31672–31681.

[77] Buey, R. M.; Barasoain, I.; Jackson, E.; Meyer, A.; Giannakakou, P.; Paterson, I.; Mooberry, S.; Andreu, J. M.; Díaz, J. F. Microtubule interactions with chemically diverse stabilizing agents: Thermodynamics of binding to the paclitaxel site predicts cytotoxicity. *Chemistry & Biology (Oxford, United Kingdom)* **2005**, *12*, 1269–1279.

[78] Mooberry, S. L.; Tien, G.; Hernandez, A. H.; Plubrukarn, A.; Davidson, B. S. Laulimalide and isolaulimalide, new paclitaxel-like microtubule-stabilizing agents. *Cancer Research* **1999**, *59*, 653–660.

[79] Vrignaud, P.; Sémiond, D.; Lejeune, P.; Bouchard, H.; Calvet, L.; Combeau, C.; Riou, J. F.; Commerçon, A.; Lavelle, F.; Bissery, M. C. Preclinical antitumor activity of cabazitaxel, a semisynthetic taxane active in taxane-resistant tumors. *Clinical Cancer Research* **2013**, *19*, 2973–2983.

[80] Peng, L. X.; Hsu, M. T.; Bonomi, M.; Agard, D. A.; Jacobson, M. P. The free energy profile of tubulin straight-bent conformational changes, with implications for microtubule assembly and drug discovery. *PLoS Computational Biology* **2014**, *10*, e1003464.

[81] Prasad, V. V. T. S.; Gopalan, R. O. G. Continued use of MDA-MB-435, a melanoma cell line, as a model for human breast cancer, even in year, 2014. *npj Breast Cancer* **2015**, *1*, 15002.

[82] Mekhail, T. M.; Markman, M. Paclitaxel in cancer therapy. *Expert Opinion on Pharmacotherapy* **2002**, *3*, 755–766.

[83] Kingston, D. G. I. In *Anticancer agents from natural products*, 2nd ed.; Cragg, G. M., Kingston, D. G. I., Newman, D. J., Eds.; CRC Press: New York, 2011; pp 123–176.

[84] Wani, M. C.; Taylor, H. L.; Wall, M. E.; Coggon, P.; McPhail, A. T. Plant antitumor agents. VI. Isolation and structure of Taxol, a novel antileukemic

and antitumor agent from Taxus brevifolia. *Journal of the American Chemical Society* **1971**, *93*, 2325–2327.

[85] Schiff, P. B.; Fant, J.; Horwitz, S. B. Promotion of microtubule assembly in vitro by Taxol. *Nature* **1979**, *277*, 665–667.

[86] Rowinsky, E. K.; Donehower, R. C. Drug therapy: Paclitaxel (Taxol). *New England Journal of Medicine* **1995**, *332*, 1004–1014.

[87] Denis, J. N.; Greene, A. E.; Guénard, D.; Guéritte-Voegelein, F.; Mangatal, L.; Potier, P. Highly efficient, practical approach to natural Taxol. *Journal of the American Chemical Society* **1988**, *110*, 5917–5919.

[88] Danhier, F.; Lecouturier, N.; Vroman, B.; Jérôme, C.; Marchand-Brynaert, J.; Feron, O.; Préat, V. Paclitaxel-loaded PEGylated PLGA-based nanoparticles: In vitro and in vivo evaluation. *Journal of Controlled Release* **2009**, *133*, 11–17.

[89] Brannon-Peppas, L.; Blanchette, J. O. Nanoparticle and targeted systems for cancer therapy. *Advanced Drug Delivery Reviews* **2004**, *56*, 1649–1659.

[90] Davis, M. E.; Chen, Z.; Shin, D. M. Nanoparticle therapeutics: An emerging treatment modality for cancer. *Nature Reviews Drug Discovery* **2008**, *7*, 771–782.

[91] Galsky, M. D.; Dritselis, A.; Kirkpatrick, P.; Oh, W. K. Cabazitaxel. *Nature Reviews Drug Discovery* **2010**, *9*, 677–678.

[92] Matesanz, R.; Trigili, C.; Rodríguez-Salarichs, J.; Zanardi, I.; Pera, B.; Nogales, A.; Fang, W.-S.; Jímenez-Barbero, J.; Canales, A.; Barasoain, I. et al. Taxanes with high potency inducing tubulin assembly overcome tumoural cell resistances. *Bioorganic & Medicinal Chemistry* **2014**, *22*, 5078–5090.

[93] Rao, S.; Krauss, N. E.; Heerding, J. M.; Swindell, C. S.; Ringel, I.; Orr, G. A.; Horwitz, S. B. 3′-(p-axidobenzamido)taxol photolabels the N-terminal 31 amino acids of β-tubulin. *Journal of Biological Chemistry* **1994**, *269*, 3132–3134.

[94] Rao, S.; Orr, G. A.; Chaudhary, A. G.; Kingston, D. G. I.; Horwitz, S. B. Characterization of the Taxol binding site on the microtubule: 2-(m-azidobenzoyl)taxol photolabels a peptide (amino acids 217–231) of β-tubulin. *Journal of Biological Chemistry* **1995**, *270*, 20235–20238.

[95] Rao, S.; He, L. F.; Chakravarty, S.; Ojima, I.; Orr, G. A.; Horwitz, S. B. Characterization of the Taxol binding site on the microtubule: Identification of Arg[282] in β-tubulin as the site of photoincorporation of a 7-benzophenone analogue of Taxol. *Journal of Biological Chemistry* **1999**, *274*, 37990–37994.

[96] Díaz, J. F.; Andreu, J. M. Assembly of purified GDP-tubulin into microtubules induced by Taxol and Taxotere: Reversibility, ligand stoichiometry, and competition. *Biochemistry* **1993**, *32*, 2747–2755.

[97] Díaz, J. F.; Menendez, M.; Andreu, J. M. Thermodynamics of ligand-induced assembly of tubulin. *Biochemistry* **1993**, *32*, 10067–10077.

[98] Odde, D. Diffusion inside microtubules. *European Biophysics Journal with Biophysics Letters* **1998**, *27*, 514–520.

[99] Ross, J. L.; Fygenson, D. K. Mobility of Taxol in microtubule bundles. *Biophysical Journal* **2003**, *84*, 3959–3967.

[100] Buey, R. M.; Calvo, E.; Barasoain, I.; Pineda, O.; Edler, M. C.; Matesanz, R.; Cerezo, G.; Vanderwal, C. D.; Day, B. W.; Sorensen, E. J. et al. Cyclostreptin binds covalently to microtubule pores and lumenal taxoid binding sites. *Nature Chemical Biology* **2007**, *3*, 117–125.

[101] Díaz, J. F.; Barasoain, I.; Andreu, J. M. Fast kinetics of Taxol binding to microtubules: Effects of solution variables and microtubule-associated proteins. *Journal of Biological Chemistry* **2003**, *278*, 8407–8419.

[102] Freedman, H.; Huzil, J. T.; Luchko, T.; Ludueña, R. F.; Tuszynski, J. A. Identification and characterization of an intermediate Taxol binding site within microtubule nanopores and a mechanism for tubulin isotype binding selectivity. *Journal of Chemical Information and Modeling* **2009**, *49*, 424–436.

[103] Magnani, M.; Maccari, G.; Andreu, J. M.; Díaz, J. F.; Botta, M. Possible binding site for paclitaxel at microtubule pores. *FEBS Journal* **2009**, *276*, 2701–2712.

[104] Maccari, G.; Mori, M.; Rodríiguez-Salarichs, J.; Fang, W.; Díaz, J. F.; Botta, M. Free energy profile and kinetics studies of paclitaxel internalization from the outer to the inner wall of microtubules. *Journal of Chemical Theory and Computation* **2012**, *9*, 698–706.

[105] Mitra, A.; Sept, D. Taxol allosterically alters the dynamics of the tubulin dimer and increases the flexibility of microtubules. *Biophysical Journal* **2008**, *95*, 3252–3258.

[106] Wang, R.; Fang, X.; Lu, Y.; Yang, C.-Y.; Wang, S. The PDBbind database: Methodologies and updates. *Journal of Medicinal Chemistry* **2005**, *48*, 4111–4119.

[107] Gebremichael, Y.; Chu, J.-W.; Voth, G. A. Intrinsic bending and structural rearrangement of tubulin dimer: Molecular dynamics simulations and coarse-grained analysis. *Biophysical Journal* **2008**, *95*, 2487–2499.

[108] Bennett, M. J.; Chik, J. K.; Slysz, G. W.; Luchko, T.; Tuszynski, J.; Sackett, D. L.; Schriemer, D. C. Structural mass spectrometry of the $\alpha\beta$-tubulin dimer supports a revised model of microtubule assembly. *Biochemistry* **2009**, *48*, 4858–4870.

[109] Grafmuller, A.; Voth, G. A. Intrinsic bending of microtubule protofilaments. *Structure* **2011**, *19*, 409–417.

[110] Grafmuller, A.; Noya, E. G.; Voth, G. A. Nucleotide-dependent lateral and longitudinal interactions in microtubules. *Journal of Molecular Biology* **2013**, *425*, 2232–2246.

[111] Natarajan, K.; Mohan, J.; Senapati, S. Relating nucleotide-dependent conformational changes in free tubulin dimers to tubulin assembly. *Biopolymers* **2013**, *99*, 282–291.

[112] Xiao, H.; Verdier-Pinard, P.; Fernandez-Fuentes, N.; Burd, B.; Angeletti, R.; Fiser, A.; Horwitz, S. B.; Orr, G. A. Insights into the mechanism of microtubule stabilization by Taxol. *Proceedings of the National Academy of Sciences* **2006**, *103*, 10166–10173.

[113] Huzil, J. T.; Chik, J. K.; Slysz, G. W.; Freedman, H.; Tuszynski, J.; Taylor, R. E.; Sackett, D. L.; Schriemer, D. C. A unique mode of microtubule stabilization induced by Peloruside A. *Journal of Molecular Biology* **2008**, *378*, 1016–1030.

[114] Matesanz, R.; Barasoain, I.; Yang, C.-G.; Wang, L.; Li, X.; de Inés, C.; Coderch, C.; Gago, F.; Barbero, J. J.; Andreu, J. M. et al. Optimization of taxane binding to microtubules: Binding affinity dissection and incremental construction of a high-affinity analog of paclitaxel. *Chemistry & Biology (Oxford, United Kingdom)* **2008**, *15*, 573–585.

[115] Buey, R. M.; Díaz, J. F.; Andreu, J. M.; O'Brate, A.; Giannakakou, P.; Nicolaou, K. C.; Sasmal, P. K.; Ritzén, A.; Namoto, K. Interaction of epothilone analogs with the paclitaxel binding site: Relationship between binding affinity, microtubule stabilization, and cytotoxicity. *Chemistry & Biology (Oxford, United Kingdom)* **2004**, *11*, 225–236.

[116] Andreu, J. M.; Díaz, J. F.; Gil, R.; de Pereda, J. M.; García de Lacoba, M.; Peyrot, V.; Briand, C.; Towns-Andrews, E.; Bordas, J. Solution structure of Taxotere-induced microtubules to 3-nm resolution: The change in protofilament number is linked to the binding of the Taxol side chain. *Journal of Biological Chemistry* **1994**, *269*, 31785–31792.

[117] Matesanz, R.; Rodríguez-Salarichs, J.; Pera, B.; Canales, A.; Andreu, J. M.; Jiménez-Barbero, J.; Bras, W.; Nogales, A.; Fang, W.-S.; Díaz, J. F. Modulation of microtubule interprotofilament interactions by modified taxanes. *Biophysical Journal* **2011**, *101*, 2970–2980.

[118] Forli, S. Epothilones: From discovery to clinical trials. *Current Topics in Medicinal Chemistry* **2014**, *14*, 2312–2321.

[119] Bollag, D. M.; McQueney, P. A.; Zhu, J.; Hensens, O.; Koupal, L.; Liesch, J.; Goetz, M.; Lazarides, E.; Woods, C. M. Epothilones, a new class of microtubule-stabilizing agents with a Taxol-like mechanism of action. *Cancer Research* **1995**, *55*, 2325–2333.

[120] Mulzer, J. Epothilone B and its derivatives as novel antitumor drugs: Total and partial synthesis and biological evaluation. *Monatshefte Für Chemie* **2000**, *131*, 205–238.

[121] Hofle, G. H.; Bedorf, N.; Steinmetz, H.; Schomburg, D.; Gerth, K.; Reichenbach, H. Epothilone A and B—Novel 16-membered macrolides with cytotoxic activity: Isolation, crystal structure, and conformation in solution. *Angewandte Chemie International Edition* **1996**, *35*, 1567–1569.

[122] Kowalski, R. J.; Giannakakou, P.; Hamel, E. Activities of the microtubule-stabilizing agents epothilones A and B with purified tubulin and in cells resistant to paclitaxel (Taxol). *Journal of Biological Chemistry* **1997**, *272*, 2534–2541.

[123] Lechleider, R. J.; Kaminskas, E.; Jiang, X.; Aziz, R.; Bullock, J.; Kasliwal, R.; Harapanhalli, R.; Pope, S.; Sridhara, R.; Leighton, J. et al. Ixabepilone in combination with capecitabine and as monotherapy for treatment of advanced breast cancer refractory to previous chemotherapies. *Clinical Cancer Research* **2008**, *14*, 4378–4384.

[124] Martello, L. A.; McDaid, H. M.; Regl, D. L.; Yang, C. P. H.; Meng, D. F.; Pettus, T. R. R.; Kaufman, M. D.; Arimoto, H.; Danishefsky, S. J.; Smith, A. B. et al. Taxol and discodermolide represent a synergistic drug combination in human carcinoma cell lines. *Clinical Cancer Research* **2000**, *6*, 1978–1987.

[125] Khrapunovich-Baine, M.; Menon, V.; Verdier-Pinard, P.; Smith, I., Amos B.; Angeletti, R. H.; Fiser, A.; Horwitz, S. B.; Xiao, H. Distinct pose of discodermolide in Taxol binding pocket drives a complementary mode of microtubule stabilization. *Biochemistry* **2009**, *48*, 11664–11677.

[126] ter Haar, E.; Kowalski, R. J.; Hamel, E.; Lin, C. M.; Longley, R. E.; Gunasekera, S. P.; Rosenkranz, H. S.; Day, B. W. Discodermolide, a cytotoxic

marine agent that stabilizes microtubules more potently than Taxol. *Biochemistry* **1996**, *35*, 243–250.

[127] Kowalski, R. J.; Giannakakou, P.; Gunasekera, S. P.; Longley, R. E.; Day, B. W.; Hamel, E. The microtubule-stabilizing agent discodermolide competitively inhibits the binding of paclitaxel (Taxol) to tubulin polymers, enhances tubulin nucleation reactions more potently than paclitaxel, and inhibits the growth of paclitaxel-resistant cells. *Molecular Pharmacology* **1997**, *52*, 613–622.

[128] Corley, D. G.; Herb, R.; Moore, R. E.; Scheuer, P. J.; Paul, V. J. Laulimalides: New potent cytotoxic macrolides from a marine sponge and a nudibranch predator. *Journal of Organic Chemistry* **1988**, *53*, 3644–3646.

[129] Quiñoá, E.; Kakou, Y.; Crews, P. Fijianolides, polyketide heterocycles from a marine sponge. *Journal of Organic Chemistry* **1988**, *53*, 3642–3644.

[130] Jefford, C. W.; Bernardinelli, G.; Tanaka, J.-I.; Higa, T. Structures and absolute configurations of the marine toxins, latrunculin A and laulimalide. *Tetrahedron Letters* **1996**, *37*, 159–162.

[131] West, L. M.; Northcote, P. T.; Battershill, C. N. Peloruside A: A potent cytotoxic macrolide isolated from the New Zealand marine sponge Mycale sp. *The Journal of Organic Chemistry* **2000**, *65*, 445–449.

[132] Kanakkanthara, A.; Wilmes, A.; O'Brate, A.; Escuin, D.; Chan, A.; Gjyrezi, A.; Crawford, J.; Rawson, P.; Kivell, B.; Northcote, P. T. et al. Peloruside- and laulimalide-resistant human ovarian carcinoma cells have β-tubulin mutations and altered expression of βII- and βIII-tubulin isotypes. *Molecular Cancer Therapeutics* **2011**, *10*, 1419–1429.

[133] Pryor, D. E.; O'Brate, A.; Bilcer, G.; Díaz, J. F.; Wang, Y.; Wang, Y.; Kabaki, M.; Jung, M. K.; Andreu, J. M.; Ghosh, A. K. et al. The microtubule stabilizing agent laulimalide does not bind in the taxoid site, kills cells resistant to paclitaxel and epothilones, and may not require its epoxide moiety for activity. *Biochemistry* **2002**, *41*, 9109–9115.

[134] Gapud, E. J.; Bai, R. L.; Ghosh, A. K.; Hamel, E. Laulimalide and paclitaxel: A comparison of their effects on tubulin assembly and their synergistic action when present simultaneously. *Molecular Pharmacology* **2004**, *66*, 113–121.

[135] Gaitanos, T. N.; Buey, R. M.; Díaz, J. F.; Northcote, P. T.; Teesdale-Spittle, P.; Andreu, J. M.; Miller, J. H. Peloruside A does not bind to the taxoid site on β-tubulin and retains its activity in multidrug-resistant cell lines. *Cancer Research* **2004**, *64*, 5063–5067.

[136] Hamel, E.; Day, B. W.; Miller, J. H.; Jung, M. K.; Northcote, P. T.; Ghosh, A. K.; Curran, D. P.; Cushman, M.; Nicolaou, K. C.; Paterson, I. et al. Synergistic effects of peloruside A and laulimalide with taxoid site drugs, but not with each other, on tubulin assembly. *Molecular Pharmacology* **2006**, *70*, 1555–1564.

[137] Hood, K. A.; West, L. M.; Rouwe, B.; Northcote, P. T.; Berridge, M. V.; Wakefield, S. J.; Miller, J. H. Peloruside A, a novel antimitotic agent with paclitaxel-like microtubule-stabilizing activity. *Cancer Research* **2002**, *62*, 3356–3360.

[138] Clark, E. A.; Hills, P. M.; Davidson, B. S.; Wender, P. A.; Mooberry, S. L. Laulimalide and synthetic laulimalide analogues are synergistic with paclitaxel and 2-methoxyestradiol. *Molecular Pharmaceutics* **2006**, *3*, 457–467.

[139] Wilmes, A.; O'Sullivan, D.; Chan, A.; Chandrahasen, C.; Paterson, I.; Northcote, P. T.; La Flamme, A. C.; Miller, J. H. Synergistic interactions between peloruside A and other microtubule-stabilizing and destabilizing agents in cultured human ovarian carcinoma cells and murine T cells. *Cancer Chemotherapy and Pharmacology* **2011**, *68*, 117–126.

[140] Thepchatri, P.; Cicero, D. O.; Monteagudo, E.; Ghosh, A. K.; Cornett, B.; Weeks, E. R.; Snyder, J. P. Conformations of laulimalide in DMSO-d6. *Journal of the American Chemical Society* **2005**, *127*, 12838–12846.

[141] Jiménez-Barbero, J.; Canales, A.; Northcote, P. T.; Buey, R. M.; Andreu, J. M.; Díaz, J. F. NMR determination of the bioactive conformation of peloruside A

bound to microtubules. *Journal of the American Chemical Society* **2006**, *128*, 8757–8765.

[142] Bennett, M. J.; Barakat, K.; Huzil, J. T.; Tuszynski, J.; Schriemer, D. C. Discovery and characterization of the laulimalide-microtubule binding mode by mass shift perturbation mapping. *Chemistry & Biology (Oxford, United Kingdom)* **2010**, *17*, 725–734.

[143] Nguyen, T. L.; Xu, X.; Gussio, R.; Ghosh, A. K.; Hamel, E. The assembly-inducing laulimalide/peloruside A binding site on tubulin: Molecular modeling and biochemical studies with [³H]peloruside A. *Journal of Chemical Information and Modeling* **2010**, *50*, 2019–2028.

[144] Liu, J. K.; Towle, M. J.; Cheng, H. S.; Saxton, P.; Reardon, C.; Wu, J. Y.; Murphy, E. A.; Kuznetsov, G.; Johannes, C. W.; Tremblay, M. R. et al. In vitro and in vivo anticancer activities of synthetic (–)-laulimalide, a marine natural product microtubule stabilizing agent. *Anticancer Research* **2007**, *27*, 1509–1518.

[145] Mooberry, S. L.; Hilinski, M. K.; Clark, E. A.; Wender, P. A. Function-oriented synthesis: biological evaluation of laulimalide analogues derived from a last step cross metathesis diversification strategy. *Molecular Pharmaceutics* **2008**, *5*, 829–838.

[146] Lu, H.; Murtagh, J.; Schwartz, E. L. The microtubule binding drug laulimalide inhibits vascular endothelial growth factor-induced human endothelial cell migration and is synergistic when combined with docetaxel (Taxotere). *Molecular Pharmacology* **2006**, *69*, 1207–1215.

[147] Gollner, A.; Altmann, K.-H.; Gertsch, J.; Mulzer, J. Synthesis and biological evaluation of a des-dihydropyran laulimalide analog. *Tetrahedron Letters* **2009**, *50*, 5790–5792.

[148] Mulzer, J.; Öhler, E. Microtubule-stabilizing marine metabolite laulimalide and its derivatives: Synthetic approaches and antitumor activity. *Chemical Reviews* **2003**, *103*, 3753–3786.

172

[149] Paterson, I.; Menche, D.; Håkansson, A. E.; Longstaff, A.; Wong, D.; Barasoain, I.; Buey, R. M.; Díaz, J. F. Design, synthesis and biological evaluation of novel, simplified analogues of laulimalide: modification of the side chain. *Bioorganic & Medicinal Chemistry Letters* **2005**, *15*, 2243–2247.

[150] Wender, P. A.; Hegde, S. G.; Hubbard, R. D.; Zhang, L.; Mooberry, S. L. Synthesis and biological evaluation of (–)-laulimalide analogues. *Organic Letters* **2003**, *5*, 3507–3509.

[151] Gallagher Jr, B. M.; Fang, F. G.; Johannes, C. W.; Pesant, M.; Tremblay, M. R.; Zhao, H.; Akasaka, K.; Li, X.-Y.; Liu, J.; Littlefield, B. A. Synthesis and biological evaluation of (–)-laulimalide analogues. *Bioorganic & Medicinal Chemistry Letters* **2004**, *14*, 575–579.

[152] Mooberry, S. L.; Randall-Hlubek, D. A.; Leal, R. M.; Hegde, S. G.; Hubbard, R. D.; Zhang, L.; Wender, P. A. Microtubule-stabilizing agents based on designed laulimalide analogues. *Proceedings of the National Academy of Sciences* **2004**, *101*, 8803–8808.

[153] Wender, P. A.; Hilinski, M. K.; Skaanderup, P. R.; Soldermann, N. G.; Mooberry, S. L. Pharmacophore mapping in the laulimalide series: Total synthesis of a vinylogue for a late-stage metathesis diversification strategy. *Organic Letters* **2006**, *8*, 4105–4108.

[154] Wermuth, G.; Ganellin, C. R.; Lindberg, P.; Mitscher, L. A. Glossary of terms used in medicinal chemistry (IUPAC Recommendations 1998). *Pure and Applied Chemistry* **1998**, *70*, 1129–1143.

[155] Sato, B.; Muramatsu, H.; Miyauchi, M.; Hori, Y.; Takase, S.; Hino, M.; Hashimoto, S.; Terano, H. A new antimitotic substance, FRI82877 I. Taxonomy, fermentation, isolation, physico-chemical properties and biological activities. *Journal of Antibiotics* **2000**, *53*, 123–130.

[156] Sato, B.; Nakajima, H.; Hori, Y.; Hino, M.; Hashimoto, S.; Terano, H. A new antimitotic substance, FR182877 II. The mechanism of action. *Journal of Antibiotics* **2000**, *53*, 204–206.

[157] Edler, M. C.; Buey, R. M.; Gussio, R.; Marcus, A. I.; Vanderwal, C. D.; Sorensen, E. J.; Díaz, J. F.; Giannakakou, P.; Ernest, H. Cyclostreptin (FR182877), an antitumor tubulin-polymerizing agent deficient in enhancing tubulin assembly despite its high affinity for the taxoid site. *Biochemistry* **2005**, *44*, 11525–11538.

[158] Vanderwal, C. D.; Vosburg, D. A.; Weiler, S.; Sorensen, E. J. An enantioselective synthesis of FR182877 provides a chemical rationalization of its structure and affords multigram quantities of its direct precursor. *Journal of the American Chemical Society* **2003**, *125*, 5393–5407.

[159] Calvo, E.; Barasoain, I.; Matesanz, R.; Pera, B.; Camafeita, E.; Pineda, O.; Hamel, E.; Vanderwal, C. D.; Andreu, J. M.; López, J. A. et al. Cyclostreptin derivatives specifically target cellular tubulin and further map the paclitaxel site. *Biochemistry* **2011**, *51*, 329–341.

[160] Chen, Z.-L.; Wang, B.-D.; Chen, M.-Q. Steroidal bitter principles from Tacca plantaginea structures of taccalonolide A and B. *Tetrahedron Letters* **1987**, *28*, 1673–1675.

[161] Chen, Z.-L.; Wang, B.-D.; Shen, J.-H. Taccalonolide-C and taccalonolide-D, 2 pentacyclic steroids of Tacca plantginea. *Phytochemistry* **1988**, *27*, 2999–3001.

[162] Shen, J.-H.; Chen, Z.-L.; Gao, Y.-S. The pentacyclic steroidal constituents of Tacca plantaginea: taccalonolide E and F. *Chinese Journal of Chemistry* **1991**, *9*, 92–94.

[163] Shen, J.-H.; Chen, Z.-L.; Gao, Y.-S. Taccalonolides from Tacca plantaginea. *Phytochemistry* **1996**, *42*, 891–893.

[164] Chen, Z.-L.; Shen, J.-H.; Gao, Y.-S.; Wichtl, M. Five Taccalonolides from Tacca plantaginea. *Planta Med* **1997**, *63*, 40–43.

[165] Mühlbauer, A.; Seip, S.; Nowak, A.; Tran, V. Five novel taccalonolides from the roots of the vietnamese plant Tacca paxiana. *Helvetica Chimica Acta* **2003**, *86*, 2065–2072.

[166] Yang, J.-Y.; Zhao, R.-H.; Chen, C.-X.; Ni, W.; Teng, F.; Hao, X.-J.; Liu, H.-Y. Taccalonolides W – Y, three new pentacyclic steroids from Tacca plantaginea. *Helvetica Chimica Acta* **2008**, *91*, 1077–1082.

[167] Rohena, C. C.; Mooberry, S. L. Recent progress with microtubule stabilizers: new compounds, binding modes and cellular activities. *Natural Product Reports* **2014**, *31*, 335–355.

[168] Li, J.; Risinger, A. L.; Mooberry, S. L. Taccalonolide microtubule stabilizers. *Bioorganic & Medicinal Chemistry* **2014**, *22*, 5091–5096.

[169] Tinley, T. L.; Randall-Hlubek, D. A.; Leal, R. M.; Jackson, E. M.; Cessac, J. W.; Quada, J. C.; Hemscheidt, T. K.; Mooberry, S. L. Taccalonolides E and A: Plant-derived steroids with microtubule-stabilizing activity. *Cancer Research* **2003**, *63*, 3211–3220.

[170] Risinger, A. L.; Mooberry, S. L. Taccalonolides: Novel microtubule stabilizers with clinical potential. *Cancer Letters* **2010**, *291*, 14–19.

[171] Li, J.; Risinger, A. L.; Peng, J.; Chen, Z.; Hu, L.; Mooberry, S. L. Potent taccalonolides, AF and AJ, inform significant structure-activity relationships and tubulin as the binding site of these microtubule stabilizers. *Journal of the American Chemical Society* **2011**, *133*, 19064–19067.

[172] Peng, J.; Risinger, A. L.; Fest, G. A.; Jackson, E. M.; Helms, G.; Polin, L. A.; Mooberry, S. L. Identification and biological activities of new taccalonolide microtubule stabilizers. *Journal of Medicinal Chemistry* **2011**, *54*, 6117–6124.

[173] Risinger, A. L.; Natarajan, M.; Thomas, J., Charles R.; Mooberry, S. L. The taccalonolides, novel microtubule stabilizers, and gamma-radiation have additive effects on cellular viability. *Cancer Letters* **2011**, *307*, 104–111.

[174] Risinger, A. L.; Mooberry, S. L. Cellular studies reveal mechanistic differences between taccalonolide A and paclitaxel. *Cell Cycle* **2011**, *10*, 2162–2171.

[175] Li, J.; Peng, J.; Risinger, A. L.; Mooberry, S. L. Hydrolysis reactions of the taccalonolides reveal structure–activity relationships. *Journal of Natural Products* **2013**, *76*, 1369–1375.

[176] Risinger, A. L.; Li, J.; Bennett, M. J.; Rohena, C. C.; Peng, J.; Schriemer, D. C.; Mooberry, S. L. Taccalonolide binding to tubulin imparts microtubule stability and potent in vivo activity. *Cancer Research* **2013**, *73*, 6780–92.

[177] Rohena, C. C.; Peng, J.; Johnson, T. A.; Crews, P.; Mooberry, S. L. Chemically diverse microtubule stabilizing agents initiate distinct mitotic defects and dys-regulated expression of key mitotic kinases. *Biochemical Pharmacology* **2013**, *85*, 1104–1114.

[178] Risinger, A. L.; Riffle, S. M.; Lopus, M.; Jordan, M. A.; Wilson, L.; Mooberry, S. L. The taccalonolides and paclitaxel cause distinct effects on microtubule dynamics and aster formation. *Molecular Cancer* **2014**, *13*.

[179] Haber, M.; Burkhart, C. A.; Regl, D. L.; Madafiglio, J.; Norris, M. D.; Horwitz, S. B. Altered expression of M2, the Class II-tubulin isotype, in a murine J774.2 cell line with a high level of Taxol resistance. *Journal of Biological Chemistry* **1995**, *270*, 31269–31275.

[180] Verdier-Pinard, P.; Wang, F.; Martello, L.; Burd, B.; Orr, G. A.; Horwitz, S. B. Analysis of tubulin isotypes and mutations from Taxol-resistant cells by combined isoelectrofocusing and mass spectrometry. *Biochemistry* **2003**, *42*, 5349–5357.

[181] Field, J. J.; Pera, B.; Calvo, E.; Canales, A.; Zurwerra, D.; Trigili, C.; Rodríguez-Salarichs, J.; Matesanz, R.; Kanakkanthara, A.; Wakefield, S. J. et al. Zampanolide, a potent new microtubule-stabilizing agent, covalently reacts with the taxane luminal site in tubulin α,β-heterodimers and microtubules. *Chemistry & Biology* **2012**, *19*, 686–698.

[182] Fojo, T.; Menefee, M. Mechanisms of multidrug resistance: The potential role of microtubule-stabilizing agents. *Annals of Oncology* **2007**, *18*, v3–v8.

[183] Kavallaris, M. Microtubules and resistance to tubulin-binding agents. *Nature Reviews Cancer* **2010**, *10*, 194–204.

[184] Huzil, J. T.; Ludueña, R. F.; Tuszynski, J. Comparative modelling of human β tubulin isotypes and implications for drug binding. *Nanotechnology* **2006**, *17*, S90.

[185] Carpenter, E. J.; Huzil, J. T.; Ludueña, R. F.; Tuszynski, J. A. Homology modeling of tubulin: Influence predictions for microtubule's biophysical properties. *European Biophysics Journal* **2006**, *36*, 35–43.

[186] Sullivan, K. F.; Cleveland, D. W. Identification of conserved isotype: Defining variable region sequences for 4 verterbrate β tubulin polypeptide classes. *Proceedings of the National Academy of Sciences* **1986**, *83*, 4327–4331.

[187] Panda, D.; Miller, H. P.; Banerjee, A.; Ludueña, R. F.; Wilson, L. Microtubule dynamics in vitro are regulated by the tubulin isotype composition. *Proceedings of the National Academy of Sciences* **1994**, *91*, 11358–11362.

[188] Huzil, J. T.; Chen, K.; Kurgan, L.; Tuszynski, J. A. The roles of β-tubulin mutations and isotype expression in acquired drug resistance. *Cancer Informatics* **2007**, *3*, 159–81.

[189] Burkhart, C. A.; Kavallaris, M.; Horwitz, S. B. The role of β-tubulin isotypes in resistance to antimitotic drugs. *Biochimica et Biophysica Acta - Reviews on Cancer* **2001**, *1471*, O1–O9.

[190] Kavallaris, M.; Kuo, D. Y. S.; Burkhart, C. A.; Regl, D. L.; Norris, M. D.; Haber, M.; Horwitz, S. B. Taxol-resistant epithelial ovarian tumors are associated with altered expression of specific β-tubulin isotypes. *Journal of Clinical Investigation* **1997**, *100*, 1282–1293.

[191] Sève, P.; Dumontet, C. Is class III β-tubulin a predictive factor in patients receiving tubulin-binding agents? *Lancet Oncology* **2008**, *9*, 168–175.

[192] St. George, M.; Ayoub, A. T.; Banerjee, A.; Churchill, C. D. M.; Winter, P.; Klobukowski, M.; Cass, C. E.; Ludueña, R. F.; Tuszynski, J. A.; Damaraju, S.

Designing and testing of novel taxanes to probe the highly complex mechanisms by which taxanes bind to microtubules and cause cytotoxicity to cancer cells. *PLoS ONE* **2015**, *10*, e0129168.

[193] Khan, I. A.; Ludueña, R. F. Different effects of vinblastine on the polymerization of isotypically purified tubulins from bovine brain. *Investigational New Drugs* **2003**, *21*, 3–13.

[194] Berrieman, H. K.; Lind, M. J.; Cawkwell, L. Do β-tubulin mutations have a role in resistance to chemotherapy? *Lancet Oncology* **2004**, *5*, 158–164.

[195] Giannakakou, P.; Sackett, D. L.; Kang, Y.-K.; Zhan, Z.; Buters, J. T. M.; Fojo, T.; Poruchynsky, M. S. Paclitaxel-resistant human ovarian cancer cells have mutant β-tubulins that exhibit impaired paclitaxel-driven polymerization. *Journal of Biological Chemistry* **1997**, *272*, 17118–17125.

[196] Giannakakou, P.; Gussio, R.; Nogales, E.; Downing, K. H.; Zaharevitz, D.; Bollbuck, B.; Poy, G.; Sackett, D.; Nicolaou, K. C.; Fojo, T. A common pharmacophore for epothilone and taxanes: Molecular basis for drug resistance conferred by tubulin mutations in human cancer cells. *Proceedings of the National Academy of Sciences* **2000**, *97*, 2904–2909.

[197] He, L. F.; Yang, C. P. H.; Horwitz, S. B. Mutations in β-tubulin map to domains involved in regulation of microtubule stability in epothilone-resistant cell lines. *Molecular Cancer Therapeutics* **2001**, *1*, 3–10.

[198] Orr, G. A.; Verdier-Pinard, P.; McDaid, H.; Horwitz, S. B. Mechanisms of Taxol resistance related to microtubules. *Oncogene* **2003**, *22*, 7280–7295.

[199] Verrills, N. M.; Flemming, C. L.; Liu, M.; Ivery, M. T.; Cobon, G. S.; Norris, M. D.; Haber, M.; Kavallaris, M. Microtubule alterations and mutations induced by desoxyepothilone B: Implications for drug-target interactions. *Chemistry & Biology* **2003**, *10*, 597–607.

[200] Yang, C. P. H.; Verdier-Pinard, P.; Wang, F.; Lippaine-Horvath, E.; He, L. F.; Li, D. S.; Hofle, G.; Ojima, I.; Orr, G. A.; Horwitz, S. B. A highly epothilone B-

resistant A549 cell line with mutations in tubulin that confer drug dependence. *Molecular Cancer Therapeutics* **2005**, *4*, 987–995.

[201] Yin, S. H.; Zeng, C. Q.; Hari, M.; Cabral, F. Random mutagenesis of β-tubulin defines a set of dispersed mutations that confer paclitaxel resistance. *Pharmaceutical Research* **2012**, *29*, 2994–3006.

[202] Yin, S. H.; Zeng, C. Q.; Hari, M.; Cabral, F. Paclitaxel resistance by random mutagenesis of α-tubulin. *Cytoskeleton* **2013**, *70*, 849–862.

[203] Natarajan, K.; Senapati, S. Understanding the basis of drug resistance of the mutants of $\alpha\beta$-tubulin dimer via molecular dynamics simulations. *PLoS ONE* **2012**, *7*, e42351.

[204] Tuszynski, J.; Craddock, T.; Mane, J.; Barakat, K.; Tseng, C.-Y.; Gajewski, M.; Winter, P.; Alisaraie, L.; Patterson, J.; Carpenter, E. et al. Modeling the yew tree tubulin and a comparison of its interaction with paclitaxel to human tubulin. *Pharmaceutical Research* **2012**, *29*, 1–15.

[205] Nobili, S.; Landini, I.; Mazzei, T.; Mini, E. Overcoming tumor multidrug resistance using drugs able to evade P-glycoprotein or to exploit its expression. *Medicinal Research Reviews* **2012**, *32*, 1220–1262.

[206] Cornell, W. D.; Cieplak, P.; Bayly, C. I.; Gould, I. R.; Merz, K. M.; Ferguson, D. M.; Spellmeyer, D. C.; Fox, T.; Caldwell, J. W.; Kollman, P. A. A second generation force field for the smulation of proteins, nucleic acids, and organic molecules. *Journal of the American Chemical Society* **1995**, *117*, 5179–5197.

[207] Salomon-Ferrer, R.; Case, D. A.; Walker, R. C. An overview of the Amber biomolecular simulation package. *Wiley Interdisciplinary Reviews: Computational Molecular Science* **2013**, *3*, 198–210.

[208] Hornak, V.; Abel, R.; Okur, A.; Strockbine, B.; Roitberg, A.; Simmerling, C. Comparison of multiple Amber force fields and development of improved protein

backbone parameters. *Proteins: Structure, Function, and Bioinformatics* **2006**, *65*, 712–725.

[209] Wang, J. M.; Wolf, R. M.; Caldwell, J. W.; Kollman, P. A.; Case, D. A. Development and testing of a general amber force field. *Journal of Computational Chemistry* **2004**, *25*, 1157–1174.

[210] Zaleśny, R., Papadopoulous, M., Meezy, P., Leszczynski, J., Eds. *Linear-Scaling Techniques in Computational Chemistry and Physics: Methods and Applications*; Challenges and Advances in Computational Chemistry and Physics; Springer: New York, 2011; Vol. 13.

[211] Kussmann, J.; Beer, M.; Ochsenfeld, C. Linear-scaling self-consistent field methods for large molecules. *Wiley Interdisciplinary Reviews: Computational Molecular Science* **2013**, *3*, 614–636.

[212] Gordon, M. S.; Mullin, J. M.; Pruitt, S. R.; Roskop, L. B.; Slipchenko, L. V.; Boatz, J. A. Accurate methods for large molecular systems. *The Journal of Physical Chemistry B* **2009**, *113*, 9646–9663.

[213] Gordon, M. S.; Fedorov, D. G.; Pruitt, S. R.; Slipchenko, L. V. Fragmentation methods: A route to accurate calculations on large systems. *Chemical Reviews* **2012**, *112*, 632–672.

[214] Fedorov, D. G.; Kitaura, K. The importance of three-body terms in the Fragment Molecular Orbital method. *The Journal of Chemical Physics* **2004**, *120*, 6832–6840.

[215] Fedorov, D.; Kitaura, K. In *The Fragment Molecular Orbital Method: Practical Applications to Large Molecular Systems*; Fedorov, D., Kitaura, K., Eds.; CRC Press: New York, 2009; pp 5–36.

[216] Fedorov, D. G.; Kitaura, K. In *Modern Methods for Theoretical Physical Chemistry of Biopolymers*; Starikov, E., Lewis, J., Tanaka, S., Eds.; Elsevier, 2006; Chapter 1, pp 3–38.

[217] Fedorov, D. G., Kitaura, K., Eds. *The Fragment Molecular Orbital method: Practical applications to large molecular systems*; CRC Press: New York, 2009.

[218] Nakano, T.; Kaminuma, T.; Sato, T.; Fukuzawa, K.; Akiyama, Y.; Uebayasi, M.; Kitaura, K. Fragment Molecular Orbital method: Use of approximate electrostatic potential. *Chemical Physics Letters* **2002**, *351*, 475–480.

[219] Fedorov, D. G.; Ishimura, K.; Ishida, T.; Kitaura, K.; Pulay, P.; Nagase, S. Accuracy of the three-body Fragment Molecular Orbital method applied to Møller–Plesset perturbation theory. *Journal of Computational Chemistry* **2007**, *28*, 1476–1484.

[220] Schmidt, M. W.; Baldridge, K. K.; Boatz, J. A.; Elbert, S. T.; Gordon, M. S.; Jensen, J. H.; Koseki, S.; Matsunaga, N.; Nguyen, K. A.; Su, S. et al. General atomic and molecular electronic structure system. *Journal of Computational Chemistry* **1993**, *14*, 1347–1363.

[221] Fedorov, D. G.; Kitaura, K. Pair interaction energy decomposition analysis. *Journal of Computational Chemistry* **2007**, *28*, 222–237.

[222] Fedorov, D. G.; Kitaura, K. Energy decomposition analysis in solution based on the Fragment Molecular Orbital method. *The Journal of Physical Chemistry A* **2012**, *116*, 704–719.

[223] Cossi, M.; Barone, V.; Cammi, R.; Tomasi, J. Ab initio study of solvated molecules: A new implementation of the polarizable continuum model. *Chemical Physics Letters* **1996**, *255*, 327–335.

[224] Barone, V.; Cossi, M.; Tomasi, J. A new definition of cavities for the computation of solvation free energies by the polarizable continuum model. *Journal of Chemical Physics* **1997**, *107*, 3210–3221.

[225] Cances, E.; Mennucci, B.; Tomasi, J. A new integral equation formalism for the polarizable continuum model: Theoretical background and applications to isotropic and anisotropic dielectrics. *Journal of Chemical Physics* **1997**, *107*, 3032–3041.

[226] Mennucci, B.; Tomasi, J. Continuum solvation models: A new approach to the problem of solute's charge distribution and cavity boundaries. *Journal of Chemical Physics* **1997**, *106*, 5151–5158.

[227] Cramer, C. J.; Truhlar, D. G. Implicit solvation models: Equilibria, structure, spectra, and dynamics. *Chemical Reviews* **1999**, *99*, 2161–2200.

[228] Cossi, M.; Scalmani, G.; Rega, N.; Barone, V. New developments in the polarizable continuum model for quantum mechanical and classical calculations on molecules in solution. *Journal of Chemical Physics* **2002**, *117*, 43–54.

[229] Cossi, M.; Rega, N.; Scalmani, G.; Barone, V. Energies, structures, and electronic properties of molecules in solution with the C-PCM solvation model. *Journal of Computational Chemistry* **2003**, *24*, 669–681.

[230] Marenich, A. V.; Cramer, C. J.; Truhlar, D. G. Universal solvation model based on solute electron density and on a continuum model of the solvent defined by the bulk dielectric constant and atomic surface tensions. *Journal of Physical Chemistry B* **2009**, *113*, 6378–6396.

[231] Fedorov, D. G.; Kitaura, K.; Li, H.; Jensen, J. H.; Gordon, M. S. The polarizable continuum model (PCM) interfaced with the Fragment Molecular Orbital method (FMO). *Journal of Computational Chemistry* **2006**, *27*, 976–985.

[232] Meagher, K. L.; Redman, L. T.; Carlson, H. A. Development of polyphosphate parameters for use with the AMBER force field. *Journal of Computational Chemistry* **2003**, *24*, 1016–1025.

[233] Jorgensen, W. L.; Chandrasekhar, J.; Madura, J. D.; Impey, R. W.; Klein, M. L. Comparison of simple potential functions for simulating liquid water. *The Journal of Chemical Physics* **1983**, *79*, 926–935.

[234] Joung, I. S.; Cheatham, T. E., III Determination of alkali and halide monovalent ion parameters for use in explicitly solvated biomolecular simulations. *The Journal of Physical Chemistry B* **2008**, *112*, 9020–9041.

[235] Joung, I. S.; Cheatham, T. E., III Molecular dynamics simulations of the dynamic and energetic properties of alkali and halide ions using water-model-specific ion parameters. *The Journal of Physical Chemistry B* **2009**, *113*, 13279–13290.

[236] Darden, T.; York, D.; Pedersen, L. Particle mesh Ewald: An N·log(N) method for Ewald sums in large systems. *The Journal of Chemical Physics* **1993**, *98*, 10089–10092.

[237] Essmann, U.; Perera, L.; Berkowitz, M. L.; Darden, T.; Lee, H.; Pedersen, L. G. A smooth particle mesh Ewald method. *The Journal of Chemical Physics* **1995**, *103*, 8577–8593.

[238] Crowley, M. F.; Darden, T. A.; Cheatham, T. E., III; Deerfield, D. W., III Adventures in improving the scaling and accuracy of a parallel molecular dynamics program. *The Journal of Supercomputing* **1997**, *11*, 255–278.

[239] Ryckaert, J.-P.; Ciccotti, G.; Berendsen, H. J. C. Numerical integration of the cartesian equations of motion of a system with constraints: Molecular dynamics of n-alkanes. *Journal of Computational Physics* **1977**, *23*, 327–341.

[240] Case, D. A.; Darden, T. A.; Cheatham, T. E., III; Simmerling, C. L.; Wang, J.; Duke, R. E.; Luo, R.; Walker, R. C.; Zhang, W.; Merz, K. M. et al. AMBER 12. 2012.

[241] Case, D.; Babin, V.; Berryman, J.; Betz, R.; Cai, Q.; Cerutti, D.; Cheatham, T. E., III; Darden, T.; Duke, R.; Gohlke, H. et al. AMBER 2015. 2015.

[242] Götz, A. W.; Williamson, M. J.; Xu, D.; Poole, D.; Le Grand, S.; Walker, R. C. Routine microsecond molecular dynamics simulations with AMBER on GPUs. 1. Generalized Born. *Journal of Chemical Theory and Computation* **2012**, *8*, 1542–1555.

[243] Le Grand, S.; Götz, A. W.; Walker, R. C. SPFP: Speed without compromise—

A mixed precision model for GPU accelerated molecular dynamics simulations. *Computer Physics Communications* **2013**, *184*, 374–380.

[244] Salomon-Ferrer, R.; Götz, A. W.; Poole, D.; Le Grand, S.; Walker, R. C. Routine microsecond molecular dynamics simulations with AMBER on GPUs. 2. Explicit solvent particle mesh Ewald. *Journal of Chemical Theory and Computation* **2013**, *9*, 3878–3888.

[245] Still, W. C.; Tempczyk, A.; Hawley, R. C.; Hendrickson, T. Semianalytical treatment of solvation for molecular mechanics and dynamics. *Journal of the American Chemical Society* **1990**, *112*, 6127–6129.

[246] Hawkins, G. D.; Cramer, C. J.; Truhlar, D. G. Parametrized models of aqueous free energies of solvation based on pairwise descreening of solute atomic charges from a dielectric medium. *The Journal of Physical Chemistry* **1996**, *100*, 19824–19839.

[247] Miller, B. R., III; McGee, T. D.; Swails, J. M.; Homeyer, N.; Gohlke, H.; Roitberg, A. E. MMPBSA.py: An efficient program for end-state free energy calculations. *Journal of Chemical Theory and Computation* **2012**, *8*, 3314–3321.

[248] Nguyen, H.; Roe, D. R.; Simmerling, C. Improved generalized Born solvent model parameters for protein simulations. *Journal of Chemical Theory and Computation* **2013**, *9*, 2020–2034.

[249] Hou, T.; Wang, J.; Li, Y.; Wang, W. Assessing the performance of the MM/PBSA and MM/GBSA methods. 1. The accuracy of binding free energy calculations based on molecular dynamics simulations. *Journal of Chemical Information and Modeling* **2011**, *51*, 69–82.

[250] Smith, D. A., Ed. *Metabolism, pharmacokinetics and toxicity of functional groups: Impact of the building blocks of medicinal chemistry on ADMET*; RSC Drug Discovery Series; RSC Publishing: Cambridge, UK, 2010.

[251] Alex, A. A.; Storer, R. I. In *Metabolism, pharmacokinetics and toxicity of functional groups: Impact of the building blocks of medicinal chemistry on ADMET*;

Smith, D. A., Ed.; RSC Drug Discovery Series; RSC Publishing: Cambridge, UK, 2010.

[252] ADMET Predictor™ version 7.0. Simulation Plus, Inc.: Lancaster, California 93534-7059; www.simulations-plus.com, 2014.

[253] Norinder, U.; Bergstrom, C. A. S. Prediction of ADMET properties. *ChemMed-Chem* **2006**, *1*, 920–937.

[254] Shao, J.; Tanner, S. W.; Thompson, N.; Cheatham, T. E., III Clustering Molecular Dynamics Trajectories: 1. Characterizing the Performance of Different Clustering Algorithms. *Journal of Chemical Theory and Computation* **2007**, *3*, 2312–2334.

[255] Frisch, M. J.; Trucks, G. W.; Schlegel, H. B.; Scuseria, G. E.; Robb, M. A.; Cheeseman, J. R.; Scalmani, G.; Barone, V.; Mennucci, B.; Petersson, G. A. et al. Gaussian 09, Revison A.02 ed. 2009.

[256] Kononova, O.; Kholodov, Y.; Theisen, K. E.; Marx, K. A.; Dima, R. I.; Ataullakhanov, F. I.; Grishchuk, E. L.; Barsegov, V. Tubulin bond energies and microtubule biomechanics determined from nanoindentation in silico. *Journal of the American Chemical Society* **2014**, *136*, 17036–17045.

[257] Kabsch, W.; Sander, C. Dictionary of protein secondary structure: Pattern recognition of hydrogen-bonded and geometrical features. *Biopolymers* **1983**, *22*, 2577–2637.

[258] Sparreboom, A.; van Asperen, J.; Mayer, U.; Schinkel, A. H.; Smit, J. W.; Meijer, D. K. F.; Borst, P.; Nooijen, W. J.; Beijnen, J. H.; van Tellingen, O. Limited oral bioavailability and active epithelial excretion of paclitaxel (Taxol) caused by P-glycoprotein in the intestine. *Proceedings of the National Academy of Sciences* **1997**, *94*, 2031–2035.

[259] Molecular Operating Environment (MOE), 2013.08. Chemical Computing Group Inc.: 1010 Sherbooke St. West, Suite #910, Montreal, QC, Canada, H3A 2R7, 2015.

[260] Cheng, Y.-C.; Prusoff, W. H. Relationship between the inhibition constant (K_I) and the concentration of inhibitor which causes 50 per cent inhibition (I_{50}) of an enzymatic reaction. *Biochemical Pharmacology* **1973**, *22*, 3099–3108.

[261] Olsson, M. H. M.; Søndergaard, C. R.; Rostkowski, M.; Jensen, J. H. PROPKA3: Consistent treatment of internal and surface residues in empirical pK_a predictions. *Journal of Chemical Theory and Computation* **2011**, *7*, 525–537.

[262] Snyder, J. P.; Nettles, J. H.; Cornett, B.; Downing, K. H.; Nogales, E. The binding conformation of Taxol in β-tubulin: A model based on electron crystallographic density. *Proceedings of the National Academy of Sciences* **2001**, *98*, 5312–5316.

[263] Vander Velde, D. G.; Georg, G. I.; Grunewald, G. L.; Gunn, C. W.; Mitscher, L. A. "Hydrophobic collapse" of Taxol and Taxotere solution conformations in mixtures of water and organic solvent. *Journal of the American Chemical Society* **1993**, *115*, 11650–11651.

[264] Gupta, M. L.; Bode, C. J.; Georg, G. I.; Himes, R. H. Understanding tubulin–Taxol interactions: Mutations that impart Taxol binding to yeast tubulin. *Proceedings of the National Academy of Sciences* **2003**, *100*, 6394–6397.

[265] Ayoub, A. T.; Craddock, T. J. A.; Klobukowski, M.; Tuszynski, J. Analysis of the strength of interfacial hydrogen bonds between tubulin dimers using quantum theory of atoms in molecules. *Biophysical Journal* **2014**, *107*, 740–750.

[266] Keskin, O.; Durell, S. R.; Bahar, I.; Jernigan, R. L.; Covell, D. G. Relating molecular flexibility to function: A case study of tubulin. *Biophysical Journal* **2002**, *83*, 663–680.

[267] Amos, L. A.; Löwe, J. The subtle allostery of microtubule dynamics. *Nature Structural & Molecular Biology* **2014**, *21*, 505–506.

186

[268] Elie-Caille, C.; Severin, F.; Helenius, J.; Howard, J.; Muller, D. J.; Hyman, A. A. Straight GDP-tubulin protofilaments form in the presence of Taxol. *Current Biology* **2007**, *17*, 1765–1770.

[269] Hobza, P. Calculations on noncovalent interactions and databases of benchmark interaction energies. *Accounts of Chemical Research* **2012**, *45*, 663–672.

[270] Fedorov, D. G.; Nagata, T.; Kitaura, K. Exploring chemistry with the Fragment Molecular Orbital method. *Physical Chemistry Chemical Physics* **2012**, *14*, 7562–7577.

[271] Yoshioka, A.; Fukuzawa, K.; Mochizuki, Y.; Yamashita, K.; Nakano, T.; Okiyama, Y.; Nobusawa, E.; Nakajima, K.; Tanaka, S. Prediction of probable mutations in influenza virus hemagglutinin protein based on large-scale ab initio Fragment Molecular Orbital calculations. *Journal of Molecular Graphics and Modelling* **2011**, *30*, 110–119.

[272] Hobza, P. The calculation of intermolecular interaction energies. *Annual Reports Section "C" (Physical Chemistry)* **2011**, *107*, 148–168.

[273] Sinnokrot, M. O.; Valeev, E. F.; Sherrill, C. D. Estimates of the ab initio limit for π–π interactions: The benzene dimer. *Journal of the American Chemical Society* **2002**, *124*, 10887–10893.

[274] Tauer, T. P.; Sherrill, C. D. Beyond the benzene dimer: An investigation of the additivity of π–π interactions. *The Journal of Physical Chemistry A* **2005**, *109*, 10475–10478.

[275] Sinnokrot, M. O.; Sherrill, C. D. High-accuracy quantum mechanical studies of π–π interactions in benzene dimers. *The Journal of Physical Chemistry A* **2006**, *110*, 10656–10668.

[276] Tsuzuki, S.; Honda, K.; Uchimaru, T.; Mikami, M.; Tanabe, K. Origin of attraction and directionality of the π–π interaction: Model chemistry calculations of benzene dimer interaction. *Journal of the American Chemical Society* **2001**, *124*, 104–112.

[277] Suenaga, M. Facio: New Computational Chemistry Environment for PC GAMESS. *Journal of Computer Chemistry, Japan* **2005**, *4*, 25–32.

[278] Suenaga, M. Development of GUI for GAMESS / FMO Calculation. *Journal of Computer Chemistry, Japan* **2008**, *7*, 33–54.

[279] Řezác, J.; Riley, K. E.; Hobza, P. S66: A well-balanced database of benchmark interaction energies relevant to biomolecular structures. *Journal of Chemical Theory and Computation* **2011**, *7*, 2427–2438.

[280] Craddock, T. J. A.; Hameroff, S. R.; Ayoub, A. T.; Klobukowski, M.; Tuszynski, J. A. Anesthetics act in quantum channels in brain microtubules to prevent consciousness. *Current Topics in Medicinal Chemistry* **2015**, *15*, 523–533.

[281] Friesen, D. E.; Craddock, T. J. A.; Kalra, A. P.; Tuszynski, J. A. Biological wires, communication systems, and implications for disease. *Biosystems* **2015**, *127*, 14–27.

Appendix A

Appendix to Chapter 2

Computational details of molecular dynamics simulations

Following the preparation of each complex, the following steps were taken:

1. 4000 steps of steepest descent minimization followed by 2000 steps of conjugate gradient minimization, with strong restraints on all solute atoms.
2. 8000 steps of steepest descent minimization followed by 4000 steps of conjugate gradient minimization, with no restraints.
3. Heating from 0 K to 100 K using the canonical ensemble for 40 ps using a time step of 1 fs, and weak restraints on all solute atoms.
4. Heating from 100 K to 300 K using the isothermal-isobaric ensemble for 200 ps using a time step of 1 fs, and weak restraints on all solute atoms.
5. At 300 K using the isothermal-isobaric ensemble to equilibrate the solvent density for 200 ps using a time step of 1 fs, with no restraints.
6. Production run at 300 K using the canonical ensemble and a time step of 2 fs with the SHAKE algorithm.
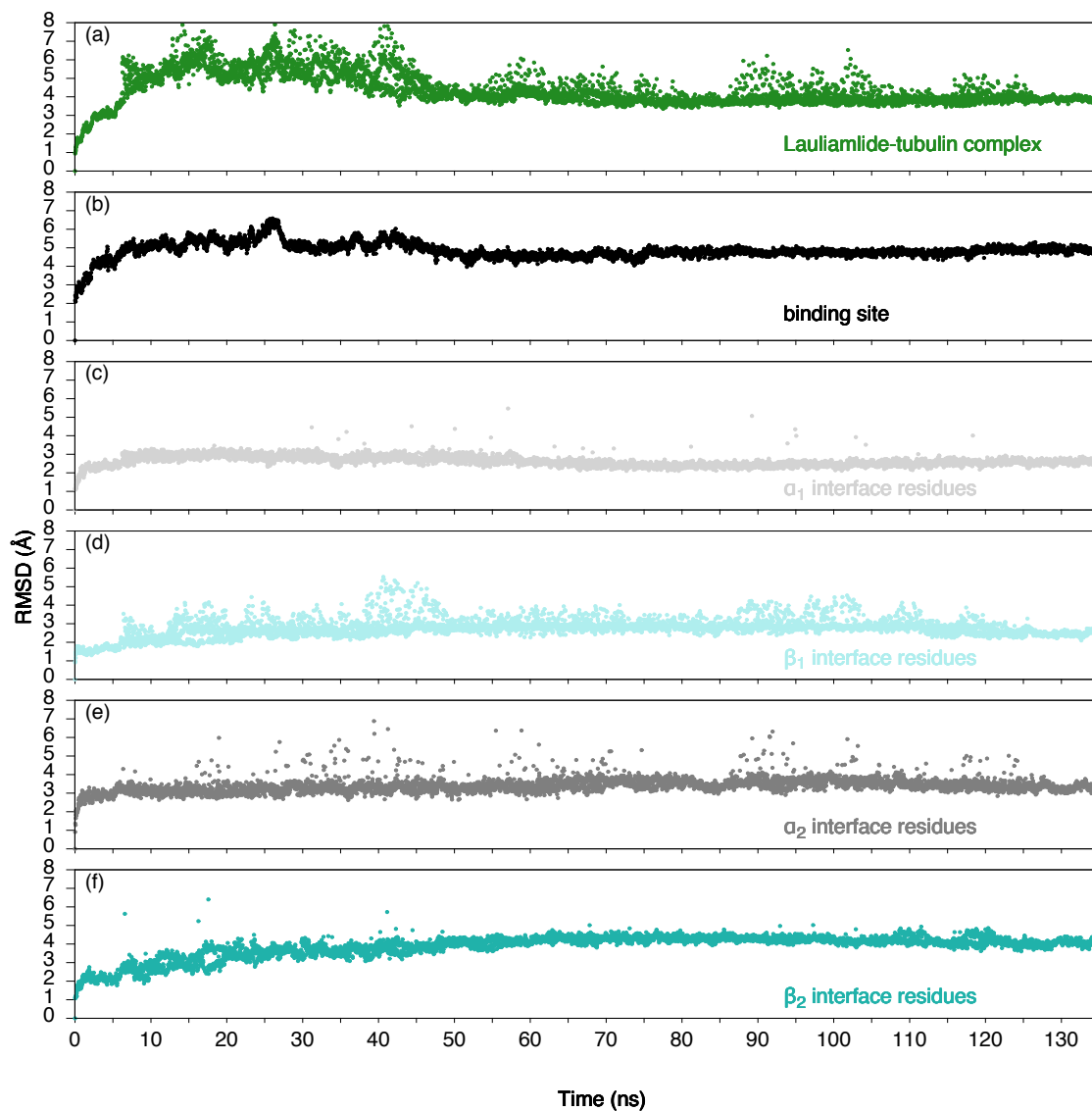
Figure A1: *Mass-weighted RMSD (Å) of (a) the backbone atoms in the LLM–(αβ-tubulin)$_2$ complex, (b) the binding site residues including LLM and nearby waters, and (c-f) residues that form the lateral contacts between the tubulin subunits.*
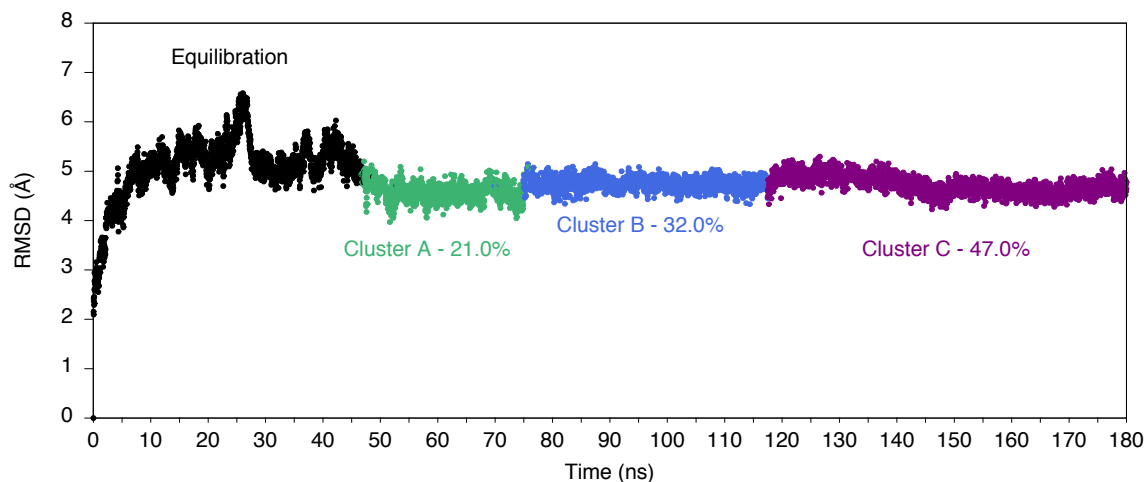
Figure A2: *Mass-weighted RMSD (Å) of the binding site atoms, coloured according to cluster, with occupancy indicated. Equilibration is shown in black. The binding site includes LLM, 20 water molecules and residues having atoms within 8 Å of LLM. Extension of the simulation up to 180 ns shows the same clusters as observed in Figure 2.3. Cluster populations over 45–180 ns are given.*
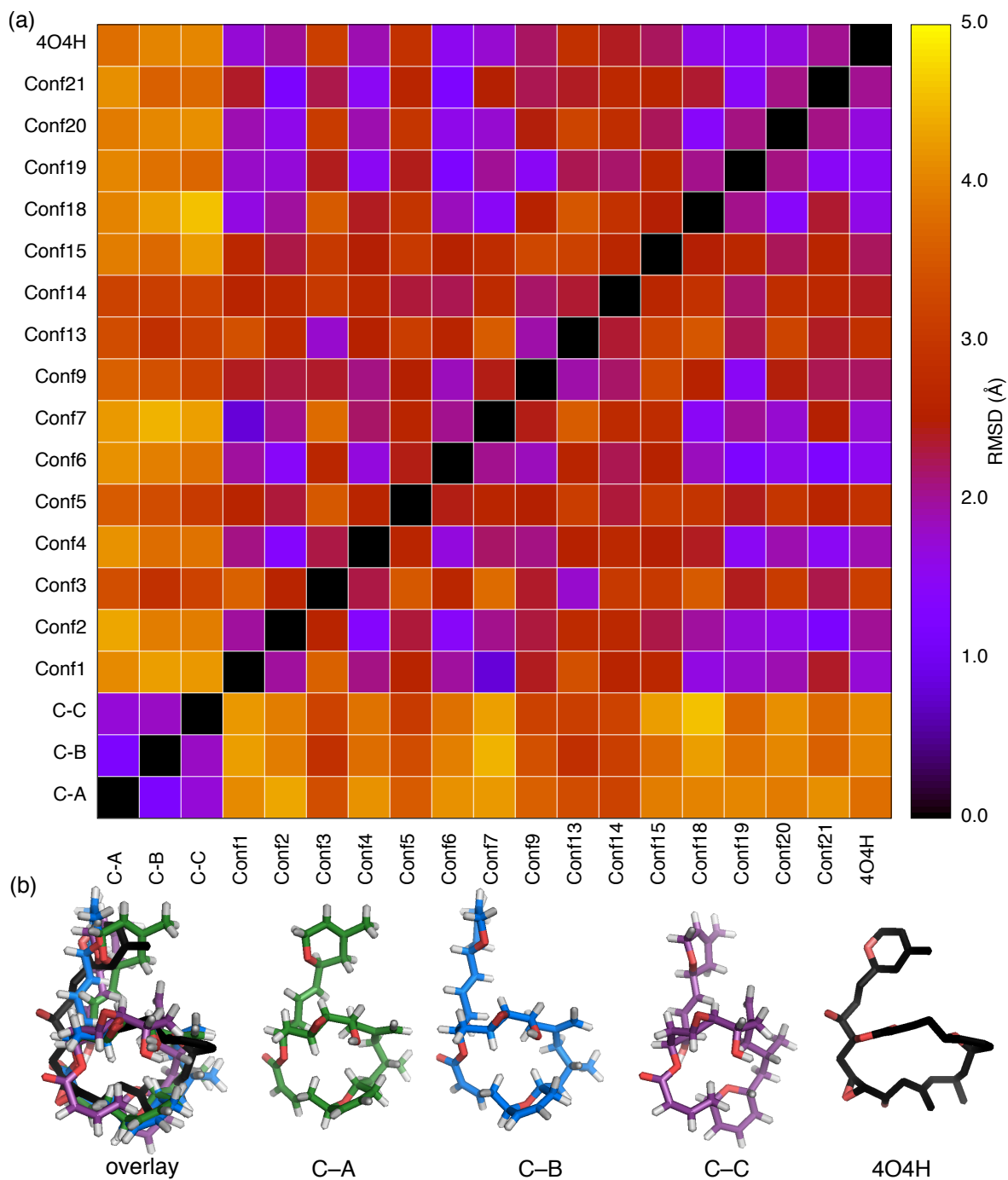
Figure A3: *Comparison of the conformation of LLM throughout the simulation with (a) the mass-weighted RMSD (Å) of LLM heavy atoms between different conformers and (b) an illustration of these conformers. C–A to C–C are the LLM conformations in the three representative clusters determined in this work. Conf1 to Conf21 represent the conformations reported by Thepchatri et al..[140] 4O4H is the conformation of LLM from the 4O4H crystal structure.[52]*
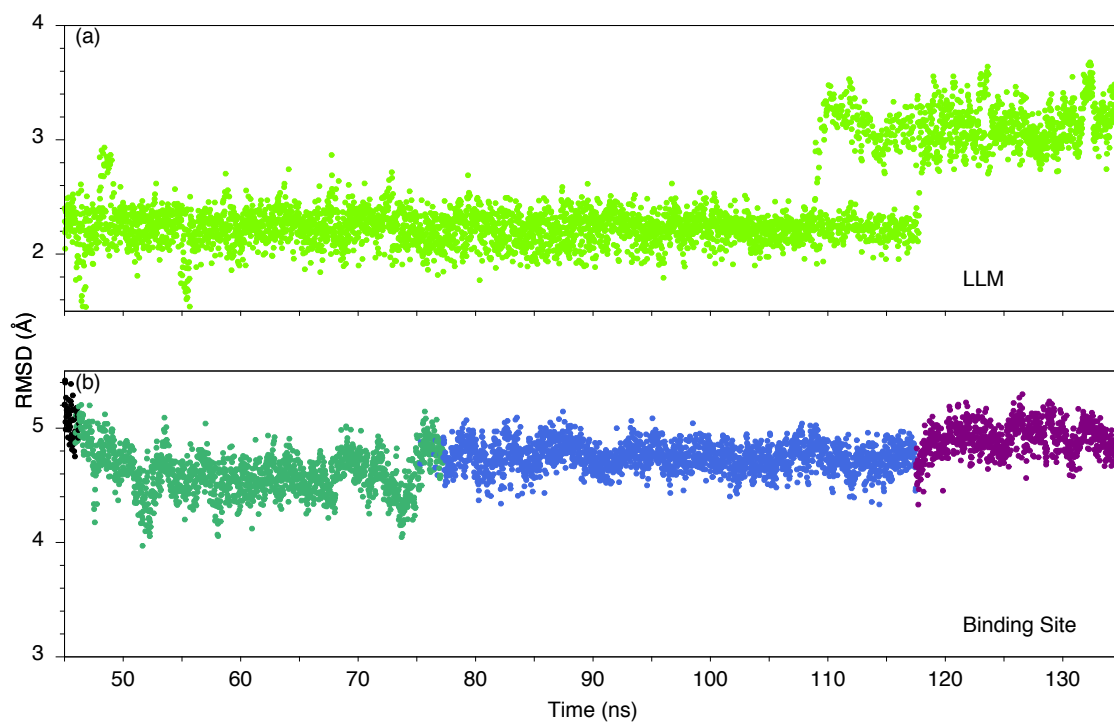
Figure A4: *Mass-weighted RMSD (Å) of the atoms of (a) LLM and (b) the binding site.*
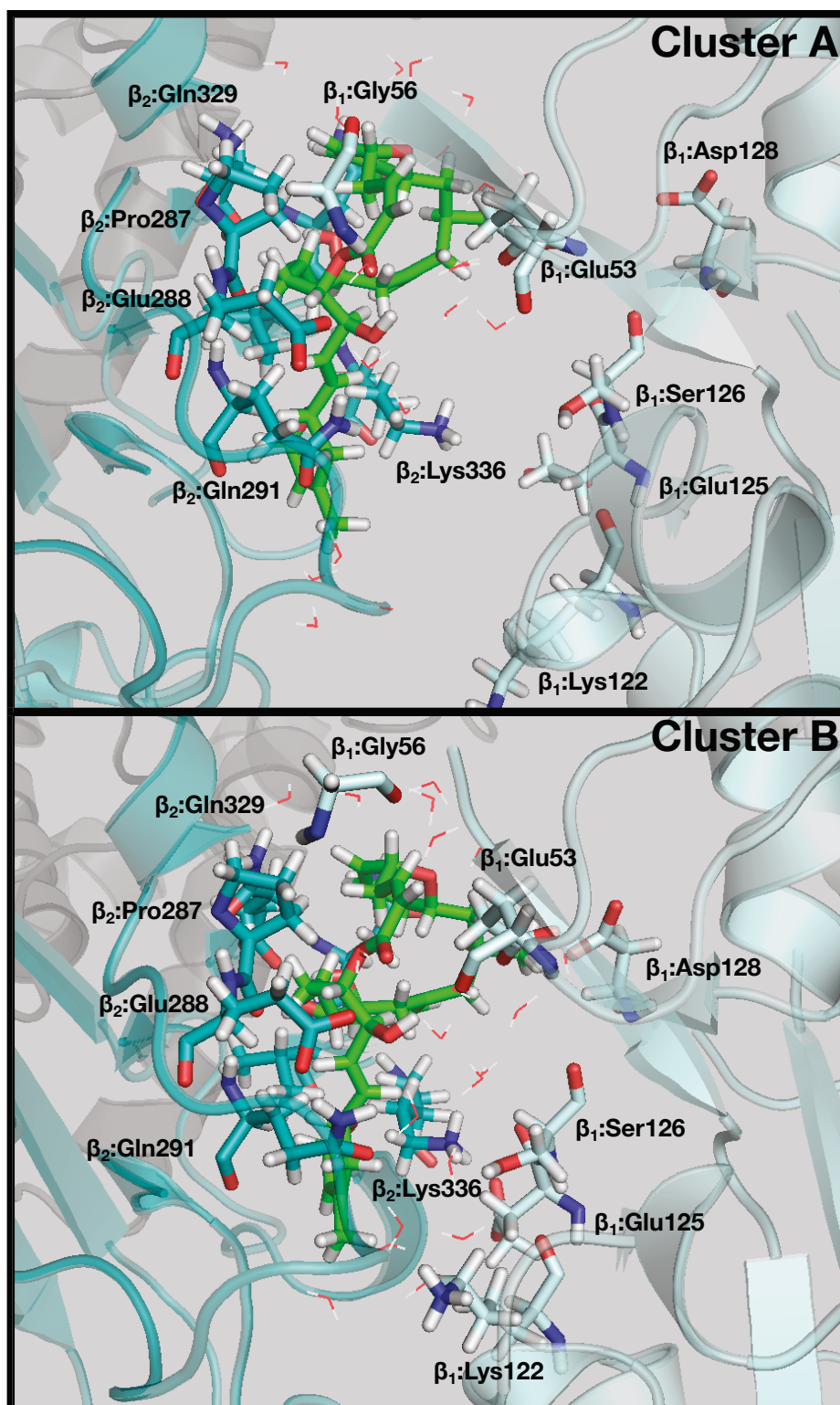
Figure A5: *A representative illustration of LLM (green) binding to β_1-tubulin (light cyan) and β_2-tubulin (teal) in different clusters. Residues β_1:Glu53, β_1:Gly56, β_1:Lys122, β_1:Glu125, β_1:Ser126, β_1:Asp128, β_2:Pro287, β_2:Glu288, β_2:Gln291, β_2:Gln329, β_2:Lys336 are shown in stick mode. Twenty binding-site waters are shown in line mode.*
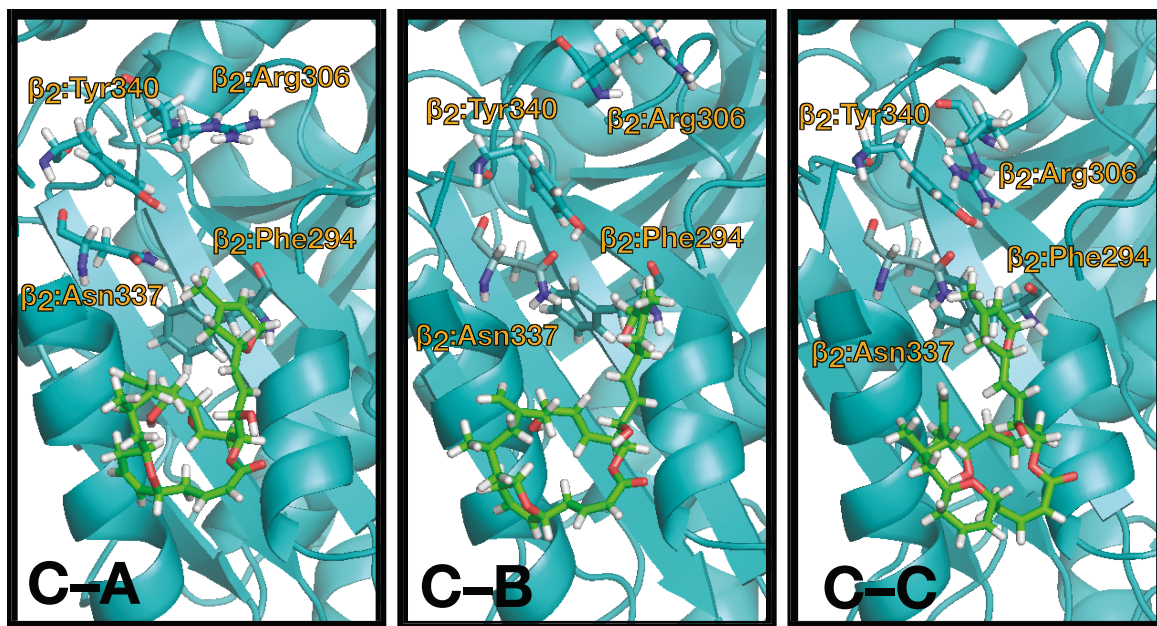
Figure A6: *Illustration of the LLM binding site on β_2 between β_2:H10 (left helix) and β_2:H9 (right helix) with residues β_2:Phe294, β_2:Arg306, β_2:Asn337 and β_2:Try340 indicated for each of the representative structures obtained from clustering. This illustration is similar to Figure 4 in Bennett et al.[142]*

Table A1: *MM/GBSA-calculated LLM–tubulin binding free energy (kJ mol^{-1}).*

	Cluster A	Cluster B	Cluster C	Average
	Residue Contributions[a]			
β_1:Glu53	-5.2	-9.6	-28.0	-11.9
β_1:Gly56	-0.9	-0.6	-1.4	-0.8
β_1:Lys122	-0.4	-3.8	-2.6	-2.5
β_1:Glu125	-1.5	-6.3	-6.1	-4.8
β_1:Ser126	-0.5	-5.6	-5.6	-4.0
β_1:Asp128	-0.8	-7.0	-3.2	-4.2
α_2:Arg221	-1.0	-4.1	-0.6	-2.4
β_2:Val186	-1.1	-1.0	-0.2	-0.9
β_2:Pro287	-16.2	-15.6	-12.3	-15.2
β_2:Glu288	-2.4	-2.1	-1.8	-2.1
β_2:Thr290	-7.8	-7.0	-9.0	-7.6
β_2:Gln291	-19.1	-18.6	-20.2	-19.0
β_2:Phe294	-7.3	-6.4	-3.8	-6.2
β_2:Asp295	-7.1	-2.0	-2.2	-3.6
β_2:Arg306	-0.1	0.0	-0.5	-0.2
β_2:Glu325	-2.1	-5.9	-0.8	-3.7
β_2:Glu328	-3.6	-5.8	-1.3	-4.2
β_2:Gln329	-23.9	-24.2	-22.2	-23.7
β_2:Met330	-1.0	-0.9	-1.2	-1.0
β_2:Leu331	-0.8	-0.7	-0.4	-0.7
β_2:Asn332	-18.9	-18.8	-10.6	-17.3
β_2:Val333	-14.9	-15.2	-14.9	-15.1
β_2:Asn335	-0.8	-0.7	-0.3	-0.6
β_2:Lys336	-18.7	-13.8	-15.3	-15.6
β_2:Asn337	-3.4	-3.3	-5.6	-3.8
β_2:Tyr340	-0.8	-0.7	-0.4	-0.6
	Secondary Structure Contributions[b]			
β_1:H1′–S2	-7.8	-12.6	-33.6	-15.0
β_1:H3	-0.6	-5.0	-3.4	-3.2
β_1:H3–S4	-3.1	-20.3	-15.8	-13.4
β_2:H9	-46.8	-44.5	-44.8	-45.3
β_2:H10	-85.7	-87.2	-68.1	-82.9
	Subunit Contributions[b]			
α_1	-0.1	-0.2	0.0	-0.2
β_1	-12.0	-38.8	-54.1	-33.4
α_2	-1.5	-4.8	-0.8	-3.0
β_2	-156.4	-147.8	-127.7	-146.4
	Ligand–Protein Binding[c]			
$\Delta G^{MM/GBSA}$	-125.7	-136.4	-108.1	-127.1
Std. Dev.	±14.6	±11.5	±15.5	±17.3

[a] Pairwise $\Delta G_{ij}^{MM/GBSA}$, Equation 1.22, contributions are not additive ($\sum \Delta G_{ij}^{MM/GBSA} \neq \Delta G^{MM/GBSA}$).; [b] Binding contributions summed over all residues in the substructure or subunit.; [c] $\Delta G^{MM/GBSA}$, Equations 1.20 and 1.21, neglecting entropy.
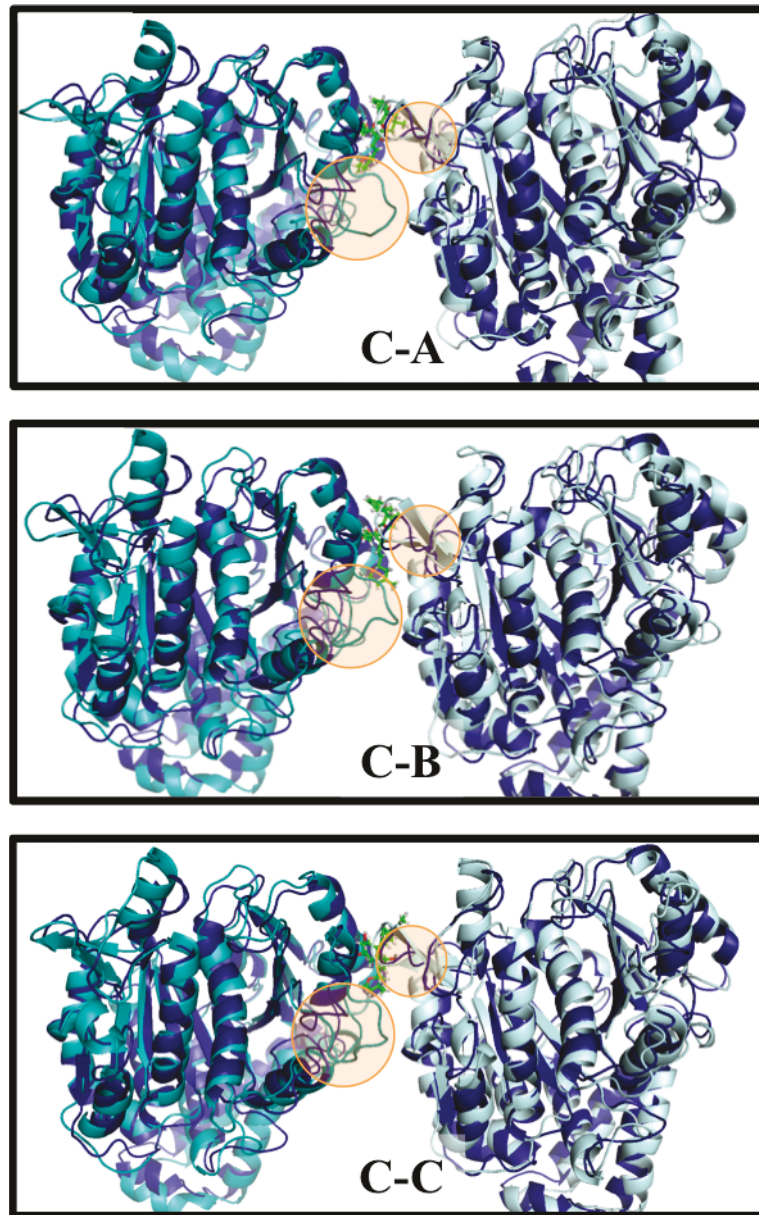
Figure A7: *An overlay of β-tubulin from the 1JFF crystal structure (dark blue) with the results of the simulation showing β_1 (light cyan) and β_2 (teal) bound to LLM (green), as viewed from the microtubule lumen. Fluctuations in the M-loop (left) and stabilization of β_1:H1′–S2 (right) are highlighted in orange.*

Appendix B

Appendix to Chapter 3

Computational details of molecular dynamics simulations

Following the preparation of each complex, the following steps were taken:

1. 4000 steps of steepest descent minimization followed by 4000 steps of conjugate gradient minimization, with weak restraints on all protein atoms greater than 3 Å from LLM. Since protein coordinates were taken from a previous simulation and are well equilibrated, protein coordinates were mostly restrained.
2. Heating from 0 K to 300 K using the canonical ensemble for 200 ps using a time step of 1 fs, with weak restraints on all protein atoms greater than 3 Å from LLM.
3. At 300 K using the isothermal-isobaric ensemble to equilibrate the solvent density for 1000 ps using a time step of 1 fs, with no restraints.
4. Production run at 300 K using the canonical ensemble and a time step of 2 fs with the SHAKE algorithm.

Figure B1: *The mass-weighted RMSD (Å) of select atoms throughout the simulation, calculated with respect to the structure at 0 ns.*
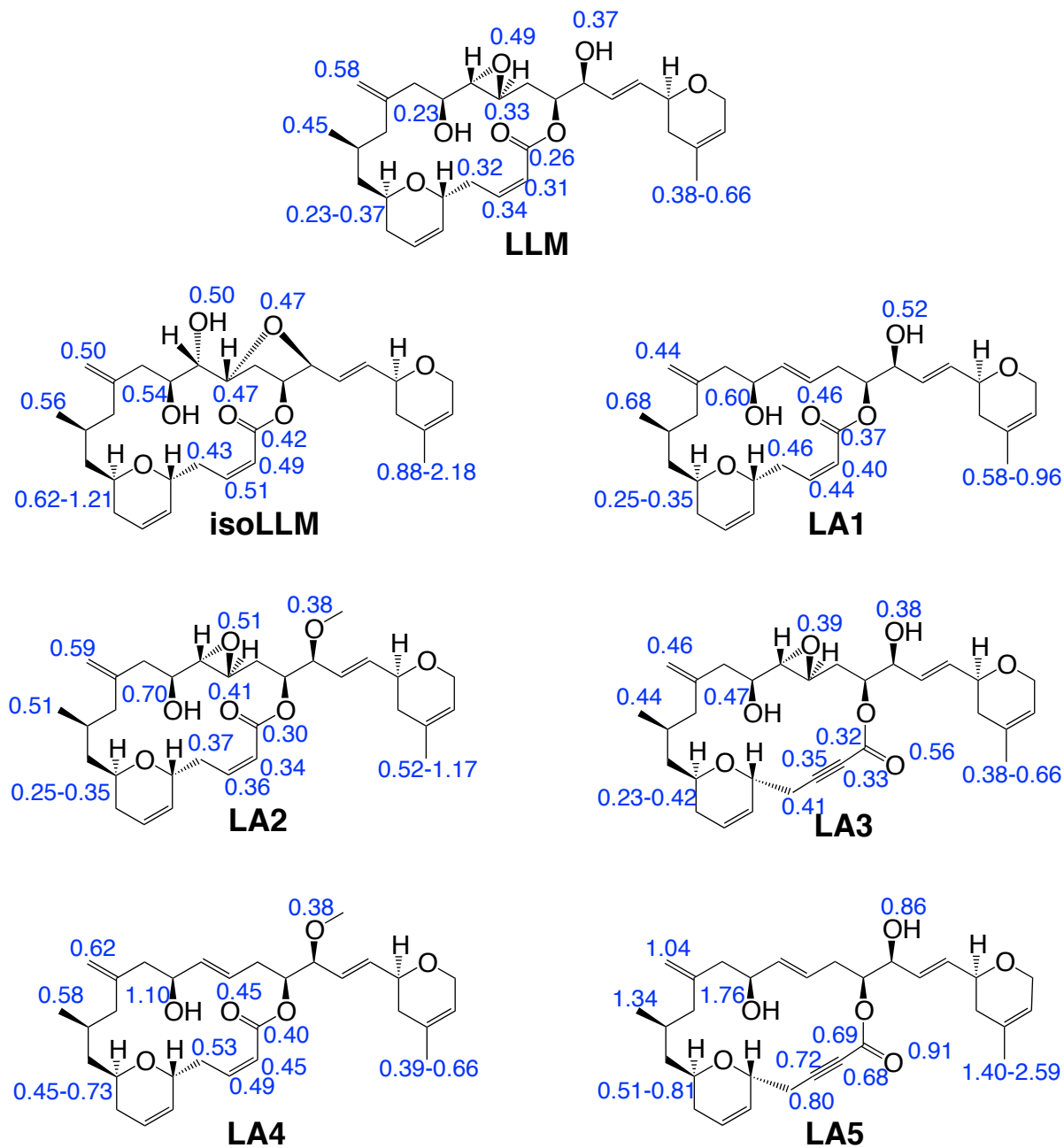
Figure B2: *The RMSF (Å) in atomic positions of select non-hydrogen atoms for the LLM series, calculated with respect to the structure at 90 ns.*
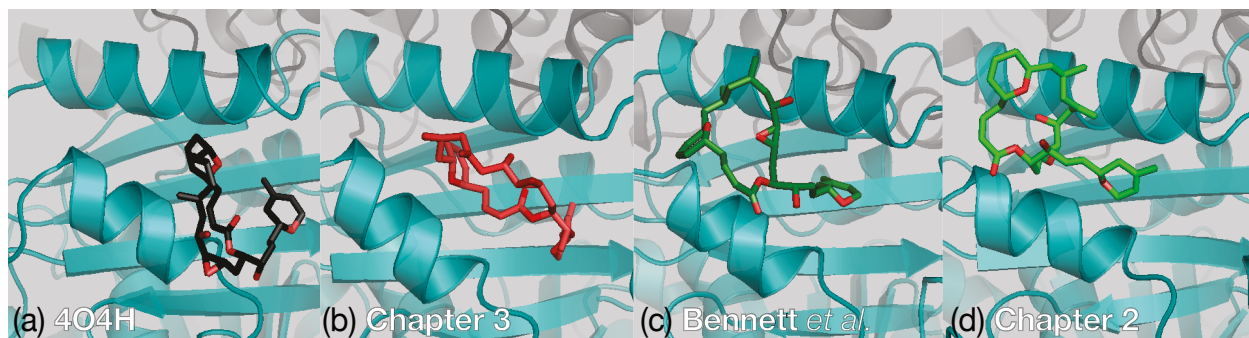
Figure B3: *A comparison of the LLM–tubulin binding site taken from (a) the 4O4H crystal structure,[52] (b) Chapter 3[2] using MD simulations to combine the 4O4H crystal structure pose with a LLM–($\alpha\beta$-tubulin)$_2$ model, (c) Bennett et al.[142] using MD simulations and a LLM–$\alpha\beta$-tubulin model, and (d) Chapter 2[1] using MD to combine the pose from Bennett et al.[142] with a LLM–($\alpha\beta$-tubulin)$_2$ model.*

Figure B4: *Interactions between the laulimalide analogues, β_1-tubulin (light cyan) residues, and β_2-tubulin (teal) residues at the LLM binding site. Viewed along the lateral interface from the β-tubulin side of the adjacent heterodimers.*

Figure B5: *An illustration of the π–π interactions present in the LLM binding site. Distances (Å) between the alkene bond and aromatic rings of β_2-tubulin residues are indicated.*

Table B1: *MM/GBSA-calculated ligand–tubulin binding free energy (kJ mol^{-1}).*

	LLM	isoLLM	LA1	LA2	LA3	LA4	LA5
Residue Contributions[a]							
β_1:Asn52	-0.3	-0.4	-0.2	-0.6	-0.3	-2.6	-0.1
β_1:Ala54	0.0	-0.1	0.0	-0.1	-0.1	-2.2	0.0
β_1:Arg121	-6.9	-3.9	-8.3	-2.1	-2.9	-3.9	-4.0
β_1:Lys122	-10.0	-19.1	-14.3	-12.1	-15.0	-14.8	-16.2
β_1:Glu125	-12.8	-8.5	-12.6	-16.0	-11.9	-12.8	-5.9
β_1:Ser126	-6.2	-9.9	-4.9	-7.2	-5.0	-13.0	-4.6
β_2:Pro287	-3.4	-0.7	-2.2	-2.0	-6.4	-6.7	-2.2
β_2:Thr290	-13.4	-6.0	-10.1	-11.4	-5.1	-10.1	-7.0
β_2:Gln291	-21.6	-30.4	-19.0	-22.2	-13.6	-17.3	-18.4
β_2:Met293	-0.8	-0.5	-0.8	-0.8	-3.4	-2.0	-2.8
β_2:Phe294	-25.6	-20.3	-25.5	-22.8	-41.2	-27.1	-43.9
β_2:Asp295	-2.1	-14.2	-3.1	-4.5	-4.7	-6.7	-8.9
β_2:Ala296	-3.6	-0.8	-4.4	-6.1	-5.0	-7.7	-8.5
β_2:Met299	-3.6	-0.1	-2.2	-4.2	-8.5	-4.4	-2.3
β_2:Met300	-0.1	-0.3	-0.1	-0.1	-4.5	-0.1	-0.8
β_2:Ala301	-0.2	-4.3	-0.1	-0.2	-5.7	-0.1	-1.9
β_2:Pro305	-9.6	-0.8	-4.9	-11.7	-8.9	-8.9	-9.3
β_2:Arg306	-3.8	-0.1	-1.6	-4.1	-1.0	-0.7	-2.5
β_2:Tyr310	-12.7	-8.4	-12.8	-11.4	-8.5	-8.7	-15.0
β_2:Val313	-2.6	-1.3	-2.4	-1.6	-0.4	-1.5	-1.7
β_2:Gln329	-9.6	-9.4	-9.1	-6.5	-15.7	-12.4	-6.4
β_2:Asn332	-5.8	-4.9	-5.9	-5.6	-7.6	-6.0	-12.9
β_2:Val333	-12.8	-14.0	-12.1	-10.3	-15.5	-10.6	-7.6
β_2:Lys336	-18.4	-12.4	-15.4	-12.1	-8.8	-23.6	-23.9
β_2:Asn337	-26.6	-17.3	-25.4	-27.0	-7.6	-22.6	-12.5
β_2:Tyr340	-8.1	-12.6	-16.6	-13.7	-18.7	-7.4	-9.5
β_2:Phe341	-4.6	-4.3	-4.9	-6.9	-1.5	-2.4	-1.9
β_2:Phe367	-3.7	-2.3	-3.0	-3.6	-6.0	-3.3	-6.4
Secondary Structure Contributions[b]							
β_1:H1′–S2	-0.8	-1.6	-0.4	-2.1	-1.0	-7.8	-0.4
β_1:H3	-19.1	-25.0	-27.1	-15.6	-19.7	-21.5	-23.1
β_1:H3–S4	-19.6	-19.2	-17.9	-23.7	-17.4	-26.5	-10.8
β_2:H9	-66.6	-60.6	-58.8	-60.6	-71.6	-65.9	-76.2
β_2:H9–H9′	-10.8	-24.9	-10.4	-17.8	-30.1	-21.0	-24.6
β_2:H9′	-13.4	-1.0	-6.7	-16.0	-10.0	-9.6	-12.0
β_2:H9′–S8	-0.4	-0.8	-0.2	-0.5	-0.3	-0.3	-0.3
β_2:S8	-16.0	-10.2	-15.8	-13.6	-9.3	-10.6	-17.3
β_2:S8–H10	0.0	0.0	0.0	0.0	0.0	0.0	0.0
β_2:H10	-50.6	-43.7	-45.4	-37.0	-49.2	-54.9	-53.8
β_2:H10–S9	-40.0	-34.9	-47.8	-48.3	-28.4	-32.8	-24.5

	LLM	isoLLM	LA1	LA2	LA3	LA4	LA5
			Subunit Contributions[b]				
β_1	-40.1	-46.5	-46.2	-41.9	-38.9	-56.8	-35.0
α_1	0.0	0.0	0.0	-0.1	0.0	0.0	0.0
β_2	-203.7	-181.1	-190.2	-199.8	-208.0	-200.1	-218.8
α_2	-0.2	-0.1	-0.2	-0.1	-0.3	-0.2	-0.2
			Ligand–Protein Binding[c]				
$\Delta G^{MM/GBSA}$	-196.6	-160.3	-187.9	-180.2	-194.7	-192.7	-205.3
Std. Dev.	±12.7	±19.4	±15.4	±14.9	±15.9	±16.9	±20.0

[a] Pairwise $\Delta G_{ij}^{MM/GBSA}$, Equation 1.22, contributions are not additive ($\sum \Delta G_{ij}^{MM/GBSA} \neq \Delta G^{MM/GBSA}$).;

[b] Binding contributions summed over all residues in the substructure or subunit.;

[c] $\Delta G^{MM/GBSA}$, Equations 1.20 and 1.21, neglecting entropy.

Table B2: *MM/GBSA-calculated lateral binding free energy (kJ mol⁻¹) between $\alpha_1\beta_1$-tubulin and the ligand–$\alpha_2\beta_2$-tubulin complex.*

	LLM	isoLLM	LA1	LA2	LA3	LA4	LA5	apo
β-tubulin Residue Contributions[a]								
β_1:Thr33$\cdots\beta_2$:Tyr281	-10.4	-1.7	-12.0	-8.5	-2.8	-0.2	-0.3	-6.5
β_1:Ala54$\cdots\beta_2$:Tyr281	-5.6	-5.6	-5.0	-4.2	-2.8	-0.5	-2.6	-5.1
β_1:Ala54$\cdots\beta_2$:Glu288	-3.2	-7.1	-0.6	-7.8	-6.2	-3.5	-1.0	-0.3
β_1:Ala55$\cdots\beta_2$:Tyr281	-4.5	-5.3	-4.3	-3.6	-5.9	-4.8	-9.8	-4.4
β_1:Ala55$\cdots\beta_2$:Ala283	-6.6	-3.7	-5.2	-4.6	-3.3	-1.7	-3.2	-6.3
β_1:Ala55$\cdots\beta_2$:Thr285	-4.2	-4.2	-4.7	-5.1	-2.2	-5.2	-1.1	-4.0
β_1:Ala55$\cdots\beta_2$:Glu288	-3.1	-9.3	-0.5	-11.2	-9.0	-8.3	-0.9	-0.2
β_1:Asn57$\cdots\beta_2$:Tyr281	-0.3	-0.5	-0.4	-0.7	-0.5	-8.2	-0.4	-0.3
β_1:Lys58$\cdots\beta_2$:Tyr281	-7.5	-9.5	-8.8	-12.9	-9.6	-6.1	-1.3	-8.6
β_1:Gln83$\cdots\beta_2$:Gln279	-3.6	-0.8	-7.6	0.0	-2.8	-1.2	-1.1	-2.7
β_1:Phe85$\cdots\beta_2$:Gln279	-3.0	-0.5	-5.4	-0.1	-1.9	-0.2	-1.0	-2.4
β_1:Arg86$\cdots\beta_2$:Ser278	-0.3	-0.8	-0.7	-18.9	-0.1	-0.1	-0.1	-0.2
β_1:Arg86$\cdots\beta_2$:Gln279	-16.1	-9.0	-13.7	-5.9	-6.2	-10.2	-9.3	-18.2
β_1:Arg86$\cdots\beta_2$:Gln280	-3.0	-1.6	-3.0	-1.7	-1.6	-1.8	-3.7	-9.9
β_1:Arg86$\cdots\beta_2$:Tyr281	-13.8	-10.2	-18.5	-6.4	-2.0	-0.2	-2.6	-13.6
β_1:Pro87$\cdots\beta_2$:Ser278	-0.2	-1.4	-1.5	-5.6	-0.7	-0.5	-0.1	-0.7
β_1:Pro87$\cdots\beta_2$:Gln279	-6.5	-7.3	-5.6	-0.6	-6.5	-4.2	-2.7	-6.1
β_1:Pro87$\cdots\beta_2$:Gln280	-7.1	-3.3	-6.6	-0.1	-1.8	-0.5	-5.7	-11.0
β_1:Asp88$\cdots\beta_2$:Ser275	-0.2	0.0	-0.4	-0.1	-0.3	-0.2	-0.3	-13.6
β_1:Asp88$\cdots\beta_2$:Arg276	-0.2	-0.1	-8.4	-1.2	-0.2	-0.2	-0.2	-0.5
β_1:Asp88$\cdots\beta_2$:Ser278	0.0	-0.1	0.0	-33.2	0.0	-0.1	0.0	0.0
β_1:Asp88$\cdots\beta_2$:Gln279	-0.1	-1.7	-0.1	-10.5	-0.4	-0.1	-0.1	-0.2
β_1:Asp88$\cdots\beta_2$:Gln280	-2.1	-3.4	-0.4	0.1	-3.7	-0.3	-1.6	-13.3
β_1:Asp88$\cdots\beta_2$:Lys297	-9.4	-0.3	-0.4	-1.3	-34.1	-5.0	-7.2	-2.6
β_1:Asp118$\cdots\beta_2$:Arg306	-26.2	-0.3	-3.1	-14.5	-25.1	-24.8	-14.0	-29.9
β_1:Arg121$\cdots$ligand	-6.9	-3.8	-8.4	-2.1	-2.9	-3.9	-4.0	—
β_1:Lys122$\cdots\beta_2$:Glu288	-0.9	-0.5	-7.8	-0.4	-0.5	-0.4	-1.2	-31.7
β_1:Lys122$\cdots\beta_2$:Gln291	-5.6	0.0	-8.4	-0.8	-3.3	-2.1	-3.9	-16.0

Continued on the next page

Continuation of Table B2

	LLM	isoLLM	LA1	LA2	LA3	LA4	LA5	apo
β_1:Lys122···ligand	-10.1	-19.2	-14.4	-12.3	-15.2	-15.0	-16.4	—
β_1:Glu125···β_2:Lys336	-38.5	-27.3	-19.9	-33.4	-34.8	-34.5	-19.5	-27.1
β_1:Glu125···β_2:Asn337	-0.2	-0.1	-0.1	-0.2	-6.3	-0.3	-0.1	-2.7
β_1:Glu125···ligand	-12.8	-8.5	-12.5	-16.0	-11.9	-12.8	-5.9	—
β_1:Ser126···ligand	-6.2	-9.8	-4.9	-7.2	-5.1	-13.0	-4.5	—
β_1:Cys127···β_2:Lys336	-0.7	-0.6	0.0	-0.3	-1.3	-1.2	-0.2	-5.6
α-tubulin Residue Contributions[a]								
α_1:Asp33···α_2:Tyr282	-0.5	-0.3	-0.1	0.0	-0.5	-7.3	-0.7	-4.5
α_1:Asp33···α_2:His283	-7.0	-2.2	-2.0	-0.1	-7.1	-4.5	-5.1	-3.1
α_1:Gln35···α_2:Tyr282	-1.7	-7.2	-2.5	-0.2	-8.3	-5.9	-4.6	-14.5
α_1:Gln35···α_2:His283	-13.0	-5.3	-3.0	-1.0	-6.0	-8.2	-5.5	-7.1
α_1:Gln35···α_2:Gln285	-2.0	-0.7	-0.5	-0.1	-2.2	-6.6	-0.7	-6.4
α_1:Glu55···α_2:Gln285	-0.2	-0.2	-0.2	-6.1	-0.1	-0.2	-0.1	-0.2
α_1:Glu55···α_2:Lys338	-0.8	-1.1	-0.6	-3.9	-1.5	-1.6	-3.2	-10.2
α_1:Thr56···α_2:Gln285	-1.1	-4.0	-5.3	-0.1	-1.0	-2.0	-0.6	-0.7
α_1:Thr56···α_2:Leu286	-13.5	-13.7	-10.6	0.0	-10.0	-13.0	-14.0	-13.5
α_1:Thr56···α_2:Ser287	-9.7	-8.4	-5.0	0.0	-6.2	-8.8	-8.3	-9.5
α_1:Thr56···α_2:Glu290	-7.4	-7.2	-4.6	-0.3	-7.4	-7.8	-7.5	-9.0
α_1:Gly57···α_2:Ser287	-6.8	-6.0	-6.3	-0.1	-4.9	-5.9	-6.7	-6.6
α_1:Ala58···α_2:His283	0.1	-0.1	-0.1	-5.7	0.0	0.0	-0.1	0.0
α_1:Ala58···α_2:Glu284	-0.1	-0.1	-0.1	-11.0	0.0	-0.1	-0.1	-0.1
α_1:Ala58···α_2:Gln285	-6.7	-6.9	-6.2	-2.9	-4.3	-5.5	-5.9	-9.5
α_1:Ala58···α_2:Ser287	-4.1	-4.4	-4.4	-0.1	-3.6	-4.6	-3.3	-4.9
α_1:Lys60···α_2:His283	-15.7	-14.0	-21.0	-0.3	-22.9	-30.4	-17.0	-19.3
α_1:Lys60···α_2:Glu284	-33.2	-4.3	-5.5	-0.4	-4.2	-4.5	-7.0	-8.2
α_1:Lys60···α_2:Gln285	-7.3	-4.5	-4.5	-0.2	-12.4	-9.6	-10.1	-11.1
α_1:Gln85···α_2:His283	-5.9	-3.7	-7.7	0.0	-9.8	-11.8	-2.2	-4.3
α_1:His88···α_2:Glu284	-1.2	-6.4	-8.0	0.0	-9.4	-3.2	-0.1	-0.4
α_1:Glu90···α_2:Arg214	-0.5	-0.4	-0.3	-6.6	-0.2	-0.2	-0.2	-0.4

Continued on the next page

207

Continuation of Table B2

	LLM	isoLLM	LA1	LA2	LA3	LA4	LA5	apo
α_1:Glu90$\cdots\alpha_2$:Arg215	-11.0	-9.1	-16.4	-2.0	-23.2	-9.6	-2.3	-24.5
α_1:Lys124$\cdots\alpha_2$:Glu297	-21.2	-35.7	-21.7	-9.9	-26.4	-22.2	-29.7	-22.3
α_1:Asp127$\cdots\alpha_2$:Asn293	-0.2	-7.2	-3.3	-0.1	0.0	-2.2	-0.1	-0.1
α_1:Asp127$\cdots\alpha_2$:Arg308	-0.3	-2.8	-0.4	-25.8	-0.3	-0.1	-0.2	0.0
α_1:Asp127$\cdots\alpha_2$:Lys338	-7.5	-6.7	-13.8	-1.2	-3.3	-5.7	-8.8	-6.8
α_1:Asp127$\cdots\alpha_2$:Thr340	-1.9	-7.0	-2.4	-0.7	-6.8	-4.3	-0.4	-0.6
α_1:Gln128$\cdots\alpha_2$:Glu290	-3.0	-5.4	-7.0	0.0	-2.9	-8.1	0.1	-2.4
α_1:Gln128$\cdots\alpha_2$:Asn293	-4.7	-10.1	-8.2	-1.2	-8.3	-4.0	-11.2	-3.9
α_1:Gln128$\cdots\alpha_2$:Glu297	-0.2	-0.3	-0.4	-9.9	-0.2	-0.2	-0.6	-0.3
α_1:Gln128$\cdots\alpha_2$:Lys338	-17.9	-15.2	-14.0	-4.2	-21.1	-18.2	-22.7	-16.6
α_1:Cys129$\cdots\alpha_2$:Lys338	-1.9	-6.5	-3.8	-1.3	-3.9	-4.1	-1.8	-1.3
α_1:Thr130$\cdots\alpha_2$:Thr337	-1.1	-5.3	-2.4	-2.1	-4.2	-4.7	-2.5	-2.8
α_1:Thr130$\cdots\alpha_2$:Lys338	-2.2	-13.0	-5.5	-8.4	-8.1	-5.5	-2.5	-1.3
Interdimer Binding[b]								
$\Delta G^{MM/GBSA}$	-183.8	-158.1	-192.3	-117.1	-173.0	-168.1	-114.5	-223.8
Std. Dev.	±30.1	±46.4	±34.4	±33.3	±38.8	±40.4	±34.0	±43.4

[a] Pairwise $\Delta G_{ij}^{MM/GBSA}$, Equation 1.22, contributions are not additive ($\sum \Delta G_{ij}^{MM/GBSA} \neq \Delta G^{MM/GBSA}$).;
[b] $\Delta G^{MM/GBSA}$, Equations 1.20 and 1.21, neglecting entropy.
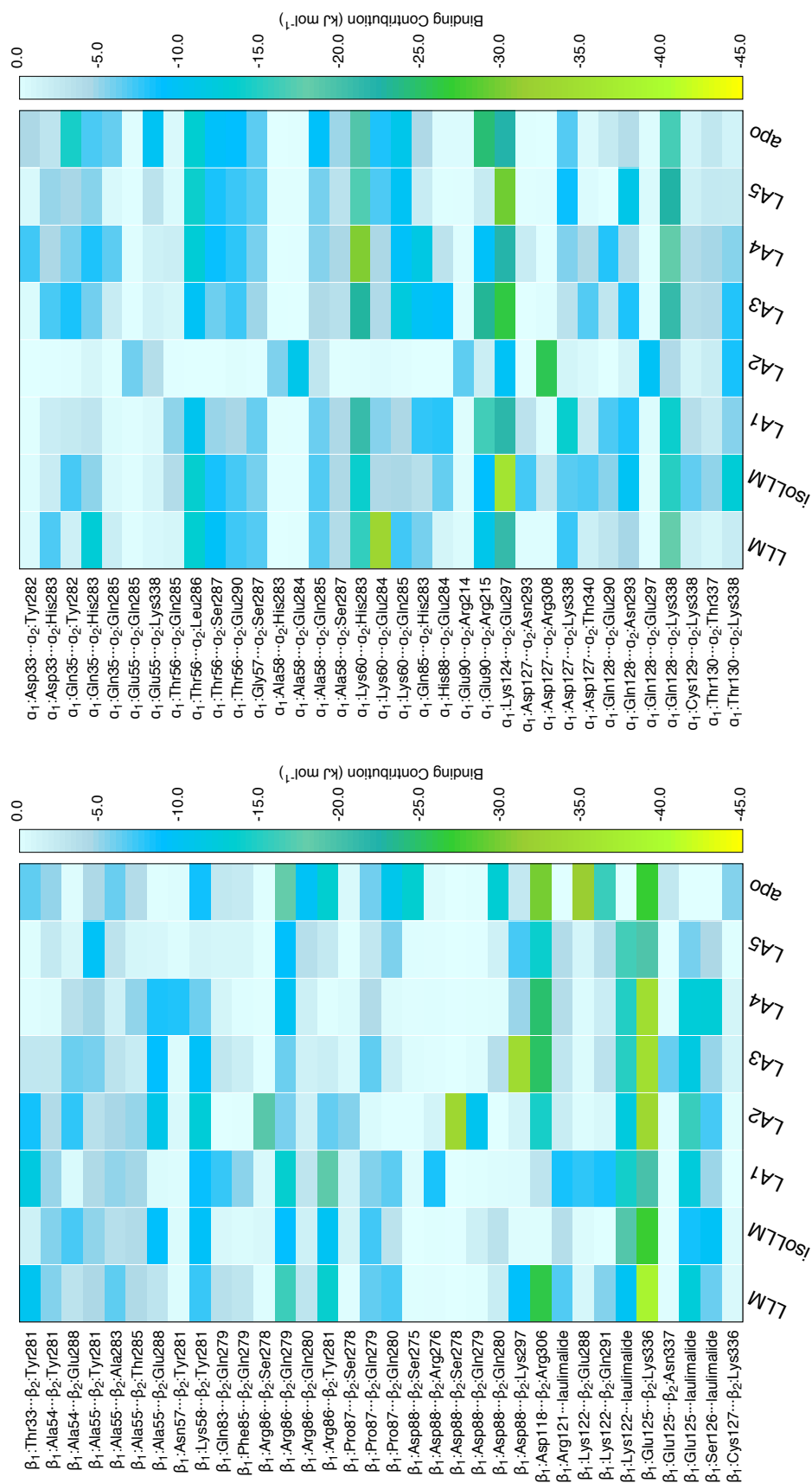
Figure B6: *Residue contributions to the lateral interdimer binding energy (kJ mol⁻¹), obtained from MM/GBSA calculations and neglecting the entropy component. Data included in Table B2.*
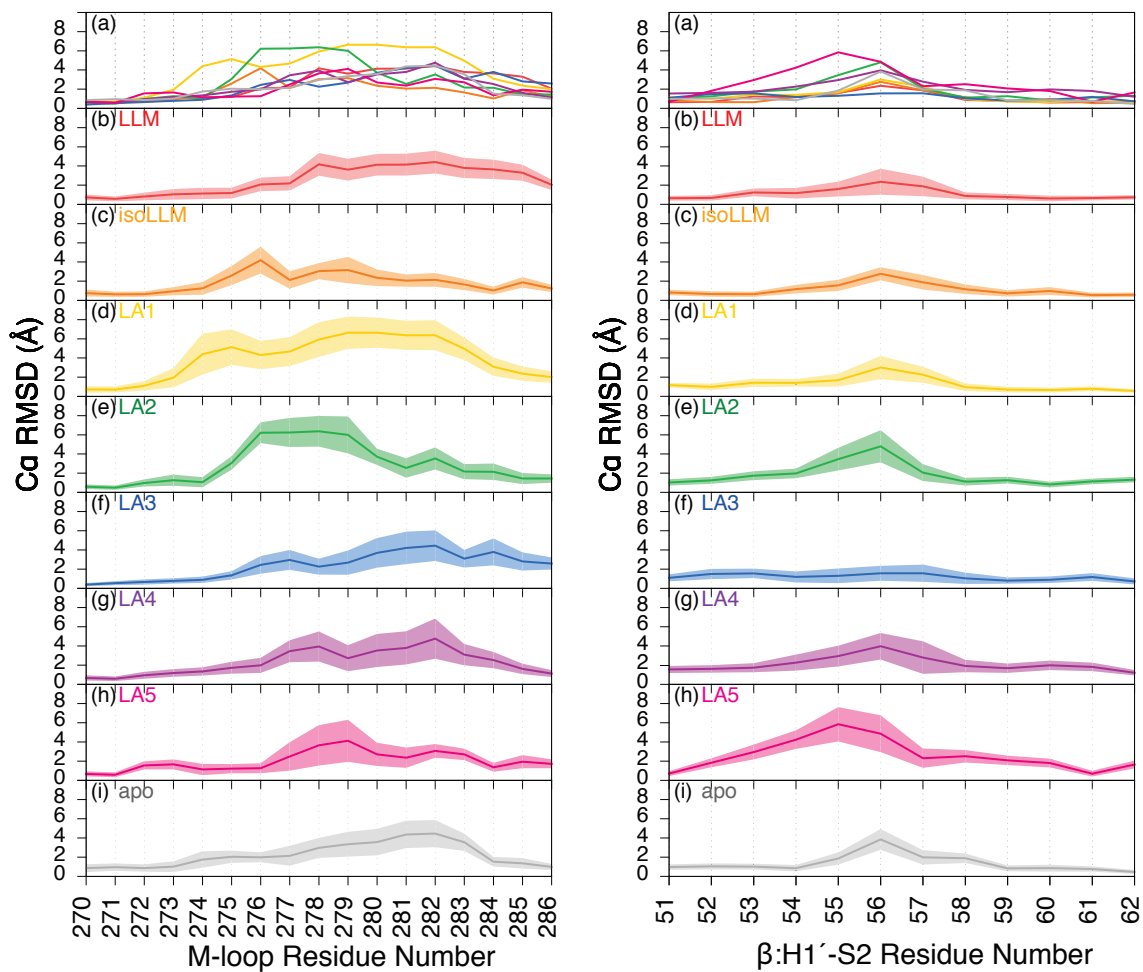
Figure B7: *The average mass-weighted RMSD of the C_α atoms (Å) for each residue, with the standard deviation shaded to indicate flexibility. Panel (a) shows an overlay of all compounds while (b–i) show the RMSDs for each complex.*
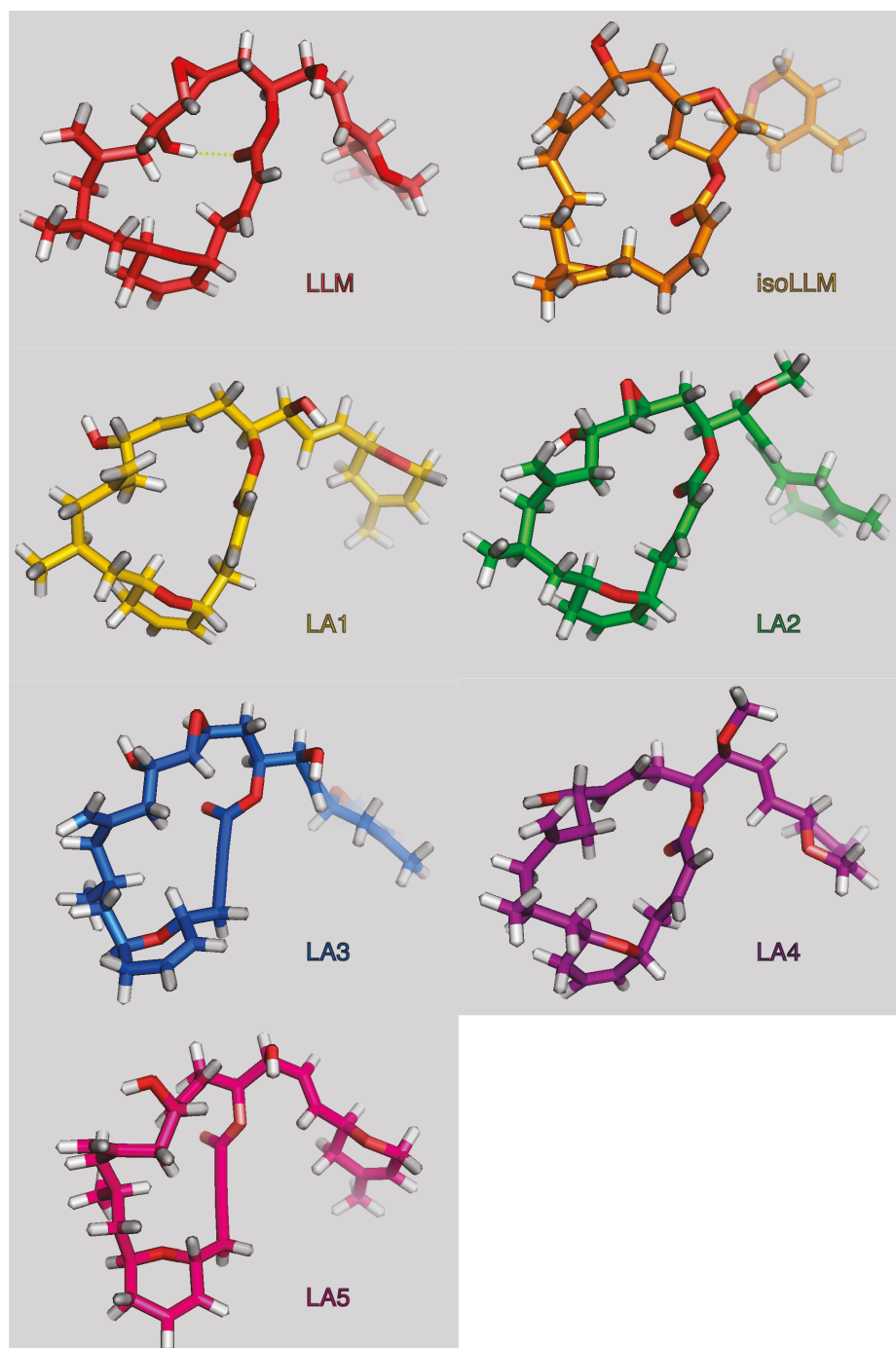
Figure B8: *A comparison of the conformations adopted by the LLM analogues. Structure taken from the end of the 90 ns simulation.*

Appendix C

Appendix to Chapter 4

Computational details of molecular dynamics simulations

Following the preparation of each complex, the following steps were taken:

1. 4000 steps of steepest descent minimization followed by 4000 steps of conjugate gradient minimization, with weak restraints on all protein atoms greater than 3 Å from LLM. Since protein coordinates were taken from a previous simulation and are well equilibrated, protein coordinates were mostly restrained.
2. Heating from 0 K to 300 K using the canonical ensemble for 200 ps using a time step of 1 fs, with weak restraints on all protein atoms greater than 3 Å from LLM.
3. At 300 K using the isothermal-isobaric ensemble to equilibrate the solvent density for 1000 ps using a time step of 1 fs, with no restraints.
4. Production run at 300 K using the canonical ensemble and a time step of 2 fs with the SHAKE algorithm.

Figure C1: *The mass-weighted RMSD (Å) of select atoms throughout the simulation, calculated with respect to the structure at 0 ns. The trajectories for LLM, LLM-15R, SVH1, and SVH4 were analyzed from 20–90 ns, while the simulation of LLM29 was analyzed from 76–155 ns and LLM32 was analyzed from 34–110 ns.*
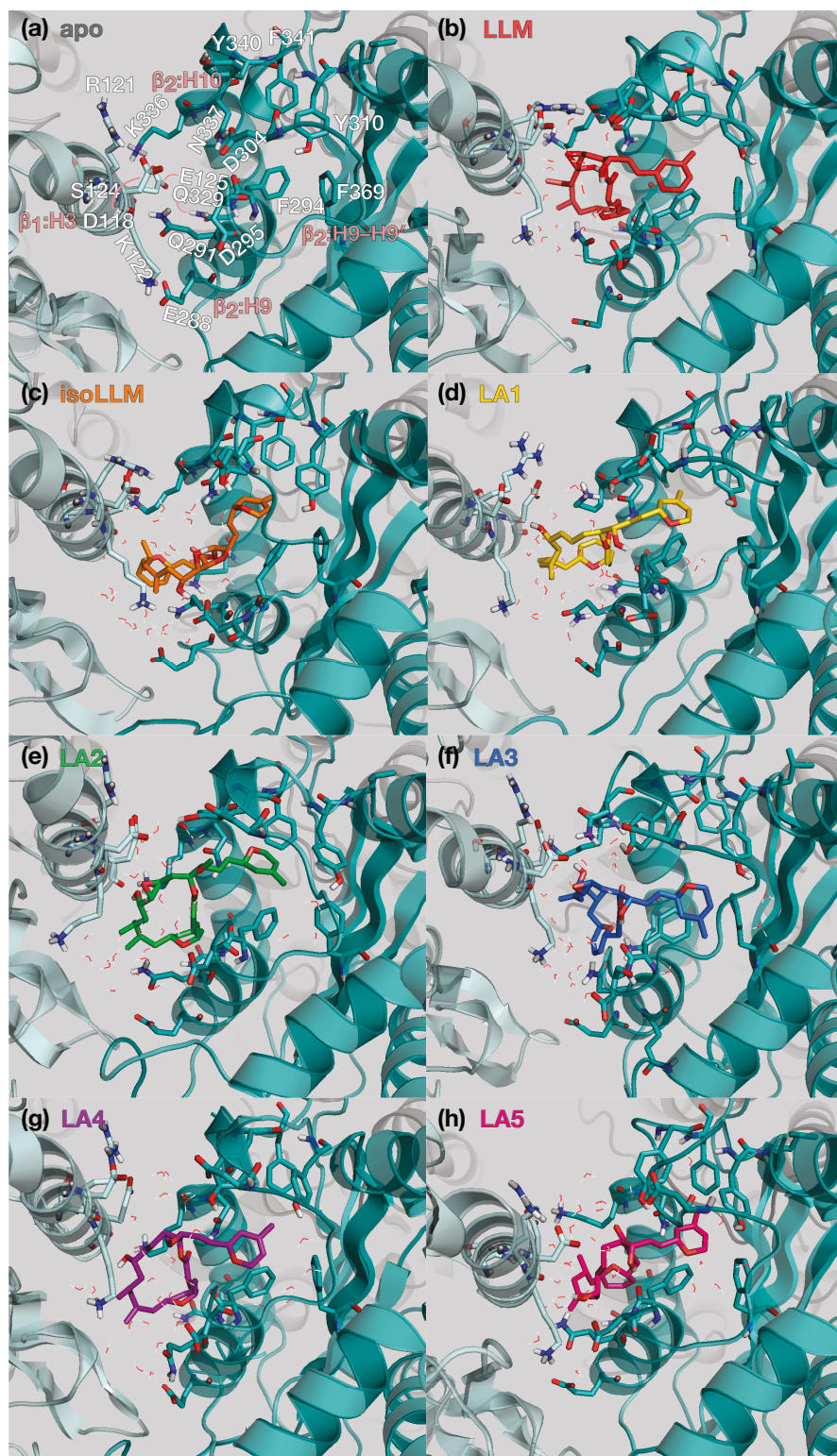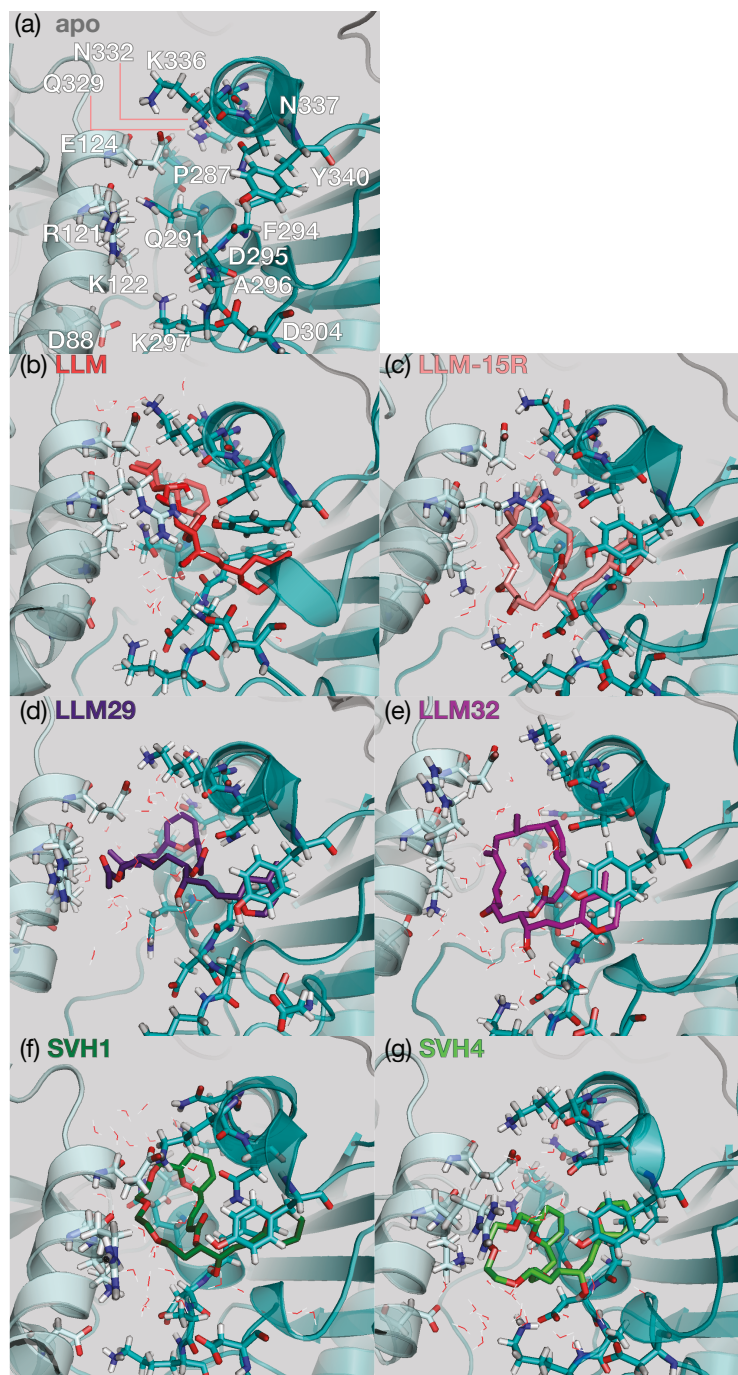
Figure C2: *Interactions between the laulimalide analogues, β_1-tubulin (light cyan) residues, and β_2-tubulin (teal) residues at the LLM binding site. Viewed along the lateral interface from the β-tubulin side of the adjacent heterodimers.*
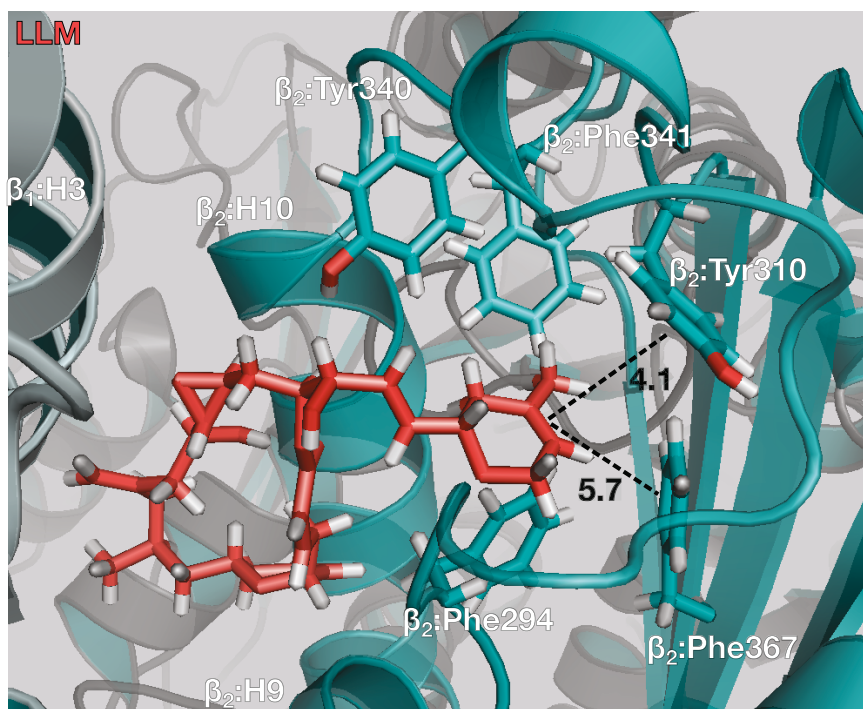
Table C1: *MM/GBSA-calculated ligand–tubulin binding free energy (kJ mol^{-1}).*

	LLM	LLM-15R	LLM29	LLM32	SVH1	SVH4
	Residue Contributions[a]					
β_1:Asn52	-0.3	-0.7	-0.1	-0.3	-0.4	-0.1
β_1:Ala54	0.0	-0.1	0.0	-0.1	0.0	-0.1
β_1:Asp118	-0.5	-1.0	-4.5	-2.9	-0.7	-11.0
β_1:Arg121	-6.9	-4.8	-10.4	-2.6	-1.8	-8.1
β_1:Lys122	-10.0	-18.2	-14.3	-14.4	-10.0	-13.4
β_1:Glu125	-12.8	-6.3	-13.3	-8.3	-9.1	-9.0
β_1:Ser126	-6.2	-3.6	-3.4	-2.5	-5.9	-1.6
β_2:Pro287	-3.4	-1.5	-7.8	-0.3	-0.7	-1.2
β_2:Thr290	-13.4	-6.0	-10.7	-5.8	-7.0	-3.9
β_2:Gln291	-21.6	-25.1	-22.7	-25.7	-15.8	-14.5
β_2:Met293	-0.8	0.0	-0.6	-0.2	-0.5	-0.2
β_2:Phe294	-25.6	-15.9	-19.3	-21.0	-33.7	-19.4
β_2:Asp295	-2.1	-30.0	-2.6	-6.8	-5.5	-9.0
β_2:Ala296	-3.6	-7.9	-2.9	-7.9	-7.3	-2.8
β_2:Lys297	-0.2	-3.5	-0.4	-1.0	-0.3	-2.2
β_2:Met299	-3.6	-0.4	-1.2	-0.7	-0.2	-0.1
β_2:Met300	-0.1	-0.1	0.0	0.0	0.0	0.0
β_2:Ala301	-0.2	-0.2	-0.2	-0.1	0.0	-0.1
β_2:Pro305	-9.6	-10.8	-1.6	-7.7	-7.9	-9.6
β_2:Arg306	-3.8	-0.4	-0.7	-5.0	-1.6	-6.9
β_2:Tyr310	-12.7	-7.3	-6.3	-4.8	-8.5	-4.2
β_2:Val313	-2.6	-0.5	-0.7	-0.3	-2.5	-0.2
β_2:Gln329	-9.6	-2.5	-13.9	-1.6	-7.8	-1.9
β_2:Asn332	-5.8	-5.4	-4.8	-6.1	-5.0	-1.7
β_2:Val333	-12.8	-13.4	-13.9	-13.8	-13.6	-9.6
β_2:Lys336	-18.4	-9.7	-8.0	-9.8	-14.7	-3.0
β_2:Asn337	-26.6	-25.6	-24.0	-25.4	-34.1	-14.8
β_2:Tyr340	-8.1	-12.6	-18.8	-16.5	-18.9	-21.8
β_2:Phe341	-4.6	-3.8	-4.2	-2.9	-7.1	-4.9
β_2:Phe367	-3.7	-0.7	-1.0	-0.3	-1.8	-0.4
	Secondary Structure Contributions[b]					
β_1:H3	-19.1	-25.6	-32.2	-21.6	-14.4	-35.5
β_1:H3–S4	-19.6	-10.1	-17.1	-10.9	-15.4	-10.8
β_1:H1'S2	-0.8	-1.5	-0.4	-0.8	-1.0	-0.5
β_2:H9	-66.6	-51.2	-66.1	-54.5	-58.9	-40.6
β_2:H9–H9'	-10.8	-43.0	-8.0	-16.9	-14.4	-14.9
β_2:H9'	-13.4	-11.6	-2.5	-12.8	-9.6	-16.7
β_2:H9'–S8	-0.4	-1.0	-0.3	-0.5	-0.4	-0.3
β_2:S8	-16.0	-8.1	-7.4	-5.3	-11.6	-4.6
β_2:S8–H10	0.0	0.0	0.0	0.0	0.0	0.0
β_2:H10	-50.6	-32.9	-44.3	-32.9	-44.3	-17.8
β_2:H10–S9	-40.0	-42.5	-47.7	-45.5	-61.0	-42.3

Continued on the next page

	LLM	LLM-15R	LLM29	LLM32	SVH1	SVH4
Subunit Contributions[b]						
β_1	-40.1	-39.2	-50.4	-34.4	-31.4	-47.5
α_1	0.0	0.0	0.0	0.0	0.0	0.0
β_2	-203.7	-193.1	-178.9	-171.9	-204.0	-139.0
α_2	-0.2	-0.1	-0.2	-0.1	-0.2	-0.1
Ligand–Protein Binding[c]						
$\Delta G^{MM/GBSA}$	-196.6	-171.4	-178.8	-148.5	-174.3	-123.7
Std. Dev.	±12.7	±21.0	±17.4	±17.9	±15.3	17.4

[a] Pairwise $\Delta G^{MM/GBSA}_{ij}$, Equation 1.22, contributions are not additive ($\sum \Delta G^{MM/GBSA}_{ij} \neq \Delta G^{MM/GBSA}$).;

[b] Binding contributions summed over all residues in the substructure or subunit.;

[c] $\Delta G^{MM/GBSA}$, Equations 1.20 and 1.21, neglecting entropy.

Appendix D

Appendix to Chapter 5

Computational details of molecular dynamics simulations

Following the preparation of each complex, the following steps were taken:

1. 2000 steps of steepest descent minimization followed by 1000 steps of conjugate gradient minimization, with strong restraints on all solute atoms.
2. 4000 steps of steepest descent minimization followed by 2000 steps of conjugate gradient minimization, with no restraints.
3. Heating from 0 K to 100 K using the canonical ensemble for 20 ps using a time step of 1 fs, and weak restraints on all solute atoms.
4. Heating from 100 K to 300 K using the isothermal-isobaric ensemble for 100 ps using a time step of 1 fs, and weak restraints on all solute atoms.
5. At 300 K using the isothermal-isobaric ensemble to equilibrate the solvent density for 100 ps using a time step of 1 fs, with no restraints.
6. Production run at 300 K using the canonical ensemble and a time step of 2 fs with the SHAKE algorithm.
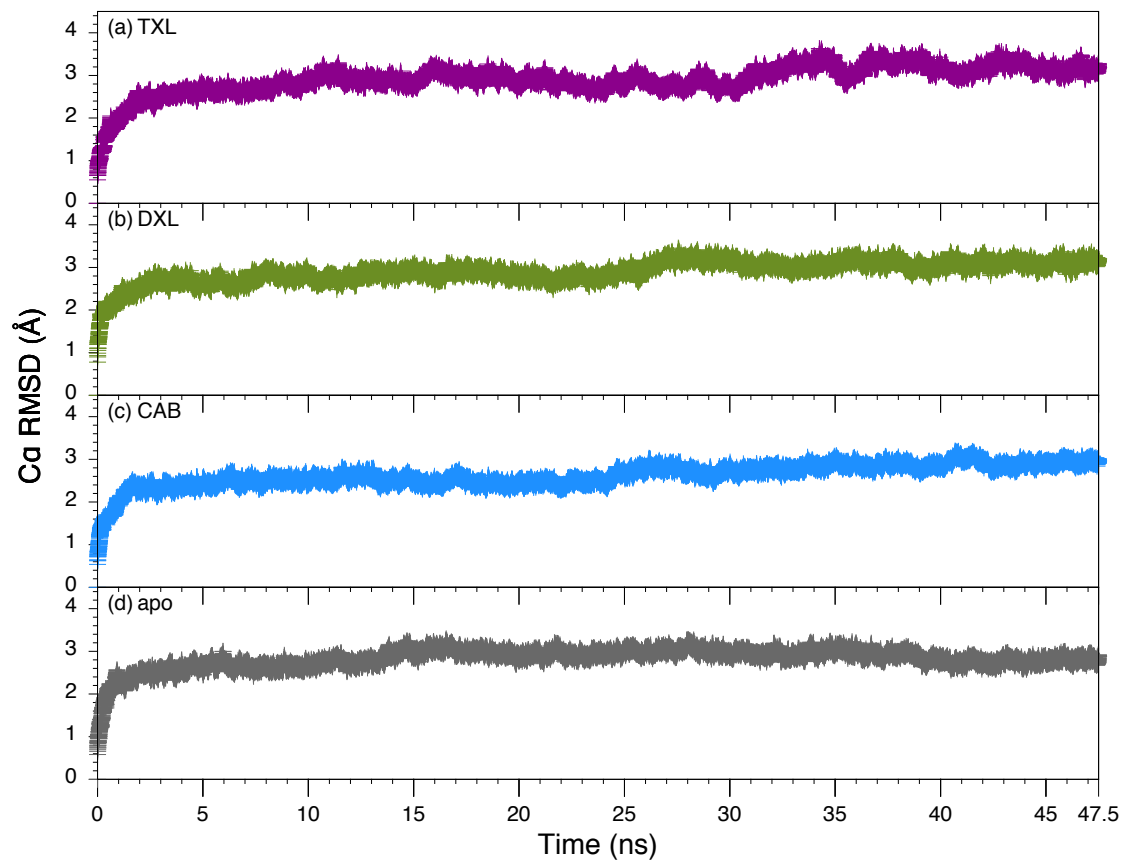
Figure D1: *The mass-weighted RMSD (Å) of the C_α atoms of the protein, when tubulin is bound to (a) TXL, (b) DXL, (c) CAB, or (d) in its apo form.*
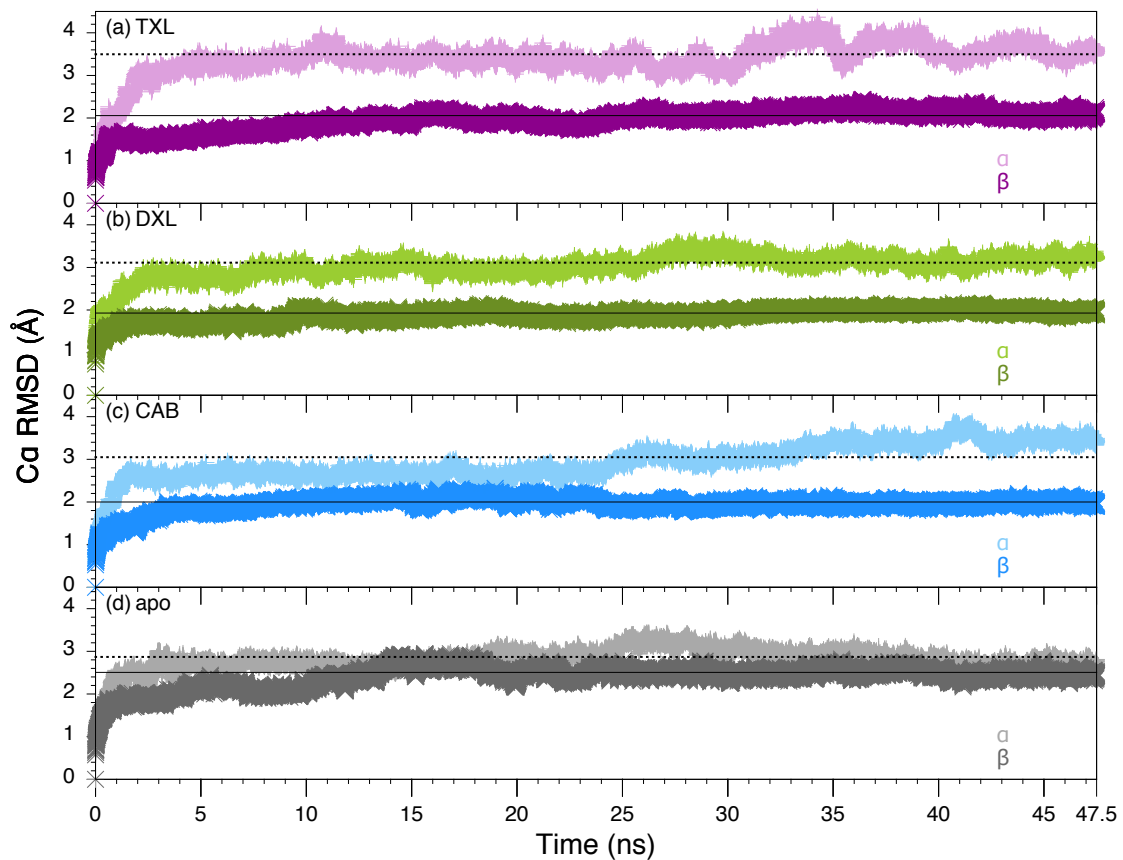
Figure D2: *The mass-weighted RMSD (Å) of the C_α atoms of each subunit, when tubulin is bound to (a) TXL, (b) DXL, (c) CAB, or (d) in its apo form. The average RMSD over the final 37.5 ns for the α- and β-tubulin subunits is indicated with dashed and solid lines, respectively.*
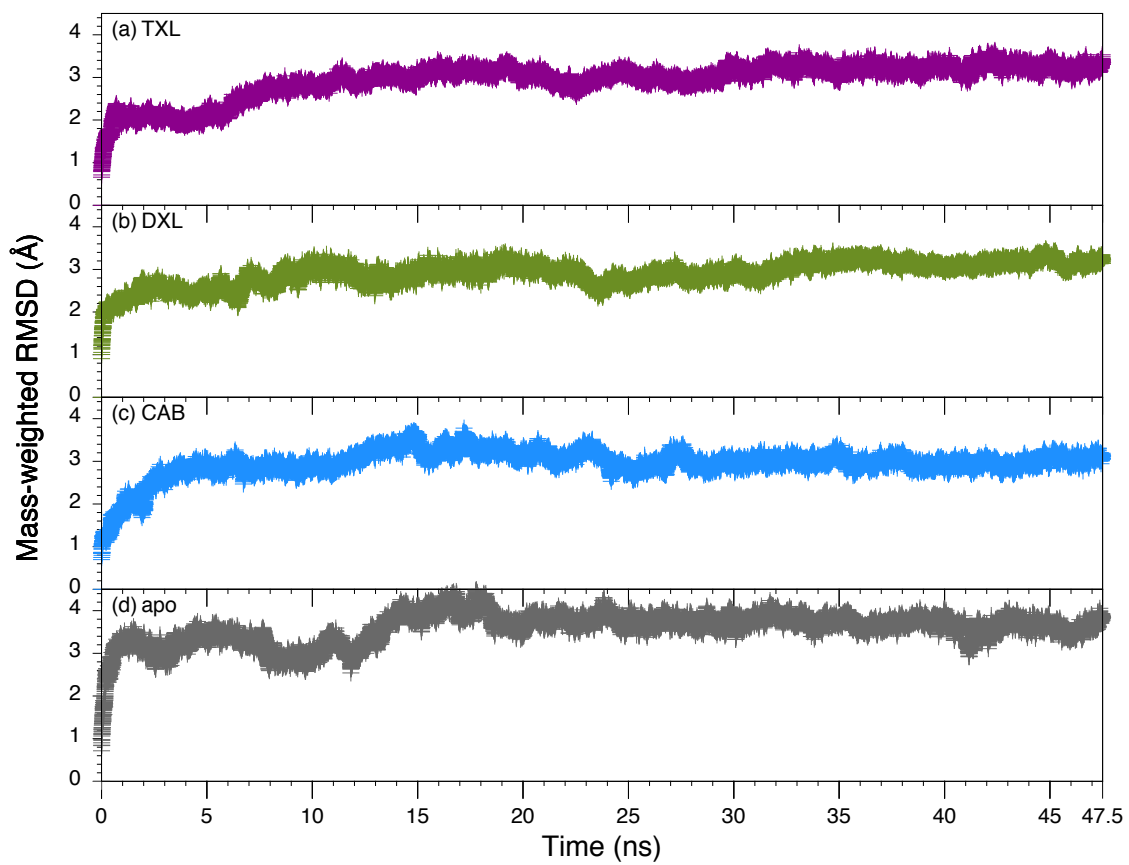
Figure D3: *The mass-weighted RMSD (Å) of the binding site atoms, including the taxane, when tubulin is bound to (a) TXL, (b) DXL, (c) CAB, or (d) in its apo form.*
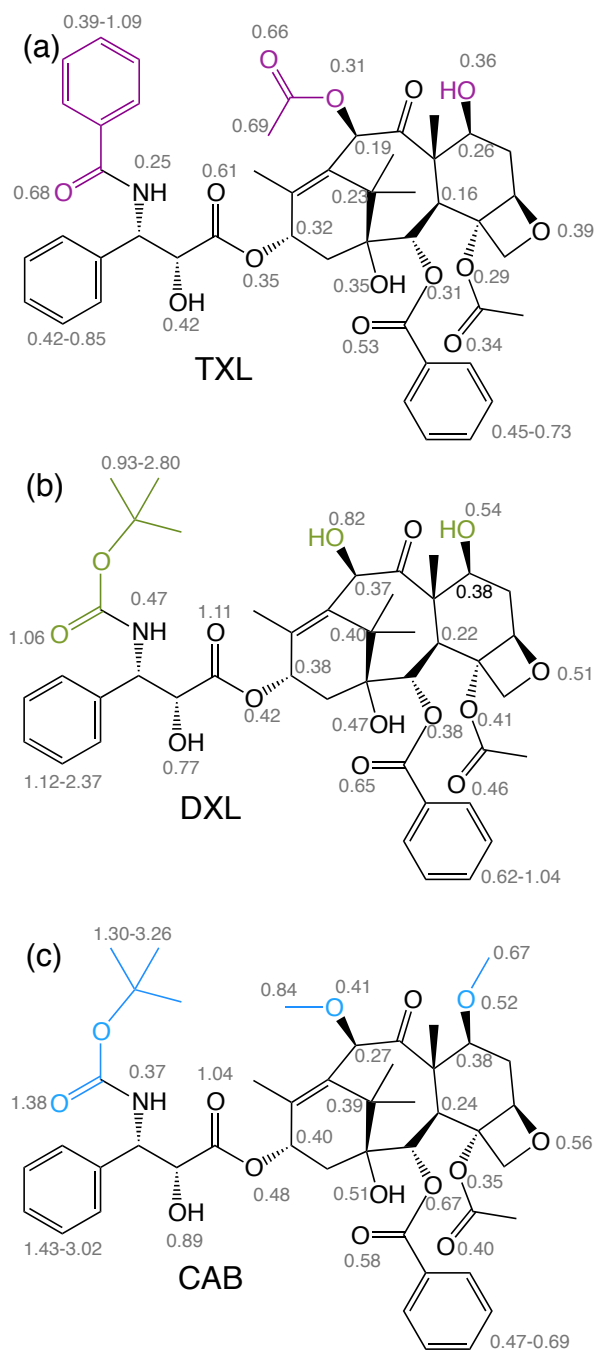
Figure D4: *The RMSF (Å) of select non-hydrogen atoms in (a) TXL, (b) DXL and (c) CAB throughout the simulation. The RMSF is calculated after an RMSD-fit of the drug coordinates in each frame to the average structure taken over 10–47.5 ns.*
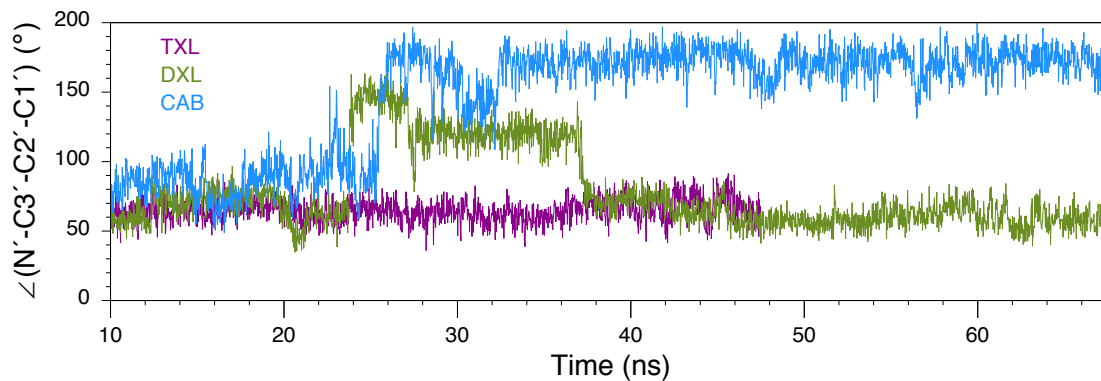
Figure D5: *Variation in the $\angle(N'-C3'-C2'-C1')$ dihedral of the taxanes.*
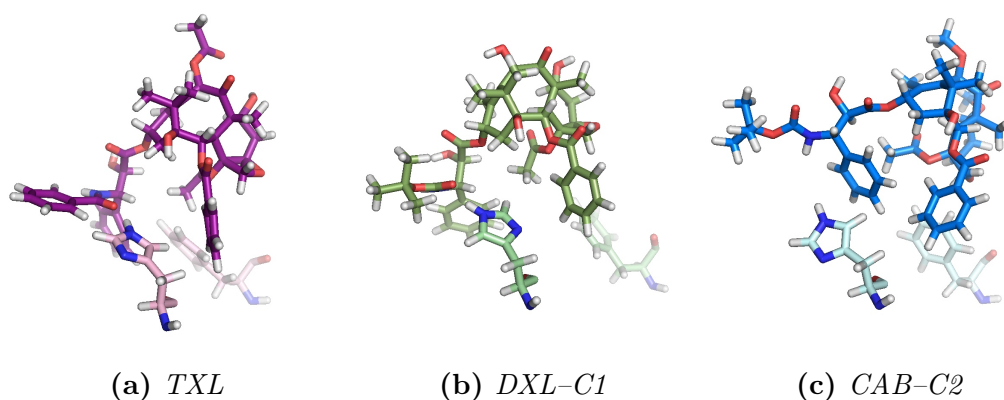
(a) *TXL* **(b)** *DXL–C1* **(c)** *CAB–C2*

Figure D6: *An illustration of the π–π interactions occurring in the taxane binding site between β:His229 and β:Phe272, and (a) TXL, (b) DXL–C1, and (c) CAB–C2. Structures taken from the end of the 47.5 ns simulation.*
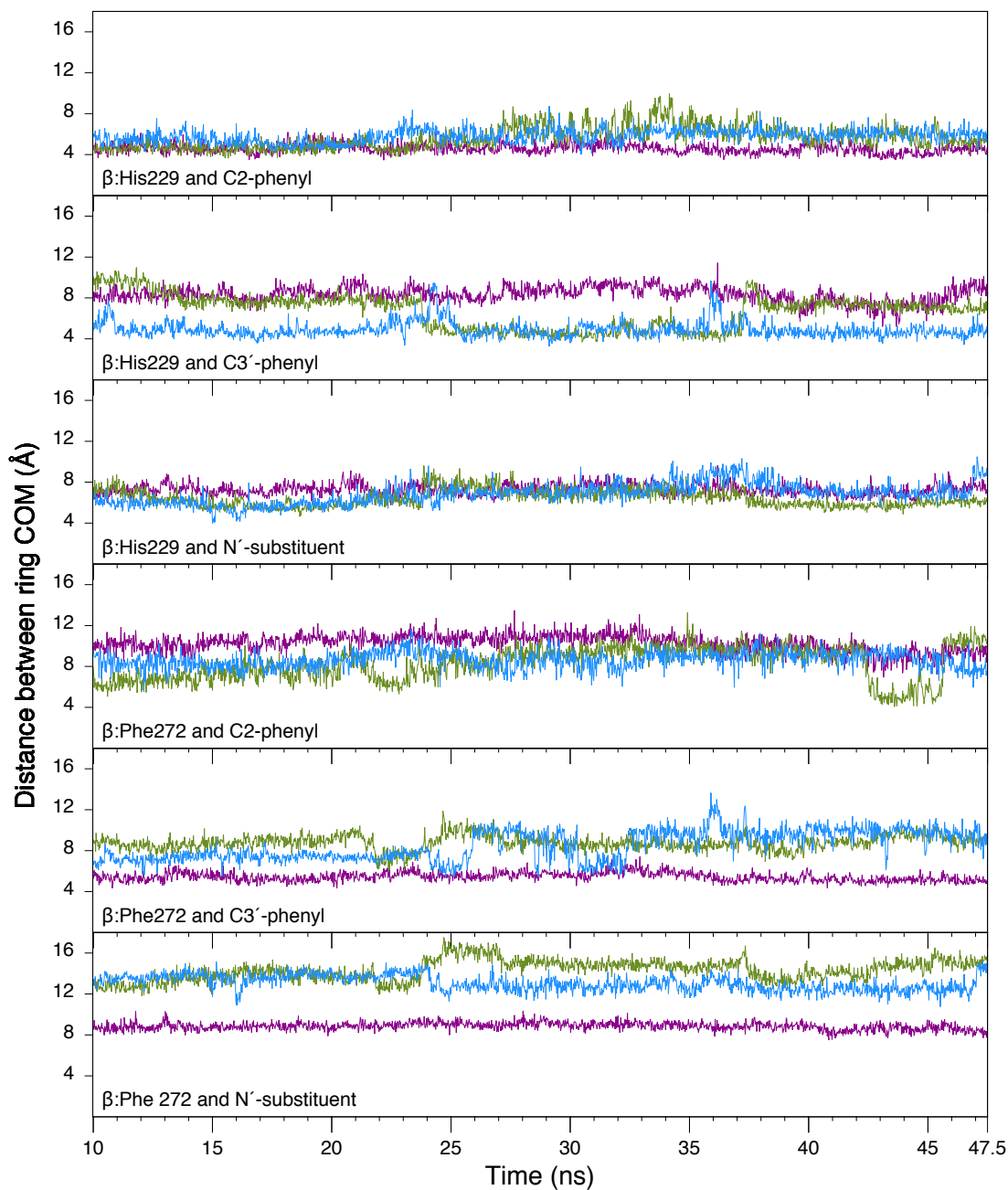
Figure D7: *Distance (Å) between centres of masses (COM) the π-rings of amino acids and the taxane phenyl rings at C2 and C3′, or the phenyl ring/t-butyl substituent at N′.*

Table D1: *Taxane–tubulin hydrogen-bond occupancy (%) over 37.5 ns.*

Acceptor[a]	Donor[a]	TXL	DXL[b]	DXL–C1	DXL–C2	CAB[b]	CAB–C1	CAB–C2
taxane C1-hydroxyl	β:Arg278 $N_{\eta2}$–H_1	-[c]	-	-	-	-	-	-
taxane C1-hydroxyl	β:Arg278 $N_{\eta1}$–H_1							-
taxane C2-carbonyl	taxane C1-hydroxyl	25.3	19.2	16.9	23.5	38.1	22.1	48.7
C2-carbonyl	Arg278 N_ϵ–H	-	-	-	-	-	-	-
taxane oxetane oxygen	β:Thr276 N–H	-	23.8	15.6	38.8	-	-	-
taxane C7-substituent	β:Gln282 N_ϵ–H_1	-	-	-	-	-	-	11.7
taxane C7-substituent	β:Gln282 N_ϵ–H_2	-	-	-	-	-	-	-
β:Thr276 $O_{\gamma1}$	taxane C7-hydroxyl	—	12.0	18.7	-	—	—	—
taxane C9-carbonyl	β:Arg278 $N_{\eta1}$–H_2	-	-	-	-	-	-	-
taxane C9-carbonyl	β:Gln282 N_ϵ–H_1	-	-	11.7	-	-	-	14.4
taxane C9-carbonyl	β:Arg284 N_ϵ–H	-	-	-	22.4	-	-	-
taxane C9-carbonyl	β:Arg284 $N_{\eta2}$–H_1	-	-	-	17.8	-	-	-
taxane C10-substituent	β:Arg284 $N_{\eta2}$–H_1	-	-	-	14.6	-	-	-
β:Arg369 O	taxane C10-hydroxyl	—[d]	36.9	18.0	70.6	—	—	—
taxane C1'-carbonyl	β:Arg369 $N_{\eta1}$–H_1	-	-	-	-	-	-	-
β:Asp26 $O_{\delta1}$	taxane C2'-hydroxyl	-	59.4	51.5	73.7	-	-	-
β:Asp26 $O_{\delta2}$	taxane C2'-hydroxyl	-	35.6	42.7	22.9	-	-	-
β:Arg369 O	taxane C2'-hydroxyl	82.5	-	-	-	-	-	-
taxane N'–H	β:Asp26 $O_{\delta1}$	-	22.7	28.9	11.6	-	-	-
taxane N'–H	β:Asp26 $O_{\delta2}$	-	20.6	31.1	-	-	-	-
N'-carbonyl	β:His229 N_ϵ–H	—	31.1	48.5	-	-	22.1	-

Table D2: *Solvent-bridged taxane–tubulin hydrogen-bond occupancy (%) over 37.5 ns.*

Interaction[a]	TXL	DXL	CAB
β:Asp26 $\cdots$ taxane	21.7	18.3	-
β:His229 $\cdots$ taxane	16.3	10.3	-
β:Pro274 $\cdots$ taxane	13.4	-	-
β:Thr276 $\cdots$ taxane	-[b]	24.9	-
β:Gln282 $\cdots$ taxane	37.5	14.9	-
β:Arg320 $\cdots$ taxane	-	11.3	-
β:Arg329 $\cdots$ taxane	-	50.6	-
β:Gly370 $\cdots$ taxane	-	10.8	-
β:Ser374 $\cdots$ taxane	-	18.8	-

[a] Hydrogen bond defined as heavy atoms within 3.0 Å and $135° \leq \angle(\text{donor–H} \cdots \text{acceptor}) \leq 180°$.
[b] Indicates an occupancy < 10 %.

Table D3: *Solvent–taxane hydrogen-bond occupancy (%) over 37.5 ns.*

Acceptor[a]	Donor[a]	TXL	DXL	CAB
water	C1-hydroxyl	34.6	44.0	-
C1-hydroxyl	water	50.2	39.3	-
C2-carbonyl	water	82.0	76.2	11.8
C2-alkoxy	water	-[b]	-	-
C4-carbonyl	water	22.4	-	-
C4-alkoxy	water	-	-	-
oxetane oxygen	water	-	-	-
water	C7-hydroxyl	83.7	59.7	—
C7-hydroxyl	water	26.0	11.8	—
C7-methoxy	water	—[c]	—	-
C9-carbonyl	water	86.3	51.1	-
C10-carbonyl	water	96.0	—	—
C10-alkoxy	water	-	—	-
water	C10-hydroxyl	—	42.1	—
C10-hydroxyl	water	—	42.1	—
C13-alkoxy	water	-	-	-
C1′-carbonyl	water	91.4	64.9	12.6
water	C2′-hydroxyl	12.4	-	10.9
C2′-hydroxyl	water	19.0	45.9	-
water	N′–H	-	-	-
N′	water	-	-	-
N′-carbonyl	water	108.1	84.0	14.6
N′-alkoxy	water	—	-	-

[a] Hydrogen bond defined as heavy atoms within 3.0 Å and $135° \leq \angle(\text{donor–} \text{H} \cdots \text{acceptor}) \leq 180°$. [b] Indicates an occupancy < 10 %.;
[c] Not applicable.

Table D4: *MM/GBSA-calculated taxane–tubulin binding free energy (kJ mol^{-1}).*

	TXL	DXL	DXL–C1	DXL–C2	CAB	CAB–C1	CAB–C2
			Residue Contributions[a]				
β:Glu22	-5.5	-8.0	-7.8	-8.4	-6.9	-6.6	-7.1
β:Val23	-20.6	-19.8	-21.1	-17.5	-10.2	-14.4	-7.4
β:Asp26	-6.2	-43.1	-46.3	-37.3	-6.7	-6.9	-6.5
β:Glu27	-0.2	-3.0	-0.6	-7.4	-0.3	-0.4	-0.3
β:Phe83	-4.2	-4.5	-6.2	-1.6	-0.4	-0.7	-0.3
β:Thr216	-7.4	-4.8	-4.7	-4.9	-0.7	-0.4	-0.9
β:Leu217	-12.4	-2.4	-2.1	-3.0	-12.9	-13.1	-12.8
β:Leu219	-0.5	-0.1	-0.1	-0.1	-3.1	-4.2	-2.4
β:Asp226	-5.2	-1.9	-2.3	-1.1	-7.8	-8.1	-7.6
β:His229	-17.1	-20.6	-23.0	-16.4	-21.7	-27.8	-17.6
β:Leu230	-7.6	-5.8	-6.4	-4.8	-7.0	-6.9	-7.2
β:Ala233	-9.1	-9.1	-10.6	-6.4	-3.5	-5.9	-1.8
β:Ser236	-4.6	-3.1	-4.5	-0.6	-1.0	-2.2	-0.2
β:Gly237	-2.5	-1.6	-2.4	-0.2	-0.1	-0.2	-0.1
β:Phe272	-7.9	-7.6	-7.8	-7.3	-7.1	-8.2	-6.4
β:Pro274	-9.2	-2.5	-1.9	-3.6	-9.7	-10.3	-9.3
β:Leu275	-16.4	-15.3	-14.6	-16.6	-9.6	-6.0	-12.0
β:Thr276	-4.0	-17.0	-18.0	-15.2	-4.8	-1.2	-7.3
β:Ser277	-0.2	-2.6	-3.2	-1.5	-0.7	-0.3	-1.0
β:Arg278	-0.9	-13.3	-13.4	-13.2	-13.5	-7.8	-17.4
β:Gln282	-13.4	-7.1	-9.1	-3.4	-13.0	-9.4	-15.4
β:Tyr283	-0.6	-0.8	-0.6	-1.2	-2.1	-0.8	-3.1
β:Arg284	-0.8	-10.6	-2.1	-25.7	-0.7	-0.4	-0.8
β:Leu286	-0.2	-0.9	-1.3	-0.1	-3.5	-3.3	-3.7
β:Arg320	-0.3	-5.1	-7.2	-1.4	-0.3	-0.4	-0.1
β:Pro360	-10.8	-7.0	-8.4	-4.4	-1.6	-1.5	-1.7
β:Arg369	-29.3	-28.8	-22.0	-40.9	-18.9	-13.9	-22.3
β:Gly370	-7.9	-2.6	-2.1	-3.5	-8.3	-6.4	-9.6
β:Leu371	-14.5	-13.0	-12.6	-13.9	-15.0	-14.8	-15.1
			Ligand–Protein Binding[b]				
$\Delta G^{MM/GBSA}$	-182.5	-195.5	-198.4	-190.5	-148.5	-143.7	-151.6
Std. Dev.	±15.0	±27.1	±30.1	±19.8	±15.2	± 15.2	±14.3

[a] Pairwise $\Delta G_{ij}^{MM/GBSA}$, Equation 1.22, contributions are not additive ($\sum \Delta G_{ij}^{MM/GBSA} \neq \Delta G^{MM/GBSA}$).; [b] $\Delta G^{MM/GBSA}$, Equations 1.20 and 1.21, neglecting entropy.
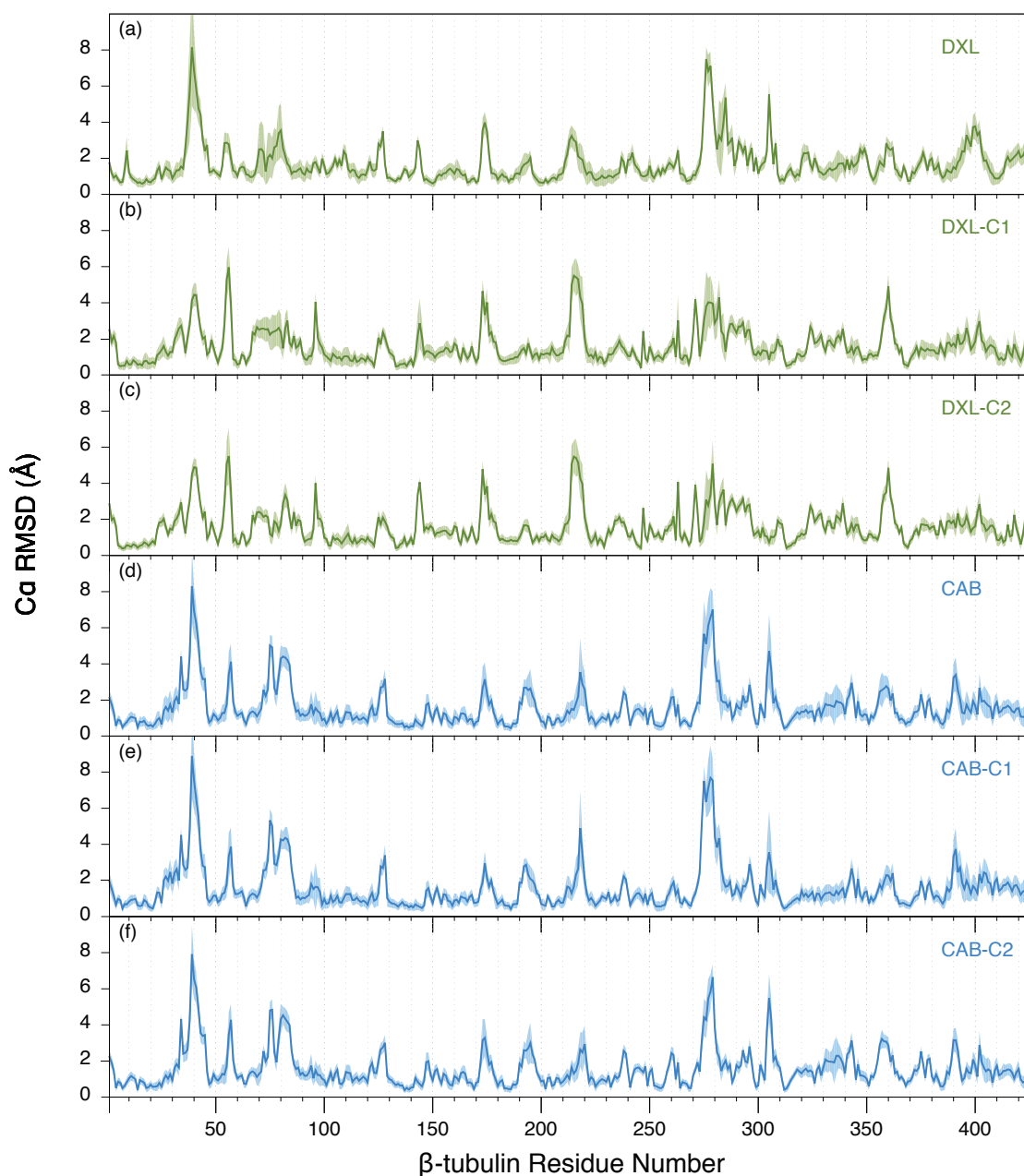
Figure D8: *The average mass-weighted RMSD of the C_α atoms for each β-tubulin residue residue, with the standard deviation shaded to indicate flexibility. Results displayed for (a) the average of DXL from 10–47.5 ns, (b) average over DXL–C1, (c) average over DXL–C2, (d) the average of CAB from 10–47.5 ns, (e) average over CAB–C1, and (f) average over CAB–C2. The residues for the β-tubulin model are numbered consecutively. Therefore, residues 1–42 in the figure correspond to residues 1–42 in 1JFF, residues 43–358 in the figure correspond to residues 45–360 in 1JFF, and residues 359–427 in the figure correspond to residues 369–437 in 1JFF.*

227
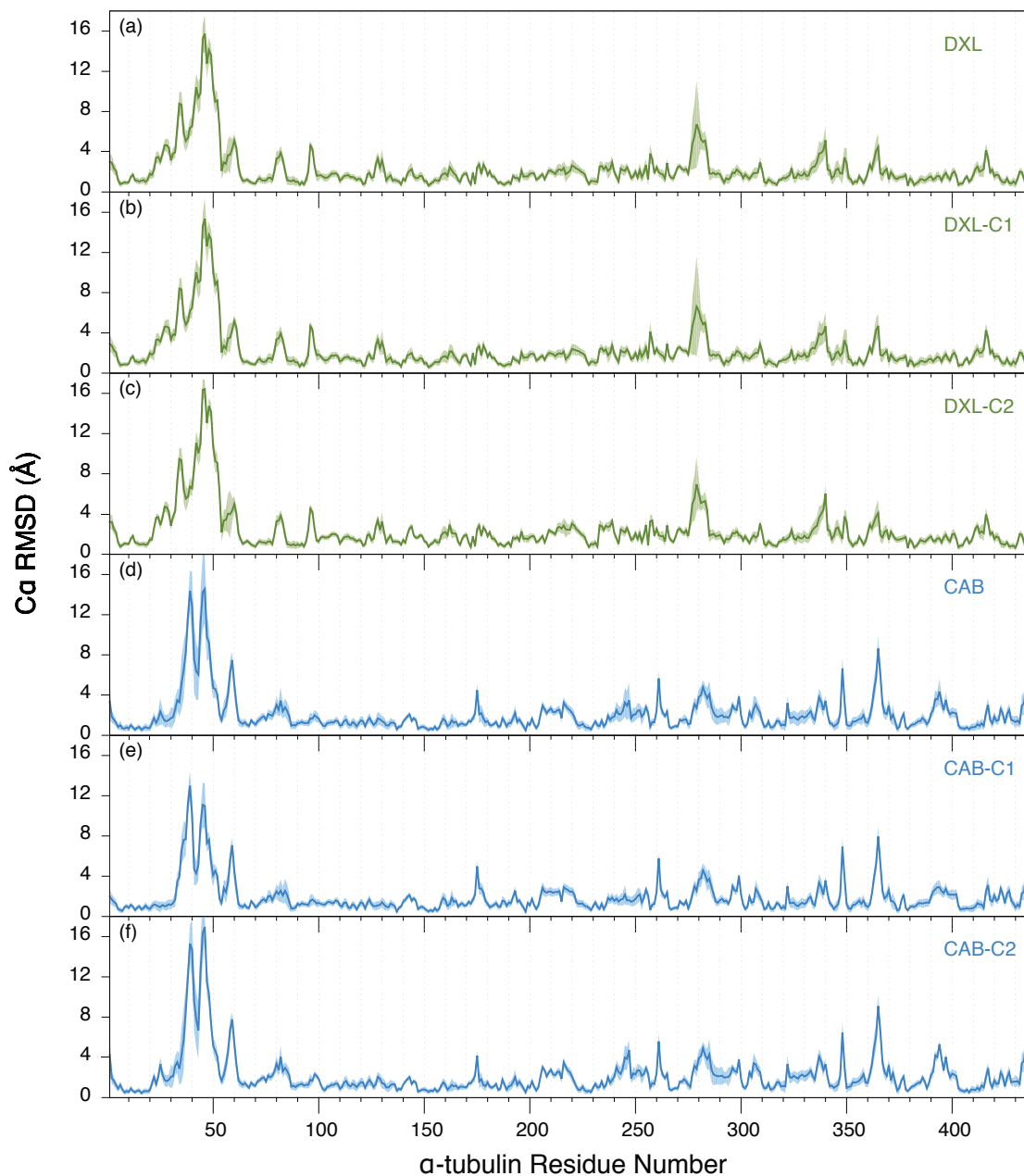
Figure D9: *The average mass-weighted RMSD of the C_α atoms for each α-tubulin residue residue, with the standard deviation shaded to indicate flexibility. Results displayed for (a) the average of DXL from 10–47.5 ns, (b) average over DXL–C1, (c) average over DXL–C2, (d) the average of CAB from 10–47.5 ns, (e) average over CAB–C1, and (f) average over CAB–C2.*

Appendix E

Appendix to Chapter 6

Table E1: *Fragment polarization energy (kJ mol^{-1}), calculated as the difference in monomer energy in a self-consistent electrostatic field by FMO-MP2 (polarized) and that calculated with MP2 (isolated).*

						Complex[a]					
Frag.[b]	2S	2PD	2T	3A	3B	3C	3D	3E	4A	4B	4C
1	-0.68	0.10	0.55	-0.72	0.08	0.46	0.80	2.01	-0.72	0.07	0.49
2	-0.68	0.10	0.92	-1.42	0.45	1.79	0.70	2.00	-1.48	0.40	1.69
3				-0.72	0.08	0.46	0.80	2.01	-1.48	0.40	0.67
4									-0.72	0.07	0.82

[a] A positive number indicates the FMO monomer is less stable than the separated monomer.;
[b] Fragments are numbered with respect to Figure 6.1 where the top monomer in each complex is designated as Fragment 1.
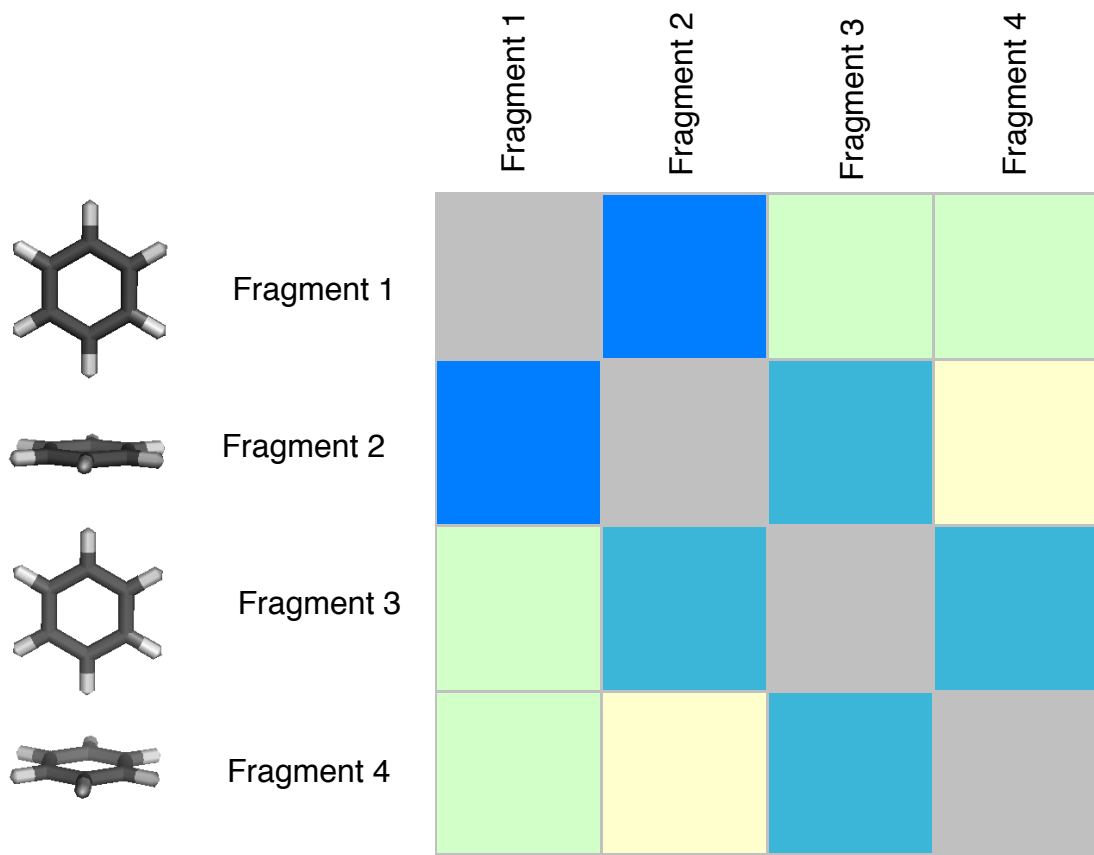
Figure E1: *An interpretation of the PIEDA results reported in subsequent figures, using structure 4C in Figure 6.1.*
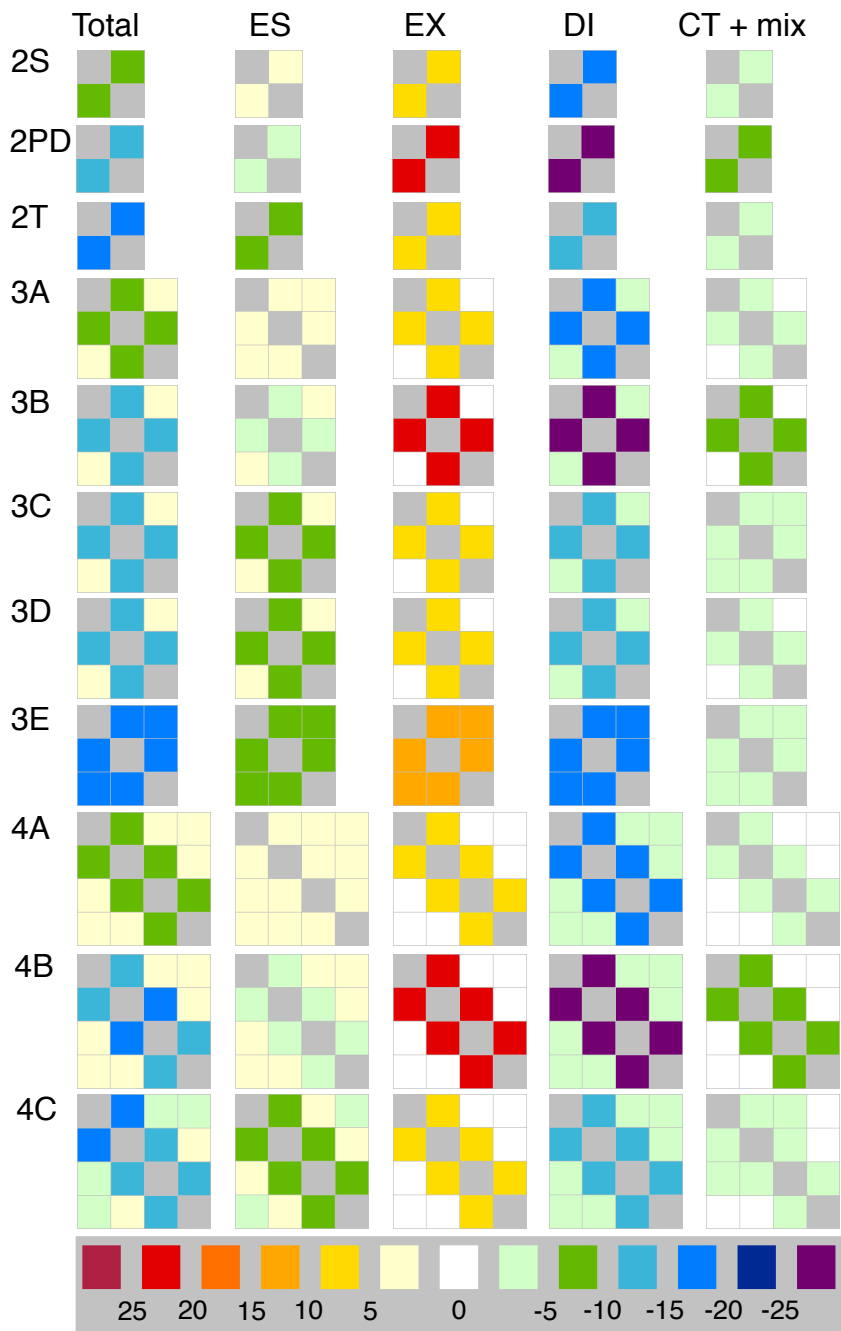
Figure E2: *PIEDA results for the $\Delta E'^{FMO2}_{full}$ interaction energies (kJ mol^{-1}) for the benzene complexes. Decomposition performed according to Equation 6.4. Figure interpreted according to Figure E1.*

Table E2: *FMO2 interaction energies ($\Delta E_{full}^{\prime FMO2}$) and PIEDA results for the benzene complexes, calculated with respect to the polarized monomers.*

Structure	$\Delta E_{full}^{\prime FMO2}$	$\Delta E^{\prime ES}$[a]	$\Delta E^{\prime EX}$[b]	$\Delta E^{\prime DI}$[c]	$\Delta E^{\prime CT+mix}$[d]
2S	-8.4	4.4	9.7	-19.4	-3.1
2PD	-14.5	-0.9	20.2	-28.1	-5.6
2T	-15.1	-6.5	9.9	-14.9	-3.7
3A	-16.7	9.3	19.3	-39.1	-6.2
3B	-29.4	-1.7	40.3	-56.9	-11.1
3C	-29.8	-12.6	19.9	-29.9	-7.3
3D	-29.2	-12.1	20.0	-29.9	-7.3
3E	-49.2	-20.9	34.2	-48.2	-13.7
4A	-25.0	14.4	28.9	-58.9	-9.3
4B	-44.4	-2.4	60.3	-85.7	-16.6
4C	-44.1	-18.3	29.9	-44.9	-10.9

[a] Electrostatic contribution.; [b] Exchange-repulsion contribution.; [c] Dispersion contribution.; [d] Charge transfer and mixed (remaining) contributions.
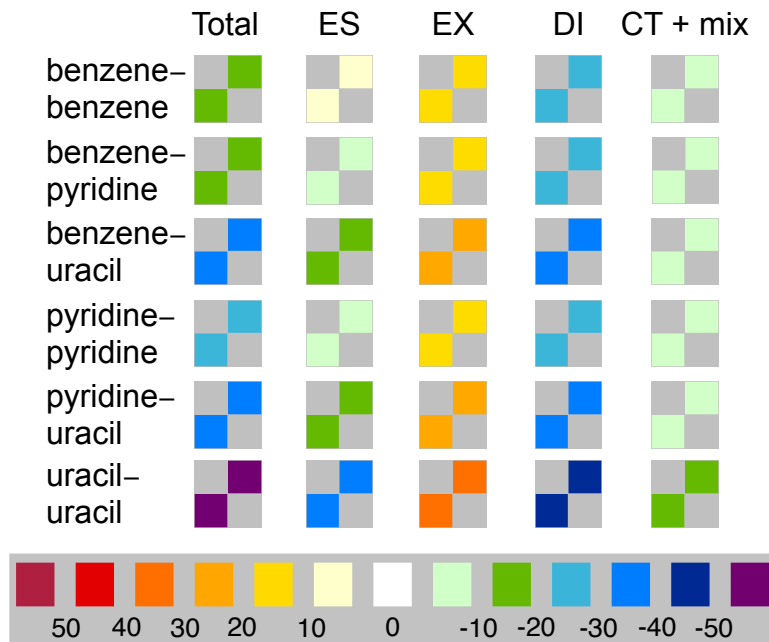
Figure E3: *PIEDA results for the $\Delta E'^{FMO2}_{full}$ interaction energies (kJ mol^{-1}) for a selection of the S66 database. Data included in Table E3. Decomposition performed according to Equation 6.4. Figure interpreted according to Figure E1.*

Table E3: *FMO2 interaction energies ($\Delta E'^{FMO2}_{full}$) and PIEDA results for a selection of the S66 database, calculated with respect to the polarized monomers.*

Structure	$\Delta E'^{FMO2}_{full}$	$\Delta E'^{ES}$(a)	$\Delta E'^{EX}$(b)	$\Delta E'^{DI}$(c)	$\Delta E'^{CT+mix}$(d)
benzene–benzene	-13.9	0.3	14.2	-23.5	-5.0
benzene–pyridine	-17.8	-3.2	16.5	-25.5	-5.5
benzene–urail	-32.4	-13.6	25.1	-35.6	-8.3
pyridine–pyridine	-20.8	-5.8	17.9	-27.0	-5.9
pyridine–uracil	-36.1	-19.4	25.9	-36.1	-8.6
uracil–uracil	-55.4	-35.7	34.4	-42.6	-11.5

(a) Electrostatic contribution.;   (b) Exchange-repulsion contribution.;
(c) Dispersion contribution.;   (d) Charge transfer and mixed (remaining) contributions.

Appendix F

Appendix to Chapter 7

Table F1: *MM/GBSA-calculated taxane–tubulin binding energy (kJ mol^{-1}) based on the structures obtained in Chapter 5, using different approaches.*

Interaction	TXL	DXL[a]	CAB[b]
taxane–$\alpha\beta$-tubulin, 37.5 ns trajectory	-182.5 $\pm$15.0	-198.4 $\pm$30.1	-151.6 $\pm$14.3
taxane–$\alpha\beta$-tubulin, final structure	-197.8	-169.2	-142.0
taxane–β-tubulin, final structure	-197.5	-167.9	-142.8

[a] Reported as DXL–C1 in Chapter 5.;   [b] Reported as CAB–C2 in Chapter 5.

Table F2: *The binding energy (kJ mol⁻¹) contribution from each 2° structure in β-tubulin to the binding of the taxanes.*

2° St.	TXL				DXL				CAB			
	HF[a]	MP2[a]	PCM[1(2)]-MP2[a]	MM/GBSA[b]	HF[a]	MP2[a]	PCM [1(2)]-MP2[a]	MM/GBSA[b]	HF[a]	MP2[a]	PCM[1(2)]-MP2[a]	MM/GBSA[b]
N-term	3.6	3.6	0.3	0.0	4.5	4.5	6.9	0.0	3.8	3.8	-5.0	0.0
S1	-0.6	-0.6	-0.2	0.0	-1.5	-1.5	-0.8	0.0	-0.5	-0.5	-0.2	0.0
S1–H1	-0.1	-0.1	-0.3	0.0	-1.1	-1.1	-1.2	0.0	-0.8	-0.8	-0.3	0.0
H1	-22.4	-56.8	-30.5	-28.2	-175.1	-264.9	-248.1	-83.9	-46.5	-54.8	-3.6	-7.7
H1–H1'	-8.9	-13.3	-7.5	-4.2	6.4	-12.7	-28.9	-9.4	-11.4	-11.6	20.3	-0.4
H1'	-0.9	-0.9	0.0	-0.1	-1.3	-1.3	0.1	-0.1	-0.2	-0.2	0.7	0.0
H1'–S2	5.0	5.0	1.7	-0.1	10.4	10.4	13.0	-0.1	6.7	6.7	-3.7	0.0
S2	-0.5	-0.5	-0.2	0.0	-0.9	-0.9	-0.3	0.0	-0.4	-0.4	0.0	0.0
S2–H2	-1.6	-1.6	0.6	0.0	-3.6	-3.6	-4.7	0.0	-3.4	-3.4	5.0	0.0
H2	-2.8	-2.8	2.0	0.0	-8.4	-8.4	-9.1	-0.1	-6.5	-6.5	5.0	0.0
H2–H2'	2.6	2.6	-1.1	-0.1	6.4	6.4	7.4	-0.1	5.3	5.3	-5.1	-0.1
H2'	-1.2	-1.2	0.0	-0.2	0.3	-1.2	-2.5	-1.7	0.2	0.2	-1.4	-0.1
H2'–H2''	3.7	3.7	-0.6	-0.1	8.9	8.9	10.9	-0.1	6.5	6.5	-3.9	0.0
H2''	-3.3	-3.3	0.2	0.0	-5.7	-5.7	-6.6	0.0	-3.8	-3.8	3.8	0.0
S3	-0.3	-0.3	0.1	0.0	-0.2	-0.2	-0.4	0.0	-0.3	-0.3	0.2	0.0
S3–H3'	0.3	0.3	-0.1	0.0	-0.3	-0.3	-0.2	0.0	0.1	0.1	-0.1	0.0
H3'	1.4	1.4	-0.3	0.0	3.0	3.0	4.3	0.0	2.5	2.5	-4.5	0.0
H3'–H3	-1.6	-1.6	0.4	0.0	-3.4	-3.4	-4.2	0.0	-2.5	-2.5	4.2	0.0
H3	-4.9	-4.9	0.6	0.0	-11.3	-11.3	-11.7	0.0	-7.4	-7.4	9.5	0.0
H3–S4	-5.2	-5.2	0.3	0.0	-8.9	-8.9	-9.1	0.0	-5.5	-5.5	8.4	0.0
S4	-0.4	-0.4	0.3	0.0	-0.6	-0.6	-0.8	0.0	-0.3	-0.3	-0.1	0.0
S4–H4	0.0	0.0	0.0	0.0	0.7	0.7	0.8	0.0	0.8	0.8	-0.4	0.0
H4	1.1	1.1	-0.1	0.0	2.5	2.5	3.2	0.0	2.2	2.2	-1.4	0.0
H4–S5	0.2	0.2	0.4	0.0	0.4	0.4	1.3	0.0	0.5	0.5	0.3	0.0
S5	-0.1	-0.1	-0.3	-0.1	-0.6	-0.6	-0.9	0.0	0.0	0.0	-1.0	0.0
S5–H5	-5.1	-5.1	0.0	-0.1	-6.5	-6.5	-6.9	0.0	-8.7	-8.7	5.7	0.0
H5	-0.3	-0.3	-0.3	0.0	-0.4	-0.4	0.2	0.0	0.1	0.1	-0.4	0.0
H5–S6	-5.7	-5.7	-0.2	0.0	-8.4	-8.4	-9.3	0.0	-5.8	-5.8	10.1	0.0

Continued on the next page

235

Continuation of Table F2

2° St.	TXL				DXL				CAB			
	HF[a]	MP2[a]	PCM[1(2)]-MP2[a]	MM/GBSA[b]	HF[a]	MP2[a]	PCM[1(2)]-MP2[a]	MM/GBSA[b]	HF[a]	MP2[a]	PCM[1(2)]-MP2[a]	MM/GBSA[b]
S6	-0.5	-0.5	-0.3	0.0	-0.4	-0.4	0.5	0.0	-0.6	-0.6	-0.1	0.0
S6–H6	0.4	0.4	0.1	-0.1	-0.5	-0.5	-0.4	0.0	0.4	0.4	-0.2	0.0
H6	3.9	2.9	6.3	-1.3	-10.6	-18.4	-31.0	-6.4	5.1	4.1	29.1	-1.5
H6–H7	-49.5	-83.1	-38.8	-26.2	-4.5	-41.9	-2.5	-26.7	-5.3	-26.3	-50.4	-8.8
H7	-15.4	-103.8	-91.4	-56.2	-47.0	-129.5	-125.5	-60.9	-25.8	-68.9	-37.9	-33.9
H7–H8	2.1	2.1	-1.4	-0.1	5.8	5.8	3.2	-0.1	3.2	3.2	0.3	-0.1
H8	7.6	7.6	1.0	0.0	11.8	11.8	14.8	0.0	8.1	8.1	-11.6	0.0
H8–S7	2.2	2.2	0.8	0.0	2.7	2.7	4.3	0.0	1.8	1.8	-4.2	0.0
S7	1.5	1.5	0.9	-0.1	0.3	0.3	0.7	-0.1	1.2	1.2	0.1	0.0
M-loop	-4.8	-93.8	-86.8	-61.2	-57.2	-94.3	-53.7	-30.0	-147.9	-236.0	-193.2	-76.4
H9	0.7	0.7	-0.1	-0.5	1.1	1.1	-6.2	-0.1	4.3	4.3	11.1	-0.6
H9–H9'	-4.5	-4.5	-0.4	-0.4	-0.9	-0.9	-5.5	-0.2	-4.1	-4.1	7.2	-0.4
H9'	0.8	0.8	-0.1	0.0	1.4	1.4	5.3	0.0	-1.1	-1.1	-8.7	0.0
H9'–S8	1.7	1.7	0.6	0.0	1.7	1.7	4.7	0.0	0.0	0.0	-6.5	0.0
S8	10.9	10.9	7.7	-0.5	6.1	4.7	20.8	-1.9	17.6	17.6	-8.9	-0.2
S8–H10	2.8	2.8	1.2	-0.1	1.5	1.5	7.7	0.0	3.2	3.2	-6.2	0.0
H10	-0.1	-0.1	0.2	0.0	-1.5	-1.5	-0.1	0.0	0.0	0.0	0.3	0.0
H10–S9	-1.4	-1.4	-0.1	0.0	-0.9	-0.9	-2.3	0.0	0.3	0.3	4.8	0.0
S9	5.1	5.1	2.1	0.0	3.1	3.1	6.0	0.0	3.0	3.0	-6.7	0.0
S9–S10	-61.0	-144.3	-148.7	-73.4	-3.2	-18.0	7.4	-18.2	16.6	-59.7	-88.3	-59.5
S10	-0.7	-0.7	0.4	-0.5	-1.0	-1.0	-0.7	-0.2	-0.2	-0.2	0.7	-0.1
H11	2.5	2.5	0.6	0.0	2.7	2.7	3.7	0.0	0.8	0.8	-1.5	0.0
H11–H11'	2.7	2.7	-0.8	0.0	5.4	5.4	9.6	0.0	2.7	2.7	-13.6	0.0
H11'	-0.1	-0.1	-0.1	0.0	-0.3	-0.3	-0.9	0.0	-0.1	-0.1	-0.3	0.0
H11'–H12	-2.6	-2.6	0.5	0.0	-5.1	-5.1	-7.3	0.0	-3.9	-3.9	7.9	0.0
H12	-12.7	-12.7	0.1	0.0	-17.5	-17.5	-28.7	0.0	-8.9	-8.9	39.2	0.0

(a) Pairwise taxane–fragment interactions ($\Delta E_{ij}^{\prime FMO2}$) calculated according to Equation 1.12, and summed over all fragments in the substructure.;
(b) Pairwise taxane–residue interactions ($\Delta G_{ij}^{MM/GBSA}$) calculated according to Equation 1.22, and summed over all residues in the substructure.

Table F3: *The PCM[1(2)]-MP2 binding energy (kJ mol^{-1}) contributions to taxane binding from fragments in select 2° structures in β-tubulin. Calculated according to Equation 1.12.*

Fragment	2° St.	‖	TXL	DXL	CAB
CYS-12	H1		0.2	-0.7	0.1
GLY-13	H1		0.0	-1.0	-0.2
ASN-14	H1		-0.1	-0.7	-0.3
GLN-15	H1		0.2	0.4	0.2
ILE-16	H1		0.6	-0.8	-0.2
GLY-17	H1		0.3	-1.5	0.1
ALA-18	H1		-0.1	-1.2	-0.4
LYS-19	H1		-6.0	14.3	-8.7
PHE-20	H1		2.5	-1.2	-0.1
TRP-21	H1		1.3	-2.6	-0.1
GLU-22	H1		3.4	-23.2	9.3
VAL-23	H1		-17.3	-30.3	0.0
ILE-24	H1		-5.4	-28.0	0.7
SER-25	H1		-2.9	-0.9	0.5
ASP-26	H1		-7.2	-170.7	-4.6
GLU-27	H1–H1′		-10.4	-22.5	2.2
HIS-28	H1–H1′		1.6	8.3	1.0
GLY-29	H1–H1′		0.6	3.7	0.2
ILE-30	H1–H1′		0.7	4.1	0.4
ASP-31	H1–H1′		-0.1	-13.4	6.8
PRO-32	H1–H1′		-0.5	-0.8	-0.4
THR-33	H1–H1′		0.7	1.4	-0.4
GLY-34	H1–H1′		0.1	1.0	0.4
SER-35	H1–H1′		-0.2	0.3	-0.2
TYR-36	H1–H1′		-0.3	-1.8	-0.8
HIS-37	H1–H1′		0.7	1.6	0.8
GLY-38	H1–H1′		0.5	0.5	0.5
ASP-39	H1–H1′		0.4	-7.8	6.2
SER-40	H1–H1′		0.0	0.7	-0.3
ASP-41	H1–H1′		-0.6	-7.7	4.9
LEU-42	H1–H1′		-0.1	0.0	-0.1
GLN-45	H1–H1′		-0.7	1.4	0.7
LEU-46	H1–H1′		-0.3	-1.4	-0.3
GLU-47	H1–H1′		-0.4	-8.5	5.3
ARG-48	H1–H1′		0.8	11.9	-6.6
TYR-53	H1′–S2		0.5	-1.3	-0.1
ASN-54	H1′–S2		-0.1	0.3	0.2
GLU-55	H1′–S2		-0.2	-7.5	4.7
ALA-56	H1′–S2		0.2	0.6	0.3
ALA-57	H1′–S2		-0.3	0.5	-0.4
GLY-58	H1′–S2		0.0	0.4	-0.1
ASN-59	H1′–S2		0.2	-0.8	0.2
LYS-60	H1′–S2		0.0	8.7	-4.9
TYR-61	H1′–S2		0.2	0.7	0.3

Continued on the next page

Continuation of Table F3

Fragment	2° St. ‖	TXL	DXL	CAB
VAL-62	H1′–S2	0.3	0.3	0.4
PRO-63	H1′–S2	-0.3	-0.2	-0.1
ARG-64	H1′–S2	1.1	11.4	-4.2
GLY-111	H3	0.0	0.1	0.0
ALA-112	H3	0.0	-0.1	-0.1
GLU-113	H3	0.4	-3.2	4.2
LEU-114	H3	0.1	0.4	0.0
VAL-115	H3	0.0	-0.2	0.0
ASP-116	H3	0.0	-4.6	4.1
SER-117	H3	0.0	-0.1	0.0
VAL-118	H3	0.1	-0.1	0.1
LEU-119	H3	0.0	-0.3	0.0
ASP-120	H3	0.3	-4.9	3.9
VAL-121	H3	0.0	0.3	0.1
VAL-122	H3	-0.1	-0.3	-0.1
ARG-123	H3	0.1	5.0	-4.0
LYS-124	H3	0.1	5.4	-4.0
GLU-125	H3	-0.2	-8.9	4.8
ASN-206	H6	-0.6	-1.4	0.1
GLU-207	H6	0.7	-8.7	8.4
ALA-208	H6	0.2	0.3	0.5
LEU-209	H6	0.2	0.0	1.1
TYR-210	H6	-0.1	-2.7	1.0
ASP-211	H6	2.7	-8.6	11.3
ILE-212	H6	1.0	0.8	1.2
CYS-213	H6	-0.7	-5.4	2.7
PHE-214	H6	2.9	-5.2	2.9
ARG-215	H6–H7	-2.7	10.3	-13.8
THR-216	H6–H7	-9.0	-10.6	0.3
LEU-217	H6–H7	-12.7	-7.9	-0.6
LYS-218	H6–H7	-11.9	4.8	-32.4
LEU-219	H6–H7	-1.8	-0.7	-3.1
THR-220	H6–H7	0.0	-1.6	0.5
THR-221	H6–H7	-0.4	0.3	-0.8
PRO-222	H6–H7	0.1	0.1	0.0
THR-223	H6–H7	-0.4	2.8	-0.5
TYR-224	H7	-0.5	-2.8	-0.9
GLY-225	H7	-0.4	-2.5	-2.0
ASP-226	H7	3.6	-17.2	11.5
LEU-227	H7	-10.4	-15.1	-15.3
ASN-228	H7	-2.2	-1.7	-0.5
HIS-229	H7	-48.4	-64.7	-15.2
LEU-230	H7	-15.5	-16.1	-20.6
VAL-231	H7	6.9	3.9	3.9
SER-232	H7	-1.8	1.6	1.8
ALA-233	H7	-1.2	-5.8	-3.5

Continuation of Table F3

Fragment	2° St.	‖	TXL	DXL	CAB
THR-234	H7		-12.7	-10.8	2.1
MET-235	H7		0.4	0.5	0.4
SER-236	H7		-2.9	-0.3	0.3
GLY-237	H7		-8.4	-6.9	-0.3
VAL-238	H7		1.5	5.1	0.0
THR-239	H7		0.7	-0.8	0.0
THR-240	H7		0.0	4.9	0.0
CYS-241	H7		-0.7	1.0	0.2
LEU-242	H7		0.7	2.1	0.3
LEU-252	H8		-0.2	-0.6	-0.1
ARG-253	H8		0.3	6.0	-5.4
LYS-254	H8		0.7	7.0	-6.4
LEU-255	H8		-0.3	0.3	-0.2
ALA-256	H8		0.0	0.2	0.0
VAL-257	H8		-0.1	0.2	0.0
ASN-258	H8		0.5	1.4	0.1
MET-259	H8		0.2	0.3	0.5
PHE-272	M-loop		-16.6	-3.0	-18.1
ALA-273	M-loop		1.1	-1.0	5.2
PRO-274	M-loop		-5.4	1.2	-6.0
LEU-275	M-loop		-41.0	-5.5	-16.0
THR-276	M-loop		-2.8	-18.3	-14.7
SER-277	M-loop		3.1	0.0	8.6
ARG-278	M-loop		-3.8	5.7	-66.6
GLY-279	M-loop		-0.5	-1.8	-9.5
SER-280	M-loop		-0.6	1.4	5.1
GLN-281	M-loop		-0.6	-0.3	-0.7
GLN-282	M-loop		-17.1	-2.4	-51.8
TYR-283	M-loop		0.0	1.7	1.1
ARG-284	M-loop		-1.7	-31.7	-22.7
ALA-285	M-loop		-0.5	0.1	-2.9
LEU-286	M-loop		0.4	0.4	-3.5
THR-287	M-loop		-0.4	-0.1	-1.7
VAL-288	M-loop		-0.6	-0.2	0.9
TYR-312	S8		-0.1	-0.6	-0.3
LEU-313	S8		0.1	0.3	-0.1
THR-314	S8		0.2	0.4	0.0
VAL-315	S8		-0.1	-0.3	0.1
ALA-316	S8		0.3	0.7	-0.3
ALA-317	S8		-0.1	-0.6	0.4
VAL-318	S8		0.6	0.7	-0.6
PHE-319	S8		-1.0	-0.7	0.8
ARG-320	S8		7.8	20.8	-9.0
GLY-321	S8–H10		-1.9	1.0	0.3
ARG-322	S8–H10		2.9	6.5	-6.7
MET-323	S8–H10		0.5	0.6	1.0

Continued on the next page

Fragment	2° St. ‖	TXL	DXL	CAB
SER-324	S8–H10 ‖	-0.2	-0.4	-0.8
VAL-351	S9 ‖	0.0	-0.3	0.1
LYS-352	S9 ‖	2.3	6.8	-6.8
THR-353	S9 ‖	-0.5	-0.8	0.1
ALA-354	S9 ‖	0.4	0.3	-0.3
VAL-355	S9 ‖	-0.5	-0.2	0.5
CYS-356	S9 ‖	0.5	0.2	-0.3
ASP-357	S9–S10 ‖	-4.3	-7.4	6.8
ILE-358	S9–S10 ‖	-0.2	0.9	0.4
PRO-359	S9–S10 ‖	-0.2	-2.5	-0.9
PRO-360	S9–S10 ‖	-5.8	-2.4	-3.4
ARG-369	S9–S10 ‖	-46.5	16.1	-29.9
GLY-370	S9–S10 ‖	-82.5	1.6	-28.6
LEU-371	S9–S10 ‖	-12.3	-1.8	-18.4
LYS-372	S9–S10 ‖	4.6	2.9	-14.5
MET-373	S9–S10 ‖	1.8	-1.0	-0.9
SER-374	S9–S10 ‖	-3.4	0.8	1.1

Table F4: *The PIEDA results for the PCM[1(2)]-MP2* ΔE_{ij}^{FMO2} *interaction energy (kJ mol^{-1}), considering the contributions to taxane binding from select fragments in β-tubulin. Calculated according to Equation 1.17.*

Fragment	2° St.	TXL total	TXL ES	TXL EX	TXL CT	TXL DI	TXL G$_{sol}$	DXL total	DXL ES	DXL EX	DXL CT	DXL DI	DXL G$_{sol}$	CAB total	CAB ES	CAB EX	CAB CT	CAB DI	CAB G$_{sol}$
LYS-19	H1	-6.0	-3.2	0.0	0.0	0.0	-2.8	14.3	10.1	0.0	1.6	-0.9	3.5	-8.7	13.1	0.0	0.0	0.0	-21.8
PHE-20	H1	2.5	1.8	0.0	0.0	0.0	0.7	-1.2	-1.4	0.0	0.7	-1.3	0.7	-0.1	-2.8	0.0	0.0	0.0	2.7
TRP-21	H1	1.3	1.0	0.0	0.0	0.0	0.3	-2.6	-2.3	0.0	0.0	0.0	-0.3	-1.0	-1.0	0.0	0.0	0.0	0.9
GLU-22	H1	3.4	-1.5	0.1	0.9	-2.0	5.9	-23.2	-18.1	5.4	-3.2	-8.9	1.6	9.3	-14.7	0.0	-0.5	-0.7	25.2
VAL-23	H1	-17.3	-2.5	10.8	-3.3	-22.3	0.0	-30.3	-9.6	19.7	-11.0	-29.2	-0.1	0.0	-0.8	0.0	0.0	0.0	0.8
ILE-24	H1	-5.4	0.5	0.8	1.2	-7.1	-0.8	-28.0	-20.1	1.2	0.8	-7.6	-2.3	0.7	-0.3	0.0	0.0	0.0	1.0
SER-25	H1	-2.9	-3.4	0.7	0.0	0.0	0.6	-0.9	0.3	0.2	0.3	-2.5	0.8	0.5	1.4	0.0	0.0	0.0	-0.9
ASP-26	H1	-7.2	-15.9	0.7	1.0	-3.0	10.0	-170.7	-183.2	120.3	-43.5	-39.4	-24.9	-4.6	-23.7	4.6	-5.1	-7.6	27.1
GLU-27	H1-H1'	-10.4	-2.6	0.9	-1.3	-4.3	-3.1	-22.5	-13.0	19.2	-6.3	-18.0	-4.5	2.2	0.6	0.0	0.0	-0.1	1.7
HIS-28	H1-H1'	1.6	1.5	0.0	0.0	0.0	0.2	8.3	6.5	0.0	0.5	-0.8	2.1	1.0	1.0	0.0	0.0	0.0	0.0
GLY-29	H1-H1'	0.6	0.9	0.0	0.0	0.0	-0.3	3.7	3.4	0.0	0.0	0.0	0.3	0.2	0.9	0.0	0.0	0.0	-0.7
ILE-30	H1-H1'	0.7	1.0	0.0	0.0	0.0	-0.3	4.1	3.3	0.0	0.0	0.0	0.8	0.4	1.1	0.0	0.0	0.0	-0.7
ASP-31	H1-H1'	-0.1	-5.1	0.0	0.0	0.0	4.9	-13.4	-9.1	0.0	0.0	0.0	-4.4	6.8	-9.1	0.0	0.0	0.0	15.9
ASP-39	H1-H1'	0.4	-2.4	0.0	0.0	0.0	2.7	-7.8	-1.2	0.0	0.0	0.0	-6.6	6.2	-4.1	0.0	0.0	0.0	10.3
SER-40	H1-H1'	0.0	0.2	0.0	0.0	0.0	-0.2	0.7	0.6	0.0	0.0	0.0	0.1	-0.3	0.3	0.0	0.0	0.0	-0.6
ASP-41	H1-H1'	-0.6	-2.9	0.0	0.0	0.0	2.3	-7.7	-3.6	0.0	0.0	0.0	-4.2	4.9	-3.3	0.0	0.0	0.0	8.2
LEU-42	H1-H1'	-0.1	0.0	0.0	0.0	0.0	-0.1	0.0	-0.1	0.0	0.0	0.0	0.2	-0.1	-0.4	0.0	0.0	0.0	-0.2
GLN-45	H1-H1'	-0.7	0.2	0.0	0.0	0.0	-0.9	1.4	1.2	0.0	0.0	0.0	0.3	0.7	0.7	0.0	0.0	0.0	1.1
LEU-46	H1-H1'	-0.3	-0.3	0.0	0.0	0.0	0.0	-1.4	-1.1	0.0	0.0	0.0	-0.3	-0.3	-0.4	0.0	0.0	0.0	0.1
GLU-47	H1-H1'	-0.4	-3.3	0.0	0.0	0.0	2.9	-8.5	-5.0	0.0	0.0	0.0	-3.4	5.3	-3.8	0.0	0.0	0.0	9.1
ARG-48	H1-H1'	0.8	5.2	0.0	0.0	0.0	-4.3	11.9	6.9	0.0	0.0	0.0	5.0	-6.6	5.6	0.0	0.0	0.0	-12.2
ASN-206	H6	-0.6	-1.0	0.0	0.0	0.0	0.4	-1.4	-1.1	0.0	0.0	0.0	-0.3	0.1	-1.1	0.0	0.0	0.0	1.2
GLU-207	H6	0.7	0.4	0.0	0.0	0.0	0.3	-8.7	-4.4	0.0	0.0	0.0	-4.3	8.4	0.2	0.0	0.0	0.0	8.2
ALA-208	H6	0.2	0.5	0.0	0.0	0.0	-0.2	0.3	0.4	0.0	0.0	0.0	-0.1	0.5	0.6	0.0	0.0	0.0	-0.1
LEU-209	H6	0.2	0.4	0.0	0.0	0.0	-0.2	0.0	0.0	0.0	0.0	0.0	0.0	1.1	1.2	0.0	0.0	0.0	0.0
TYR-210	H6	-0.1	-0.3	0.0	0.0	0.0	0.3	-2.7	-1.9	0.0	0.0	0.0	-0.8	1.0	0.0	0.0	0.0	0.0	1.1
ASP-211	H6	2.7	3.9	0.0	0.0	0.0	-1.3	-8.6	-2.8	0.0	0.0	0.0	-5.8	11.3	3.6	0.0	0.0	0.0	7.7
ILE-212	H6	1.0	1.6	0.0	0.0	0.0	-0.6	1.8	1.8	0.0	0.0	0.0	-1.0	1.2	1.6	0.0	0.0	0.0	-0.4
CYS-213	H6	-0.7	0.2	0.0	0.0	-1.0	0.2	-5.4	-0.3	0.0	0.0	-5.5	-2.4	2.7	1.5	0.0	1.1	-1.0	1.0
PHE-214	H6	2.9	4.2	0.0	0.0	0.0	-1.3	-5.2	-1.2	2.7	0.2	-2.3	-2.4	2.9	-3.8	0.0	0.0	0.0	-0.9
ARG-215	H6-H7	-2.7	-3.5	0.0	0.0	0.0	0.8	10.3	5.0	0.1	0.5	0.0	5.2	-13.8	-5.3	0.0	0.0	0.0	-8.5
THR-216	H6-H7	-9.0	-2.9	3.5	-1.5	-6.7	-1.4	-10.6	-1.7	16.3	-5.2	-21.1	1.1	0.3	1.6	0.0	0.0	0.0	-1.2
LEU-217	H6-H7	-12.7	-0.1	19.2	-6.6	-24.7	-0.6	-7.9	11.5	6.2	-2.8	-14.8	-7.9	-0.6	-0.6	0.0	0.0	0.0	-3.5
LYS-218	H6-H7	-11.9	-62.2	0.0	-0.6	-2.3	53.2	4.8	-35.5	0.1	0.6	-1.5	41.1	-32.4	-29.7	28.0	-4.2	-20.4	-3.0
LEU-219	H6-H7	-1.8	-0.8	0.0	0.0	0.0	-1.0	-0.7	-4.0	0.0	0.0	0.0	3.3	-3.1	-2.0	0.0	0.9	-0.6	-1.1
THR-220	H6-H7	0.4	-0.1	0.0	0.0	0.0	0.4	-1.6	-0.6	0.0	0.0	0.0	-0.9	0.5	-0.6	0.0	0.0	0.0	0.5
THR-221	H6-H7	-0.4	-0.8	0.0	0.0	0.0	-0.8	0.3	0.6	0.0	0.0	0.0	-0.4	0.8	0.2	0.0	0.0	0.0	-0.2
PRO-222	H6-H7	0.1	0.8	0.0	0.0	0.0	-0.5	0.1	1.1	0.0	0.0	0.0	-1.0	0.0	0.2	0.0	0.0	0.0	-0.2
THR-223	H6-H7	-0.4	-1.0	0.0	0.0	0.0	0.5	2.8	1.7	0.0	0.0	0.0	1.1	-0.5	0.2	0.0	0.0	0.0	-0.7
TYR-224	H6-H7	-0.5	-0.9	0.0	0.0	0.0	0.5	-2.5	-1.9	0.0	0.0	0.0	-0.8	-0.9	-2.0	0.0	0.0	0.0	1.1
GLY-225	H7	-0.4	-0.9	0.0	0.0	0.0	-1.7	-2.5	-1.8	0.0	0.0	0.0	-0.7	-2.0	-2.0	0.0	0.0	0.0	0.0
ASP-226	H7	3.6	5.5	0.0	1.0	-1.2	1.6	-17.2	-4.8	0.1	0.8	-2.0	-11.3	11.5	-8.8	1.0	0.4	-4.1	23.0
LEU-227	H7	-10.4	-8.0	0.3	-1.1	-3.3	0.1	-15.1	-10.8	0.4	-0.2	-3.3	-1.3	-15.3	-13.6	0.6	-1.2	-4.0	2.9
ASN-228	H7	-2.2	-3.0	0.0	1.1	-0.3	-0.2	-1.7	-2.3	0.0	0.0	0.0	0.7	-0.5	-0.2	0.0	0.6	-0.5	-0.3
HIS-229	H7	-48.4	-31.8	21.0	-6.5	-31.0	-0.3	-64.7	-50.6	27.5	-9.5	-31.8	-0.3	-15.2	1.4	10.7	-2.4	-18.1	-6.8
LEU-230	H7	-15.5	-9.6	20.7	-5.1	-21.1	0.8	-16.1	-9.3	3.5	-1.4	-1.2	0.3	-20.6	-14.5	5.0	-5.7	-13.0	7.6
VAL-231	H7	6.9	2.1	0.8	4.7	-1.5	-0.1	3.9	1.8	0.1	1.5	0.0	1.6	3.9	4.7	0.2	0.3	-1.1	-0.2
SER-232	H7	-1.8	-1.7	0.0	0.0	0.0	-0.1	1.6	1.1	0.0	0.0	0.0	0.5	1.8	2.8	0.0	0.0	0.0	-0.9

241

Continuation of Table F4

Fragment	2° St.	TXL						DXL						CAB					
		total	ES	EX	CT	DI	G_{sol}	total	ES	EX	CT	DI	G_{sol}	total	ES	EX	CT	DI	G_{sol}
ALA-233	H7	-1.2	5.3	4.2	-1.0	-7.4	-2.4	-5.8	1.6	10.1	-1.4	-12.0	-4.1	-3.5	1.7	0.1	-0.3	-1.9	-3.1
THR-234	H7	-12.7	-9.4	6.0	-1.9	-7.1	-0.3	-10.8	-10.3	3.2	0.8	-7.2	2.6	2.1	3.8	0.0	-1.0	-0.3	-0.3
MET-235	H7	0.4	0.6	0.0	0.6	-0.5	-0.4	-0.5	1.3	0.0	1.3	-0.4	-1.6	0.4	1.7	0.0	0.0	0.0	-1.3
SER-236	H7	-2.9	1.2	4.9	-0.3	-7.1	-1.6	-0.3	4.5	10.4	-4.9	-10.8	0.4	0.3	2.9	0.0	0.0	0.0	-2.7
GLY-237	H7	-8.4	-3.6	1.9	-0.6	-5.5	-0.7	-6.9	-4.9	0.4	-0.2	-2.9	-2.3	-0.3	0.1	0.0	0.0	0.0	-0.4
VAL-238	H7	1.5	1.8	0.1	0.7	-0.4	-0.6	-5.1	4.7	0.0	-0.2	-0.4	0.6	0.0	0.8	0.0	0.0	0.0	-0.8
THR-239	H7	0.7	0.7	0.0	0.0	0.0	0.1	-0.8	0.3	0.0	0.0	0.0	-1.1	0.0	1.2	0.0	0.0	0.0	-1.3
THR-240	H7	0.0	2.3	0.0	-0.2	-1.9	-0.2	4.9	4.0	0.0	0.6	0.0	1.0	0.2	0.4	0.0	0.0	0.0	-0.7
CYS-241	H7	-0.7	-0.5	0.0	0.0	0.0	-0.2	-0.8	1.8	0.0	0.0	-0.8	0.0	0.2	0.7	0.0	0.0	0.0	-0.1
LEU-242	H7	0.7	0.7	0.0	0.0	0.0	0.0	2.1	1.7	0.0	0.0	0.0	0.4	0.3	0.9	0.0	0.0	0.0	-0.6
PHE-272	M-loop	-16.6	-5.3	13.8	-4.2	-18.9	-2.0	-3.0	-0.4	0.0	-0.3	-1.7	-0.6	-18.1	-8.4	3.2	-3.2	-10.1	0.3
ALA-273	M-loop	1.1	1.3	0.0	0.0	0.0	-0.2	-1.0	-1.1	0.0	0.0	0.0	0.0	5.2	4.7	0.0	0.0	0.0	0.5
PRO-274	M-loop	-5.4	-3.5	2.5	-2.4	-7.1	-1.9	1.2	1.4	0.0	0.0	0.0	-0.2	-6.0	1.7	1.1	-1.0	-5.8	-2.0
LEU-275	M-loop	-41.0	-20.2	38.5	-15.4	-43.5	-0.4	-5.5	-1.3	0.4	-0.3	-5.9	1.6	-16.0	-13.2	9.7	-5.5	-22.7	-3.3
THR-276	M-loop	-2.8	3.2	0.8	2.5	-6.5	-2.7	-18.3	-4.8	9.5	-7.2	-14.5	-1.3	-14.7	9.8	0.1	1.0	-2.3	-0.3
SER-277	M-loop	3.1	6.5	0.0	-0.4	-1.3	-1.6	0.0	6.1	0.1	-1.1	-2.7	-2.4	8.6	9.8	0.0	0.7	-1.5	-0.5
ARG-278	M-loop	-3.8	-21.0	0.0	0.0	0.0	17.2	5.7	-6.3	0.0	0.0	0.0	12.0	-66.6	-71.5	18.2	-6.4	-25.0	18.1
GLY-279	M-loop	-0.5	-2.6	0.0	0.0	0.0	2.0	-1.8	-2.7	0.0	0.0	0.0	0.9	-9.5	-10.2	0.0	0.1	-0.2	0.7
SER-280	M-loop	-0.6	-0.2	0.0	0.0	0.0	-0.5	-1.4	1.8	0.0	0.0	0.0	-0.4	5.1	3.7	0.0	0.0	0.0	1.5
GLN-281	M-loop	-0.6	-0.2	0.0	0.0	0.0	-0.4	-0.3	0.9	0.0	0.0	0.0	-1.2	-0.7	-2.3	0.0	0.0	0.0	1.6
GLN-282	M-loop	-17.1	-5.6	2.3	-4.4	-10.9	-9.7	-2.4	-0.1	0.0	-0.7	-0.9	-0.8	-51.8	-43.7	17.2	-8.1	-15.4	-1.8
TYR-283	M-loop	0.0	4.1	0.0	-0.2	-0.7	-3.2	1.7	1.2	0.7	0.0	0.0	0.5	1.1	1.0	0.0	-0.3	-2.5	2.8
ARG-284	M-loop	-1.7	-6.4	0.0	0.0	0.0	4.8	-31.7	-33.1	4.7	-6.2	-11.5	14.4	-22.7	-9.8	0.0	0.0	-0.3	-12.6
ALA-285	M-loop	-0.5	0.5	0.0	0.0	0.0	-1.0	0.4	1.1	0.0	0.0	0.0	-0.5	-2.9	-1.7	0.0	0.0	0.0	-1.2
LEU-286	M-loop	0.4	1.2	0.0	0.0	0.0	-0.9	0.4	0.8	0.0	0.0	0.0	-0.5	-3.5	1.0	0.2	0.1	-2.4	-2.4
THR-287	M-loop	-0.4	-1.6	0.0	0.0	0.0	1.2	-0.1	0.0	0.0	0.0	0.0	-0.1	-1.7	-3.4	0.0	0.1	0.0	1.7
VAL-288	M-loop	-0.6	-0.1	0.0	0.0	0.0	-0.5	-0.2	-0.2	0.0	0.0	0.0	0.1	0.9	0.8	0.0	0.0	0.0	0.1
ARG-320	S8	7.8	14.2	0.0	0.0	0.0	-6.4	20.8	10.9	0.0	-0.8	-1.3	12.0	-9.0	19.7	0.0	0.0	0.0	-28.7
LYS-352	S9	2.3	4.9	0.0	0.0	0.0	-2.7	6.8	4.3	0.0	0.0	0.0	2.6	-6.8	2.9	0.0	0.0	0.0	-9.7
ASP-357	S9-S10	-4.3	-7.3	0.0	0.0	0.0	3.1	-7.4	-2.5	0.0	0.0	0.0	-5.0	6.8	-5.3	0.0	0.0	0.0	12.0
ILE-358	S9-S10	-0.2	0.1	0.0	0.0	0.0	-0.2	0.9	1.0	0.0	0.0	0.0	-0.1	0.4	-0.5	0.0	0.0	0.0	-0.1
PRO-359	S9-S10	-0.2	-0.1	0.0	0.0	0.0	-0.1	-2.5	-2.5	0.0	0.0	0.0	0.0	-0.9	-0.3	0.0	0.0	0.0	-0.7
PRO-360	S9-S10	-5.8	-2.3	2.2	-3.7	-7.7	1.1	-2.4	-1.2	0.0	0.0	0.0	-1.2	-3.4	1.9	0.0	0.7	-1.2	-4.8
ARG-369	S9-S10	-46.5	-12.3	12.0	-12.2	-30.6	-3.4	16.1	1.6	1.8	-3.7	-11.0	27.4	-29.9	15.9	21.5	-8.7	-30.1	-28.5
GLY-370	S9-S10	-82.5	-87.2	39.1	-12.8	-17.9	-3.8	1.6	3.9	0.0	-1.2	-1.8	0.6	-28.6	-18.7	9.2	-7.3	-16.7	5.0
LEU-371	S9-S10	-12.3	3.9	13.8	-7.3	-25.6	2.8	-1.8	2.5	0.0	-1.1	-1.9	-1.3	-18.4	-8.9	12.6	-4.5	-27.6	10.0
LYS-372	S9-S10	1.8	12.0	0.0	-1.3	-0.5	-5.6	2.9	-4.9	0.0	0.0	0.0	7.9	-0.9	10.1	0.0	0.0	-0.6	-24.0
MET-373	S9-S10	-3.4	-2.2	0.0	-0.8	0.0	-0.4	-1.0	-1.1	0.0	0.0	0.0	0.1	1.1	2.0	0.0	0.0	0.0	-2.8
SER-374	S9-S10	2.5	-2.8	0.0	0.0	-1.0	1.3	0.8	1.3	0.0	0.0	0.0	-0.4	-0.9	-0.1	0.0	0.0	0.0	1.2
GDP			-0.8	0.0	0.0	0.0	3.3	-21.1	-12.8	0.0	0.0	0.0	-8.3	18.0	-9.1	0.0	0.0	0.0	27.1